UC Irvine
UC Irvine Electronic Theses and Dissertations

Title
Iron Pyrite Absorbers for Solar Photovoltaic Energy Conversion

Permalink
https://escholarship.org/uc/item/8042w4kd

Author
Limpinsel, Moritz

Publication Date
2015

Copyright Information
This work is made available under the terms of a Creative Commons Attribution-NonCommercial-ShareAlike License, availalbe at https://creativecommons.org/licenses/by-nc-sa/4.0/

Peer reviewed|Thesis/dissertation

eScholarship.org Powered by the California Digital Library
University of California

UNIVERSITY OF CALIFORNIA,
IRVINE

Iron Pyrite Absorbers for Solar Photovoltaic Energy Conversion

DISSERTATION

submitted in partial satisfaction of the requirements
for the degree of

DOCTOR OF PHILOSOPHY

in Chemical and Materials Physics

by

Moritz Limpinsel

Dissertation Committee:
Professor Matt Law, Chair
Professor John Hemminger
Professor Robert Corn

2015

Part of section 4.1 adapted with permission from [22]. © 2012 American Physical Society
Part of section 3.1, section 2.1.3 and section 5.3.2 adapted with permission from [6]. © 2012 WILEY-VCH Verlag
Part of section 3.1 adapted with permission from [97]. © 2013 American Chemical Society
Part of section 4.4 and section 2.1.2 adapted with permission from [70]. © 2014 The Royal Society of Chemistry
All other materials © 2015 Moritz Limpinsel

DEDICATION

This work is dedicated to my parents, Hans-Dieter Limpinsel and Christel Limpinsel. None of this would have been possible without their emotional and financial support, adamant belief in me, and their boundless and unconditional love for me.

Danke!

TABLE OF CONTENTS

LIST OF FIGURES

LIST OF TABLES

ACKNOWLEDGMENTS

Getting to this point, sitting here writing the acknowledgments of my PhD thesis, was a major project and a wild adventure. It was only made possible by the help of many others, who I would like to thank here.

I would like to thank my advisor Prof. Matt Law for guiding my research in these past years. I feel very fortunate that I was given every opportunity in his lab, to work on a DOE project while being free to pursue my own research ideas. Among the many things I learned while working for and with Prof. Law, I appreciate his strict adherence to scientific method, deep knowledge of literature and perfection in execution. It remains a mystery to me how he found the time, but he always managed to stay on top of my research, be quickly responsive to all my questions and show me the nuts and bolts of vacuum equipment hands-on in lab. Thanks to his brilliant and foresighted research proposals, I had access to state-of-the-art equipment in our lab, at UCI LEXI and with collaborators nationwide. I acknowledge financial support from the U.S. Department of Energy under Contract No. DE-EE0005324, funded by the SunShot Next Generation Photovoltaics II (NextGenPVII) program.

My fellow graduate student researchers were outstanding. Many of them went out of their way and invested their own scarce time to help me. There are too many to mention all, but I do need to give a special thanks to soon-to-be-Dr. Nima Farhi, Dr. Nick Berry, Dr. Amanda Weber, Dr. Jason Tolentino and Dr. Vineet Nair!

Staff at UCI was very helpful and made this work possible. I used many facilities and appreciate the ease of access to all of them and the knowledgeable and supportive staff who keep them running. A special thank you goes to Lee Moritz of the Physical Sciences Machine Shop, Dr. Qiyin Lin and Dr. Jian-Guo Zheng of LEXI, Steve Kaiser and Cyril McCormick of the electronics shop, and Jake Hes of INRF.

This work is dedicated to my parents, who I cannot acknowledge enough. I also very grateful to my big sister Caro and my nieces Lea and Anna, all of who I missed dearly these last years. Thank you for being so patient and supportive, and for your many thoughtful letters and packages that brightened my days. I love you and I am looking forward to living close to you again one day!

I came here all alone in 2010, knowing no one. Fresh off the boat, I was lucky to meet so many fascinating people and I am blessed to call many of them my friends today. Roommates, fellow international students, co-workers, brilliant chemists, physicists and engineers, surfer bros and girls, gym buddies, yogis and philosophers. You know who you are, thanks for being a part of my life!

Last but not least, I would like to thank my girlfriend Salma. Her last name translates to *math*, and if that isn't destiny, then I don't know what is. Thanks Joon for distracting me from work when I needed it, supporting my work when I needed it, and for all our awesome adventures together... To many more!

CURRICULUM VITAE

Moritz Limpinsel

EDUCATION

Doctor of Philosophy in Chemistry and Materials Physics **2015**
University of California, Irvine *Irvine, California*

Diplom in Nanotechnology **2009**
University of Würzburg *Würzburg, Germany*

Vordiplom in Physics **2005**
University of Würzburg *Würzburg, Germany*

RESEARCH EXPERIENCE

Graduate Research Assistant **2010–2015**
University of California, Irvine *Irvine, California*

Graduate Research Assistant **2008–2009**
University of Würzburg *Würzburg, Germany*

TEACHING EXPERIENCE

Teaching Assistant **2010–2011**
University of California, Irvine *Irvine, California*

Teaching Assistant **2007–2008**
University of Würzburg *Würzburg, Germany*

REFEREED JOURNAL PUBLICATIONS

An inversion layer at the surface of n-type iron pyrite **2014**
M. Limpinsel, N. Farhi, N. Berry, J. Lindemuth, C. L. Perkins, Q. Lin and M. Law
Energy & Environmental Science

Iron pyrite thin films synthesized from an $Fe(acac)_3$ ink **2013**
S. Seefeld, M. Limpinsel, Y. Liu, N. Farhi, Y. N. Zhang, N. Berry, J. Kwon, C. Perkins, J. C. Hemminger, R. Q. Wu and M. Law
Journal of the American Chemical Society

Atmospheric-pressure chemical vapor deposition of iron pyrite thin films **2012**
N. Berry, M. Cheng, C. Perkins, M. Limpinsel, J. C. Hemminger and M. Law
Advanced Energy Materials

Pseudodielectric function and critical point energies of iron pyrite **2012**
S. Choi, J. Hu, L. S. Abdallah, M. Limpinsel, Y. N. Zhang, S. Zollner, R. Q. Wu and M. Law
Physical Review B

Photocurrent in bulk heterojunction solar cells **2010**
M. Limpinsel, A. Wagenpfahl, M. Mingebach, C. Deibel and V. Dyakonov
Physical Review B

Polymeric squaraine dyes as electron donors in bulk heterojunction solar cells **2010**
S. F. Voelker, S. Uemura, M. Limpinsel, M. Mingebach, C. Deibel and V. Dyakonov
Macromolecular Chemistry and Physics

REFEREED CONFERENCE PUBLICATIONS

Strategies for increasing the photovoltage of solid-state iron pyrite solar cells **2014**
M. Limpinsel, N. Farhi, N. Berry, A. Weber, J. Lindemuth, C. L. Perkins, Q. Lin and M. Law
MRS Electronic Materials Conference

Strategies for increasing the photovoltage of iron pyrite for photocells **2014**
M. Limpinsel, N. Farhi, N. Berry, A. Weber, J. Lindemuth, C. L. Perkins, Q. Lin and M. Law
MRS National Spring Meeting

Electrical transport and compensation in iron pyrite (FeS_2) **2013**
M. Limpinsel, N. Berry, N. Farhi, Q. Lin, J. Lindemuth and M. Law
245^{th} ACS National Meeting

Electrical transport and compensation in iron pyrite (FeS_2) **2013**
M. Limpinsel, N. Berry, N. Farhi, Q. Lin, J. Lindemuth and M. Law
MRS National Spring Meeting

Bulk vs. surface recombination in polymer-fullerene solar cells **2009**
C. Deibel, T. Strobel, A. Wagenpfahl, M. Limpinsel, M. Mingebach and V. Dyakonov
SPIE photonic devices and applications, conference proceedings paper

ABSTRACT OF THE DISSERTATION

Iron Pyrite Absorbers for Solar Photovoltaic Energy Conversion

By

Moritz Limpinsel

Doctor of Philosophy in Chemical and Materials Physics

University of California, Irvine, 2015

Professor Matt Law, Chair

Iron pyrite (cubic FeS_2) is an earth-abundant, non-toxic semiconductor with great potential as an absorber material in future large-scale deployment of solar photovoltaic panels. The surprisingly small photo-voltage generated by this material (< 0.2 V) has limited its solar cell efficiency and prevented its commercial development to date. The origin of this limitation has been discussed over the past 30 years, and is addressed here. Electrical measurements of high-purity single crystals are used to show that there is a thin, conductive inversion layer on the surface of n-type pyrite. Tunneling of charge carriers across this inversion layer can result in losses that account for the low voltage of pyrite solar cells. This finding is in line with experiments presented here that show a clear dependence of electrical transport properties on the surface-to-bulk ratio of a given pyrite material. The hole-rich surface can explain why the great majority of pyrite thin films are reported to be p-type regardless of synthesis technique or composition. A quantitative model for multilayer transport in pyrite is established that can be used to predict the effect of surface passivation, and methodically evaluate a variety of suggested passivation treatments. Chemical etching, as well as annealing in certain atmospheres, can substantially reduce the conductivity of the inversion layer, and further treatments are proposed to eliminate it. Lastly, novel all-solid-state pn-heterojunction solar cells with pyrite absorbers are presented, that overcome the 0.2 eV photo-voltage limitation. Overall, this work represents an important step towards

fully understanding the short-comings of pyrite absorbers. A clear path forward, along with the necessary tools and methods, is shown to enable pyrite to live up to its potential of becoming a low-cost, non-toxic, earth-abundant absorber material for deployment of solar photovoltaics on the terawatt scale.

1” by 1” pyrite thin film with photo-patterned silver logo

Chapter 1

Introduction

1.1 Solar Photovoltaics as a Renewable Energy Source

One of the great challenges of our time is to find inexpensive, widely-available, clean and safe alternatives to fossil and nuclear fuels. Clean in this context means without pollution, emission of green-house gases or other harmful effects on people or environment. Solar energy fits this bill and is widely expected to continue, combined with other renewable energy sources, to replace non-renewable energy sources. Solar energy generation can be divided into three different but often complementary approaches, as shown in figure 1.1. The first approach is to use the sun's thermal energy to heat a medium, for example water, oil or molten salt. This thermal energy can be used for heating, stored in the medium for later use, or it can generate steam from water to drive turbines, outputting electric energy. The second approach is to mimic photosynthesis and let the sunlight drive a photochemical process to create a fuel, for example by splitting water into oxygen and hydrogen. The third approach is to directly convert sunlight into electric energy via the photovoltaic effect[29] in semiconductors.

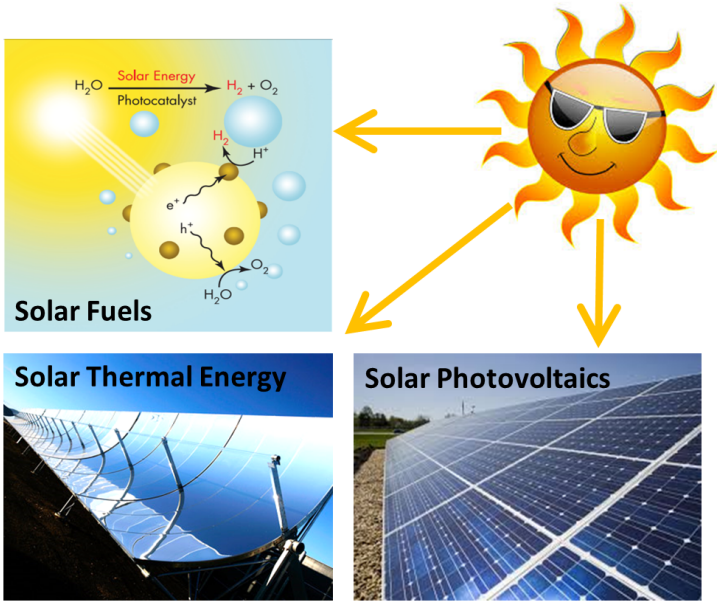

Figure 1.1: Three approaches to harvest the sun's energy.

The basic principles of a photovoltaic cell are shown in fig. 1.2. The dominant technology for a long time has been crystalline silicon (Si), and it still is today. Si can be doped n-type (for example with P) and p-type (for example with B) by thermal diffusion, enabling pn-homojunctions in the same Si wafer. The such created pn-junction turns into a photovoltaic cell under illumination, by creating electron-hole pairs (excitons) and splitting them in the internally created electric field.

Photovoltaic (PV) panels have been used to harvest the sun's energy for satellites since the 1950s, but their cost has long been limiting them to niche applications such as space travel, off-grid installations and mobile devices. The last decade however has seen a remarkable transformation of the PV industry and market. For the first time, generation of electricity by this renewable energy source became price-competitive with electricity from fossil fuels without subsidies in many sun-rich countries.[27,10] This so-called "grid-parity" is driving massive growth of PV installations world-wide (fig. 1.3).

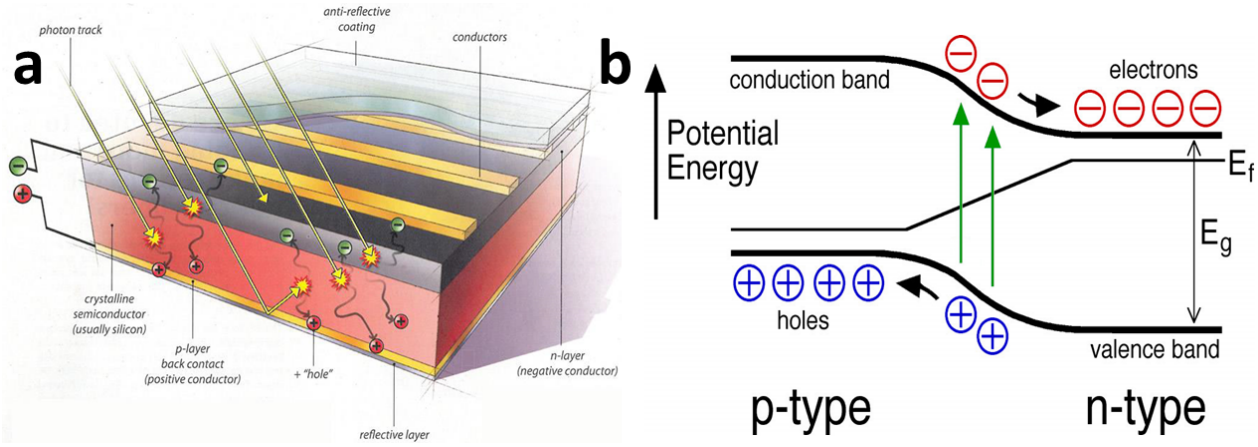

Figure 1.2: Basic principles of a photovoltaic cell. (a) Diagram showing the device architecture most commonly used in photovoltaics cells. Light is absorbed in both p-type and n-type layer (for example Si), creating electron-hole pairs, called excitons. These excitons are split in the internal electric field, and electrons are collected at the top contact, holes at the back contact. Image courtesy of Kurt Struve, SEIA. (b) Schematic energy band diagram for illuminated pn-junction, illustrating the same process of charge generation and separation. Under these non-equilibrium conditions, the Fermi level is different in n-type and p-type layer, the difference is the maximum obtainable photo-voltage V_{OC}. Image courtesy of UW MRSEC Education Group.

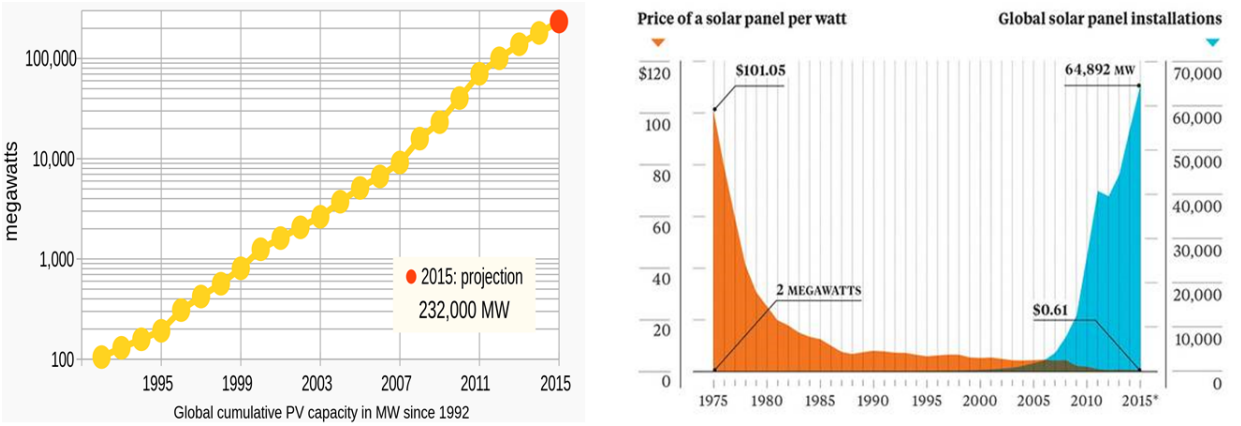

Figure 1.3: Cumulative PV installations and economies of scale. Left: Global cumulative PV installations since 1992, showing exponential growth rate. Right: While yearly global installations (blue, right axis) grow exponentially, solar panel prices (orange, left axis) follow roughly with an exponential decrease, as expected for economies of scale. Both images by Ramez Naam.

This growth in PV installations was driven partially by state initiatives and subsidies, but more importantly by ever decreasing costs of PV panels (fig. 1.3). This cost reduction was made possible by intensive research on silicon, the dominant absorber material used for PV panels, advances in materials science, lean fabrication methods and economies of scale. In addition to improvements in silicon-based PV technology, new absorber materials were developed and contributed to keep pressure on the PV industry to reduce costs. the most notable new materials developed as PV absorbers are CdTe and CIGS.

In order to enable further growth of PV as a global energy source, and for future deployment on the TW scale, the absorber material has to be inexpensive, nontoxic and earth-abundant. The fundamental problem with silicon is that its absorption coefficient is so low that absorber layers have to be about 100 μm thick in order to capture enough light. But the absorber thickness also has to comparable to the minority carrier diffusion length in order to efficiently capture charge carriers, which imposes the need for extreme purity on silicon. Single crystal silicon wafers have to produced by very energy-intensive methods to achieve the necessary level of purity. While advances in fabrication technology have brought this cost down, this purity requirement poses a limit to how much further costs can be reduced for silicon-based PV panels.

1.2 Earth-Abundant Semiconductors for Large Scale Photovoltaics

The ideal photovoltaic absorber material will be earth-abundant, inexpensive and non-toxic, to allow mass production. Silicon matches all these. Additionally, there are some requirements for material properties. First, the electric band gap should be close to the ideal range of 1.0 - 1.6 eV, again matched by Silicon (1.12 eV). Second, the absorption coefficient α

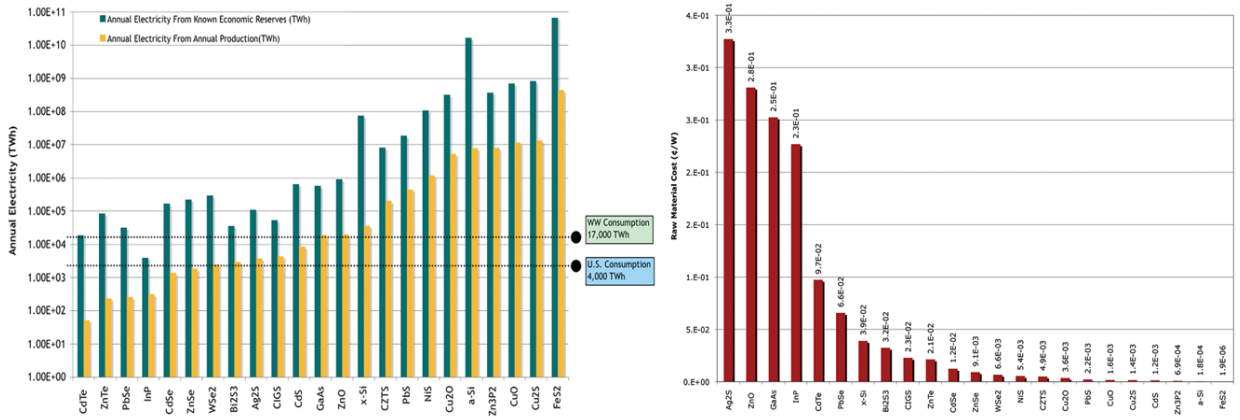

Figure 1.4: Potential for electricity production and raw material cost. Both figures are taken from [113]. Left: Annual electricity production potential, based on known economic reserves (blue) and annual production (yellow), for 23 inorganic PV materials. Right: Minimum cost (US cent/W) for 23 inorganic PV materials, base on raw material cost.

should be greater than 10^5 cm^{-1} above the band gap, to allow for ultra-thin absorber layers that reduce cost and also allow for flexible and light-weight solar panels. This is where Si is lacking, with $\alpha < 10^4$ cm^{-1} for most of the visible spectrum. Lastly, material parameters like charge carrier mobilities and lifetimes have to be sufficiently large to make a given absorber material in a given solar cell architecture efficient.

In a recent study by Wadia et al.,[113] a wide range of potential PV absorber materials was evaluated for availability and cost for terawatt-scale installation (see fig. 1.4). Iron Pyrite FeS_2 topped the list for both metrics, re-sparking research interest in a material that had been studied in the 1980s and 1990s for solar applications.

1.3 Iron Pyrite FeS_2

1.3.1 Review of Material Properties

Iron pyrite FeS_2 (henceforth referred to as "pyrite") is an earth-abundant, rock-forming mineral. As stated above, pyrite has huge potential for inexpensive terawatt-scale generation of photovoltaic energy. Like silicon, it is earth-abundant, non-toxic and has both suitable band gap and carrier diffusion length. In addition, its absorption coefficient is about 1000 times higher than silicon's, allowing for absorber layers as thin as 100 nm. This makes pyrite a very interesting material to study for PV applications.

Pyrite crystallizes in a cubic $Pa\overline{3}$ lattice, that can be envisioned by replacing the the sodium ions in NaCl with Fe^{2+} ions and the chloride ions with S_2^{2-} 'dumbbells'. In its pure form, pyrite is a semiconductor, but phase impurities that can cause metallic behavior are common in natural crystals. Upon heating, pyrite loses elemental sulfur and undergoes transitions to greigite (Fe_3S_4), smythite (Fe_9S_{11}), pyrrhotite (Fe_7S_8) and troilite (FeS). Further, there is another metastable phase of FeS_2, the orthorhombic marcasite. Its formation energy is slightly higher than that of pyrite, so it can be removed by thermal annealing. However, in order to prevent sulfur loss and creation of the sulfur deficient phase, this thermal annealing has to be performed in sulfur rich atmosphere.

Pyrite was studied for use in solar photovoltaics in the 1980s and 1990s, most notably in the group of Helmut Tributsch in Berlin. This was motivated by successful preparation of phase-pure pyrite thin films and single crystals with suitable carrier diffusion length and electronic band gap. Experimental values for the band gap have been obtained with different techniques and scatter significantly, but the most reliable studies agree on a value of 0.9 eV for an indirect band gap and a direct transition at slightly higher energy.[34,90] The valence band is derived from Fe 3d states, while the conduction band edge is mostly derived from S 3p states (see figure 1.6)

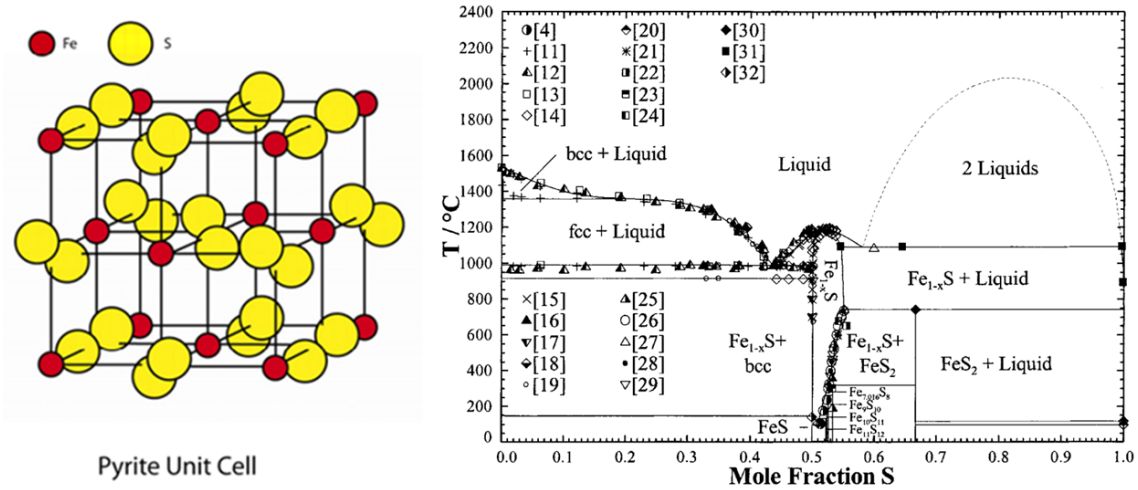

Figure 1.5: Left: Unit cell of iron pyrite FeS_2, image courtesy of Matt Law. Right: Fe-S phase diagram, reproduced from [114].

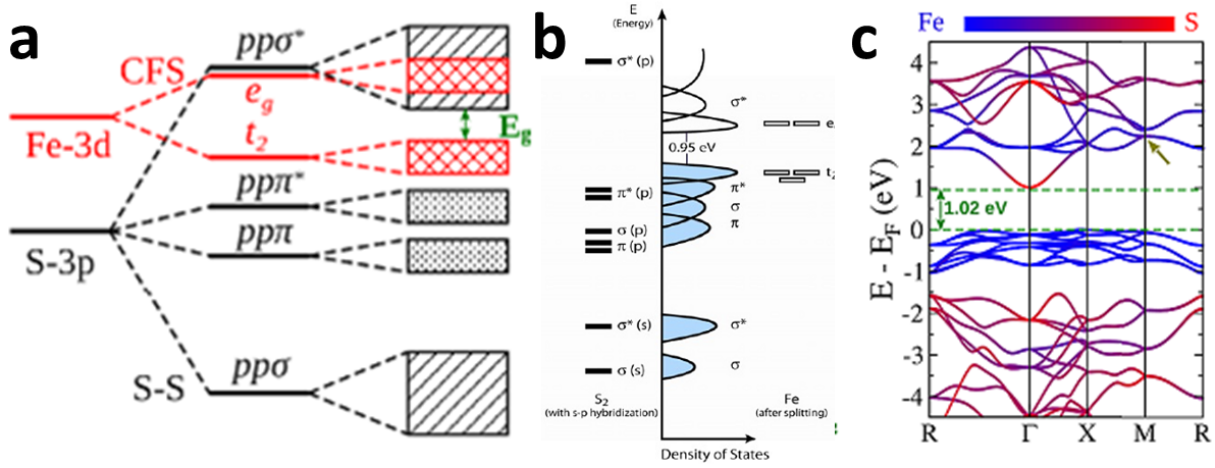

Figure 1.6: Electronic structure of bulk pyrite. (a) and (b): Schematic band structure derived from atomic Fe and S states. (c): DFT calculated band structure of bulk pyrite with a color scale indicating the contributions from Fe and S atoms. Images reproduced from reproduced from [33] and [53].

Synthetic single crystals of high quality have been grown by chemical vapor transport[40] and in a tellurium flux.[41] Electrodes prepared from these crystals demonstrated high photocurrents in liquid junctions to the I^-/I^{3-} redox couple in electrochemical cells.[36] However, the overall power conversion efficiency (PCE) was limited to 2.8 % because of a low open-circuit voltage (V_{OC}) of only about 200 mV. Several explanation for this unexpectedly low V_{OC} have been discussed in literature.

(i) Marcasite, the polymorph of pyrite, has long been suspected to have a much smaller band gap,[107] thus having detrimental effects even in very low concentrations. However more recent studies suggests this not to be the case.[102,97]

(ii) Sulfur deficiencies in pyrite have been discussed in literature. For nominally stoichiometric FeS_2 there are two possible ways that sulfur deficiencies might be hard to detect, but detrimental to electronic properties. First, small concentrations of sulfur vacancies (on the order of 1% or less) would be hard to detect by mass spectroscopy, but could create defect states in the band gap in significant concentration. Second, small amounts of sulfur deficient, secondary phases with domains on the nm scale would be hard to detect by structural analysis (XRD, Raman spectroscopy), especially if those phases are amorphous.

(iii) At the surface of a pyrite crystal Fe atoms are under-coordinated with five S atoms instead of the 6 S atoms octahedrally surrounding every Fe in the bulk lattice. This loss of symmetry causes the Fe 3d states to lose their degeneracy and split into surface states that lie within the band gap.

(iv) If the band gap is significantly lower than the generally accepted value of 0.9 eV, this could easily explain the low V_{OC} results. Most values reported for pyrite's band gap are obtained from optical absorption measurements, which might not be sensitive enough to pick up a low density of states in a hypothetical tail of states extending below the conduction band or above the valence band. Careful electric resistivity measurements in the intrinsic regime are necessary to test this.

As shown in great detail below, the present work rules out explanations (i) and (iv). Expla-

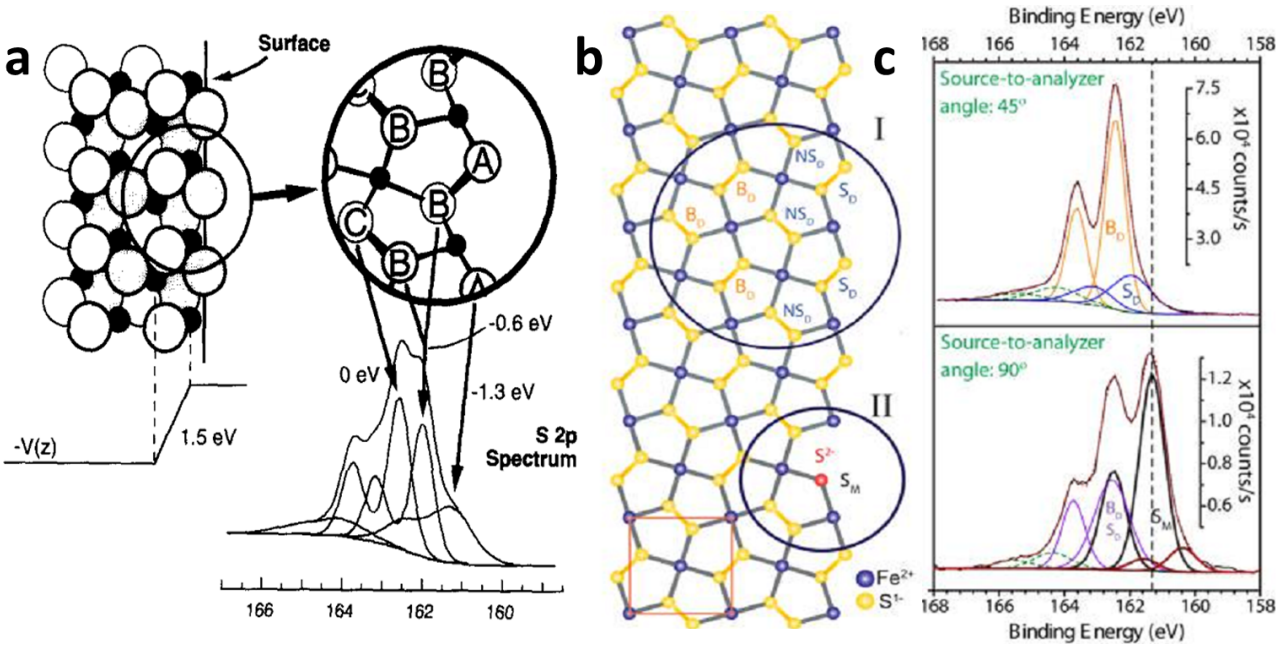

Figure 1.7: XPS study of sulfur species at the pyrite 100 surface. (a) Assignment of the S 2p spectral components to the S atoms near the surface, reproduced from Bronold et al. 1994.[14] Left: arrangement of the atoms (black dots Fe, circles S) and potential normal to the surface. Right: magnification of the outermost atomic layers, separation of S atoms into three types, and assignment to the spectrum. Panels (b) and (c) confirm these earlier results, reproduced from Caban-Acevedo et al. 2014.[19] (b) Circle I shows the intrinsic outermost surface (S_D), near-surface (NS_D) and bulk-like (B_D) disulfide (S_2^{2-}) species. Circle II shows a representations of the sulfur monomer (S^{2-}) species resulting from sulfur vacancies (S_M). (c) S 2p peak comparison between spectrometers with a geometry of 45° (45° takeoff angle, ∼60° acceptance angle) and 90° (45° takeoff angle, ∼4° acceptance angle).

nation (ii) is likely a contributing factor, and the most likely reason for the high concentration of deep bulk donor states discussed in this work. However, pyrite can never be an efficient PV absorber material without understanding and passivating its problematic surface (explanation (iii)). The surface is focus of much of this work, which is why a summary of past findings of pyrite surface characterization is given here.

Figure 1.7a shows XPS results of a pyrite 100 surface, from a single crystal cleaved in ultra-high vacuum (UHV), published in 1994 by Bronold et al.[14] Upon cleavage, both Fe - S and S - S bonds must be broken. Single sulfur atoms should have higher electron density than sulfur atoms in a S_2^{2-} dumbbell, and sulfur atoms in a dumbbell right at the surface

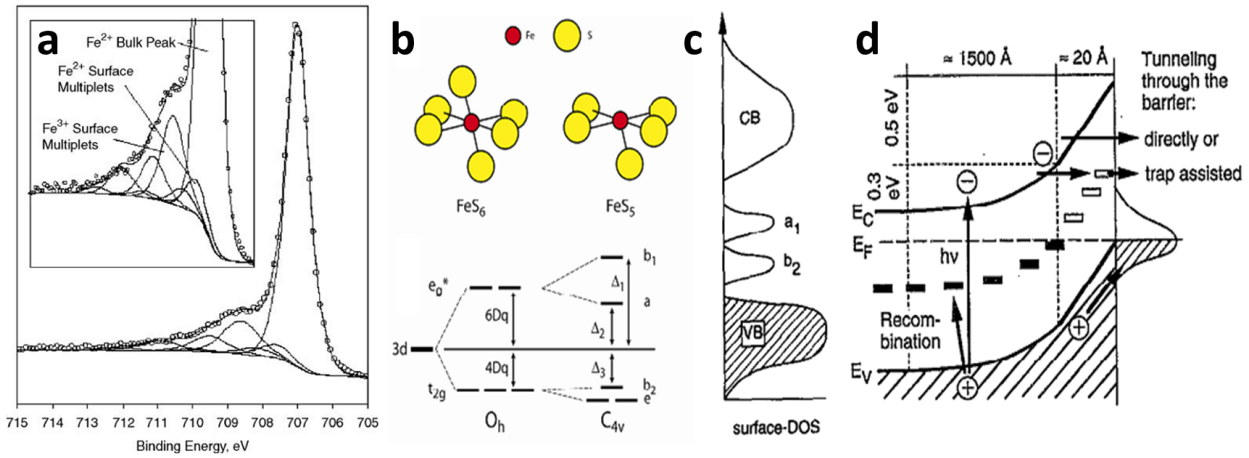

Figure 1.8: XPS study of iron species at the pyrite 100 surface and consequences for electronic structure. (a) Fe 2p spectrum of the pristine pyrite fractured surface, reproduced from Oertzen et al. 2006.[112] The data is fit using bulk Fe^{2+}, as well as blue-shifted Fe^{2+} and Fe^{3+} multiplets due to Fe-S bond fracture. (b) and (c): Loss of octahedral coordination for surface iron, adapted from Bronold et al. 1994.[14] The surface Fe^{2+} site coordination is reduced from 6- to 5-fold and from O_h (bulk) to C_{4v} (surface) symmetry, resulting in the two intra-gap states a a_1 and b_2 shown in (c). (d) Surface band diagram, reproduced from Bronold et al. 1994.[13] The combination of mid-gap donor states and surface acceptor states results in a steep potential drop (≈20 $\AA$) near the surface and a regular depletion layer of about 1500 $\AA$ width. Tunneling losses through the narrow potential barrier at the surface are indicated.

should still have higher electron density than in dumbbells in the bulk. And indeed the XPS data can clearly distinguish between these three sulfur species (A, B and C). This result was confirmed by other authors for (UHV cleaved or chemically cleaned) pristine pyrite surfaces.[82,28,93,112] Additional confirmation comes from depth-profiling by angle-resolved XPS, as shown in fig. 1.7c.[19]

While S 2p peaks are more extensively studied to understand the pyrite surface, due to larger peak shifts that are easier deconvoluted, the Fe 2p spectra confirm the picture of cleaved Fe-S bonds, without reconstruction of the surface in vacuum. As shown in fig. 1.8a, a UHV-cleaved pyrite 100 surface exhibits a high-energy tail on the Fe 2p peak. This tail can be deconvoluted into contributions from Fe^{2+} and Fe^{3+} surface species. The Fe^{2+} surface energy is shifted relative to the Fe^{2+} bulk energy due to loss of octahedral coordination (fig. 1.8b). The loss of symmetry results, according to crystal field theory, in a splitting of the Fe 3d

orbitals (fig. 1.8b) and introduction of two electronic defect states. The first, derived from the e_g^* orbital and denoted a_1 in fig. 1.8c, is close to mid-gap, while the second, derive from the t_{2g} orbital and denoted b_2, is close to the valence-band (VB) maximum. It is likely that a_1 acts a s a deep donor and b_2 acts as a shallow acceptor state. It was suggested by Bronold et al. that this symmetry-reduction, caused by S-vacancy point-defects, is also causing deep donor states in the bulk, and results in a band diagram as shown in fig. 1.8d. In this scenario, a very steep band bending near the surface would enable tunneling losses that limit the photo-voltage V_{OC} in pyrite.[13] However, more recent DFT calculations seem to rule out a significant number of S-vacancy states in the bulk, at least as simple point-defects.[52] As mentioned, he high-energy tail of the Fe 2p peak has a contribution from surface Fe^{3+}. This species is likely formed by charge transfer to lone S^- that was created by homolytic S - S bond cleavage, making it monosulfide S^{2-}, which is also observed in XPS (eq. (1.1) and eq. (1.2)).

$$S_2^{2-} \rightarrow S^- + S^- \tag{1.1}$$

$$S^- + Fe^{2+} \rightarrow S^{2-} + Fe^{3+} \tag{1.2}$$

It should be noted that Fe^{3+} is observed on surface cleaved in UHV, without any oxygen present.[82,112] However, these Fe^{3+} sites are an important intermediate for surface oxidation in the presence of O_2 or H_2O. An oxidation mechanism in ambient conditions proposed by Schaufuss et al.[93] is shown in fig. 1.9.

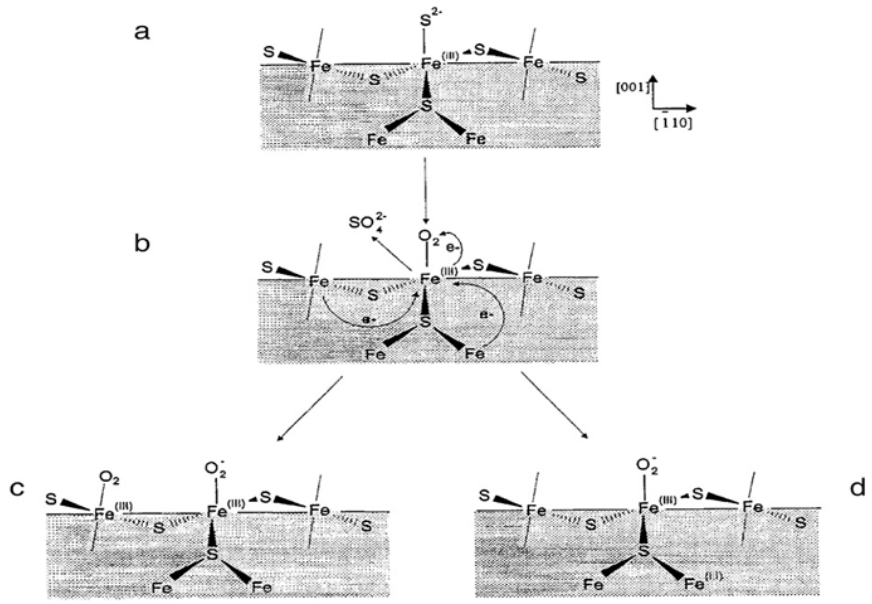

Figure 1.9: Oxidation mechanism for the pyrite surface, after Schaufuss et al.[93] (a) Vacuum-fractured surface after charge transfer from Fe(II) to S^-. (b) Surface after oxidation of S^{2-} and adsorption of oxygen at Fe(III) surface sites. (c) Electron transfer from adjacent Fe(II) surface sites, producing new Fe(III) sites equivalent to the initial Fe(III) centers. (d) Result of the electron transfer from adjacent bulk Fe atoms forming the Fe(III) sites in the bulk, which may propagate oxidation into the depth. Figure reproduced from [79].

1.3.2 Open Questions

While all reports agree that low open circuit voltage ($V_{OC} \leq 0.2$ eV)) is the main reason for poor solar cell performance, the cause of this problem is not well understood yet. As mentioned above, Bronold et al. suggested a mechanism that is consistent with most reports published to date,[14,13] but direct observation and quantization of the surface defect state is still lacking, keeping discussions about other possibilities, like nano-scale phase-impurities, alive. A few open question regarding pyrite's suitability as a solar absorber material remain, and will be addressed in this work. For example it is puzzling that all (nominally intrinsic) thin films are p-type, while all (nominally intrinsic) single crystals are n-type. There is also some doubt about the whether the electronic and optical band gaps really agree with the long-accepted value of 0.95 eV, or if maybe one is smaller. Further, a change of electrical transport mechanism at low temperatures is observed, along with an uncommon minimum and sign change in the Hall coefficient R_H, neither of which are understood yet.

1.3.3 Scope of This Work

This work addresses and answers a number of open questions regarding pyrite's material properties and suitability as a solar absorber. It represents an important step towards fully understanding the short-comings of pyrite absorbers, and developing the methods necessary to enable pyrite to live up to its potential of becoming a low-cost, non-toxic, earth-abundant absorber material for deployment of solar photovoltaics on the terawatt scale.

Chapter 2 gives an overview of all experimental and computational methods used in this work. Chapter 3 summarizes important findings on a variety of pyrite thin films, that were characterized regarding their electrical transport properties and later used to fabricate solar cells, along with findings on other thin films relevant for these solar cells. The electrical transport properties of these thin films are compared to macroscopic single crystals as well

as mesoscopic systems in chapter 4, demonstrating the dependence on surface/bulk ratio. This dependence on surface properties is then discussed in more detail in the same chapter, and a quantitative transport model is introduced that takes into account parallel transport in bulk and surface. Base on this model and ultra-high purity single crystals, preliminary results on surface passivation are presented. Chapter 5 presents work on pyrite solar cells, including novel, all solid state pn-heterojunction thin film solar cells, that overcome the 0.2 eV photo-voltage limitation. Finally, chapter 6 summarizes the whole dissertation and gives suggestions for follow-up work in order to maximize its impact.

Chapter 2

Methods

2.1 Synthesis of Iron Pyrite

Pyrite single crystals of regular shape and impressive size can be found in nature, purchased inexpensively and have been used in many scientific studies before. However, it was found after some initial experiments that their often poor elemental purity results in large variations of electronic properties, making these crystals unfit for meaningful analysis of fundamental material properties. High-purity pyrite samples, both single crystals and polycrystalline thin films, were thus synthesized by a number of methods as described below.

2.1.1 Chemical Vapor Transport (CVT)

A carrier gas like Br_2 or Cl_2 can be used to transport pyrite in a quartz tube across a temperature gradient from high to low temperature.[40] At the cold end, one or more single crystals will nucleate and grow over the course of several days. Guided by previously published results, single crystals up to 3 mm in size were grown using the following procedure:

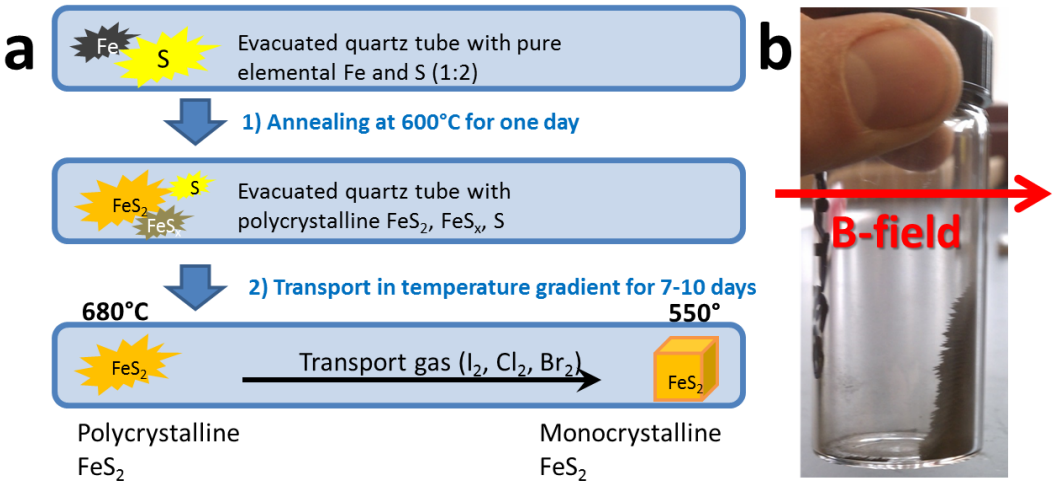

Figure 2.1: Chemical Vapor Transport (CVT) method for growing phase-pure pyrite single crystals. (a) Schematic showing the two reaction steps for 1) obtaining polycrystalline FeS_2 and 2) growth of monocrystalline FeS_2. (b) A magnetic field is used to separate the FeS_2 precursor from magnetic Fe_xS_y phases after step 1.

Polycrystalline precursor material was obtained by reacting elemental iron powder (4N purity) and elemental sulfur (5N purity) in a molar ratio of 1:2. The reaction took place in evacuated quartz tubes at 600 °C for one day. The resulting material was always a mix of pyrite FeS_2 and pyrrhotite FeS_x (determined by X-ray diffraction (XRD)), along with some sulfur left unreacted in the quartz tube. This is a result by reaction kinetics: the diffusion of sulfur through pyrrhotite is orders of magnitude slower than through iron.[78] One solution to this is to finely grind the mixed material, add sulfur and repeat the reaction, increasing the pyrite content every time. But another method was found to be more practical and time-efficient. A strong magnet was used to filter out the ferrimagnetic pyrrhotite leaving behind the diamagnetic pyrite (fig. 2.1). This method worked well to obtain multiple grams of pyrite precursor material per batch. The chemical vapor transport (CVT) was then carried out by adding $FeBr_2$ or $FeCl_2$ (5N purity) to the pyrite precursor in a quartz tube of about 15 cm length and placing it in a temperature gradient of 680 to 550 °C. After 7 - 10 days, multiple pyrite crystals up to 26 mg in size were found at the cold end.

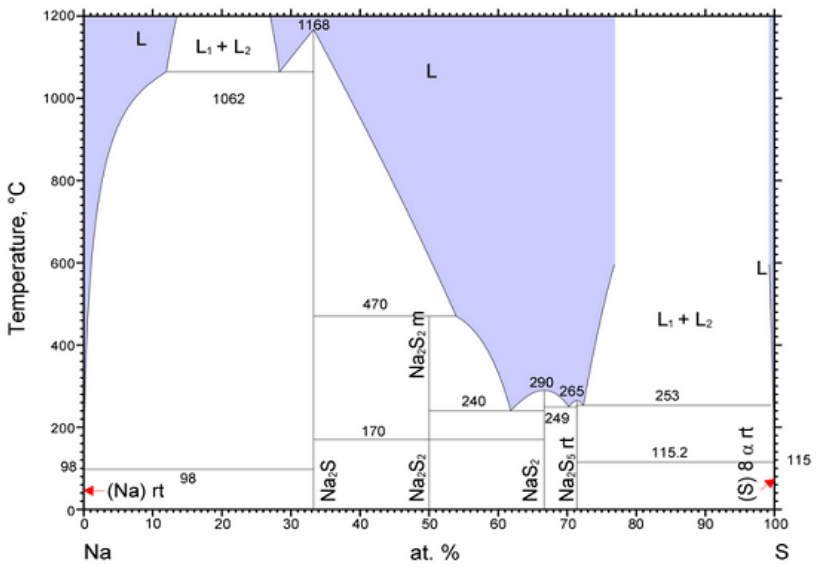

Figure 2.2: Na-S binary phase diagram (data from [91]). Mixtures of Na_2S and S have eutectics as low as 240 °C. There is also a region of binary liquid immiscibility above 253 °C near the sulfur-rich end of the system.

2.1.2 Flux Growth

Our lab developed a novel method of flux growth for pyrite single crystals that yields single crystals up to 1000 mg in a single day. The method was introduced by Nick Berry and improved upon by Nima Farhi, and provided high-quality pyrite single crystals that were so crucial for this work. The following procedure is published in [70].

Pyrite single crystals were synthesized in sodium polysulfide flux[94, 60] by heating an evacuated quartz ampoule containing a crucible filled with high-purity iron, sulfur, and Na_2S to 780 °C and cooling to room temperature over ∼24 hours. Na_2S-sulfur is an excellent flux for pyrite crystallization because it is liquid over a wide range of composition and temperature (see fig. 2.2), shares a common anion with pyrite, and features a cation that does not incorporate into pyrite to any significant degree (< 200 ppb according to secondary ion mass spectrometry measurements (see table 4.1).

Starting materials of the highest available purity (metals basis) were further purified each to remove possible nonmetal impurities such as water and oxygen. Iron powder (99.998%, 22 mesh, Alfa Aesar) was loaded into a pyrolytic boron nitride (pBN) crucible and reduced in a quartz tube furnace in a flow of 5% H_2/95% Ar at 300 °C for 15 hours to remove water and surface oxides. Higher temperatures (> 450 °C) led to undesirable agglomeration of the iron powder. Sulfur powder (99.9995%, Alfa Aesar) was degassed and dried in a quartz flask under a dynamic vacuum of ˜30 mTorr at 130 °C for 3 hours. $Na_2S{\cdot}9H_2O$ (> 99.99%, Aldrich) was crushed, then dried and degassed in a quartz flask under a dynamic ∼30 mTorr vacuum at 300 °C for 5 hours, resulting in a mixture of fine colorless and yellow powder (Na_2S and polysulfides, respectively). After purification, all three starting materials were immediately transferred to an N_2-filled glovebox (< 0.1 ppm O_2, LC Technologies) without exposure to air.

Pyrite crystals were grown in alumina crucibles (99.5%, LSP Ceramics) or pBN crucibles (99.999%, Morgan Technical Ceramics) sealed in evacuated quartz ampoules. All procedures were performed rigorously air free. 0.50 grams of iron (8.9 mmol) was placed in the bottom of the crucible, followed by 0.71 grams of Na_2S (9.1 mmol) and 1.29 grams of sulfur (40.2 mmol). The crucible was then loaded in a quartz tube and the tube was connected to a vacuum hose with a closed isolation valve. This apparatus was removed from the glovebox, attached to a vacuum manifold, purged with 99.999% Ar, pump/purged to < 20 mTorr three times, and sealed at < 20 mTorr with a hydrogen/oxygen torch. The quartz ampoule was held vertically the entire time to avoid mixing or spilling the contents of the crucible. The ampoule was placed in the center of a vertical tube furnace, heated at a rate of 13 °C min^{-1} to 780 °C, held at 780 °C for 6 hours, cooled to 625 °C over 24 hours, and finally cooled naturally to room temperature over 5 hours (36 hours total). The crucible was then removed from the ampoule and placed in a beaker of Millipore water for several hours to dissolve the flux. 80% of the time this procedure results in one large pyrite crystal, while several smaller crystals are produced 20% of the time. The crystals are sonicated in Millipore

water to remove flux residue, rinsed many times with Millipore water, dried, and stored in the glovebox.

2.1.3 Chemical Vapor Deposition (CVD)

Our lab developed a novel method to grow thin films of polycrystalline pyrite on a variety of substrates by Chemical Vapor Deposition (CVD). The method was introduced by Nick Berry and later used by Nima Farhi to produce high-quality pyrite thin films that were so important for this work. This work focuses on the electrical properties of these thin films, and only a summarized procedure is given below. They are fully discussed in [6].

Pyrite thin films were grown in a homemade atmospheric pressure hot wall chemical vapor deposition reactor consisting of two collinear single-zone 1 in. quartz tube furnaces. The upstream furnace was loaded with an alumina boat containing iron(III) acetylacetonate ($\geq$99.9%, Aldrich) at 150 °C, while the downstream furnace was heated to 300 °C and served as the growth zone. The sulfur precursor, tert-butyl disulfide (97%, Aldrich) was introduced directly into the growth zone by vapor entrainment in an argon flow from a stirred bubbler held at 60 °C in an oil bath. Flow rates for the iron and sulfur precursors (150 and 350 sccm, respectively) and a separate argon stream (500 sccm) were controlled by three digital mass flow controllers (Aalborg). A plug of quartz wool placed immediately upstream of the growth furnace was used to mix the precursor vapors to achieve uniform CVD growth on substrates loaded in a row within the quartz reaction tube. Soda lime glass substrates were cleaned by acetone and isopropanol and then placed in a NOCHROMIX cleaning solution overnight, followed by a DI water rinse. Molybdenum-coated glass, silicon, and quartz substrates were sonicated in acetone and isopropanol and then dried with ultra-high-purity nitrogen.

Sulfur annealing was performed in 14 mm inner diameter quartz ampoules loaded with a film and a predetermined mass of solid elemental sulfur (99.999%, Alfa Aesar). Loaded ampoules were evacuated and purged with 99.999% argon three times and then evacuated to < 20

mTorr and flame sealed with an oxygen-hydrogen torch. Sealed ampoules were placed in a programmable box furnace set to ramp to the desired temperature in one hour and dwell at that temperature for 2 – 8 h before cooling down naturally. Ampoules were placed in the furnace such that bulk sulfur would not condense on the films upon cooling. See [6] for details.

2.1.4 Pyrite Ink

Our lab developed several novel methods to grow thin films of polycrystalline pyrite on a variety of substrates by solution-phase deposition.[97,74,116] Two of these methods, both using a novel molecular ink recipe, supplied pyrite thin films that were important for the present study, so they shall be briefly introduced here. The first method was developed by Sean Seefeld, details are published in [97]. The second was developed by Amanda Weber, details in [116]

2.1.4.1 $Fe(acac)_3$ Recipe

A spin-coating ink was prepared by dissolving 0.7 g of Fe(III) acetylacetonate (2 mmol) and 0.1 g of elemental sulfur (3.1 mmol) in 2 mL of pyridine and sonicating the mixture at 50 °C for 6 h. Molybdenum-coated glass substrates were used as received, while fused quartz substrates were cleaned by sonication in acetone and isopropanol. Ink films were made by spin coating 175 μL of the solution onto clean 1 in.^{2} substrates (2000 rpm for 60 s) in a N_2-filled glovebox. The sample was then placed on a cold hot plate and heated in air to 320 °C (for 1 mm thick substrates) or 370 °C (for 3 mm thick substrates) over the course of 10 min, after which it was immediately moved to the edge of the hot plate to cool for $5 - 10$ s and placed in a cool Petri dish. Two additional deposition and baking steps were used to produce films with a target pyrite thickness of ∼300 nm. The ink films were then annealed

in 1 atm of flowing H_2S gas (390 °C for 12 h) to yield mixed-phase pyrite/marcasite thin films. The marcasite impurity was eliminated by annealing the films in evacuated 125 × 14 mm^2 quartz ampules containing 100 mg of elemental sulfur and 100 mTorr of argon. See [97] for more details.

2.1.4.2 Elemental Precursor Recipe

Ink synthesis and deposition were carried out inside an N_2-filled glovebox. To make the molecular ink, 0.16 g (5 mmol, 1 M) of sulfur powder was dissolved in 4.3 mL of DMSO and 0.7 mL of ethanolamine (ETA). The mixture was stirred at room temperature for 12-16 h in a glovebox. Then, 0.093 g (1.67 mmol, 0.33 M) of iron powder was added and the solution stirred for an additional 20-24 h. To remove any agglomerates, the inks were centrifuged (4400 rpm, 1.5 min) immediately prior to deposition. Ink layers were deposited onto various substrates (glass, silicon, Mo-coated glass, quartz) by spin coating (2000 rpm, 20 s), then baked on a preheated hotplate at 320 °C for 3 min and cooled on the edge of the hotplate to room temperature. Two cycles of spin coating and baking were used to obtain ˜300 nm thick films. Quartz and boro-aluminosilicate glass substrates (Corning Eagle XG) were soaked in NOCHROMIX overnight, sonicated in acetone and isopropanol, rinsed with Millipore water, and dried with compressed air. Silicon substrates were cleaned as stated above except without the NOCHROMIX soak; once dry, the Si substrates were cleaned in O_2 plasma for 40 s and used immediately. Mo-coated glass substrates were prepared by sputter deposition, see section 2.2.1. The dried ink films were then annealed in 1 atm of flowing H_2S gas at 390 °C for 12 h, except for films on glass which were annealed at 350 °C using a 6 h ramp and a 6 h dwell. Since these "H_2S annealed" films contain both pyrite and marcasite, they were subsequently annealed in evacuated quartz ampoules containing 25 mg of sulfur (0.3 atm) and 100 μg of Na_2S at 500 °C for 3 h to produce phase-pure pyrite films. The Na_2S was added via pipette of a solution of Na_2S in methanol. Substrates were placed 3

cm from one end of the quartz ampoule to prevent Na_2S or sulfur from condensing onto the surface of the films. See [116] for more details.

2.2 Deposition and Patterning of Thin Films

In addition to pyrite thin films, other materials were deposited for solar fabrication and evaluation of surface passivation treatment. These deposition techniques are described in this section, along with a method to pattern pyrite thin films using photo-lithography.

2.2.1 Sputter Deposition

Sputtering, also called physical vapor deposition, is a common tool to deposit thin films of a wide variety of materials uniformly on almost any substrate. Ionized gas atoms (typically Ar^+) are accelerated onto the surface of a target material, physically removing cluster of atoms, which then fly towards and stick on the substrate. Reactive sputtering adds reactive gases like oxygen to the Ar gas in order to grow oxides, sulfides or nitrides.

Figure 2.3 shows diagrams for a typical magnetron sputtering setup, like the one used for this work in bottom-up geometry. The target sits on top of an arrangement of magnets, on top of a water-cooled electrode that is powered by either direct current (DC) or radio frequency (RF) power supply. The electrons of the plasma are confined to a certain area above the target by the magnetic field, which increases sputtering yield compared to sputtering without magnetic fields. Plasma dynamic are quite different for DC and RF excitation. Electrons can follow the 13.56 MHz RF frequency, while the heaver ions due to their inertia cannot. The necessary discharge voltage V_{DC} measured at the target is several times larger in DC sputtering.

For this work, a seven source magnetron sputter tool (AJA International Inc.), attached to

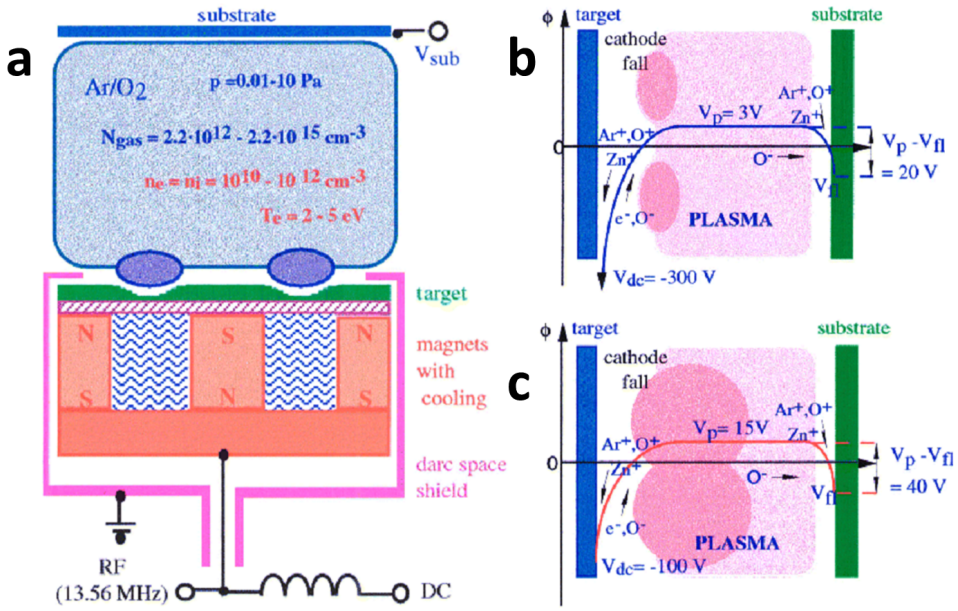

Figure 2.3: The technique of magnetron sputtering, by Ellmer et al.[30] (a) Diagram of a magnetron sputtering setup, with both RF and DC power sources connected to gun and vacuum chamber. Typical plasma parameters (ion density N_{gas}, electron density n_e, plasma temperature T_e) for a magnetron plasma during ZnO deposition are shown. (b) Potential distribution in a DC powered magnetron sputtering discharge for ZnO deposition. (c) Potential distribution for RF powered magnetron sputtering discharge. Figure reproduced from [30].

Film Material	Target	Purity	Supplier	Power (W)	p_{Ar} (mTorr)
Mo	Mo	3.5N	AJA	180 (DC)	2.0
Fe	Fe	3.5N	AJA	180 (DC)	2.0
ZnS	ZnS	4N	SAM	75 (RF)	2.2 (0 - 2% H_2S)
CdS	ZnS	4N	AJA	60 (RF)	2.3 (0 - 2% H_2S)
ZnO	ZnO	4.5N	SAM	75 (RF)	2.9 (2% O_2)
AZO	ZnO:Al (5%)	4N	SAM	110 (RF)	2.0
NiO	Ni	3.5N	AJA	100 (RF)	2.4 (2 - 15% O_2)

Table 2.1: Target properties and typical deposition parameters used for magnetron sputtering. AJA = AJA Internatonal Inc., SAM = Stanford Advanced Materials, DC = Direct Current Power, RF = Radio Frequency Power

a glovebox for air-free sample handling, was used to deposit a variety of metal, oxide and sulfide thin films in bottom-up geometry. Typical base pressure before deposition was 8E-8 Torr. Argon and oxygen gas (both 5N purity) were connected to the chamber via mass-flow controllers (MFCs). Two sources of H_2 gas were also connected via MFCs: a 2% H_2 in 98% Ar lecture bottle and a 100% H_2 tank, both in safety cabinets with sensors ad engineering safety mechanisms. A dry roughing pump (Adixen ACP15G) with corrosion resistance was used behind the turbo molecular pump (Shimadzu TMP-803LM) to ensure compatibility with the H_2S gas. In order to prevent thermal shock all ceramic targets were subject to power up/down ramps of $\sim$3 s/W, all metal targets to $\sim$1 s/W. Sputter target properties for all relevant materials and their typical sputter conditions are summarized in table 2.1. For definition of film patterns a number of stainless steel shadow masks were fabricated that could attach to the substrate holder, as shown in fig. 2.4.

Sputtering a magnetic material like Fe presented special challenges. A modified magnet arrangement was used inside the gun, with the center array of magnets replace by an iron chuck. Because the target screens the magnetic field to some extend, high power and high Ar partial pressure ($>$ 100 mTorr) was necessary to ignite a plasma. Further, the magnetized Fe target was prone to shorting due to magnetic attraction to metal flakes formed in the sputter chamber, which made maintenance necessary often.

Figure 2.4: Shadow mask for sputter deposition and resulting quasi-random patterns on the backing plate. The top left image shows one of the shadow masks used for sputter deposition. It is machined from stainless steel to hold 28 (glass) substrates of 12 x 12 mm size. The other images shows patterns found on the backing plate of the substrate holder after several deposition runs with different masks.

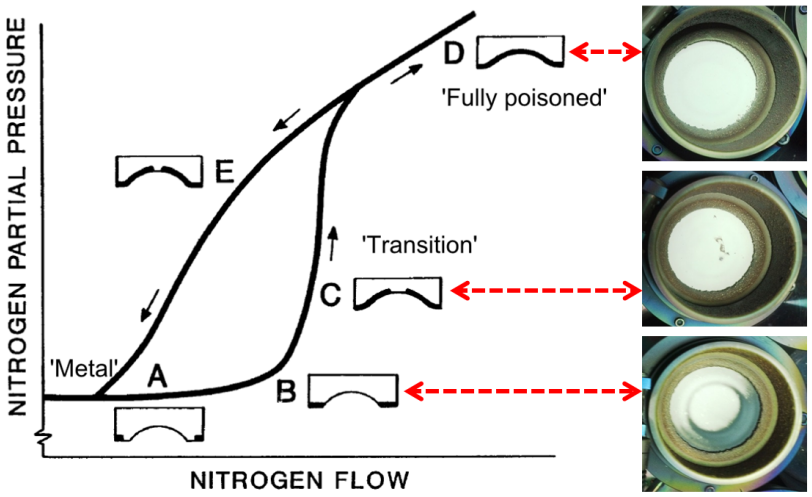

Figure 2.5: Issue of target surface control and partial pressure hysteresis in reactive sputtering. The diagram on the left is taken from [100] and shows the 'poisoning' of a metal target (Ti) observed in reactive sputtering. The activated gas here is N_2, causing oxidation of the metal to TiN. Varying the gas flow rate results in a hysteresis loop of the partial pressure. Without feedback control it is hard to maintain a well defined surface stoichiometry. The images on the right are taken from a ZnS target used in this work, after prolonged sputtering with different H_2S contents in the plasma (increasing H_2S exposure from top to bottom). They qualitatively correlate to the target conditions in the diagram, as indicates by the red arrows.

Compound semiconductors like ZnS, ZnO, NiO and TiN can be sputtered either from a metal target (Zn, Ni, Ti) using a reactive gas supply (H_2, O_2, N_2), or from ceramic targets of the desired compound. In both cases, good control over the target surface condition is crucial to obtain the desired film stoichiometry. Reactive sputtering is commonly done in industry using feedback control to prevent the hysteresis effect shown in fig. 2.5. To 'lock in' the target surface at a desired deposition condition (usually optimized for deposition rate or film stoichiometry), a pressure reading is used as feedback to control the flow of reactive gas via an MFC.[100]

Particularly relevant for this work (see section 5.3.2) it was found that nominally identical ZnS targets (same vendor) give different results and that a single target gives different results over its lifetime, likely due to changes in the surface composition (see fig. 5.8e). This went along with observed changes in the V_{DC} voltage during deposition ranging from 0 to 270 V. Variations in solar cell results suggested a strong dependence of ZnS film properties

on H_2S concentration and ZnS target surface stoichiometry. This was confirmed by test stacks of Mo/AZO/ZnO/ZnS/ZnO/AZO/Mo containing ZnS layers deposited back-to-back using different H_2S concentrations. As shown in fig. 5.8c the through-plane resistivity of the ZnS film is orders of magnitude higher when even small amounts of H_2S are present in the plasma, in this case the measured current is in the noise floor of the setup used. No change of appearance or morphology in SEM images (fig. 5.8d) for different H_2S content was observed. For future studies of ZnS/FeS_2 junctions made by reactive sputtering of the ZnS buffer, it will be necessary to implement feedback control for the H_2 gas supply.

2.2.2 Thermal Evaporation

Thermal evaporation is a common tool to deposit metal thin films uniformly on almost any substrate. In an evacuated chamber the metal of choice is resistively heated to increase its vapor pressure, resulting in typical deposition rates of $\mathring{A}$/s.

For this work, a homemade two source thermal evaporator inside a nitrogen-filled glovebox was used to deposit metal thin films in bottom-up geometry. Base pressure was 3 x 10^{-6} Torr and typical deposition rates were 0.5 - 2.0 $\mathring{A}$/s. A calibrated quartz crystal was used to monitor deposition rate.

2.2.3 Atomic Layer Deposition (ALD)

Atomic Layer Deposition (ALD) is a method of depositing oxides and sulfides in an atomic layer-by-layer fashion, with growth occurring on every surface of the substrate that is accessible to the reactive gases used. This makes it a very powerful tool for surface passivation of polycrystalline films, where internal surfaces are inaccessible to other deposition methods like sputtering.

For this work, crystalline ZnS was deposited in a homemade continuous wave ALD system

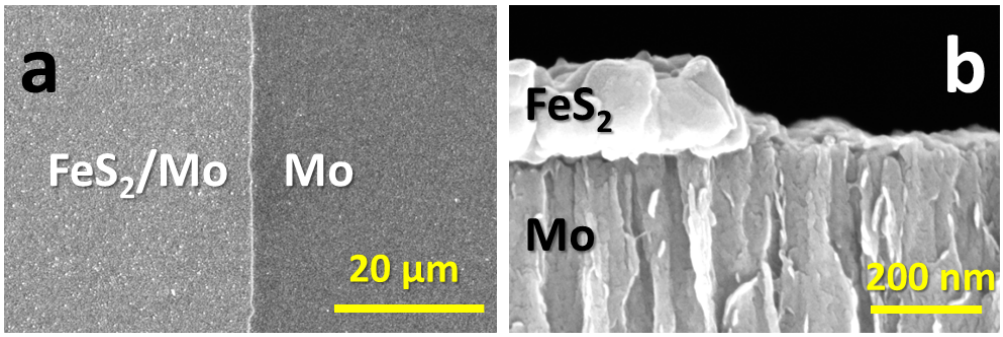

Figure 2.6: Pyrite thin film on Mo-coated glass patterned by photolithography shown in (a) SEM top-down and (b) cross section view.

inside a nitrogen-filled glovebox using diethylzinc (DEZ) and hydrogen disulfide (H_2S) at a substrate temperature of 100 °C and a base pressure of 100 mTorr. Pulse and purge times for DEZ were 30 ms and 30 s, respectively. Pulse and purge times for H_2S were 9 ms and 30 s, respectively.

2.2.4 Photolithography

Patterning of pyrite thin films was found to be a necessary step in the fabrication of solar cell devices (see section 5.3.2). Though shadow masks were successfully used to pattern the deposition of films via CVD, photo lithography was found to be a more precise for patterning and moreover also applicable to pyrite films made via the ink method. Since the majority of solar cells fabricated for this work were based on pyrite films grown on a Mo back contact, which partially converts to MoS_2 in the necessary sulfurization step (see section 3.2), it was important to identify an etch that selectively dissolves the pyrite film, but leaves the back contact intact. It was found that 10 M nitric acid is suited for this, as described in the following recipe.

Pyrite films on Mo/MoS_2 were taken out of their ampules after the sulfurization step (see section 2.1.3, section 2.1.4), taken to a yellow light room and spin-coated with photo-resist (Shipley 1808) at 2500 RPM for 40 s, followed by 6000 RPM for 5 s. The resist was then

soft-baked at 90 °C for 1 h in air, followed by exposure to UV light (400 W for 2.5 s) through a contact shadow mask (printed transparency). The films were then developed for 30 s in MF-319, followed by a rinse in DI water and blow-drying in nitrogen. To remove the unprotected areas, the pyrite films were then dipped for 12 s into 10 M nitric acid, followed by a DI water rinse. Finally the resist was removed by swirling in acetone, followed by a rinse in methanol and blow-drying in nitrogen.

A similar procedure was used to define a sharp edge for Mo films. Instead of 10 M nitric acid (which does not etch Mo), a 2:3:3 mixture of nitric acid (conc.), phosphoric acid (conc.) and water (DI) was used to etch Mo in 12 s.

2.3 Preparation of Single Crystal Samples

2.3.1 Sectioning and Polishing

For many electronical and especially optical characterization techniques it is crucial to have a semiconductor surface with known crystal orientation and minimal roughness. Atomic flatness of a semiconductor surface is an important requisite for accurate determination of optical properties (providing perfect mirror-like reflectivity) as well as many surface science tools. Great care was taken to identify optimum conditions for sectioning, polishing and characterizing pyrite single crystals. Qualitative surface appearance and flatness along with calculated RMS roughness were evaluated using atomic-force microscopy (AFM) in tapping mode, giving a z-direction resolution of < 100 pm.

Single crystals were mounted in epoxy (Buehler EpoxyCure) for sectioning. A slow-speed diamond saw (Model 650, South Bay Technology) was used to cut 400 – 1000 mm thick slabs from crystals parallel to their largest surface facet. The slabs were then released from the epoxy by soaking in dichloromethane for 2 hours. To obtain fine-polished surfaces with < 2

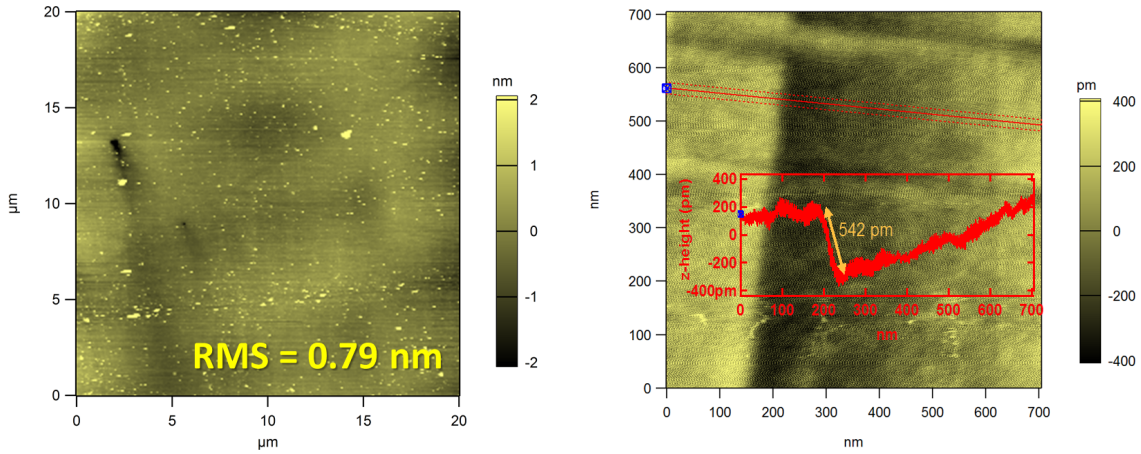

Figure 2.7: Atomic-force microscope images demonstrating pyrite single crystal slices polished to atomic flatness. Left: 20 x 20 μm scan box showing atomically flat surface over extended area, sprinkles with nm size pyrite particles (confirmed by EDS). RMS roughness calculated over this area is only 0.79 nm. Right: 700 x 700 nm scan box showing showing atomic flatness and unit cell step edge. The inset shows the z-height for the section show in red, confirming a step height equaling the unit cell dimension of 542 pm.

nm RMS roughness, as-cut slabs were mounted on steel stubs with Crystalbond^{TM}, then first polished sequentially with SiC paper of grit size 600, 800, and 1000, followed by sequential lapping with 3 μm and 1 μm diamond slurries and, finally, 20 minutes of lapping with 50 nm alumina slurry (Buehler MasterPrep). Crystalbond^{TM} was dissolved with acetone and residual slurry particles were removed by sonication in Millipore water.

2.3.2 Wet Passivation Treatments

In an attempt to remove or reduce the surface inversion layer (see section 4.6), several wet passivation treatments were evaluated. The most successful and most frequently applied treatment was an etch in piranha solution. Etching was carried out using freshly prepared piranha solution (3:1 concentrated H_2SO_4 to 30% H_2O_2). Unless otherwise noted, samples were immersed in piranha for 2 minutes and then rinsed with deionized water and methanol and blown dry.

2.3.3 Fabrication of Pellets

To test how the surface to bulk ratio in the same material affects electronic properties of pyrite, high-quality single crystals grown by the CVT or flux method were ground into fine powder and pressed it into pellets, drastically increasing the surface to bulk ratio. The powder obtained by hand-grinding with mortar and pestle had particle sizes ranging from 100s of nm to several μm (as determined by SEM imaging of powder suspended in MeOH, drop-cast on Si wafers). Even smaller particle sizes on the order of 100 nm, comparable to grain sizes in the pyrite thin films, could be obtained by ball-milling pyrite powder over 24 h with zirconia beads in EtOH. A quantification of average particle size was not attempted, as size distribution was very broad in every batch. More monodisperse powers might be obtainable by using different ball-milling conditions or employing mesh filters. The pressing step utilized a heavy-duty hydraulic press and machining steel grade dies. The powders were pressed under 200,000 psi at room temperature for 5 min into pellets of 10 mm diameter and 1 mm thickness, suitable for electrical measurements. The pellets were typically 40 - 50% dense (w.r.t. pyrite's bulk density), and required careful handling in order not to break apart.

2.3.4 Electron Beam Lithography (EBL)

Another way to test how the surface to bulk ratio in the same material affects electronic properties of pyrite, is to compare electrical properties of thin film to those of one of the single grains the films are composed of. However, while measuring the film is trivial, contacting a single grain is somewhat challenging. Prolonged annealing in sulfur atmosphere can yield grains up to 5 μm in size.[116] These grains were drop-cast onto SiO_2 substrates, and electron-beam lithography (EBL) was used to define contact lines to individual grains. All EBL writing steps were performed using a FEI Magellan electron microscope. NPGS

software (JC Nabity Lithography Systems) was used to program the microscope to automatically write the desired patterns by exposing the resist with a pre-determined dose.

Step 1: 100 areas with contact bars were defined, called 'boxes'. For this, a 200 nm thick film of poly(methyl methacrylate) (PMMA, MicroChem A3) was spincast on a clean SiO_2 substrate at 1200 RPM, followed by a baking step (5 min at 150 °C in air). The PMMA was then exposed using NPGS and developed by immersion for 70 s in a 3:1 mix of isopropanol (IPA) and methyl isobutyl ketone (MIBK), followed by 10 s in pure IPA and 10 s in DI water. 100 nm of Ag or Au were then deposited by thermal evaporation, followed by a lift-off step in acetone.

Step 2: Pyrite grains were dispersed from their glass substrates by sonication in methanol and then drop-cast onto the substrate containing the 100 boxes. SEM imaging was used to find and record the exact position of grains of interest within certain boxes.

Step 3: The PMMA deposition and soft-bake from step 1 was repeated. Prior tests confirmed that this processing step does not change the position of $> 80\%$ of pyrite grains. Using the SEM in imaging mode, the boxes of interest were then once again identified and aligned, taking great care to use only very short imaging times ('snapshots') in order to prevent exposure of the PMMA. Relying on the precise x-y-stage of the instrument, the beam was then centered 'blindly' (without imaging) centered on a grain of interest, guided by the previously taken image. Aligned this way, NPGS was then used to write four lines of $\sim$100 nm width from the grain to the four surrounding contact bars (see fig. 2.8). Necessary length and angle of the lines was also know from the previously taken images. The same deposition and lift-off steps as in step 2 were then used to obtain Ag lines. The completed samples were then imaged again by SEM to evaluate the contacts on the grains of interest.

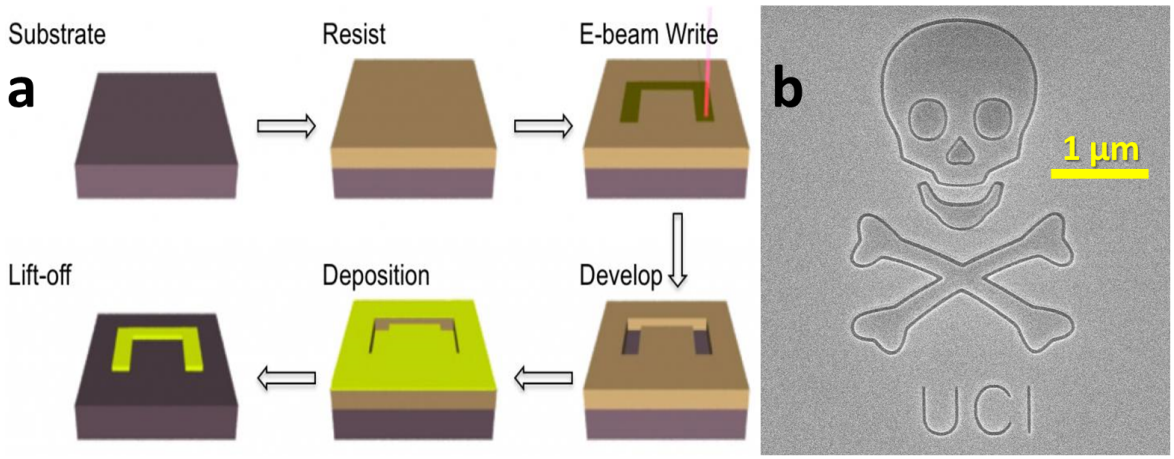

Figure 2.8: Electron Beam Lithography (EBL). (a) Schematic showing the process steps involved to create a (metal) feature on a substrate. Image adapted from Elionix Inc. (b) Test pattern written into PMMA using FEI Magellan SEM and NPGS software at UCI's LEXI facility.

2.3.5 Ohmic Contacts

Ohmic contacts are electrical contacts to a test sample that have no energy barrier associated with the contact itself and the entire voltage drop happens across the sample. An important characteristic of such a contact is that the current-voltage curve is linear through the origin at all temperatures. Ohmic contacts are important for electrical measurements of semiconductors, though some methods such as the Van der Pauw method somewhat alleviate the need for perfectly ohmic contacts.

Making ohmic contacts to pyrite thin films was found to be very easy, with every metal tested giving good results. Placing naked test pins directly on the film worked well enough, but typically a silver contact was made using colloidal silver paste to reduce mechanical wear on the film and increase reproducibility.

Ohmic contacts on single crystals are a little harder to achieve, especially for high-purity crystals and low temperatures. It was also found that not all facets (200, 111, 110, etc.) give equal results. For best results, the single crystal area for contacting was carefully scratched with a diamond scribe to locally increase surface roughness and expose all facets. An In/Ga eutectic was then applied, followed by colloidal silver paste.

2.4 Structural & Elemental Characterization

As pyrite FeS_2 has a polymorph, marcasite, as well as a tendency to form sulfur-deficient phases like pyrrhotite, it is often important to confirm phase-purity of a pyrite sample with very high accuracy. In order to deduce intrinsic material properties of pyrite, without possible effects of phase impurities or extrinsic dopants, great efforts were taken to rule out phase impurities and elemental contaminations with the highest precision.

2.4.1 X-Ray Diffraction (XRD)

Structure determination by single crystal X-ray diffraction was performed on a Bruker SMART APEX II diffractometer using ∼0.2 mm specimens removed from as-grown single crystals. Diffraction data were collected on a CCD area detector using Mo Ka radiation ($\lambda = 0.71073$ $\mathring{A}$). A full sphere of data was collected for each crystal. The APEX2 software package was used for data collection and determination of unit cell parameters. Data were absorption corrected using SADABS-2008/1. The structures were solved by direct methods and refined by a full-matrix least squares routine on F^2 with SHELXL97. The diffraction symmetry was m3 and the systematic absences were consistent with the cubic space group $Pa\bar{3}$.

Thin film X-ray diffraction (including room-temperature rocking curves, 2θ-ω scans, and pole figures) was performed on a Rigaku SmartLab diffractometer. X-ray rocking curves and 2θ-ω scans were acquired on the SmartLab configured with a Ge(440) x 4 monochromator featuring an angular resolution of 5.4 arcseconds.

Synchrotron XRD measurements were performed on pulverized crystals in capillary transmission mode at Beamline 11-BM of the Advanced Photon Source ($\lambda = 0.413141$ $\mathring{A}$) at Argonne National Laboratory.

X-ray tomography measurements were performed on a Zeiss Xradia 410 Versa with a 4x objective lens.

2.4.2 Raman Spectroscopy

It was found that Raman spectroscopy is a useful complementary tool to XRD when looking for phase-impurities of low-concentration in pyrite, especially marcasite. Due to the strong optical absorption of pyrite this method is limited to a few 10s of nm from the surface, and some phases like pyrrhotite are not Raman active. But to detect or rule out the important marcasite polymorph, Raman spectroscopy was found more sensitive than regular (non-beamline) XRD methods.

All Raman spectroscopy utilized a Renishaw inVia confocal Raman microscope with a 50x objective lens and a 523 nm laser operating at less than 5 mW. Samples were measured in air.

2.4.3 Mass Spectroscopy

Elemental composition of the crystals was determined by Evans Analytical Group using glow discharge mass spectrometry (GDMS), instrumental gas analysis (IGA), inductively coupled plasma optical emission spectroscopy (ICP-OES), and secondary ion mass spectrometry (SIMS).

GDMS measurements were performed on a VG 9000 GDMS instrument (Thermo Scientific). Powdered pyrite specimens were pressed into high purity In foil (99.99999%) previously cleaned with acid to remove surface impurities. Impurities in the In foil were analyzed prior to elemental analysis of each sample. Glow discharge conditions of 1.0 kV, 2.0 mA, and 100 Pa of 99.9999% Ar were used for all measurements. Samples were pre-sputtered for five minutes prior to data acquisition. The intensities of the ion beams were measured with

a Faraday cup for iron, sulfur and indium isotopes and a Daly conversion detector for all analytes in the samples. The efficiency of the detectors was calibrated using ^{180}Ta (relative isotopic abundance of 0.012%) measured on the Daly detector and ^{180}Ta (relative isotopic abundance of 99.99%) measured on the Faraday cup during analysis of pure Ta metal. Scan points per peak were 70 channels, DAC steps of 7 with integration times of 100 and 160 ms for the Daly detector and Faraday cup, respectively.

IGA measurements were performed on a Leco TC 600 oxygen/nitrogen analyzer, a Horiba EMIA-820V carbon/sulfur analyzer, and a Horiba EMGA-621W hydrogen analyzer. Samples were prepared in a glovebox by loading small crystal pieces into Sn capsules for the inert gas fusion measurements.

ICP-OES measurements used a PerkinElmer Optima 7300V spectrometer operating at 1300 W. 0.1 g samples were digested in a closed vessel containing 2 mL HNO_3 and 6 mL HCl in 5 mL H_2O in an Anton Paar multiwave 3000 microwave (HF100 rotor).

Secondary ion mass spectrometry (SIMS) was performed on a PerkinElmer Physical Electronics Model 6600 dynamic SIMS instrument using 4 keV Cs ions for anions (S, O, H, C, F, and Cl) and 5 keV O_2 ions for cations (Na, K, Mg, Ca, Cr, and Al). Estimated detection limits were 1E15 atoms cm^{-3} for Na, K, Al, Mg, Cr, and Ca, 5E17 atoms cm^{-3} for C, 2E18 atoms cm^{-3} for O and H, and 5E16 atoms cm^{-3} for F and Cl. Atomic concentrations are accurate to within a factor of two for oxygen and a factor of five for all other elements. The depth scale was quantified by measuring the analysis craters with a stylus profilometer.

2.4.4 Energy-Dispersive X-ray Spectroscopy (EDS)

Energy dispersive spectroscopy (EDS) is a technique to probe elemental or chemical composition of a sample by exciting it with X-rays and detecting emitted high-energy photons that are characteristic of every elements's unique atomic structure.

EDS was performed in the SEM system described below, equipped with an X-ray source and 80 mm^2 detector by Oxford Instruments, using the with AZtec software package.

2.4.5 Photoelectron Spectroscopy (UPS/XPS)

Angle-integrated UPS spectra were acquired using He I radiation in normal emission using a customized Physical Electronics Model 5600 photoelectron spectroscopy system.[88] Data were taken at room temperature on "as-polished" crystals and after a NH_4F/UV-ozone cleaning process[70] performed within the glovebox portion of the cluster tool, to which the photoemission system is directly attached. Satellites due to non-monochromatic He I radiation were subtracted numerically. The binding energy scale of the spectrometer was calibrated using sputter-cleaned metal foils.

2.5 Optical & Morphological Characterization

2.5.1 Scanning Electron Microscopy (SEM)

All scanning electron microscope (SEM) images were acquired on a FEI Magellan 400 XHR SEM at UCI's LEXI facility.

2.5.2 Atomic Force Microscopy (AFM)

Surface topography was measured using an Asylum MFP-3D atomic force microscope (AFM) in tapping (AC) mode.

2.5.3 Optical Absorption Spectroscopy

Optical transmission and reflectance spectra were acquired on a PerkinElmer Lambda 950 spectrophotometer equipped with an integrating sphere. A Janis ST-100 cryostat was attached for temperature-dependent measurements.

2.5.4 Spectral Ellipsometry

Spectroscopic ellipsometry (SE) was used to determine the pseudodielectric function $\epsilon = \epsilon_1 + i\epsilon_2$ spectrum of a natural pyrite single crystal at 77 K. SE data were acquired by Dr. Sukgeun Choi at NREL from 0.5 to 4.5 eV at 77 K using a rotating-analyzer type ellipsometer equipped with a computer-controlled Berek wave plate compensator (J.A. Woollam Inc., VASE system). The sample temperature was modulated by a liquid-nitrogen cooled variable-temperature cryostat. The angle of incidence was 70 degrees and the step size was 0.01 eV. To increase the signal-to-noise ratio, each data point was recorded after averaging 100 analyzer cycles (100 revolutions per measurement).

2.6 Electrical Characterization

2.6.1 Temperature-Dependent Resistivity and Hall Effect

Hall effect and resistivity data were acquired in-house from 80 to 350 K on an Ecopia HMS-5000 instrument (0.55 T magnet) inside an N_2-filled glovebox using the van der Pauw method.[110] Single crystal samples were mounted with thermal grease (Apiezon Type N) to a glass slide bonded to the sample stage. Thin films samples on insulating substrates (glass, quartz) were mounted directly with thermal grease. Ohmic contacts were achieved

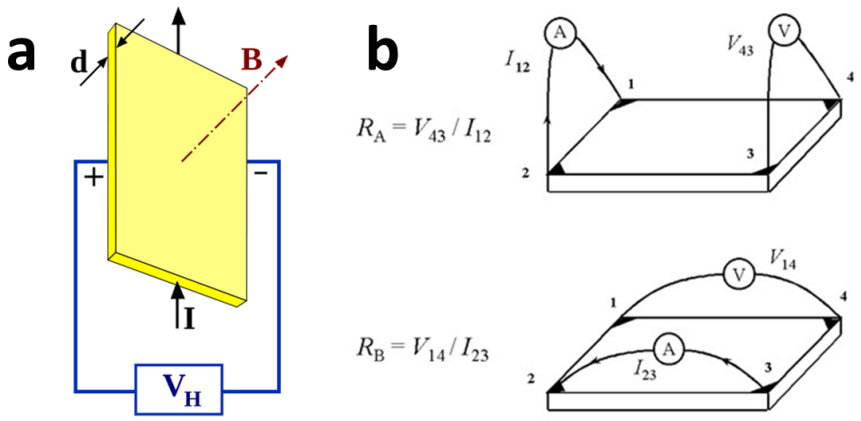

Figure 2.9: Hall Effect and Van der Pauw method. (a) Diagram illustrating gemoetry in a typical Hall Effect measurement, with magnetic field B, applied current I and measured Hall voltage V_H all perpendicular to each other. The sample of thickness d is perpendicular to B. Image taken from Wikipedia. (b) Diagram showing the two minimum required measurements required in the Van der Pauw method. Image taken from the original publication [110].

with In/Ga eutectic or colloidal silver paste in all cases and verified by taking linear current-voltage curves. The Hall coefficient was calculated as $R_H = \frac{V_H d}{IB}$, where V_H is the measured Hall voltage, d the crystal thickness, I the applied current, and B the magnetic field strength. The applied current was adjusted from nA to mA range according to sample resistivity.

For the data shown in fig. 4.11, additional Hall effect data were also acquired at Lake Shore Cryotronics on a Model 9709A Hall Measurement System using a DC field strength of 2 T from 40 – 350 K and a 8404 AC/DC HMS using an AC field strength of 0.63 T RMS from 350 – 700 K. Ohmic contacts were made with colloidal silver paste. The applied current was adjusted from 50 – 100 nA at 40 K to 8 – 10 mA at 700 K. Conductivity values from the different measurement setups showed excellent agreement across the range of overlapping temperatures. Magnetoresistance measurements were performed in the 9709A system using a DC field strength of up to 90 kOe. The current at 300 K and 70 K was 10 mA and 100 nA, respectively. The resistivity at each magnetic field was calculated using the standard van der Pauw method. Additional high-temperature conductivity data of pyrite were obtained in a four point geometry by heating single crystals with an as-grown top surface and as-cut

bottom surface to 750 K on a hotplate inside an N_2-filled glovebox. The samples were heated rapidly (30 – 60 minutes) to minimize the loss of surface sulfur and conversion of the surface of the pyrite crystal to polycrystalline pyrrhotites (Fe_xS_y) and/or troilite (FeS). Data were recorded during both heating and cooling to check for thermal hysteresis due to this surface phase transition. In all cases, the cooling curve showed an unchanged slope and $< 20\%$ higher conductivity. The applied current was adjusted from 1 mA at 300 K to 10 – 100 mA at 750 K to account for the change in sample conductivity.

2.6.1.1 Unipolar Approximation

A Hall effect measurement is typically combined with a conductivity measurement, yielding the two values R_H and σ.

$$R_H = \frac{p\mu_h^2 - n\mu_e^2}{e(p\mu_h - n\mu_e)^2} \tag{2.1}$$

$$\sigma = e(p\mu_h - n\mu_e) \tag{2.2}$$

In order to extract carrier concentrations n, p and carrier mobilities μ_e, μ_h (and then calculate further parameters like E_F) from eq. (2.1) and eq. (2.2), the *unipolar approximation* is often used, which reduces them to

$$R_H = \frac{-1}{ne} \;\; ; \;\; R_H = \frac{1}{pe} \tag{2.3}$$

$$\sigma = -en\mu_e \;\; ; \;\; \sigma = ep\mu_h \tag{2.4}$$

for n-type and p-type materials respectively. However, this approximation is only valid when $n \gg p$ or $n \ll p$. In the high-temperature intrinsic region for example the unipolar approximation is not valid. It is also not valid for an inhomogeneous semiconductor that has p-type surfaces and n-type bulk, as discussed in detail in section 4.4.2. For this more complicated scenarios the unipolar approximation is an over-simplification, yet it is falsely used across literature, and yields erroneous results. In these cases eq. (2.1) and eq. (2.2) cannot be solved analytically, instead a numerical model is necessary as discussed in section 4.4.2.

2.6.2 Seebeck Coefficient

In a simple setup the sign of the Seebeck Coefficient could be determined for thin films. A film on insulating substrate (glass, quartz) was placed across a 1 - 2 mm gap between two identical plates of steel. The first plate was held at room temperature, while the second plate was pre-heated on a hotplate to 100 - 300 °C and then quickly put into place adjacent to the first plate. While thermal equilibrium between the steel plates and the sample was established, a multimeter with needles probes was used to measure the voltage drop across the film. The sign of this voltage indicates the sign of the Seebeck coefficient.

2.6.3 Carrier Lifetime

The method to measure carrier lifetimes used for this work is called time-resolved microwave reflectivity (TRMC). Setups at the National Renewable Energy Lab (NREL) and University of Wuerzburg, Germany were used for this, and experiments conducted by Dr. Steve Johnson and Andreas Fritze respectively. TRMC is based on measuring the reflectance of microwaves off a semiconductor sample, which is excited by a laser. Excitation by the laser creates additional carriers, which increases carrier density and thus changes the reflectivity for microwaves. Using pulsed laser, lock-in amplifier and time-resolved detection

of microwave field strength, the decay in carrier density can be recorded. From this raw data, assumptions about carrier recombination mechanisms must be made to fit the data and extract carrier lifetimes.

2.6.4 Solar Cell Testing

2.6.4.1 Solid State Cells

Current-voltage curves of solid state solar cells were measured inside a nitrogen-filled glovebox in the dark and under illumination using tungsten needle probes, connected via shielded triax cables to a Keithley 2636 source-measure unit (SMU). Cells were illuminated using a Newport Oriel solar simulator.
Additional temperature-dependent measurements were taken in a Janis ST-100 cryostat connected to the same SMU, using illumination by a tungsten halogen lamp.

2.6.4.2 Wet Junction Cells

Current-voltage curves of solid state solar cells were measured in the dark and under illumination using a Princeton Applied Research 273A potentiometer in a three-electrode setup. Pyrite working electrode, platinum counter electrode and Ag/AgCl reference electrode were placed in an electrolyte solution containing 0.7 M HI, 0.15 M CaI_2 and 0.03 M I_2 in acetonitrile at a pH of 0.35.

2.7 Data Modeling

2.7.1 Electrical Transport

Electrical transport in both pyrite thin films and single crystals shows unusual temperature activation behavior. 'Well-behaved' semiconductors show a temperature-activated conductivity of the form

$$\sigma = \sigma_0 e^{(\frac{E_a}{k_B T})^p} \tag{2.5}$$

, where p = 1 for band transport. This form results in straight lines when plotting conductivity data in an Arrhenius plot (log(σ) vs. 1/T). Values smaller than unity for p can indicate one of several forms of hopping as the dominant transport mechanism, though one should be careful to conclude on hopping transport solely based on this. A useful method to extract the value p from raw data by linearizing it was first suggested by Zabrodskii[125] and utilizes a plot of $ln(-\frac{d\ ln(\rho)}{d\ ln(T)})$ vs. ln(T). The slope of such a Zabrodskii plot then corresponds to -p.

However, Arrhenius plots of conductivity data of polycrystalline films of pyrite do not show straight lines. These curved Arrhenius plots can be interpreted as a temperature-dependent activation energy $E_a = E_a(T)$, and were discussed before for other polycrystalline materials, such as silicon.[98] To explain this, Werner suggested a transport model for such polycrystalline films that takes into account grain boundaries acting as energy barriers and a Gaussian distribution of their height.[117] The resulting form of the resistivity is

$$\rho = \rho_0 e^{q(\Phi - \frac{\sigma_\Phi^2}{2k_B T/q}/k_B T)} \tag{2.6}$$

, where Φ is the average barrier energy height and σ_Φ is its standard deviation.

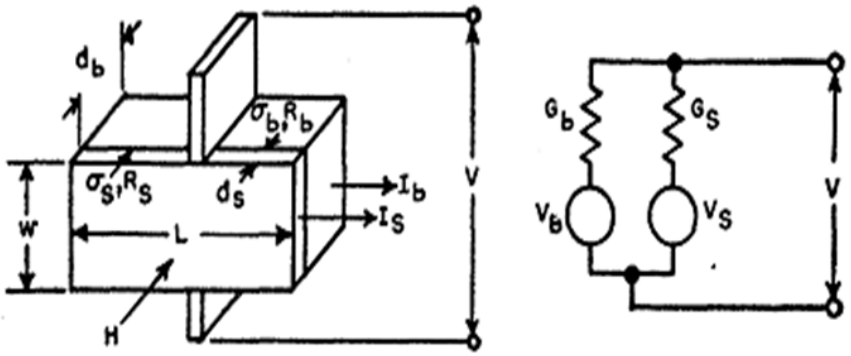

Figure 2.10: Conductivity and Hall Effect in a multi-layer system, according to Petritz. Image taken from [89].

2.7.2 Hall Effect Data and Multilayer Model

Electrical conductivity and Hall coefficient data of pyrte single crystals were modeled following the multilayer conduction model of Petritz,[89] see fig. 2.10.

In this work, implementation of the model assumes that electrical transport occurs in parallel through three layers – the crystal bulk and identical surface inversion layers on the top and bottom of the single crystal slab – while neglecting currents across their interfaces. Calculation of the Fermi level (E_F), carrier concentrations (n and p), conductivity (σ), and Hall coefficient (R_H) of the bulk and surface layers utilizes the charge neutrality condition:

$$N_D^+ + p = N_A^- + n \tag{2.7}$$

where N_D^+ and N_A^- are the concentrations of ionized donors and acceptors, given by[103]

$$N_D^+ = \frac{N_D}{1 + e^{\frac{(E_F(T) - E_D)}{k_B T}}} \tag{2.8}$$

$$N_A^- = \frac{N_A}{1 + e^{\frac{(E_A - E_F(T))}{k_B T}}} \tag{2.9}$$

Here, N_D and N_A are the concentrations of donors and acceptors and E_D and E_A are their respective energy levels. The carrier concentrations are given by

$$n(T) = \int_{E_C}^{\infty} DOS(E) \left(\frac{1}{e^{\frac{E - E_F(T)}{k_B T}} + 1} \right) dE \tag{2.10}$$

$$p(T) = \int_{-\infty}^{E_V} DOS(E) \left(1 - \frac{1}{e^{\frac{E - E_F(T)}{k_B T}} + 1} \right) dE \tag{2.11}$$

Because the valence and conduction bands of pyrite are probably not parabolic, a parabolic DOS(E) is compared against an explicit numerical DOS(E) obtained from recent density functional theory (DFT) calculations of the pyrite band structure.[52] In accord with literature and the optical measurements shown in section 4.4.3, we use a temperature-dependent band gap, $E_g(T) = E_g(0) - \frac{T^2 \cdot 0.00189\ eV\ K^{-1}}{T + 1915\ K}$, and assume equal shifting of the conduction and valence band edges with temperature.[62,58] The calculation is performed by substituting eqs. (2.8) to (2.11) into eq. (2.7) to give a self-consistent expression for the Fermi level $E_F(T)$ that is numerically solved at each temperature. After calculating n(T) and p(T) from $E_F(T)$, the conductivity σ(T) and Hall coefficient R_H(T) are obtained from the general expressions given in eq. (2.1) and eq. (2.2) above, where the temperature-dependent carrier mobilities m_e and m_h are extrapolated from unipolar regions of the Hall data. The electron mobility follows a $T^{-2.5}$ law at temperatures above ~150 K, as expected for phonon scattering. Finally, the contributions of the bulk and surface layers are combined to determine the total σ(T) and

$R_H(T)$:[89]

$$\sigma_{total} = \sigma_b \frac{d_b}{d} + 2\sigma_s \frac{d_s}{d} \tag{2.12}$$

$$R_{H,total} = R_{H,b}(\frac{\sigma_b}{\sigma_{total}})^2 + 2R_{H,s}(\frac{\sigma_s}{\sigma_{total}})^2 \tag{2.13}$$

where d_b and d_s are the thicknesses of the bulk and the surface layers, respectively, and $d = d_b + 2\ d_s$ is the total slab thickness. Overall, there are five free parameters used for modeling the Hall data (N_D, N_A, E_D, E_A, and m_h) as well as four quantities parameterized from experimental data or theory (DOS(E), $E_g(0)$, m_e, d_s). Some calculations also included compensation in the bulk by adding a bulk acceptor with concentration $N_{A,bulk}$ and ionization energy E_A - E_V = 50 meV. The calculation routine was implemented in Igor Pro 6.12, see appendix for the code.

2.7.3 Band Structure

The software program 1D Poisson (http://www3.nd.edu/demand/) by G. Snider was used to calculate band edge energies and carrier concentrations as a function of distance from the crystal surface. The inversion layer was modeled by assuming a Schottky barrier at the surface of n-type pyrite (with N_D and E_D taken from Hall effect results) with a barrier height chosen so that the Fermi level was located ∼100 meV above the valence band edge, in agreement with UPS results.

2.8 Solar Cell Fabrication

2.8.1 Single Crystal Junctions

Single crystal slabs grown by the flux method (section 2.1.2) were studied as photoabsorbers in wet junctions and in solid-state Schottky junctions.

2.8.1.1 Wet Junctions

The record efficiency for any pyrite solar cell to date (2.8% PCE under non-standard spectrum[35]) was reported for a wet junction with an electrolyte containing the I^-/I_3^- redox couple. This let us to replicate that setup to test our flux grown single crystals.

Crystal slabs were cut, polished and etched in piranha, then mounted on a conductive wire and covered in epoxy, with only one facet left free. InGa eutectic and colloidal Ag were used to make ohmic contacts. The such prepared working electrode was then place in a three-neck electrochemical cell along with a platinum counter electrode and a Ag/AgCl reference electrode in a typical three-cell configuration.[33] An aqueous electrolyte was prepared fresh with 0.7 M HI, 0.15 M CaI_2, 0.03 M I_2 (pH = 0.35). The I^-/I_3^- redox couple in highly acidic solutions had been reported in the past to prevent corrosion of the pyrite electrode and yield best photo-activity.[33] The electrochemical cell was connected to a Potentiometer and measured at different sweep rates in the dark and under illumination with AM1.5G light from a solar simulator through a quartz window.

2.8.1.2 Solid-state Schottky- and Heterojunctions

Solid-state junctions were made from polished single crystal slabs by depositing a metal (Schottky junction) or semiconductor (heterojunction) through a shadow mask by thermal

evaporation or sputtering. The pyrite crystal was contacted on the bottom using InGa eutectic, colloidal graphite and/or colloidal silver, while the junction material was contacted either directly with a probe needle or with a small dot of colloidal silver. See fig. 5.3 for images and discussion of completed junctions.

2.8.2 Thin Film p-n Heterojunctions

Given that (at least unpassivated) pyrite thin films are p-type, our initial device design was inspired by commercially successful designs used in CIGS and CdTe solar cells. For this, a molybdenum back contact was sputtered on pre-cleaned glass substrates. Two different kinds of glass substrates were tested, the first with high Na content (soda-lime glass), the second one with very low Na content (borosilicate). Depending on the cell layout used (see section 5.3.2), the Mo layer was either unpatterned or patterned by sputter deposition through a shadow mask. The pyrite absorber was then grown on top by one of the methods described in section 2.1, including all necessary annealing steps to achieve phase-pure pyrite. The crucial step then is to form a pn-junction to an n-type window layer. For this layer, ZnS seems a promising candidate: it has been successfully demonstrated in Cu(In,Ga)(S,Se) cells and has the same lattice constant as pyrite in its cubic phase. ZnS was mainly deposited by reactive sputtering from a ZnS target, but we also tested chemical bath deposition (CBD). Alternative junction partners tested were CdS, ZnO and NiO. All additional layers (ZnO, TCO, metal top contact) were deposited by sputtering. See section 5.3.2 for schematics and SEM cross sections of all device stacks tested.

While many different recipes were tested in the course of this work, this is the detailed recipe used to fabricate the highly rectifying and photo-active diodes based on CVD pyrite film, that are shown in fig. 5.10 and fig. 5.11. Note that this recipe does not include steps for patterning. Patterning of layers is necessary to improve reproducibility by avoiding punch-throughs (see section 5.3.2), but no ideal solution was found and champion devices were

made without any patterning in the 'mesa' layout.

1) 12 x 12 mm glass substrates (Corning Eagle XG borosilicate, pre-cut and pre-cleaned by Thin Film Devices, Inc.) were loaded into the AJA vacuum chamber and pumped down to $< 10^{-7}$ Torr.

2) Glass substrates inside the vacuum chamber were heated to 100 °C and plasma-etched for 5 min in an argon-oxygen plasma (50 W RF power, 20 mTorr of 50% oxygen and 50% argon) immediately prior to Mo deposition.

3) Mo films were deposited at 100 ° in 2.0 mTorr 99.999% pure Ar gas from a 99.95% pure Mo target (AJA). Deposition for 65 min at 180 W DC power resulted in ∼800 nm thick films with < 1 Ω/square sheet resistance.

4) Mo-coated glass substrates were handed to over to Nima Farhi for CVD deposition of FeS_2 absorber, followed by sulfurization. See [6] for details.

5) Sealed quartz ampules containing phase-pure pyrite films on Mo/MoS_2 back contact and residual sulfur were received from Nima Farhi.

6) Quartz ampules were scored with a diamond scribe, then opened inside the glovebox. It was found that a strong score in combination with breaking the tip of the ampule before breaking the ampule at the score reduces the amount of micro quartz shards that end up on the film. Films were handled with a vacuum pen, blown off with nitrogen gas and loaded into the sputter chamber.

7) Samples inside the sputter chamber were evacuated to $< 10^{-7}$ Torr, then briefly heated to 225 °C. As soon as this temperature was reached, it was reduced to 100 °. The ZnS target was pre-sputtered at 2.3 mTorr (1% H_2, 99% Ar) and 30 W RF power for 5 min, before the gun shutter was opened for deposition. Deposition was done first for 10 min at 30 W, then for 50 min at 75 W. All ramps for the ZnS target were 3 W/s. Immediately after ZnS deposition, intrinsic ZnO was deposited with the substrate still at 100 °C, 2.8 mTorr (1% O_2, 99% Ar) and 75 W RF power for 150 min.

8) The devices were then brought back into the glovebox to attach a shadow mask below the sample holder, in order to define the cell top contacts. Analog to step 7), Al-doped ZnO (AZO) was then deposited at 100 °C using 110 W RF power for 70 min in 2.3 mTorr pure Ar.

9) The finished devices were handled carefully to avoid scratching, and air-exposure was minimized. They were transferred to a probe station with solar simulator illumination and very carefully contacted with needle probes to measure JV characteristics.

Chapter 3

Pyrite and Other Relevant Thin Films

3.1 Pyrite Thin Films

As discussed in section 2.1.3 and section 2.1.4, high-quality pyrite thin films were supplied in-house by Nick Berry, Nima Farhi, Sean Seefeld and Amanda Weber. All films were rigorously phase-pure unless noted otherwise, and possess appropriate morphological and optical characteristics for application in solar cells. While the details of these films are discussed elsewhere,[6,97,116] in the present work these films were used to study electrical properties of polycrystalline pyrite films, compare them to single crystals, and for their application in thin film solar cells (section 5.3.2).

3.1.1 Comparison of Thin Films Made by Different Routes

Pyrite thin films have been prepared in the past by many techniques, including the sulfurization of iron thin films,[39,24,76,77,115,87,46] sputtering,[69,119,7] flash evaporation,[26,25] electrodeposition,[81,67] spray pyrolysis,[120] molecular beam epitaxy,[12] and chemical vapor deposition

(CVD, see fig. 3.1). Our group recently also developed a number of recipes to make pyrite thin films from inks.[90,97,74,116]

Interestingly, all FeS_2 films — regardless of their phase purity or growth substrate — show very similar electrical properties, that is, thermally activated p-type conductivity with a relatively low room-temperature resistivity ($\approx 1\ \Omega$ cm) and low mobility. While this holds for all fabrication methods, it is shown as an example for CVD films reported in literature(using different chemistries) in fig. 3.1. Also shown is an Arrhenius plot of temperature-dependent conductivity data for representative thin films made in our lab by the three methods mentioned above ('CVD', 'Fe(acac)$_3$ ink' and 'elemental ink'). All three films have almost identical transport properties, though made from very different routes and having different impurities (see fig. 3.2). This negligible electrical impact of phase and elemental impurities suggests that transport in pyrite thin films may be dominated by robust surface effects rather than bulk properties.

3.1.2 Effect of Marcasite Impurity

Marcasite is the orthorhombic FeS_2 polymorph of pyrite. It is meta-stable, with its formation energy only slightly higher than pyrite and thus can be converted readily to pyrite at elevated temperatures. However, pyrite starts to lose sulfur from the lattice at elevated temperatures in ambient conditions in the absence of a high sulfur partial pressure, resulting in sulfur deficient Fe_xS_y phases. It is therefor necessary to anneal mixed-phase pyrite/marcasite films in a sulfur atmosphere to achieve phase-pure pyrite films. Details of this process are discussed elsewhere.[6,116] Marcasite phase impurities was often suggested as one of the reasons for poor electrical transport properties in pyrite thin films (i.e., high doping, low carrier mobility) and corresponding low photo-voltage.

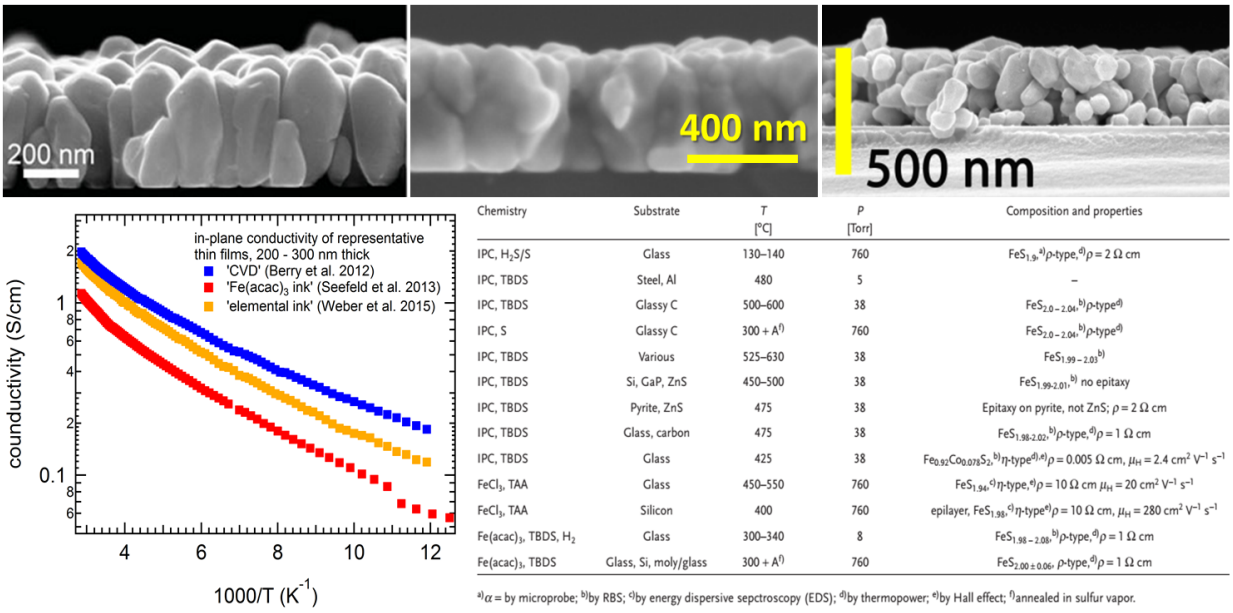

Chemistry	Substrate	T [°C]	P [Torr]	Composition and properties
IPC, H_2S/S	Glass	130–140	760	$FeS_{1.9}$,[a] ρ-type,[d] ρ = 2 Ω cm
IPC, TBDS	Steel, Al	480	5	–
IPC, TBDS	Glassy C	500–600	38	$FeS_{2.0-2.04}$,[b] ρ-type[d]
IPC, S	Glassy C	300 + A[f]	760	$FeS_{2.0-2.04}$,[b] ρ-type[d]
IPC, TBDS	Various	525–630	38	$FeS_{1.99-2.03}$[b]
IPC, TBDS	Si, GaP, ZnS	450–500	38	$FeS_{1.99-2.01}$,[b] no epitaxy
IPC, TBDS	Pyrite, ZnS	475	38	Epitaxy on pyrite, not ZnS; ρ = 2 Ω cm
IPC, TBDS	Glass, carbon	475	38	$FeS_{1.98-2.02}$,[b] ρ-type,[d] ρ = 1 Ω cm
IPC, TBDS	Glass	425	38	$Fe_{0.92}Co_{0.078}S_2$,[b] η-type[d,e] ρ = 0.005 Ω cm, μ_H = 2.4 $cm^2 V^{-1} s^{-1}$
$FeCl_3$, TAA	Glass	450–550	760	$FeS_{1.94}$,[c] η-type,[e] ρ = 10 Ω cm μ_H = 20 $cm^2 V^{-1} s^{-1}$
$FeCl_3$, TAA	Silicon	400	760	epilayer, $FeS_{1.98}$,[c] η-type[e] ρ = 10 Ω cm, μ_H = 280 $cm^2 V^{-1} s^{-1}$
$Fe(acac)_3$, TBDS, H_2	Glass	300–340	8	$FeS_{1.98-2.08}$,[b] ρ-type,[d] ρ = 1 Ω cm
$Fe(acac)_3$, TBDS	Glass, Si, moly/glass	300 + A[f]	760	$FeS_{2.00\pm0.06}$, ρ-type,[d] ρ = 1 Ω cm

[a] α = by microprobe; [b] by RBS; [c] by energy dispersive sepctroscopy (EDS); [d] by thermopower; [e] by Hall effect; [f] annealed in sulfur vapor.

Figure 3.1: Comparison of pyrite thin films grown by different methods. Top row: SEM images of pyrite thin films grown on quartz substrates in our lab by (left) chemical vapor deposition (CVD, section 2.1.3), (center) $Fe(acac)_3$ ink method (section 2.1.4) and (right) elemental ink method (section 2.1.4). Bottom left: Arrhenius plot of temperature-dependent conductivity data for representative thin films made in our lab by the three methods. Interestingly, all three films have almost identical transport properties, though made from very different routes and having different impurities. This is in line with an even wider range of films in literature having very similar transport properties, as shown here for example for CVD made films. Bottom right: Literature overview of pyrite thin films grown by chemical vapor deposition (CVD). The films in the last row are the 'CVD method' films used in this study.[6] IPC = iron pentacarbonyl; TBDS = tert-butyl disulfide; TAA = thioacetamide. Figure adapted from [6], [97] and [116].

Impurity (ppm)	Ink Mo/glass	Ink Si	$Fe(acac)_3$ Mo/Si	CVD Si
oxygen	2440	204	1750	1990
potassium	1	1	50	2
sodium	1300	5	165	20
carbon	205	155	900	8610
hydrogen	1130	1075	20-100	1530
aluminum	<1	<1	165	100
calcium	4	10	2-6	30

Figure 3.2: Elemental impurity content of pyrite thin films from the different methods used for this work. Values from SIMS after sputtering into the bulk of the film. Figure adapted from [116].

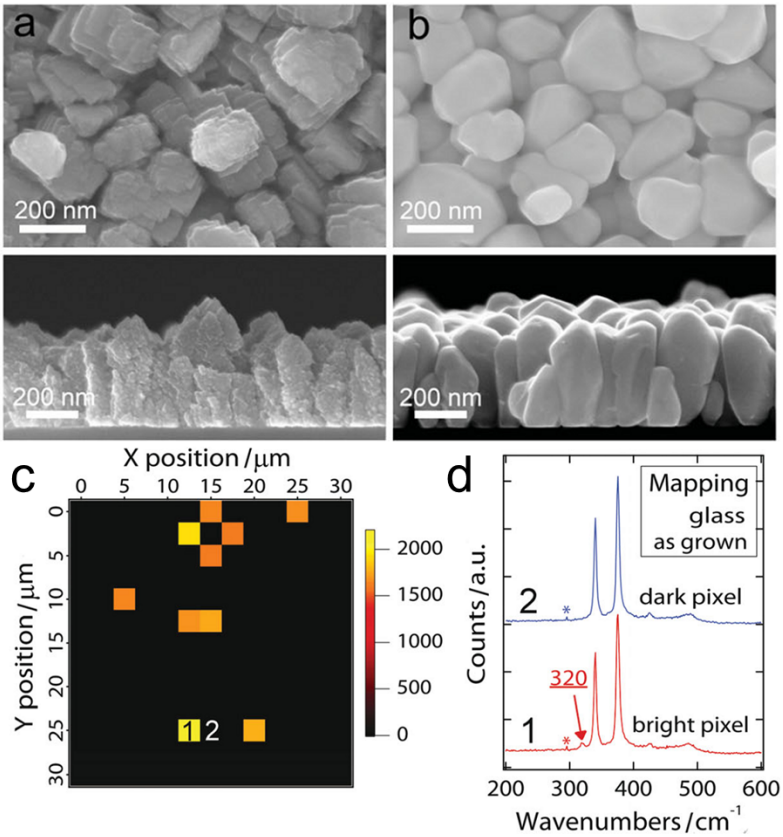

Figure 3.3: Marcasite impurity in pyrite thin films: morphology and distribution. This figure shows data that were taken on films made by the CVD method, but are representative for all three methods discussed in the text. (a) SEM top-down and cross-section image of mixed-phase pyrite/marcasite film. (b) Same images for phase-pure pyrite film. (c) Raman map (integrated 323 cm^{-1} band) showing inhomogeneous distribution of marcasite impurity in a mixed-phase film ($\sim$5% total marcasite content). (d) Spectra collected from adjacent bright and dark pixels ("1" and "2" on the map). Figure adapted from [6]

As shown in fig. 3.3 a film with ∼5% marcasite content has an inhomogeneous distribution of marcasite domains, as revealed by Raman mapping. The marcasite 'hot spots' are confined to areas smaller than 2.5 μm x 2.5 μm (the map resolution) and distributed randomly. Limited by the spatial resolution of the Raman microscope, correlation of the Raman map with SEM topography images was not possible. No clearly 'marcasite-like' crystallites (by size, shape, faceting or SEM contrast) could be identified.

Figure 3.4 shows optical absorption spectra of mixed-phase and pure pyrite films. The fact that a substantial marcasite impurity is almost invisible in the optical absorption spectra of our mixed-phase films raises renewed questions about the band gap and optical functions of marcasite. Marcasite is thought to have a band gap of ∼0.34 eV, which would make it unsuitable for solar energy conversion in bulk form and a deleterious phase impurity in pyrite.[107] Sun et al. recently challenged this notion by presenting rigorous DFT calculations indicating that marcasite probably has a larger band gap than pyrite.[102] These authors pointed out that the purported value of the marcasite gap is based on variable-temperature resistivity data from a single natural marcasite crystal published in 1980.[56] Fitting of resistivity data is an unreliable way to determine the band gap of a semiconductor of unknown purity and carrier mobility, and should be verified with additional techniques. Our lab confirmed the results of Sun et al. using our own DFT calculations of marcasite, finding the band gaps of marcasite and pyrite to be 0.79 and 0.63 eV, respectively, at the generalized gradient approximation (GGA) level of theory (see [97] for details). Our mixed-phase marcasite/pyrite thin films provide an opportunity to test these DFT predictions against experimental data. As shown in fig. 3.4, experimental absorption data agrees very well with the DFT calculations and both agree that the marcasite band gap is not smaller than the pyrite band gap.

We conclude that the marcasite electronic and optical band gaps are at least as large as those of pyrite. Rather than being inherently unsuitable for solar energy conversion, pure marcasite films, if they can be synthesized, may very well have better optical and electronic properties than pyrite itself. However, our results do not imply that marcasite is necessarily

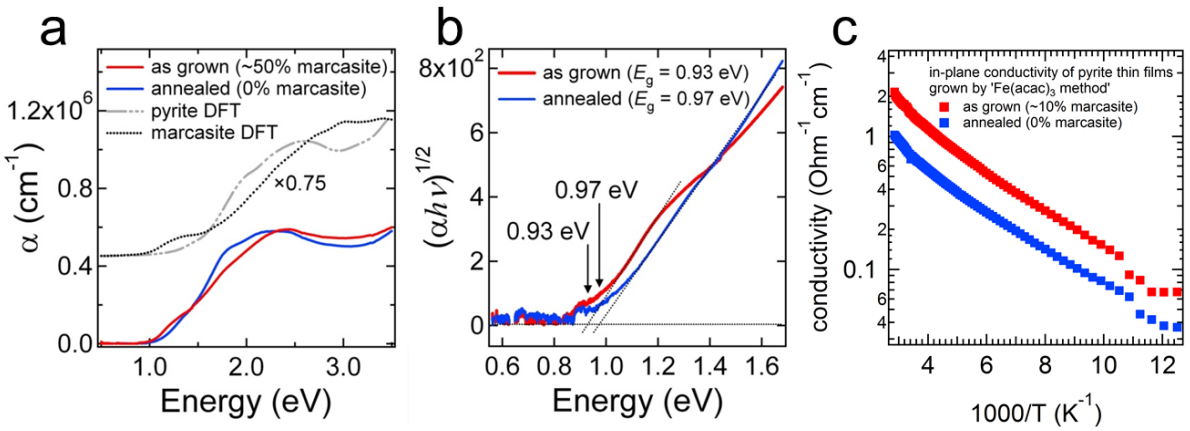

Figure 3.4: Marcasite impurity in pyrite thin films: optical and electrical effects. (a) Absorptivity spectra of an as-grown film (red) containing ∼50% marcasite and an annealed film (blue) with no marcasite content, as well as calculated spectra for pyrite (gray hashes) and marcasite (black dots). The marcasite spectrum is the average of the optical functions along the [100], [010], and [001] directions of the orthorhombic crystal. The calculated spectra are scaled by a factor of 0.75 and offset for clarity. (b) Plot of $(\alpha h\nu)^{1/2}$ versus energy used to estimate the band gap of the two films shown in (a). (c) Arrhenius plot comparing temperature-dependent conductivity data of mixed-phase and phase-pure pyrite film. Note that the marcasite content of the mixed-phase film is lower here (∼10%). The temperature-dependence and activation energies are identical, with the mixed-phase film having a higher absolute conductivity by about a factor of 2. Figure adapted from [97]

a benign impurity in pyrite. Comparing electrical transport in mixed-phase and phase-pure pyrite films (fig. 3.4), we find that they are very similar, with identical activation energies and slightly higher absolute conductivity for mixed-phase films. It should be noted that this comparison of electrical transport might be somewhat convoluted by the effect of grain-growth that also occurs during the sulfurization process that converts a mixed-phase film to a phase-pure pyrite film. See [6], [97] and [116] for more details.

Although marcasite almost certainly has a larger gap than pyrite and similar absorptivity, the existence of band edge offsets and electronic defects at the pyrite/marcasite interface as well as other types of disorder may result in degraded electronic properties for mixed-phase pyrite/marcasite thin films for solar cell applications. We therefore continue to believe that the synthesis of phase-pure films, whether pyrite or marcasite, remains desirable for solar energy applications. Thus all further data and conclusions in this study (unless noted otherwise) are based on rigorously phase-pure pyrite thin films.

3.1.3 Electrical Transport in Polycrystalline Thin Films

The electrical properties of FeS_2 films on glass and quartz substrates were assessed by variable-temperature Hall effect measurements in a van der Pauw geometry. The dark resistivity of pure pyrite films is on the order of 1 Ω cm at room temperature and increases by about a factor of 20 - 30 upon cooling to 80 K. We found no difference between pure pyrite films made on glass and quartz substrates. Arrhenius plots of the resistivity are curved (see discussion below), with activation energies varying from $\sim$20 meV at 100 K to $\sim$50 meV at 350 K. The temperature dependence of the resistivity is characteristic of a highly doped but non-degenerate semiconductor. The in-plane Hall mobility of these films was too low to be measured (< 1 cm^2/Vs), which also prevented determination of the carrier type from the sign

of the Hall voltage. However, qualitative thermopower measurements always indicated that the films were p-type. The fact that these general features — low resistivity, low mobility, and p-type transport — have been reported for nearly all unintentionally doped pyrite thin films regardless of fabrication method may imply that transport in polycrystalline pyrite films is governed by surface/interface effects rather than bulk properties. Even marcasite phase impurities do not change transport properties appreciable (see above).

The insensitivity of FeS_2 electrical properties to both bulk phase impurities and substrate-derived elemental impurities is evidence that charge transport in polycrystalline pyrite films is controlled by surface effects, for example, a conductive inversion layer, that is quite insensitive to variations in bulk composition. Our electrical results are in good agreement with literature. Unintentionally doped polycrystalline pyrite thin films are always reported to be p-type by in-plane thermopower and (less frequently, due to the low carrier mobility) Hall measurements and feature a narrow range of low resistivity ($0.5 - 10\ \Omega$ cm), high carrier concentration ($10^{18} - 10^{20}$ cm^{-3}), and low mobility (< 2 cm^2/Vs) regardless of the preparation method and S:Fe stoichiometry.[51,3] This is true of purportedly sulfur-deficient[115,69,51,106,75] and iron-deficient[115,32,51,106,75] films made by CVD, sputtering,[69,119] sulfurization of iron films,[77,115,46] and molecular beam epitaxy.[12] Only by intentional doping with donors such as Cl, Br, or Co have n-type polycrystalline pyrite thin films been made.[84,104]

There are at least three credible explanations for the ubiquitous electrical behavior of nominally un-doped pyrite thin films: phase impurities, accidental oxygen doping, and surface effects. First, pyrite samples may inevitably (due to thermodynamic considerations) contain nano-scale inclusions of metallic, sulfur-deficient phases. This idea[124] seems at odds with the experimental evidence, particularly the very high external quantum efficiency of pyrite photo-electrochemical[33] and Schottky[16,15] solar cells and sensitive magnetic measurements that show no evidence of pyrrhotite or other magnetic sulfur-deficient phases above ppm levels in properly prepared pyrite films.[106] A second possibility is that all pyrite films are contaminated with oxygen and that oxygen acts as an efficient acceptor to produce highly-

doped, p-type films. Sun et al.[102] has argued that pyrite synthesized in iron-rich, oxidizing conditions may be contaminated with substitutional oxygen (O_S defects) at a concentration of $\sim 10^{19}$ cm^{-3} and that O_S impurities are p-type dopants. Concern over oxygen is reasonable given the potential for oxygen incorporation in pyrite films made by different methods. However, films prepared by the three methods used for this study vary in O_2 content from 200 to 2000 ppm, yet their electrical transport properties are virtually identical. Moreover, our own density functional theory calculations show that O_S is neither an acceptor nor a donor in bulk pyrite.[52] Experimental evidence from ultra-pure single crystals with oxygen levels below 10 ppm in the bulk rules out oxygen as a bulk dopant table 4.1.

Surface effects provide a third explanation for the universal electrical behavior of nominally undoped pyrite films. As argued by Tributsch and co-workers[51] 20 years ago, the similarity of the electrical characteristics regardless of stoichiometry and preparation method suggests that the electrical behavior of pyrite thin films is not determined by the bulk properties of the crystallites but rather by their surface properties. Given the well-known reactivity of pyrite surfaces,[79] it is reasonable to expect that surface composition and/or electronic effects are very important for pyrite thin films and may be responsible for their measured electrical properties.

We now return to discuss the curved Arrhenius plots (fig. 3.5) and analyze the temperature dependence of the conductivity to gain further insight on the transport mechanism in these thin films. A curvature in Arrhenius plot for the conductivity corresponds to a temperature-dependent activation energy $E_a = E_a(T)$ and indicates that $p \neq 1$ in $\sigma = \sigma_0 \exp(-\frac{E_a}{k_B T})^p)$, meaning that simple activated band transport is not the dominant mechanism. Using the Zabrodskii method, we find that a value of $p \approx 0.4$ - 0.6 can fit the data better, yet still fails to capture well the rapidly increasing E_a at high temperatures. A value of $p = 0.5$ is often interpreted as a sign for Efros-Shklovskii variable range hopping (ES-VRH) transport. The curved Arrhenius can also be fit by the model proposed by Werner that considers transport in polycrystalline films to be limited by thermionic emission across inhomogeneous grain

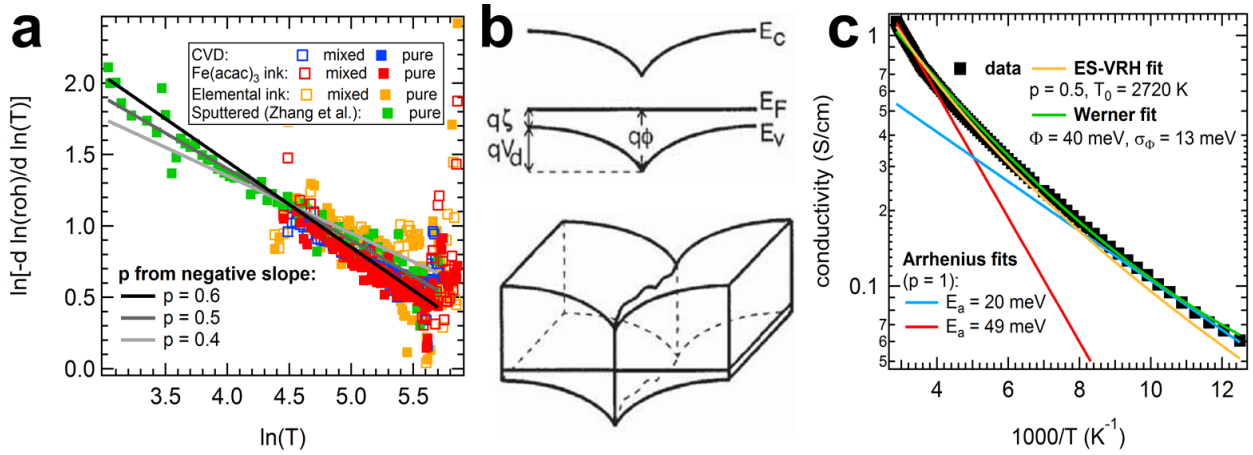

Figure 3.5: Electrical transport in polycrystalline pyrite thin films. (a) Zabrodskii plot[125] to linearize $\sigma = \sigma_0 \exp(-\frac{E_a}{k_B T})^p)$ for thin films made by the three methods discussed in the text, before ('mixed') and after ('pure') sulfurization to eliminate the marcasite impurity, along with sputtered films from [126]. For all data $0.4 \leq p \leq 0.6$. (b) Diagram taken showing (top) the band diagram of a homogenous depletion boundary in a p-type material and (bottom) an inhomogenous boundary with potential fluctuations. The Werner model assumes thermionic emission over grain boundaries and a Gaussian distribution of barrier heights. Adapted from [117] (c) Temperature-dependent conductivity data from a representative thin film along with Arrhenius (p = 1) fits in the high and low temperature regions, ES-VRH (p = 0.5) fit and Werner model fit.

boundaries with a Gaussian distribution of barrier heights.[117] Figure 3.5 shows a comparison of simple Arrhenius fit, ES-VRH fit and Werner fit for a representative thin film. It is apparent that a Arrhenius fit cannot account for the curvature (i.e., $E_a = E_a(T)$). The ES-VRH fits are better, but need to invoke a hopping transport mechanism that is hard to reconcile with pyrite, especially the magnetoresistance data discussed in section 4.4.2. The Werner model fits the data very well, but its picture of transport *across* grain boundaries is at odds with the picture of surface dominated transport implying transport *along* grain boundaries. To resolve the question of the dominant transport mechanism and obtain a quantitative model in pyrite thin films, a wider range of temperatures needs be evaluated, especially to see if transport can change to bulk-dominated n-type conduction at elevated temperatures for high-quality thin films. Qualitatively though, all results presented here and in section 4.4.2 are in line with a hole-rich surface layer that is dominating transport at room temperature and below.

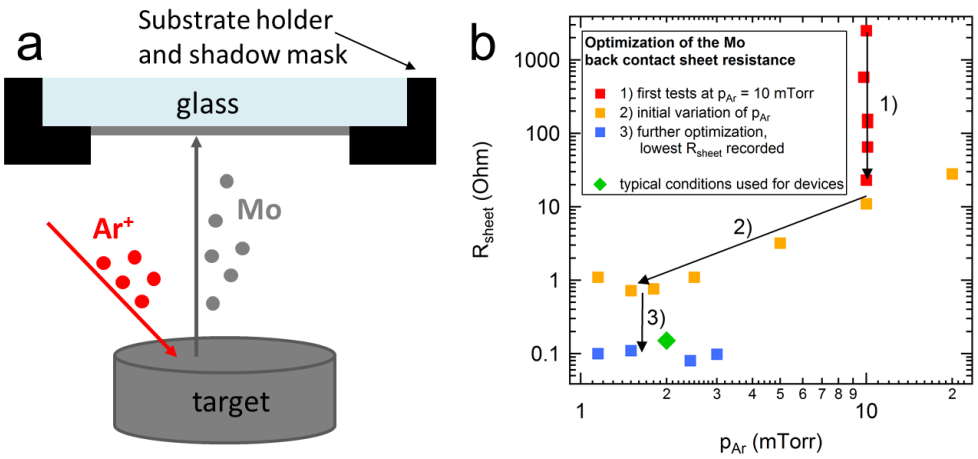

Figure 3.6: Deposition of Mo films on glass substrates by DC magnetron sputtering. (a) Diagram showing a glass substrate that is partially masked by the substrate holder. Ar^+ ions are accelerated and slammed into the Mo target where they kinetically knock out clusters of Mo atoms that then deposit on the unmasked area of the substrate. (b) Evolution of Mo films made in our lab, as evaluated by the sheet resistance R_{sheet}. Low sheet resistance of a metal film is a good measure for crystallinity and perfection.

3.2 MoS_{2-x} Films Obtained by Sulfurization from Mo

Molybdenum was chosen as the back contact for pyrite heterojunction solar cells mainly due to two advantages. First, Mo has a low work function of 4.3 - 4.9 eV (depending on the face),[55] making it a potentially ohmic back contact for p-type pyrite films. Second, Mo has already been shown to survive harsh sulfurization (selenization) conditions in the fabrication of $Cu(In,Ga)(S,Se)_2$ solar cells, where it forms a Mo/MoS_2 ($Mo/MoSe_2$) bilayer. As discussed below, processing of pyrite films on Mo requires harsher and longer sulfurization than in the case of $Cu(In,Ga)(S,Se)_2$, making thicker Mo/MoS_2 layers necessary.

DC sputtered Mo films were initially optimized for high density, high crystallinity and low sheet resistance. Films thus optimized to $< 1\ \Omega$/square passed the 'scotch tape test' before and after sulfurization for 4 h at 550 °C in a quartz ampule containing 50 mg sulfur.

As shown in fig. 3.7, prolonged sulfurization of Mo films causes a gradual phase conversion from top to bottom, along a sharp line, and eventually full conversion to MoS_2. The conver-

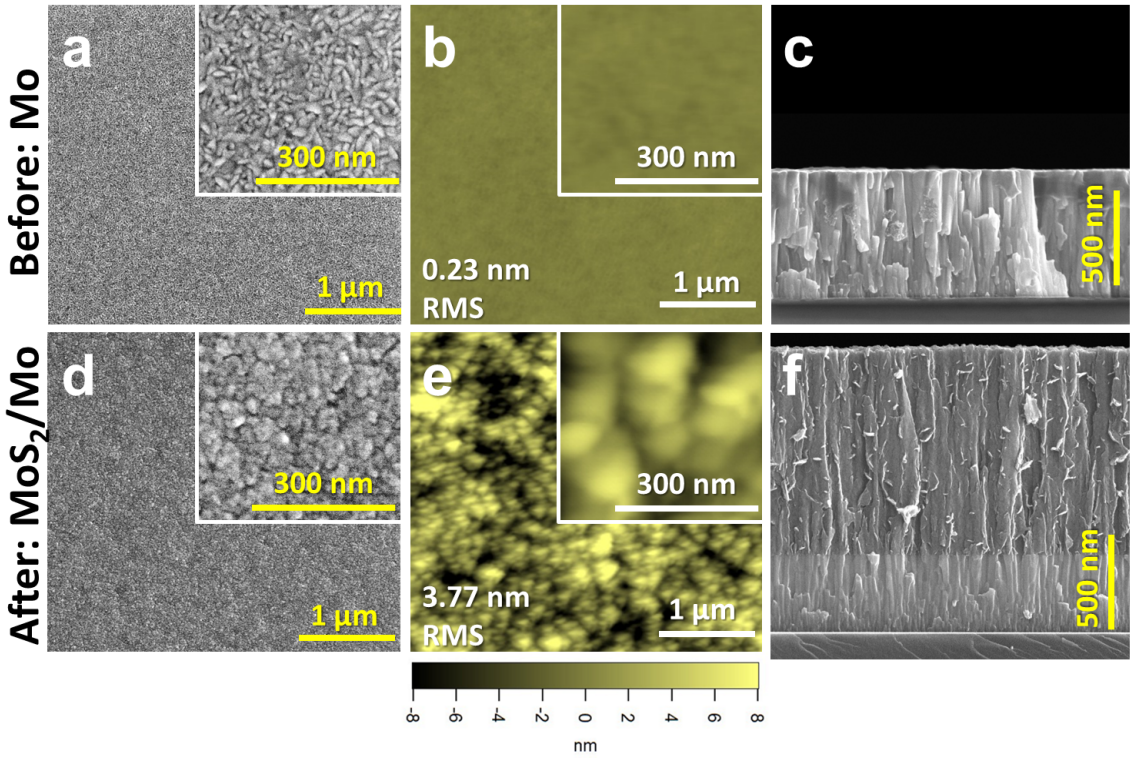

Figure 3.7: Mo films before and after sulfurization: topography and morphology. The top row shows (a) SEM top-down image, (b) AFM tomography and (c) SEM cross sectional image of a Mo film as deposited on glass. The bottom row (d, e, f) shows the same film after sulfurization for 3 hours at 515 °C.

sion front is seen as a change in contrast in SEM images, and is remarkably sharp, indicating diffusion of sulfur into the Mo is very slow compared to competing processes. The conversion process goes along with a large increase in film thickness by a factor of 3.6, as expected by the ratio of MoS_2 to Mo unit cell volume. Surface roughness is increased slightly, going from the typical 'dead fish' topography of Mo films to a slightly rougher MoS_2 surface, but still smooth enough for solar cell purposes.

For a lack of reports on polycrystalline MoS_2 films in literature and their importance for pyrite solar cell fabrication (section 5.3.2), they were investigated more closely to learn about their electrical and optical properties.

The first challenge was to obtain completely converted MoS_2 films from Mo films, without any Mo left that would impact film characterization. For a given Mo film thickness, too short

of a sulfurization time resulted in a thin residual Mo metal layer, while too long sulfurization often resulted in the MoS_2 film flaking off. Carefully tuning sulfurization time and controlling composition by SEM cross-sectional imaging finally resulted in fully converted MoS_2 films without Mo residue. For these films (see fig. 3.8), the optical band gap was estimated to $\sim$1.6 eV.

Strikingly, it was observed that MoS_2 conductivity continues to drop upon prolonged sulfurization, even after the Mo layer is completely converted, according to ultra-high resolution SEM. All these experiments were conducted with a large number of identical Mo films on glass, that were then sulfurized using the same sulfur atmosphere, same heating and cooling ramps, but different dwell times at 515 °C. For example, for the 52 nm Mo films shown in fig. 3.8d, conductivity drops from $\sim 10^5$ to $\sim 10^4$ S/cm within the first hour of sulfurization. This decrease is easily explained by the decrease in Mo thickness. The contribution of MoS_2 conductivity is still negligible compared to the metal. Then, after 90 min dwell time, film conductivity drops to $\sim$1 S/cm, which is less than the value expected from a single monolayer of Mo. Also, no Mo layer is seen in ultra-high resolution SEM for this film. Thus, we attribute this conductivity value to MoS_2. Now, surprisingly, an even longer dwell time of 120 min results in a further reduced film conductivity of $\sim 10^{-4}$ S/cm. A similar decrease in conductivity is observed for initially thicker (110 and 800 nm) Mo films. Since the films look unchanged by SEM (still compact) upon further sulfurization (after the Mo phase already disappeared), and no new phases are seen in XRD, this drastic further decrease in conductivity is attributed to a change in film stoichiometry. It suggests that 'just' fully converted films are in fact MoS_{2-x}, with x = 0 only reached after prolonged sulfurization, and that the initially higher conductivity of $> 10^{-4}$ S/cm may be caused by S-vacancies.

To probe the majority carrier type and activation energy of these MoS_{2-x} films, thermopower and Hall effect data were taken, as shown in fig. 3.8f-g. Thermopower measurements suggest that the dominant carrier type changes from holes to electrons shortly after the Mo film is completely converted, after which the sign of the thermo-voltage stays positive and the

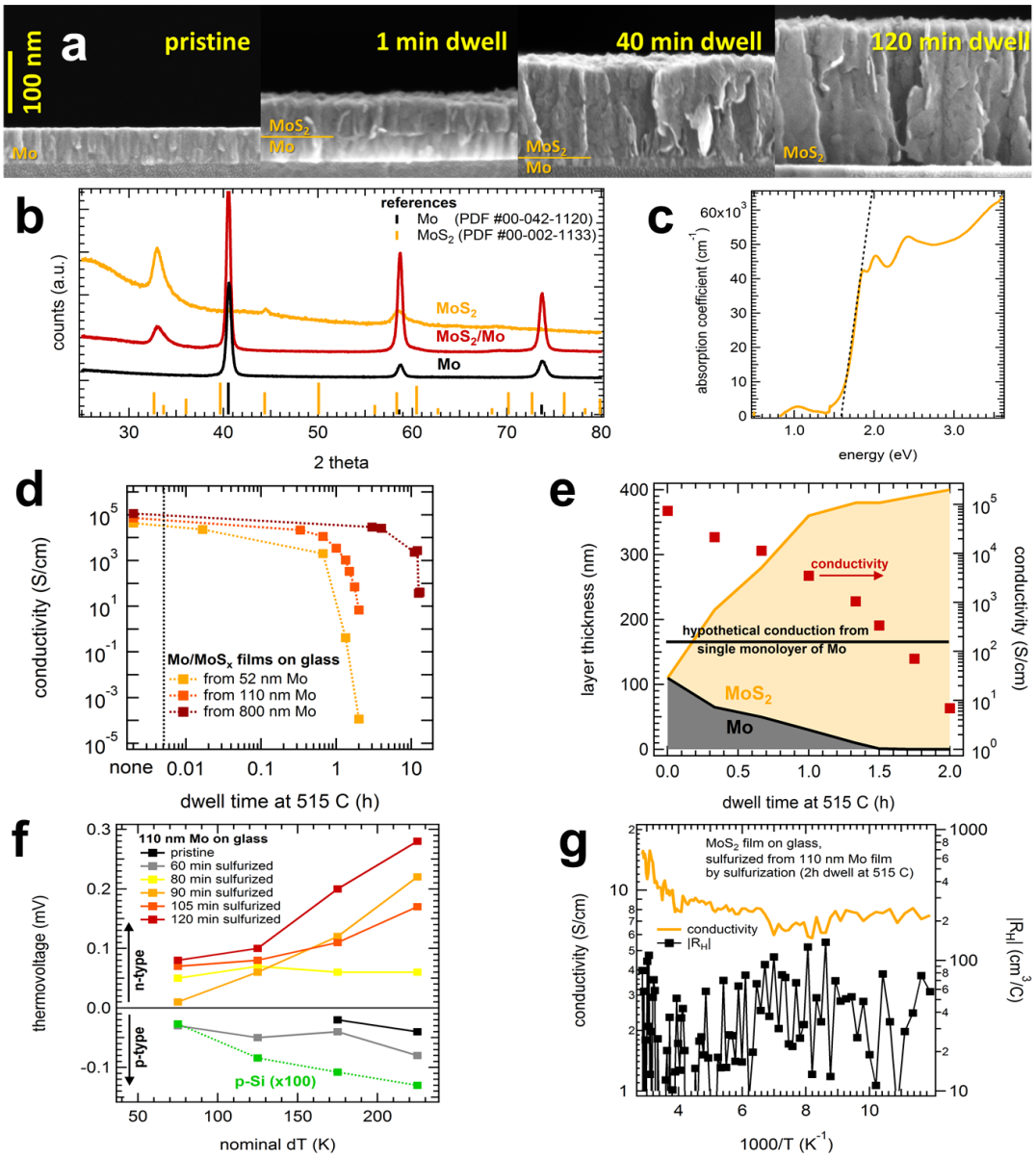

Figure 3.8: Sulfurization of Mo films on glass. See text for detailed explanation. (a) SEM cross sections of the progression from Mo to MoS_2, with phase boundary indicated by horizontal orange line. (b) XRD patterns of pristine Mo, partially converted and almost completely converted film. (c) Absorption coefficient of MoS_2 film obtained by complete sulfurization. Extrapolation of the band edge gives $E_g \approx 1.6$ eV, in good agreement with literature. (d) Progression of film conductivity as a function of dwell time during sulfurization, starting from Mo films of 52, 110 and 800 nm thickness. (e) Conductivity and layer thickness (from SEM cross sectional imaging) of the 110 nm batch shown in (d), as a function of dwell time. Hypothetical conductivity from a single monolayer of Mo metal is indicated by horizontal black line. (f) Evolution of the thermovoltage between hot and cold end of sulfurized Mo films. (g) Conductivity and absolute Hall coefficient $|R_H|$ for a MoS_2 film (last data point in panel (e)).

magnitude increases (as conductivity decreases). Temperature-dependent Hall effect and conductivity data indicate that MoS_{2-x} is a highly doped n-type semiconductor (with $E_g \approx$ 1.6 eV), showing a small positive activation energy only at room temperature and above. The sign of R_H fluctuates randomly, preventing a confirmation of majority carrier type by this method.

3.3 NiO

As discussed in detail above, pyrite thin films are universally p-type, which is likely a result of a strong surface inversion layer.[6,70] If this surface layer was successfully passivated, the entire films would likely become n-type, just as single crystals. In such a scenario a transparent p-type semiconductor would be the natural choice to fabricate pn-heterojunctions. There are not many known transparent p-type materials, especially such that have a tunable doping level and can be deposited by sputtering. One interesting candidate is NiO, a wide-band gap material that, when sputtered at the right conditions, shows high transparency and low doping levels.

NiO recently received much attention as an electron-blocking layer (EBL) or hole-transport layer (HTL) in organic photovoltaics (OPV).[86,118] Some studies employed magnetron sputtering of NiO, both from Ni[72,5] and NiO targets.[92,21] Across literature, resistivity of the NiO layer, which is potentially very important for a FeS_2/NiO heterojunction, has never exceeded 15 Ω cm. In this work, NiO films deposited by RF magnetron sputtering were studied as a function of O_2 content in the O_2/Ar plasma.

Figure 3.9 shows structure, transmission and electrical transport properties of the NiO films obtained by reactive RF sputtering from a Ni target onto glass substrates. Without any oxygen present, Ni metal films are deposited, with very low sheet resistance on the order of 1 Ω/square and no transmission in the visible spectrum. Addition of even 2% oxygen

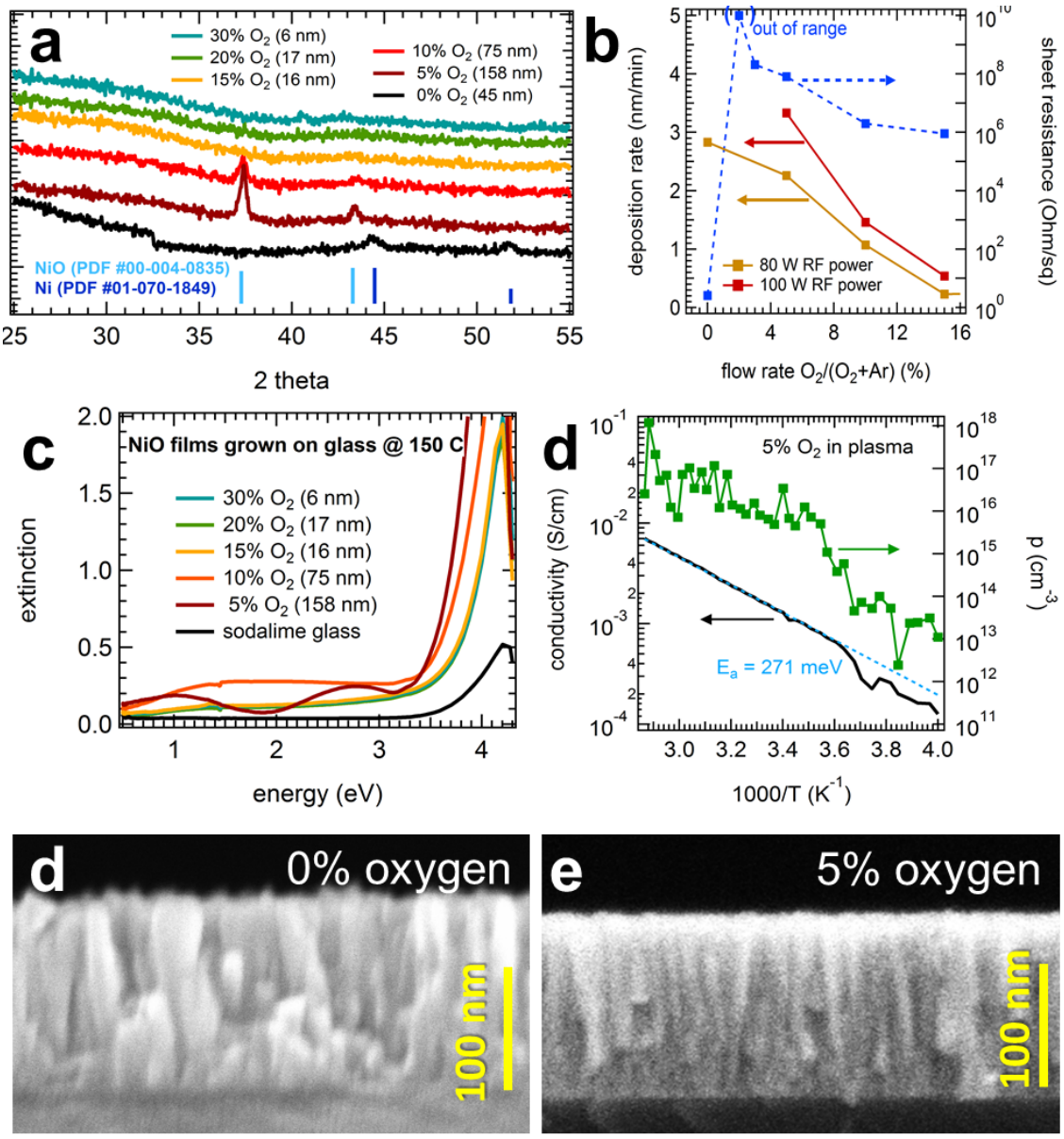

Figure 3.9: Properties of NiO films made by reactive RF sputtering from a Ni target. (a) XRD patterns of Ni and NiO films sputtered on glass substrates, along with Ni and NiO reference pattern. Note the large difference in film thicknesses. (b) Plot of deposition rate (left axis) and sheet resistance (right axis) as a function of oxygen partial pressure. The sheet resistance of the film deposited at 3% oxygen content is out of measurement range, and at least 10^{10} Ω/square. (c) Optical extinction of NiO films on soda-lime glass. Note the large difference in film thicknesses. Films sputtered with 0% O_2 are metallic Ni and completely opaque (not shown). (d) Conductivity (left axis) and hole concentration (right axis) from Hall effect measurements for a NiO film deposited with 5% oxygen in the plasma. SEM cross-sectional views showing morphology of Ni (d) and NiO (e) films deposited on glass.

already changes this drastically, with higher oxygen contents resulting in a gradual decrease in deposition rate (fig. 3.9b). Figure 3.9a shows XRD pattern of NiO films deposited with 5 - 30 % O_2 in Ar. Thickness is not constant here, and some films are much too thin to give a well-defined pattern. For low oxygen content films, the 111 and 200 peaks of NiO can be identified, while the Ni peaks are gone. Sheet resistance increases sharply upon addition of small oxygen concentrations, then decreases with further addition of oxygen. The maximum resistivity was observed for 3% oxygen content, with $R_{sheet} \geq 10^{10}$ Ω/square. Figure 3.9d shows temperature dependent conductivity and hole concentration (measured by Hall effect) for a film deposited at room temperature. The activation energy for conduction is $\sim$270 meV, suggesting a deep acceptor state. Hole concentration and conductivity at room temperature are 10^{16} cm^{-3} and 10^{-3} S/cm respectively. This conductivity value represents the lowest known to the author for a NiO film. As shown in fig. 3.9c, optical extinction data for these films shows an optical band gap of $\sim$3.4 eV, in good agreement with literature. The 5% film is the most promising for use as p-type window layer in devices, as a $\sim$160 nm thick film shows transmission of 50 - 80% (extinction 0.1 - 0.3) in a wide window ranging up to 3.3 eV.

Chapter 4

Pyrite Single Crystals

Towards the ultimate goal of developing a high-throughput method to fabricate inexpensive pyrite thin film absorbers, pyrite single crystals were studied in detail. Single crystals can be found in nature around the world and were the starting point for this study. While these natural crystals can be very large and of high crystalline perfection, they tend to have high levels of elemental impurities that can alter their electrical properties drastically compared to intrinsic pyrite. For this reason, synthetic single crystals were grown to study more intrinsic material properties. Based on the results of this study and the transport model developed (section 4.4.2), they can also be used as a test platform to quantitatively evaluate a wide range of surface passivation treatments (section 4.6).

4.1 Crystals Found in Nature

Despite the general short-comings of natural pyrite crystals (common presence of phase impurities, doping with many different elements, internal voids, low carrier mobility), specimen of high quality can be found from a small number of famous sites in Turkey, Spain and Peru.

One particularly well-suited natural crystal served as the basis for a study of optical properties, in particular pseudo-dielectric function and critical point energies of pyrite. A beautiful octahedral natural crystal, originally found in Erzurum, Turkey, was graciously provided by Dr. Andre Puschnig of Naturhistorisches Museum Basel (catalog number 18249).

The study was done in collaboration with S.G. Choi, L.S. Abdallah and S. Zollner (spectral ellipsometry), J. Hu and R.W. Wu (DFT) and M. Law (principal investigator).[22] Phase purity of the natural pyrite crystal was confirmed by power X-ray diffraction (XRD) (fig. 4.1a) and electrical transport characterized by temperature-dependent Hall effect measurements (fig. 4.1c,d). One of the eight <111> facets was sectioned and fine-polished to < 2 nm roughness (fig. 4.1b) in order to conduct spectral ellipsometry (SE) measurements on it.

The complex dielectric function $\epsilon = \epsilon_1 + i\ \epsilon_2$ and complex refractive index N = n + ik are important for understanding the electronic structure of PV materials and developing PV device structures. Prior to this work, only a limited number of ϵ and N spectra were available for pyrite from electronic structure calculations[64,111,1,109] or optical reflectance measurements.[8,96,101,38] Moreover, significant discrepancies exist among the reported spectra and no trustworthy theoretical explanation has been made available so far.

Both DFT calculated and SE-determined ϵ spectra of the natural pyrite crystal are shown in fig. 4.2. They reveal several above-bandgap optical structures associated with interband critical points (CPs).[23] To elucidate the electronic origin of each CP structure, SE data was compared to (density functional theory) DFT calculations for bulk pyrite with the same computational details used in earlier work[52] (omitting the U-correction term to best fit the experimental spectra).

Two prominent CP features are evident in the SE data at ∼2.0 eV and ∼4.0 eV, as also observed in early studies.[1,109,8,96,101,38] Although the calculations slightly overestimate the CP energies below 3 eV and underestimate those above it, the overall agreement between experimental and theoretical results is obvious. All six of the major CP features observed experimentally are captured in the DFT calculations. The calculated value of the static

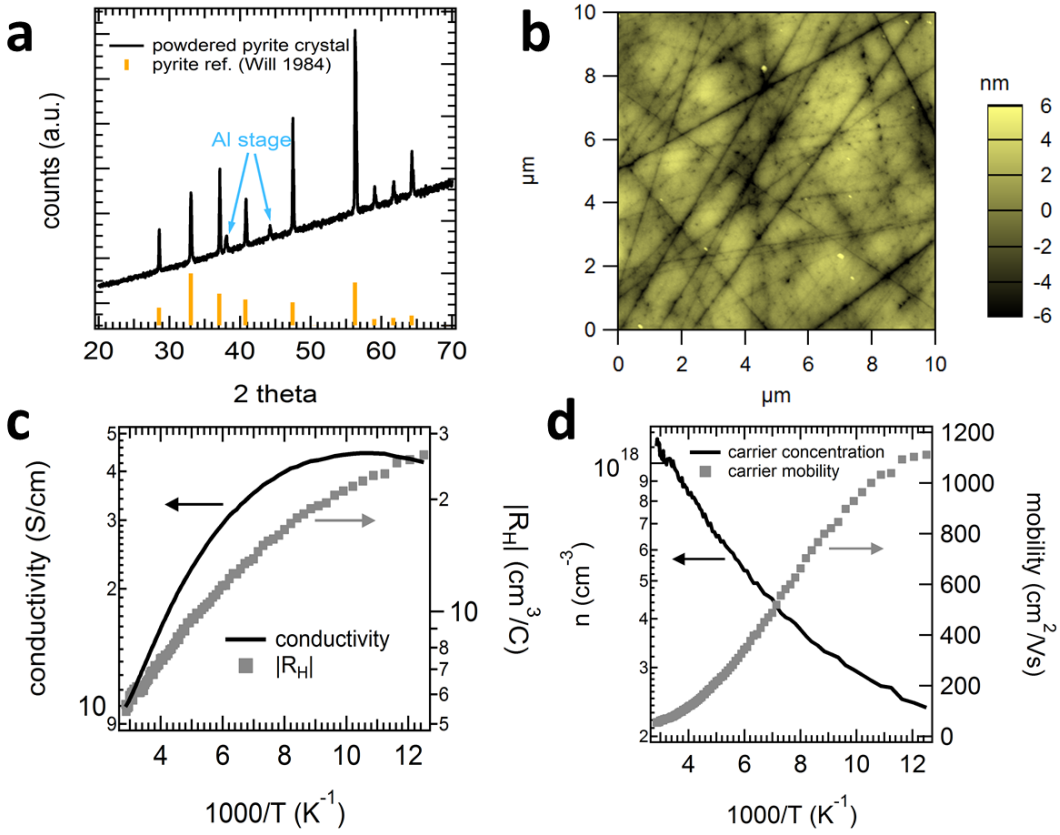

Figure 4.1: Chararcterization of the natural crystal used for spectral ellipsometry (SE) study. (a) X-ray diffraction pattern of a powdered slice of the crystal, showing phase-pure pyrite, along with a pyrite reference pattern. (b) AFM topography scan, showing a 10 × 10 μm area of the polished crystal with 1.8 nm RMS roughness. (c) Temperature-dependent conductivity and absolute Hall coefficient $|R_H|$ and (d) carrier concentration and mobility from 80 - 350 K, calculated from Hall effect measurements using unipolar approximation.

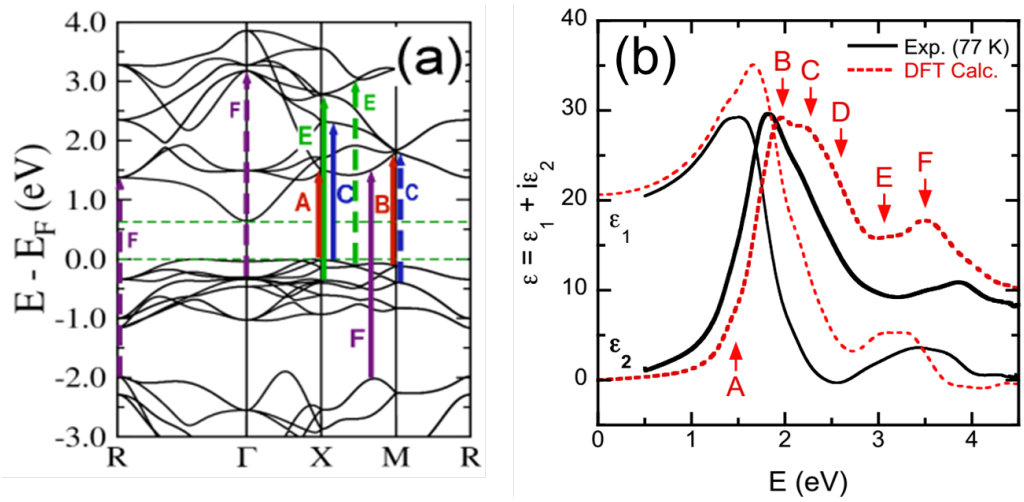

Figure 4.2: Comparison of dielectric spectrum and critical point energies (CPs) from DFT calculations and spectral ellipsometry (SE). (a) Band structure of bulk pyrite, with arrows denoting the main transitions associated with the CPs. (b) Experimental (solid black lines) and calculated (dashed red lines) ϵ spectra for a pyrite crystal. Experimental data were taken at 77 K on a fine-polished <111> surface. The major CP features seen in the calculated ϵ_2 spectrum are labeled alphabetically, and correspond to the transitions in (a). Figure reproduced from [22].

dielectric constant ($\epsilon_\infty = 21$) is also consistent with the experimental data. Figure 4.2 shows the correlation of CP to DFT calculated band structure. For a full discussion of all transition, see reference [22].

Although the bandgap energy of pyrite is thought to be ~0.9 eV, the SE data show nonzero $< \epsilon_2 >$ values below the bandgap rather than an abrupt fundamental absorption edge. This is attributed in part to lifetime broadening and also the presence of native oxides on the crystal surface as well as the nanometer-scale surface roughness.[34,64] Oxidation of pyrite surfaces can be very rapid[28] and the formation of surface oxides was inevitable during sample preparation. A multilayer analysis was not attempted in this study. Another possible cause of the nonzero absorption below 0.95 eV includes surface and bulk defects that may induce states within the bandgap. See section 4.4 for further discussion of defect states and band tails.

4.2 Growth by Chemical Vapor Transport (CVT)

Chemical Vapor Transport (CVT) of a polycrystalline FeS_2 precursor in a halogen transport agent (section 2.1.1) yielded pyrite single crystals of high quality. Growth rate was slow, on the order of mg/day, the largest crystal grown had a mass of 26 mg. Using Cl as transport agent resulted in slower growth compared to Br, which is why most crystals were grown using Br. Iodine was also tested, but resulted in even slower transport and smaller crystals. The shape of almost all crystals was cuboid, ranging from perfect cubes to thin, square plates. The dominance of the 100 facet is noteworthy, though some cubes had 111 facets at the corners, see fig. 4.3.

While the first step of the CVT synthesis (section 2.1.1) produced numerous S-deficient phases along with pyrite, the transported products found at the cold end after the second step were almost exclusively phase-pure pyrite, with only some smaller crystals showing secondary phases. Phase-purity was verified routinely in-house by powdering crystals and recording XRD patterns in 2θ-ω geometry. To further verify absence of S-deficient phases at trace amounts, powdered crystals were also measured with ultra-high resolution synchrotron XRD (fig. 4.3b), showing again only pyrite peaks.

Electrical transport was characterized using temperature-dependent conductivity and Hall Effect data, shown in fig. 4.3c,d. Compared to the best natural crystal measured (n-type, lowest doping), conductivity was higher at room temperature and lower at low temperatures. In contrast, the absolute Hall coefficient $|R_H|$ was lower at room temperature and higher at low temperatures. Using the unipolar approximation (section 2.6.1.1), this translates to higher n-type doping and higher electron mobility in the CVT crystals, paired with lower compensation. The donor activation energy at room temperature is similar, with $E_D = 150$ - 200 meV. Both this natural crystal and all CVT crystals show a maximum in $|R_H|$, which is unexpected for homogeneous semiconductors, and will be discussed in detail in section 4.4.2. Comparing CVT crystals grown with Cl and Br as transport agents, no large differences

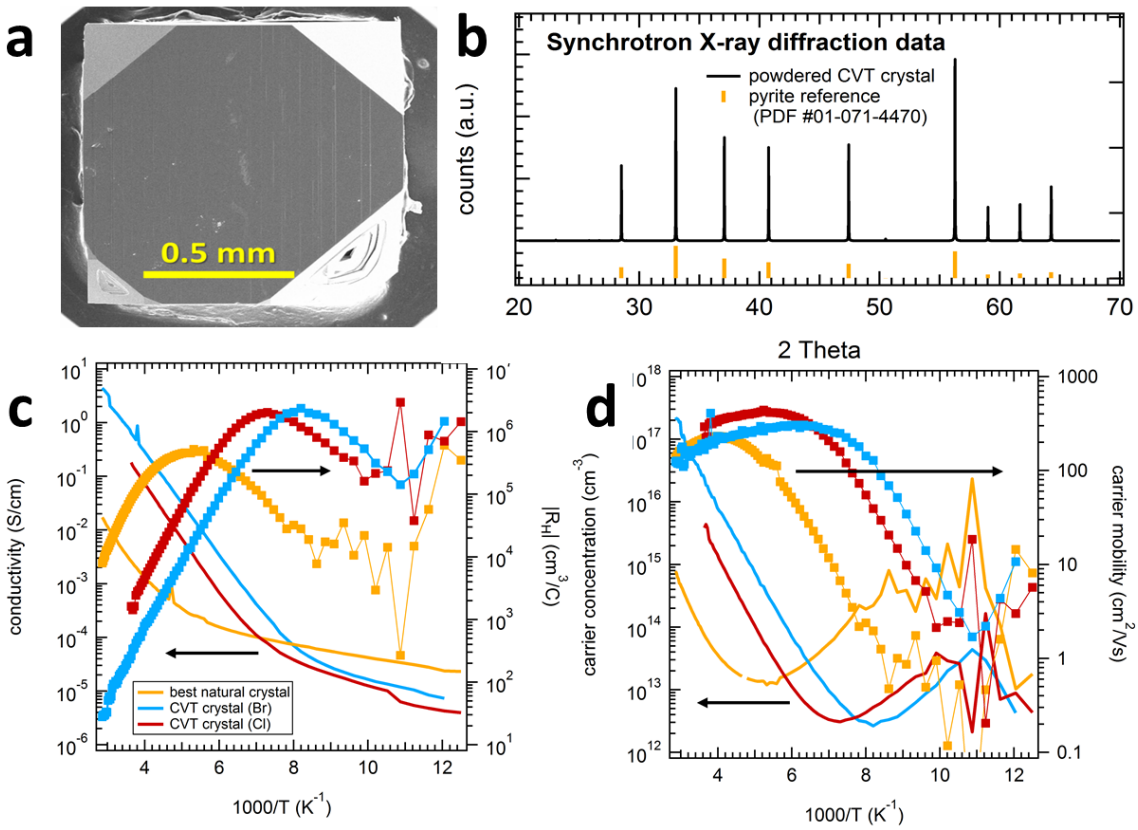

Figure 4.3: Pyrite Single Crystals Grown by Chemical Vapor Transport. (a) SEM image of cuboid crystal as grown, showing large 100 facets and 111 facets at the corners. (b) Synchrotron XRD pattern of powdered CVT crystal, recorded at Argonne National Lab. Even at this extreme resolution no secondary phases are detected, all peaks index to cubic FeS_2. (c) Temperature-dependent conductivity and Hall Effect data of CVT crystals, compared to a natural crystal. (d) Carrier concentration and mobility, calculated using unipolar approximation.

were found. The highest electron mobility recorded was 430 cm^2/Vs at 190 K for a crystal grown with Cl transport agent.

At this point, comparing electrical transport in polycrystalline thin films (section 3.1) and single crystals (see fig. 4.4), it is already obvious that their properties differ vastly. The main differences are (i) different polarity at room temperature: electron transport is dominant in single crystals, hole transport is dominant in thin films. (ii) Activation energy of single crystals and thin films is similar at low temperature, but much higher for single crystals at room temperature. (iii) High electron mobility in single crystals, while carrier mobility in

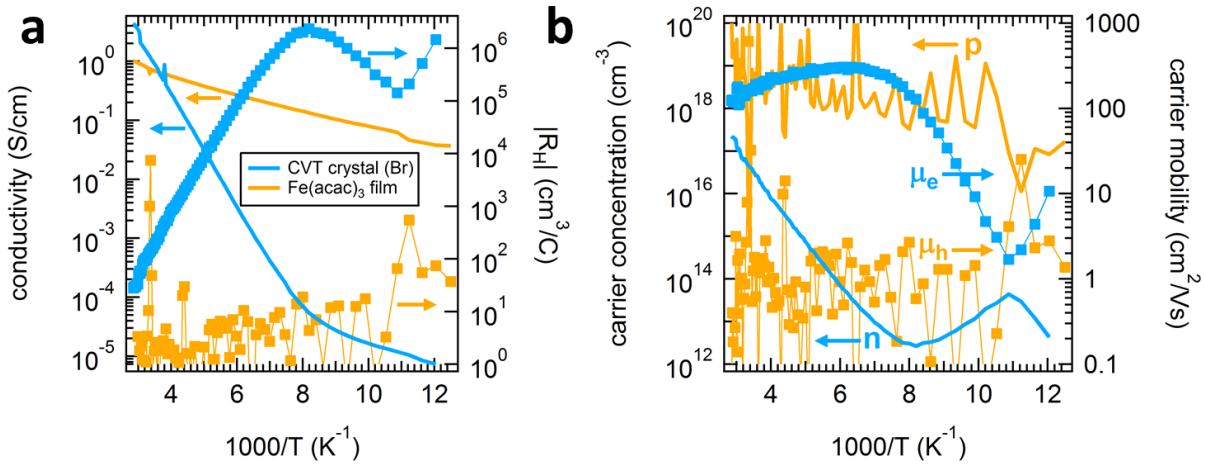

Figure 4.4: Comparison of electrical transport in a representative, high-quality CVT crystal (Cl transport, in blue) and representative thin film ($Fe(acac)_3$-ink, in orange). (a) Conductivity data, measured in Van der Pauw geometry, is shown as solid lines and on the left axis. The absolute of the Hall coefficient R_H is shown as squares and on the right axis. (b) Carrier concentration (solid lines, left axis) and carrier mobility (sqaures, right axis), as calculated using unipolar approximation. The sign of the R_H raw data fluctuates randomly for thin films, making a reliable assignment of majority carrier type as well as calculation of carrier mobility impossible. However, due to clear p-type behavior from thermopower measurements (at 300 K), we assign p-type transport (p, μ_h) at all T. See section 4.4.2 for a full discussion of majority carrier type, compensation and the validity of the unipolar approximation.

thin films is too low (< 1 cm^2/Vs) to measure reliably. This leads to (iv) single crystals having higher conductivity at high temperatures, similar conductivity at room temperature and much lower conductivity at low temperatures. As the surface to bulk ratio is the most obvious difference between these systems, mesoscopic systems with intermediate surface/bulk ratios were studied next.

4.3 Mesoscopic Systems

To test the hypothesis that surface states, and thus the surface to bulk ratio, is responsible for the drastic differences in electronic transport between pyrite single crystals and thin films, two experiments were designed. The first approach aims to increase the surface to bulk ratio of a well-characterized single crystal, by crushing the crystal into powder of a defined particle

size and then cold-pressing that powder into a pellet. The second approach aims to measure a single grain of a polycrystalline pyrite thin film.

4.3.1 Microcrystalline Pellets

As described in section 2.3.3, pellets were pressed from pyrite powder obtained from single crystals by ball-milling or mortar and pestle. 200,000 psi of pressure were applied for 5 min at room temperature, resulting in pellets that were stable for electrical measurements, if carefully handled.

Pellets made from a variety of natural and CVT grown single crystals were tested. Surprisingly it was found that the conductivity as a function of temperature was almost independent of the original crystal's conductivity. Even pellets made from heavily doped natural crystals with metal-like conductivity showed the same result as pellets made from our cleanest CVT crystals. This indicates that transport in pellets is dominated by grain boundaries and grain surfaces, not the grain bulk. It was indeed found by qualitative measurements of the Seebeck coefficient that pellets are p-type, even though made from n-type single crystals. In line with this, it was found that particle size had an effect on pellets conductivity. In one experiment (fig. 4.5d) powder was obtained from the same single crystal by two methods, first by mortar and pestle ('medium powder') and second by ball-milling ('extra fine powder'). As expected, smaller grains, equaling higher surface area, result in higher conductivity. The effect of sulfur annealing was also tested, to see if any defect states on the newly created surfaces could be passivated. It was found that annealing in sulfur slightly increases pellet conductivity, while light annealing in inert N_2 atmosphere has no effect (fig. 4.5c).

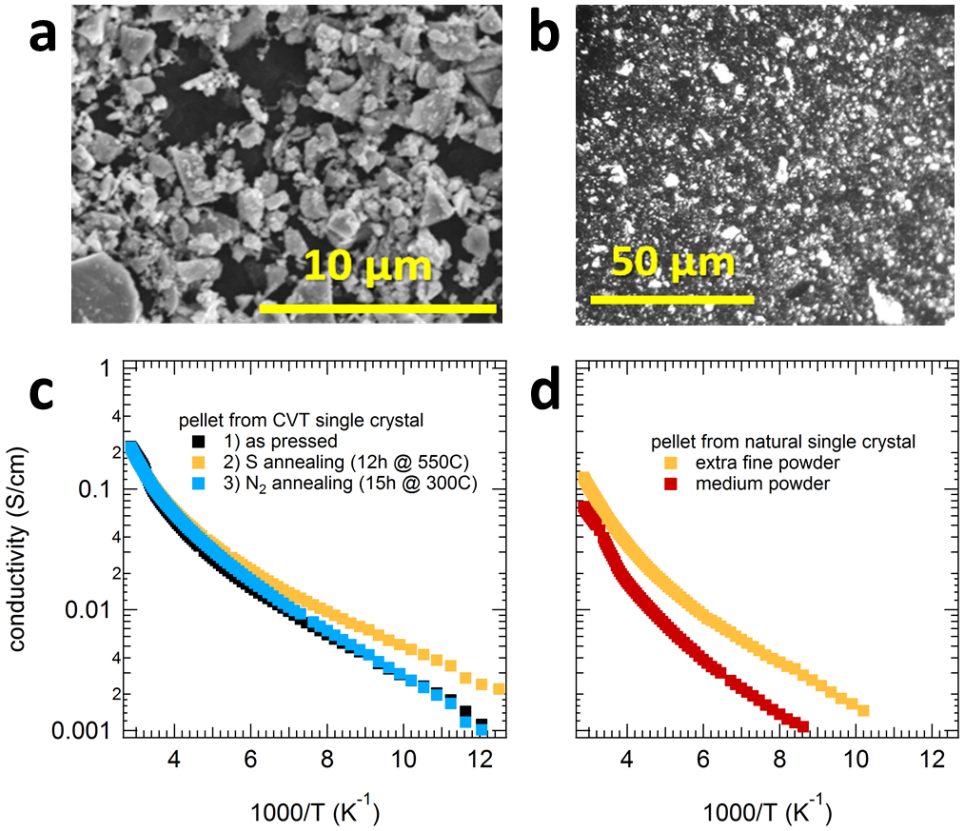

Figure 4.5: Microcrystalline Pyrite Pellets from Cold-Pressed Powder. (a) SEM image of pyrite powder obtained with mortar and pestle. (b) Optical microscope image of resulting pellet cold-pressed at 200,000 psi. Panels (c) and (d) show temperature-dependent conductivity data, measured in Van der Pauw geometry. (c) Shows that annealing in sulfur increases pellet conductivity slightly, while light annealing in inert N_2 atmosphere has no effect. (d) Shows that particle size had measurable effect on pellet conductivity: as expected smaller grains, equaling higher surface area, result in higher conductivity.

4.3.2 Single Nanocrystals

As described in section 2.3.4, individual grains that make up pyrite thin films can be grown further by sulfurization, up to several μm in size.[116] These nanocrystals were drop-cast from diluted suspension onto silica substrates, resulting in a random distribution of crystals like the one shown in fig. 4.6. The goal was to contact individual nanocrystals with metal lines from four sides and perform electrical transport measurements in Van der Pauw geometry. Unfortunately it turned out to be very difficult to have the metal lines stick to the pyrite nanocrystals. Ag and Al were tried, and for both metals the contact lines would fracture (inset of fig. 4.6). The nanocrystal's height was typically 1000 nm or more, while the metal line thickness was 200 nm or less, mostly limited by the PMMA thickness. This ratio would require free hanging metal lines which evidently did not survive the processing steps.

While this approach was eventually abandoned, it could be made to work in the future by using smaller nanocrystals, thicker metal lines, modified nanocrystal surfaces for better adhesion, an insulating underlayer under the metal lines or a combination of these factors. Another approach to measure pyrite nanocrystals would be to use a micro-manipulator tool to directly contact the crystals with needle probes. Such a tool is now available at UCI's LEXI facility. In the meantime, a group at the University of Wisconsin successfully measured transport in single pyrite nanocrystals.[20] Using sulfurization from iron salts ($FeCl_2$, $FeBr_2$) they synthesized nanocrystals that were contacted by EBL (fig. 4.6). Strikingly, the temperature-dependent conductivity data is very similar to the data from pellets obtained in the present work (fig. 4.7). Although no Hall effect measurements were performed on these nanocrystals, field effect measurements also suggest holes as the dominant carrier type, as expected for a nano-scale object with high surface to bulk ratio. See [20] for details.

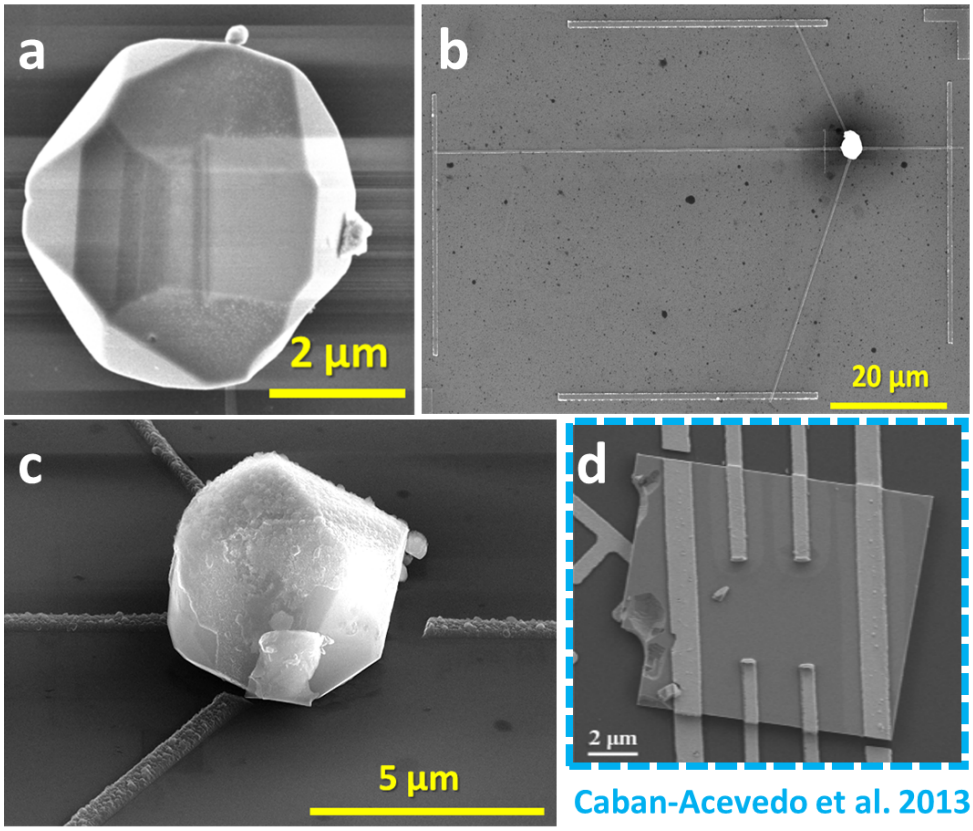

Figure 4.6: Single Nanocrystals of Pyrite Contacted by Electron Beam Lithographyy (EBL). (a) Single grain as drop-cast onto silica substrate. (b) Four metal lines are drawn to a nanocrystal that randomly landed in one of 100 predefined boxes. (c) Close-up image of (c) showing that the metal lines are ripped off close to the particle. (d) SEM image reproduced from Caban-Acevedo et al.,[20] showing a pyrite nanoplate successfully contacted by EBL. See [20] for details.

4.3.3 Conclusions

Figure 4.7a shows a direct comparison of temperature-dependent conductivity for a natural single crystal and a CVT grown single crystal to their respective pellets, made by crushing and pressing the single crystal material. While natural and CVT grown single crystals differ a lot, pellets pressed from each crystal are very similar. Pellets are surface-dominated and show the same temperature-dependence and activation energy as thin films. Figure 4.7b summarizes temperature-dependent conductivity for a representative single crystal, pellet (both CVT grown), and a thin film, along with a single nanocrystal (data for the latter taken from [20]). Dominant carrier type was determined by Hall effect for single crystals, and pellets, by thermopower for thin films, and by field effect for the nanocrystals. Note the similar activation energy for a p-type regimes, and that the temperature at which the p-to-n transition occurs shifts to lower temperatures with lower surface to bulk ratio. Figure 4.7c shows the normalized conductivity for the high-temperature region. It is striking that activation energy (negative slope) decreases with increasing surface-to-bulk ratio from a macroscopic single crystal, to a microcrystalline pellet made from the same, to nano-scale single crystal, to a nanocrystalline thin film. At higher temperatures the pellet, then the single nanocrystal and eventually even the film show higher activation energy as the n-type bulk starts to dominate the p-type surface carriers.

The conclusion of this section is that by increasing the surface to bulk ratio of a given pyrite material, surface conduction becomes more dominant. As shown in fig. 4.7, transport in pyrite thin films is dominated by p-type surface conduction at all temperatures, and can be described by the Werner model. Pellets show similar transport, though with lower overall conduction, possibly due to poor coupling of the grains. The activation energy of pellets and nanocrystals is the same as thin films at room temperature and below. However, both show a region of higher activation energy above room temperature, suggesting a transition to an n-type regime. This n-type regime is observed for all CVT grown single crystals at

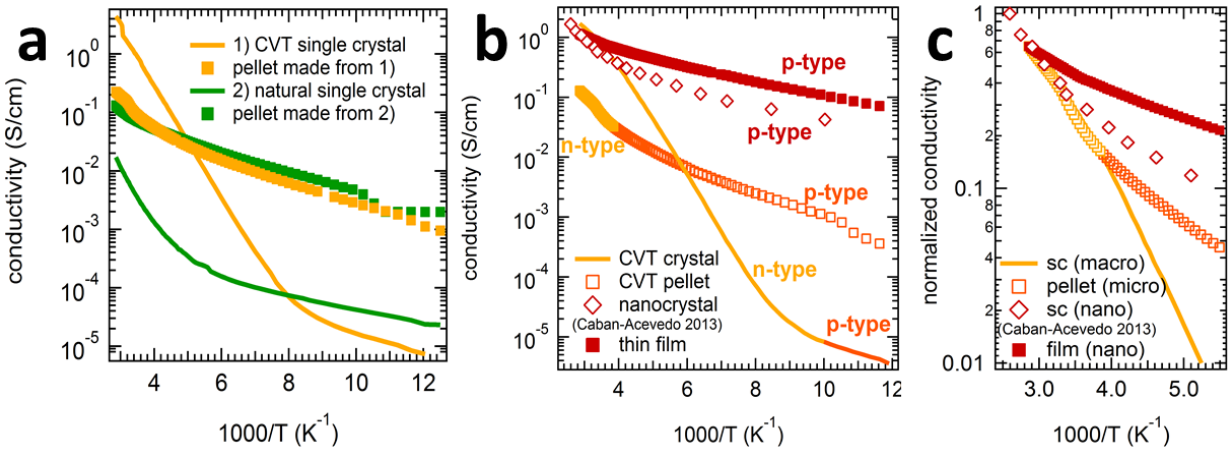

Figure 4.7: (a) Comparison of temperature-dependent conductivity for pyrite single crystals and pellets made from these single crystals. (b) Representative conductivity data for pyrite single crystal, pellet, thin film and single nanocrystal. Data of the latter taken from [20]. Temperature regimes for n-type and p-type transport are indicated. (c) Normalized conductivity for the high-temperature region of panel (b).

room temperature and down to about 110 - 140 K, where the activation energy decreases to the $\sim$ 30 meV value of thin films and pellets, and transport becomes hole-dominated. These interesting findings will be quantified and discussed in more detail in section 4.4.2.

4.4 Flux Grown Single Crystals

This section summarizes a study that was done in collaboration with N. Farhi (flux growth and XRD), N. Berry (flux growth), J. Lindemuth (complementary Hall Effect and MR measurements), C.L. Perkins (UPS), Q. Lin (XRD) and M. Law (principal investigator).[70] Thank also goes to J. Tolentino for help with variable-temperature absorption spectroscopy and B. Mercado for single crystal XRD data.

To improve upon the understanding gained in the previous section, more pyrite single crystals of larger size and even higher quality were needed. They were supplied from a flux growth synthesis. As described in 2.1.2, our lab developed a novel method of flux growth for pyrite single crystals that yields single crystals up to 1 g in 24 h. The method was

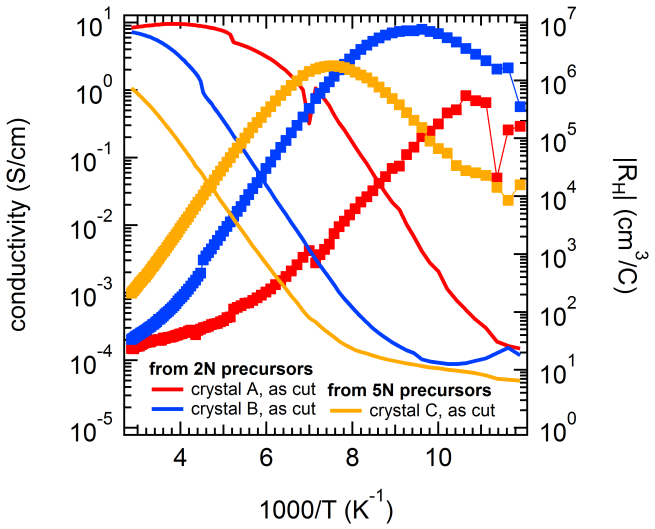

Figure 4.8: Impact of precursor purity on electrical transport in flux grown pyrite single crystals. Conductivity (solid lines, left axis) and Hall coefficient $|R_H|$ (squares, right axis) are plotted vs. temperature for crystals made from 2N (99%) and 5N (99.999%) pure Fe and S precursors. Only the crystal made from 5N precursors (crystal C) reveals a peculiar maximum in $|R_H|$ along with a flattening of the conductivity at low temperatures. These phenomena are superimposed by doping effects in crystals A and B. Further, crystal C is representative of flux crystals grown from 5N precursors and can be fit well with the model described in section 4.4.2, while crystals A and B are very different. This variance of electronic properties is also typical for crystals with low purity, and can be seen in natural crystals.

introduced by Nick Berry and championed by Nima Farhi, and provided high-quality pyrite single crystals that were so crucial for this work. It produces larger and purer, crystallographically perfect pyrite crystals more quickly than alternative approaches such as chemical vapor transport (CVT). The high purity of these crystals proved critical for revealing via Hall effect measurements a hole-rich layer at the surface of pyrite (see fig. 4.8).

Above (section 1.3.2, section 4.3) it was argued that the explanation most consistent with the experimental data (low photo-voltages from pyrite single crystals, high p-type conductivity of pyrite thin films regardless of composition or preparation method, effect of surface to bulk ratio seen in pellets and nanocrystal studies) is that pyrite has a hole-rich surface layer that results in a leaky and/or small potential energy barrier at the surface. An additional question that has not been addressed satisfactorily in literature is the origin and explanation

of the observed maximum in $|R_H|$ (see section 1.3.2).

In this study, the existence of an inversion layer on the surface of high-quality n-type pyrite single crystals is demonstrated using variable temperature Hall effect and valence band photoemission measurements. It is shown that the surface layer is electrically conductive and dominates transport when the number of surface holes becomes substantially larger than the number of bulk electrons (i.e., for samples with high surface/bulk ratio and/or low temperatures). We find that the conductance of the inversion layer can be altered by physicochemical treatments of the pyrite surface, suggesting that it may be possible to eliminate this hole-rich layer and boost the V_{OC} of pyrite solar cells by passivating surface states and near-surface defects.

4.4.1 Structural and Elemental Characterization

The basic structural characterization of the flux grown crystals is shown in fig. 4.9. The flux synthesis produces highly-faceted but non-cubic crystals with a typical size of 8 x 8 x 6 mm (limited by the size of our crucibles). Most of the facets are optically flat with a golden mirror finish, but some have a large density of macro-steps and small terraces (fig. 4.9a). High-resolution synchrotron powder XRD patterns of crushed crystals index to pyrite with a room temperature lattice constant of 5.41741 $\pm$ 0.00087 $\AA$, and show no trace of other crystalline or amorphous phases (fig. 4.9b). Likewise, Raman spectra feature only sharp pyrite peaks (fig. 4.9c). Slabs were cut with a diamond saw parallel to prominent facets and polished to $\sim$2 nm RMS roughness using SiC paper and a series of slurries (see section 2.3.1). Wide-angle 2θ - ω XRD scans show the slabs are single crystals with (111) or, less often, (210) orientation (fig. 4.9e). (111) rocking curve peak widths of 6 – 9 arcseconds indicate that the pyrite slabs have a very high degree of crystalline perfection, comparable to commercial silicon wafers (fig. 4.9f). To determine whether the crystals are in fact single crystalline throughout their volume, we acquired 2θ-ω and pole figure data of slabs cut in

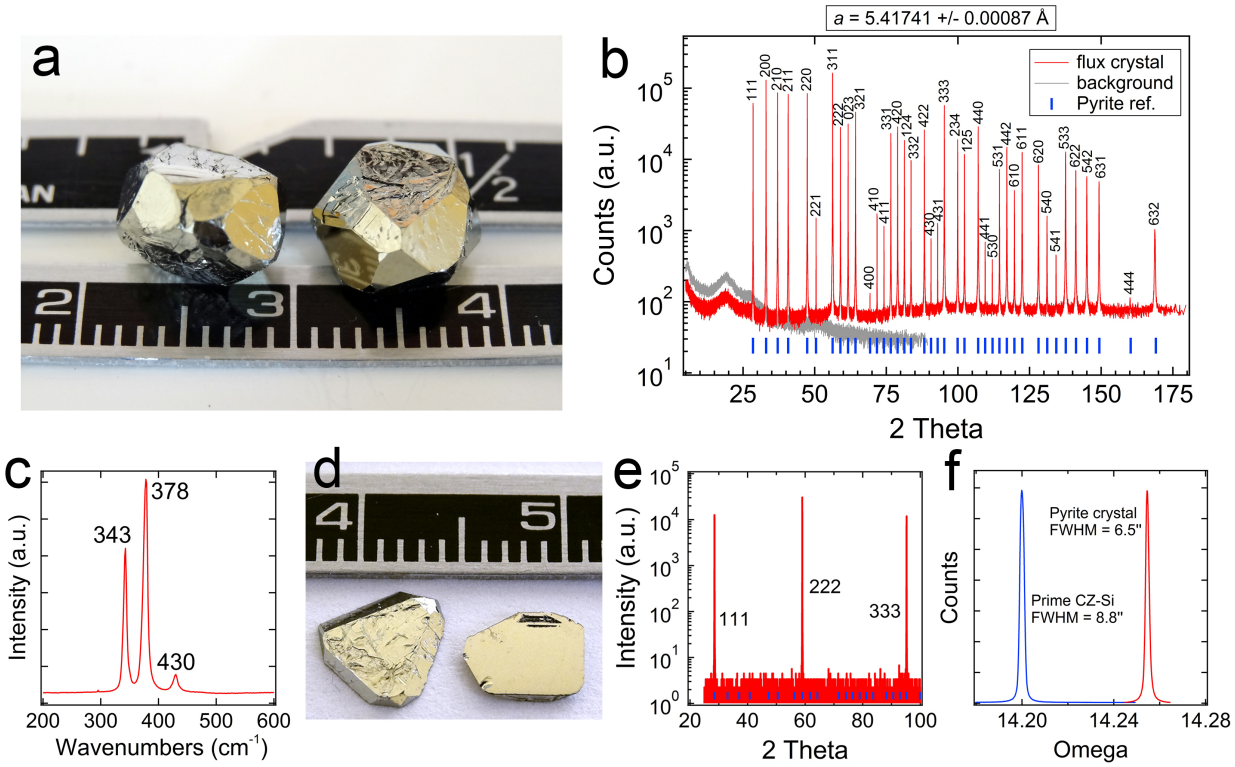

Figure 4.9: Pyrite single crystals grown in a Na_2S-sulfur flux. (a) Photograph of two as-grown crystals. Scale is in centimeters. (b) Synchrotron XRD pattern of a powdered crystal on a log scale. All 39 reflections index to pyrite and no other phases are detected. A linear least squares fit of the data gives a cubic lattice parameter of 5.41741 $\pm$ 0.00087 $\mathring{A}$ at room temperature. The background pattern is for an empty capillary tube. Small blue bars near the x-axis denote the pyrite reference peaks. (c) Typical Raman spectrum of a pyrite slab. All peaks correspond to pyrite.[6] (d) Photograph of pyrite slabs showing a heavily stepped as-grown facet (left) and a polished facet (right). (e) 2θ-ω XRD scan on a log scale of a polished slice with (111) orientation. Small blue bars near the x-axis denote the pyrite reference peaks. (f) (111) rocking curves for a pyrite slab and a prime grade CZ-grown Si wafer. The pyrite slab shows a FWHM of 6.5 arcseconds, compared to 8.8 arcseconds for the Si wafer. Figure reproduced from [70].

several orthogonal orientations and found that nearly all specimens are indeed highly-perfect single crystals (data not shown), although a few samples showed evidence of a small number of slightly mis-oriented grains in pole figures. Crystal structure refinement yielded site occupancy factors of 1.00 ± 0.04 for both Fe and S, indicating a stoichiometry of $FeS_{2.0}$ within the error of the refinement. This agrees well with a sulfur-to-iron ratio of 1.988 ± 0.03 (i.e., $FeS_{2.0}$ within experimental error) determined by closed-vessel inductively coupled plasma optical emission spectroscopy (ICP-OES) analysis of an as-grown crystal, particularly considering the tendency for sulfur to be lost to the gas phase during pyrite digestion.[31] Overall, these results show that the flux synthesis produces large, high-quality, and stoichiometric pyrite single crystals.

A disadvantage of the flux synthesis is that the pyrite crystals always contain macroscopic voids. These voids are clearly visible by eye upon sectioning an as-grown crystal. X-ray tomography was employed to image the voids in several as-grown crystals. 3D reconstructions show that some regions of each crystal contain localized networks of elongated and globular voids (fig. B.7). Some of the voids open to the external surface of the crystal, while others are closed. The density of several crystals was measured by helium pycnometry to be 4.904(3) – 4.959(3) g cm^{-3}, or 97.9 – 99.0 % of the theoretical density of pyrite (5.011 g cm^{-3} at room temperature). Since pycnometry measures the skeletal volume (i.e., the volume of the crystal plus any voids inaccessible to He), we conclude that only a relatively small fraction of the void volume is closed. Crucially, the top ∼1 mm of most crystals is completely free of voids, while the void density increases toward the bottom of the crystal (i.e., where the crystal touches the crucible). All electrical and optical measurements described in this study used void-free slabs in order to avoid potential complications from empty volume effects.
The bulk elemental composition of the crystals was determined by glow discharge mass spectrometry (GDMS), instrumental gas analysis (IGA), and secondary ion mass spectroscopy (SIMS), as described in section 2.4.3. GDMS provides a full elemental survey (Li – U) with ppb – ppm detection limits, while IGA measures gas-forming elements (O, C, N, H, S) over

a wide dynamic range (ppm to percent levels). SIMS is a surface probe that samples a much smaller amount of material than either GDMS or IGA ($\sim$0.5 mg versus $>$ 10 mg). Table 1 lists all impurities detected in the crystals by the three techniques. Based on the GDMS/IGA data, the total impurity content of the crystals excluding oxygen, carbon and hydrogen is $\sim$25 ppm, with the only elements above 1 ppm being Cr (6.4 ppm), B (6.3 ppm), Si (4.2 ppm), Na (4.2 ppm), and Cl (1.1 ppm). Chromium is a known impurity in our iron starting material (see figures A.2 - A.1 in the appendix for information on the impurity content of precursors) and can be eliminated by using commercial batches of iron that are free of chromium. Since the sodium was largely removed by thoroughly rinsing crushed crystals in water, we believe that sodium is present only on the surface of the crystals (as residual flux) and not as substitutional or interstitial impurities in the pyrite lattice. SIMS data confirm this interpretation (see below). The origin of the boron, silicon, and chlorine contamination is less clear. Boron is present regardless of whether pBN or alumina crucibles are used in the syntheses, so it must originate from the Na_2S precursor or, less likely, the quartz ampoule. Silicon probably comes from the quartz. If we disregard Na, our crystals are 99.998 % pure on a "metals" basis, making them the purest pyrite crystals yet reported.[73,95,119,66,65]

Although the metal levels are very low, high concentrations of oxygen (1775 ppm) and carbon (533 ppm) were detected by IGA, and we could not reliably quantify the hydrogen content by IGA due to instrument complications from sulfur. Oxygen, carbon, and hydrogen could have important electronic effects if these elements were in the lattice rather than on the surface of the crystals. We used SIMS depth profiling to verify the concentration of oxygen, carbon, and a group of other trace elements (H, Cr, Al, F, Cl, Na, K, Mg, and Ca) in several locations on three different pyrite crystals. As seen in fig. 4.10, SIMS profiles show that the concentration of oxygen and carbon is only 1 – 5 ppm in the bulk of the crystals, much lower than the values determined from IGA. The higher concentration of oxygen and carbon near the surface of the crystals – which probably results mainly from surface particle contamination (unavoidable for samples prepared in non-UHV conditions) – is insufficient

Element	GDMS/IGA concentration (ppm at.)	SIMS concentration (ppm at.)
O	1775[a]	1-4
C	533[a]	1-2
N	DL(<28)	NM
H	?[b]	(15, 52, 560)[c]
Cr	6.4	(1, 3, 82)[c]
B	6.3	NM
Si	4.2	NM
Na	4.2[a]	<0.006-0.2
Cl	1.1	0.05-0.2
Ni	0.9	NM
Ca	0.4	<0.003-0.2
Al	0.4	0.07-0.2
Mg	0.3	<0.002-0.08
P	0.1	NM
F	DL(<1)	<0.03-0.2
K	DL(<0.1)	0.0004-0.3

Table 4.1: Table summarizing elemental analysis of pyrite flux crystals grown in pBN crucibles by GDMS, IGA, and SIMS.
[a] Oxygen, carbon, and sodium are present on the crystal surface, with very little in the lattice. [b] Hydrogen could not be accurately measured by IGA. [c] Values listed for three different crystals to show variability. All unlisted elements (Li–U) were below GDMS detection limits (0.01–0.5 ppm at. for most elements). SIMS data are average bulk values (>500 nm from the crystal surface). DL = below detection limit; NM = not measured

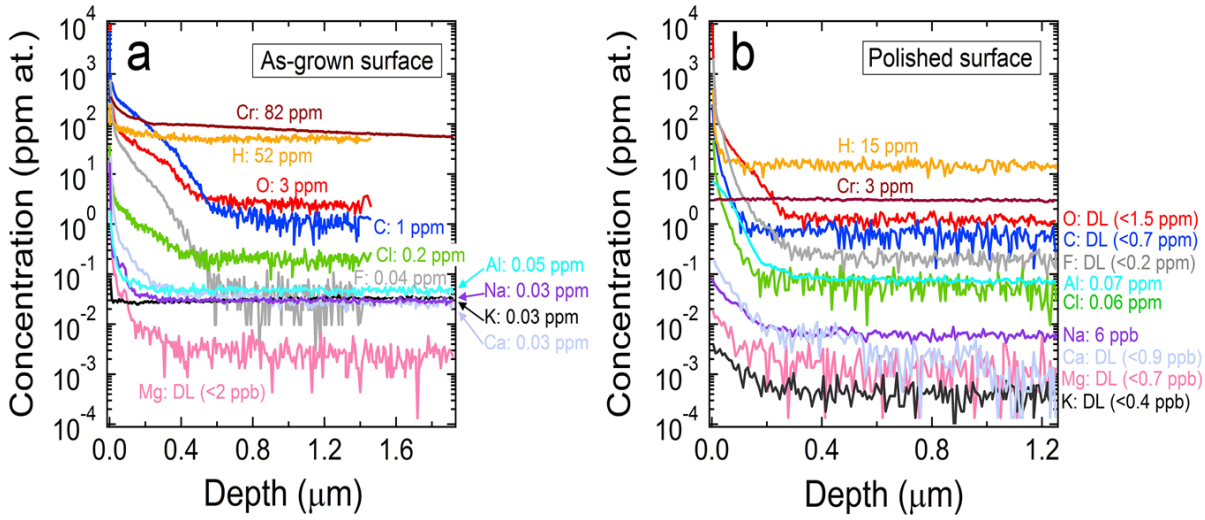

Figure 4.10: SIMS depth profiles of (a) an as-grown surface and (b) a polished surface of two different pyrite crystals. DL = below detection limit. Figure reproduced from [70].

to reconcile the IGA and SIMS results, implying sources of oxygen/carbon that the SIMS experiments do not detect. Based on these combined data, we conclude that the oxygen and carbon contamination sits mostly on the surface of the crystals and is present in the pyrite lattice only in ppm concentrations.

SIMS also shows a substantial, sample-dependent concentration of hydrogen (15, 52, and 560 ppm in three different samples) and chromium (1, 3, and 82 ppm) in the pyrite bulk. Hydrogen is a ubiquitous impurity that may originate from our H_2-reduced iron precursor, incompletely-dried Na_2S or sulfur precursors, or several other potential sources. Hydrogen may act as an electronic dopant in pyrite. Chromium is from the iron precursor, as mentioned above. All other elements monitored by SIMS were below ~0.2 ppm, in rough agreement with GDMS results. The variation in impurity concentration from sample to sample probably reflects variations in precursor purity and sample processing, but we cannot rule out the possibility that the crystals have an inhomogeneous impurity distribution. Future work will assess the homogeneity of the crystals at different length scales. Based on the combined GDMS, IGA, and SIMS data, we conclude that (i) our crystals have a total

lattice impurity content of ∼80 ppm (assuming ∼52 ppm of hydrogen on average), making them ∼99.992% pure overall, (ii) hydrogen is the major extrinsic impurity, and (iii) surface particle contamination is responsible for the high levels of oxygen and carbon detected by IGA.

4.4.2 Hall Effect Studies

Hall effect data were collected on pyrite (111) and (210) slabs in van der Pauw geometry over a temperature range of 40 – 700 K (see section 2.6.1). Figure 4.11 plots the conductivity σ and the absolute value of the Hall coefficient $|R_H|$ versus inverse temperature for a typical sample. The conductivity decreases by a factor of $\sim 10^8$ with decreasing temperature and shows three distinct linear regions of progressively smaller activation energy: (I) $E_a \sim 375$ meV for $T > 500$ K; (II) $E_a \sim 163$ meV for $350\ K > T > 130$ K; (III) $E_a \sim 24$ meV for $T < 90$ K. We assign region I as the intrinsic region, where the activation energy is related to the band gap of pyrite. Region I is discussed in more detail in section 4.4.3. In region II, the crystal is clearly n-type (large negative value of R_H) and transport is dominated by the ionization of donor states. Since $n \gg p$ in this extrinsic region, the Hall coefficient simplifies to $R_H = -1/ne$ and the Hall data can be used to estimate the free electron density n, mobility m_e, donor concentration N_D, and donor energy E_D. At 300 K, $n = 5 \times 10^{15}$ cm^{-3} and $m_e = 245$ cm^2 V^{-1} s^{-1}.

We consider two limiting cases for determining E_D and N_D from the slope of $R_H(T)$ in region II. The slope in this region corresponds to an activation energy of ∼195 meV for n(T). We note that the E_a of $\sigma(T)$ is somewhat different (∼165 meV) because σ is the product of two temperature-dependent quantities, n(T) and $m_e(T)$, while $R_H(T)$ in the unipolar region depends only on n(T). If we first assume that the crystals are uncompensated ($N_A/N_D = 0$, where N_A is the concentration of acceptors), then the Fermi level is located about halfway

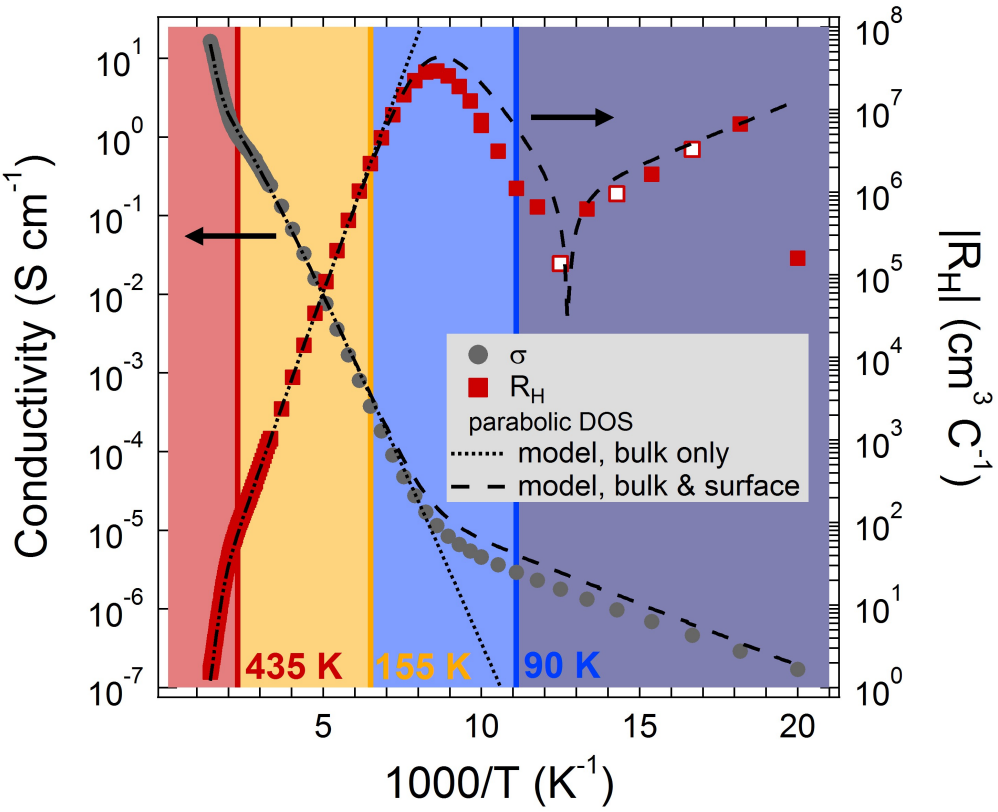

Figure 4.11: Raw Hall effect data (σ and $|R_H|$) for a pyrite (111) slab with a thickness of 1040 mm. The conductivity shows three linear regions with activation energies of 375 meV, 163 meV, and 24 meV, respectively. The Hall coefficient exhibits unusual behavior, including a minimum at ∼120 K and a sign change from negative (electron dominant) to positive (hole dominant) at ∼80 K. Red squares indicate negative values of R_H, while red and white squares are positive values. The sign of R_H varies at low temperature because the Hall voltage V_H is very small in this regime. The high-temperature data can be fit with a model that considers only a homogeneous crystal with a single donor (dotted traces). A three-layer model (n-type bulk plus p-type surface on each side of the crystal) is needed to fit the data over the entire temperature range (dashed traces; see section 2.7.2). This fit uses the normal parabolic DOS(E) functions, the free electron approximation, and the Fermi–Dirac distribution function, assuming zero compensation of bulk and surface. See fig. B.2 for fits that include the bulk compensation ratio as a free parameter. Using instead numerical DOS(E) values obtained from density functional theory (DFT) calculations of the pyrite band structure[52] results in fits that are systematically better at low temperature but worse at high temperature (see fig. B.3 for the fits, fig. 4.16 for a comparison of the two types of DOS(E) functions used in the modeling, and fig. B.4 for a comparison of modeling results using the two DOS(E) functions). Fit parameters are shown in table 4.2. The sample is intrinsic at high temperatures (red region). With decreasing temperature, transport becomes dominated by bulk electrons (yellow), enters a transition region of mixed electron and hole conduction (blue), and then becomes dominated by surface holes as the bulk electrons are frozen out (gray). Figure reproduced from [70].

between E_D and the conduction band edge E_C, such that (E_C - E_D)/2 $\approx$ 195 meV. In this case, the donor ionization energy E_C - E_D is $\sim$390 meV and, using the approximation $N_D \sim n e^{(E_C - E_D)/2k_BT}$, we find N_D = 9 x 10^{18} cm^{-3} (equivalent to $\sim$120 ppm). However, it is extremely unlikely for a compound semiconductor to be completely uncompensated. At $\sim$60% compensation (see fig. B.2 for justification of this value), the Fermi level is essentially equal to the donor level, making E_C - E_D $\sim$ 195 meV. In this case, the donor ionization energy determined from R_H(T) is approximately 195 meV, while N_D remains unchanged. Since including compensation changes little other than the energy of the donor state, we assume zero compensation in most of the remainder of this study. We believe that the donor is probably a native defect (most likely a sulfur vacancy or vacancy cluster), since hydrogen is the only extrinsic impurity with a concentration higher than $\sim 10^{18}$ cm^{-3} yet the Hall data show no clear correlation to the hydrogen concentration. A graph of electron density and mobility that assumes (necessarily but wrongly) the validity of the single carrier approximation for all temperatures is shown for illustration in fig. 4.12. The mobility in region II varies with temperature as $T^{-2.0}$ to $T^{-2.5}$, implying that phonon scattering limits the mobility at intermediate temperatures, as it does in most high-quality single crystals. The mobility peaks at values up to 1930 cm^2 $V^{-1}s^{-1}$ at $\sim$120 K before appearing to decrease at lower temperatures. However, as discussed below, conduction from 90 – 155 K is mixed between bulk electrons and surface holes, making $R_H \neq -\frac{-1}{ne}$. As a result, the peak electron mobility in fig. 4.12 is probably underestimated and the mobility values in this intermediate range of temperatures have no clear physical meaning.

The Hall coefficient exhibits unusual behavior at temperatures below $\sim$155 K. Instead of showing the expected monotonic increase in magnitude due to carrier freeze out, $|R_H|$ of the pyrite samples reaches a maximum at $\sim$120 K, decreases, and then passes through zero at $\sim$80 K and changes sign from negative (electron dominant) to positive (hole dominant) at lower temperatures. This sign change appears as a cusp in $|R_H(T)|$ in fig. 4.11. Such an R_H extremum and sign reversal cannot occur in a doped or compensated semiconductor away

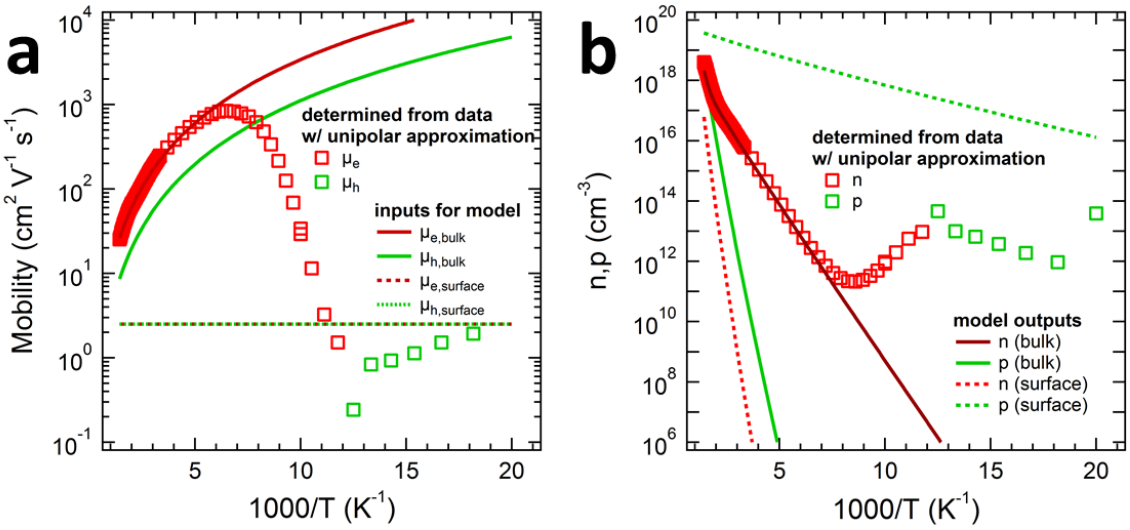

Figure 4.12: (a) Mobility and (b) concentration of free electrons (red markers) and holes (green markers) as calculated from the Hall data in fig. 4.11 assuming validity of the unipolar approximation at all temperatures (i.e., n,p = $1/|R_H e|$). Note that this approximation is violated in regions of mixed electron and hole conduction (i.e., the intrinsic region and the temperature range of 80 - 150 K). Solid and dashed curves denote the values used to parameterize the model. These values match the data in the unipolar regions (>150 K for electrons and <80 K for holes). Electron mobility in the bulk, $\mu_{e,bulk}$, follows a $T^{-2.5}$ dependence at high T, as is common for phonon scattering.[54] Hole mobility in the bulk, $\mu_{h,bulk}$, is assumed to be 1/3 of $\mu_{e,bulk}$ at all T. Note that the value of $\mu_{e,bulk}$ is irrelevant at low T and $\mu_{h,bulk}$ is irrelevant at all T due to the low carrier concentrations. Thus, no assumptions about bulk mobility at low T were necessary to model the data. For example, including ionized impurity scattering at low T had no effect on the fits (as expected). Hole mobility in the surface layer, $\mu_{h,surface}$, was estimated from low T data using the unipolar approximation. We found values ranging from 0.1 to 10 cm^2/Vs and used the best fit result of ~2 cm^2/Vs in the model. Electron surface mobility is irrelevant due to negligible carrier concentration and was set to $\mu_{e,surface} = \mu_{h,surface}$ for simplicity. Note that the concentration of holes used to model the surface layer (dotted green line in (b)) is five orders of magnitude higher than the data points because p_{bulk} is calculated from the data is with respect to the bulk while $p_{surface}$ is calculated with respect to just the surface layer, which is about 10^5 times thinner than the bulk. Figure adapted from [70].

from the intrinsic region unless (a) the mobility of holes becomes many orders of magnitude larger than that of electrons at low temperature, (b) the mechanism of charge transport changes from band conduction to some form of hopping below ∼155 K, or (c) conduction in a p-type surface inversion layer dominates the low-temperature transport. To test premise (a), we calculated $R_H(T)$ self-consistently for widely-varying combinations of dopant density, dopant ionization energy, and carrier mobility and found that low-temperature R_H sign changes can occur only when $m_e(T)$ or $m_h(T)$ is unphysical, such as when $m_h(T)$ increases exponentially by many decades with decreasing temperature (see fig. 4.13 for all conceivable scenarios). We conclude that the observed $R_H(T)$ behavior must be due to either a transition to hopping transport (premise b) or surface conduction (premise c).

Conduction by hopping between localized states in a compensated single crystal can cause unusual R_H behavior – including extrema and possibly sign reversals – that might in principle explain our $R_H(T)$ data.[44,99] Only a few reports have presented non-monotonic $R_H(T)$ data from pyrite.[95,47,49,50,108] Most notably, Tomm et al. observed a maximum in $|R_H|$ similar to ours, but with no sign reversal.[108] These authors attributed the R_H turnover to a transition to hopping conduction at lower temperatures, without providing evidence to support this interpretation. Various types of hopping transport have also been reported recently in single-crystal pyrite nanostructures[20] and mixed-phase pyrite thin films containing metallic Fe grains.[126] To test for hopping conduction in our crystals, we first determined the temperature dependence of the low-temperature resistivity (region III in our notation).
The resistivity ρ of a single crystal typically takes the form $\rho(T) = \rho_0 \exp[(T_0/T)^p]$, where p = 1 can indicate either band conduction or nearest neighbor hopping, p = 1/2 usually corresponds to Efros–Shklovskii variable range hopping (ES VRH), and p = 1/4 is characteristic of Mott variable range hopping.[99] To determine the value of p, we linearized $\rho(T)$ using the Zabrodskii method described in [125], giving $\ln(-\frac{d\ln(\rho)}{d\ln(T)}) = \text{constant} - p\ln(T)$. Fits of the low-temperature resistivity data yield $p \approx 0.53$ from 40 – 100 K, consistent with ES VRH (see fig. 4.14). In Gaussian cgs units, $T_0 = 2.8\ e^2/(\kappa a k_B)$, where κ is the dielectric constant

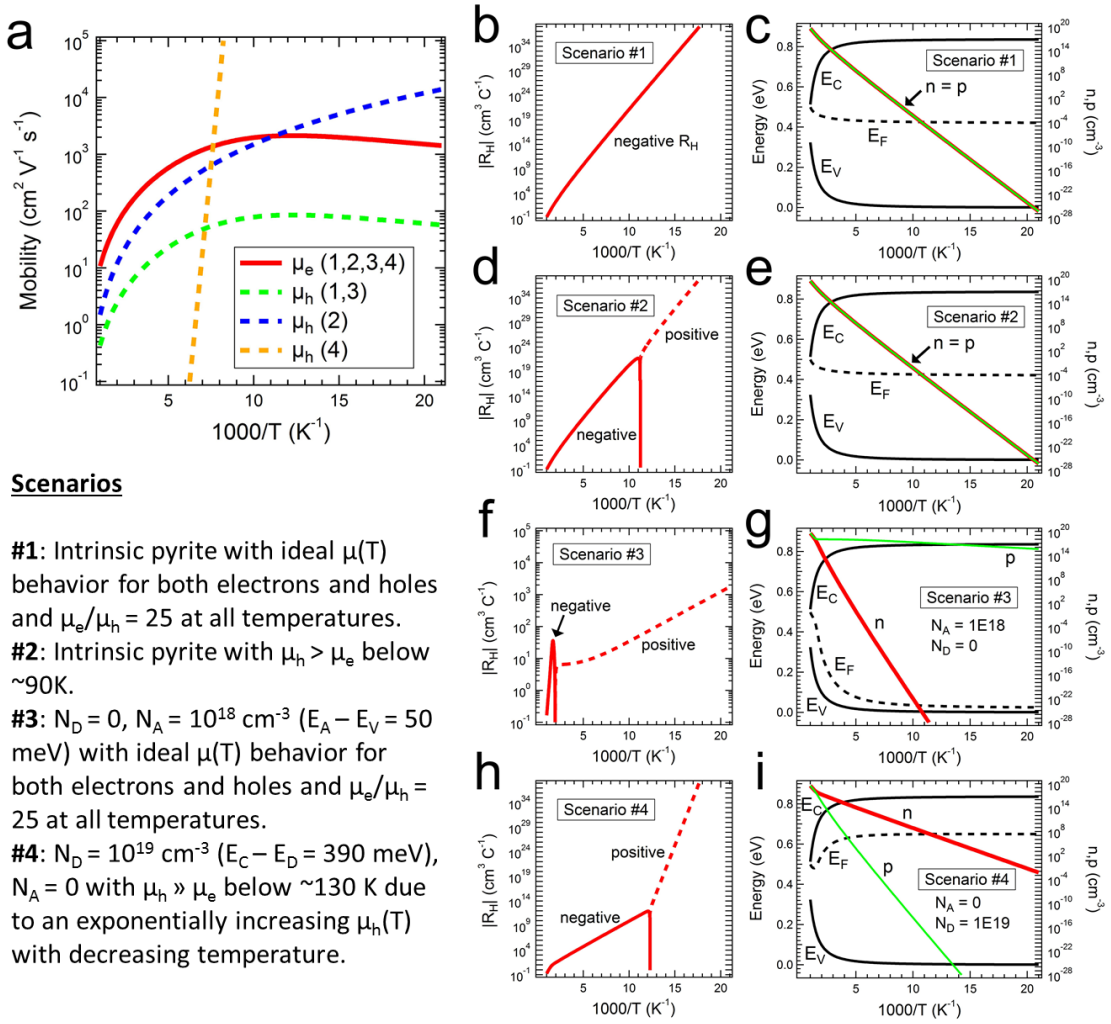

Figure 4.13: Self-consistent calculations of $|R_H(T)|$ for a homogeneous semiconductor at different combinations of doping and μ(T). (a) Plots of the mobility functions used to calculate the various scenarios. (b) $|R_H(T)|$ for Scenario #1: R_H is negative at all temperatures because n = p but $\mu_e > \mu_h$. $|R_H|$ increases monotonically as the carriers freeze out. (c) Corresponding band diagram showing E_F (dotted line), n (red line), p (green line), E_V, and E_C versus inverse temperature. (d) $|R_H(T)|$ for Scenario #2: Since n = p, R_H takes the sign of whichever carrier has the higher mobility. Therefore, R_H changes sign at ~90 K. Since the flux crystals are far from intrinsic, this scenario is not relevant to the case at hand. (e) Corresponding band diagram. (f) $|R_H(T)|$ for Scenario #3: R_H is negative in the intrinsic region because n ≈ p but $\mu_e > \mu_h$. R_H changes sign when p > n outside of the intrinsic region due to the acceptor doping. This R_H behavior is typical for doped semiconductors. (g) Corresponding band diagram. (h) $|R_H(T)|$ for Scenario #4: This type of non-physical μ_h(T) function is required in order to overcome the large difference between n and p and force R_H to change sign at low temperatures. Note that low to moderate p-type doping ($N_A < 10^{19}$ cm^{-3}) would be fully compensated and would not change this scenario. The physical irrelevance of this scenario illustrates the practical impossibility of an R_H sign change occurring in a homogeneous doped semiconductor outside of the intrinsic region. (i) Corresponding band diagram. All calculations employed parabolic DOS(E) functions. Figure reproduced from [70].

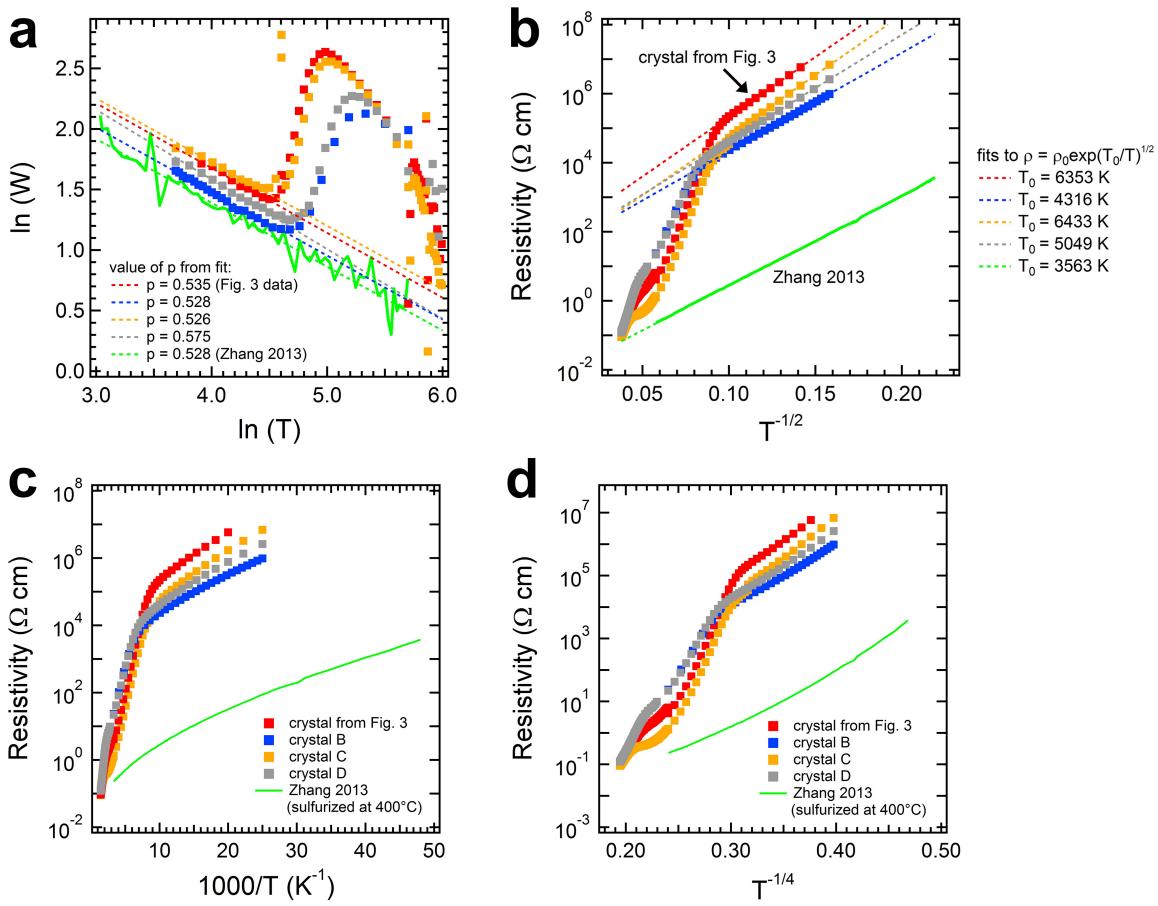

Figure 4.14: Low-temperature resistivity data and fits. (a) Logarithmic derivative plots to linearize $\rho(T) = \rho_0\ exp[(T_0/T)^p]$ in order to determine the value of p. Here, $\ln(W) = \ln(-\frac{d(ln\ \rho)}{d(ln\ T)})$. Data are shown for four pyrite single crystals (including the crystal used in fig. 4.11), plus a mixed-phase thin film annealed at 400 °C from [126]. The value of p ranges from 0.53 to 0.58. (b) The data plotted versus $T^{-1/2}$, along with fits to the linear regions at low temperature. The value of T_0 ranges from 3550 to 6350 K. (c) Plots versus T^{-1} and (d) $T^{-1/4}$. Figure reproduced from [70].

of pyrite (κ = 20.5, see section 4.1) and a is the characteristic radius of the localized state participating in VRH. Given the limiting values of E_D extracted from $R_H(T)$ (i.e., E_C - E_D = 0.390 eV for zero compensation and E_C - E_D = 0.195 eV for finite compensation) and assuming an effective electron mass of 0.45 m_e,[52] our samples have a = $\hbar/\sqrt{2mE_D}$ = 4.6 - 6.6 $\mathring{A}$ and thus T_0 = 3480 – 4920 K.[99] Note that this a is smaller than the Bohr radius of electrons in pyrite ($a_{Bohr} \approx 23$ $\mathring{A}$)[52] because the state radius decreases as $E_D^{-1/2}$, making deep donors smaller than shallow donors. Fits to the data from four crystals give T_0 = 3550 – 6350 K (fig. 4.14), in reasonable agreement with the value expected from ES VRH theory. We conclude that the low-temperature ρ(T) data are generally consistent with ES VRH. However, hopping in single crystals, and especially VRH, usually occurs at much lower temperatures and with significantly smaller activation energies than is observed here.

We therefore sought to confirm ES VRH transport by measuring the dependence of the transverse magnetoresistance (MR = 100(ρ(H) - ρ(0))/ρ(0)) on magnetic field and temperature. If conduction in a doped semiconductor is due to band transport rather than hopping, the resistivity should have a weak parabolic dependence on the magnetic field H, i.e., $\rho(H) \approx \rho_0[1 + \mu^2(\mu_0 H)^2]$, when the field is weak (i.e., $|\mu\mu_0 H| < 1$), where μ is the majority carrier mobility and μ_0 is the magnetic permeability.[18] On the other hand, a characteristic feature of any type of hopping conduction is a large positive MR that increases exponentially with the strength of the magnetic field as

$$\rho(H) = \rho_0 \, exp(AH^m), \tag{4.1}$$

where the value of m and the form of A depend on H.[99,37] The large positive MR is due to compression of the wavefunctions of localized states by the field that causes a rapid decrease in overlap between the tails of these states. For nearest-neighbor hopping in weak magnetic fields (i.e., when the magnetic length $\lambda = \sqrt{c\hbar/eH}$ is much larger than the characteristic radius of the impurity state) m = 2 and A = 0.036 $ae^2/Nc^2\hbar^2$, where N is the impurity

concentration.[99] Since $\lambda \geq 85$ $\AA$ and a ≤ 6.6 $\AA$ for our samples, the condition $\lambda \gg$ a is satisfied and the weak-field regime applies. A second condition for weak-field hopping MR is light to moderate doping of the semiconductor (i.e., $Na^3 < 1$).[99] Using N $\sim 10^{19}$ cm^3 for our crystals, we find $Na^3 \sim 0.001 - 0.003$, well within the range of validity of this equation. Using eq. (4.1) with weak-field values for m and A, we predict only a very small MR of ∼0.04% at our maximum field of 90 kOe. An even smaller MR (0.0007 – 0.0032%) is expected if ES VRH is the conduction mechanism at low temperature (see eq. (4.2) below).

Figure 4.15 shows typical magnetoresistance data for a pyrite crystal at 70 K and 300 K. The MR is weak and positive at these and all other temperatures measured (30 – 300 K). The maximum value of the MR at 70 K is ∼0.3%, which is ∼8 times larger than expected for nearest-neighbor hopping and > 95 times larger than expected for ES VRH. We find that the 70 K data can be fit equally well to a parabolic (band transport) or exponential (ES VRH; see eq. (4.2)) field dependence, but the extracted values of μ (63 cm^2 V^{-1} s^{-1}) and T_0 (106,000 – 278,000 K) are unreasonably large (fig. 4.15). We conclude that ρ(H) obeys neither expression and cannot be used to distinguish between band and hopping conduction in these samples. The fact that even the 300 K MR data fit well to an exponential, hopping-type function suggests that ρ(H) is of limited use in determining the transport mechanism when the MR is small and positive.

The temperature dependence of the MR is also inconsistent with hopping. The typical temperature dependence of MR for ES VRH is

$$\rho(H) = \rho_0 \; exp[(ta^4/\lambda^4)(T_0/T)^{3/2}], \tag{4.2}$$

with t = 0.0015.[99] Using a = 4.6 – 6.6 $\AA$ and T_0 = 3480 – 4920 K, eq. (4.2) predicts the MR to increase by less than 0.01% from 100 K to 30 K at our strongest field (90 kOe). Plots of MR vs. T from 30 – 300 K are shown in fig. 4.15. Although the low temperature (< 100 K) data are too scattered to reliably determine the temperature dependence of MR at weaker

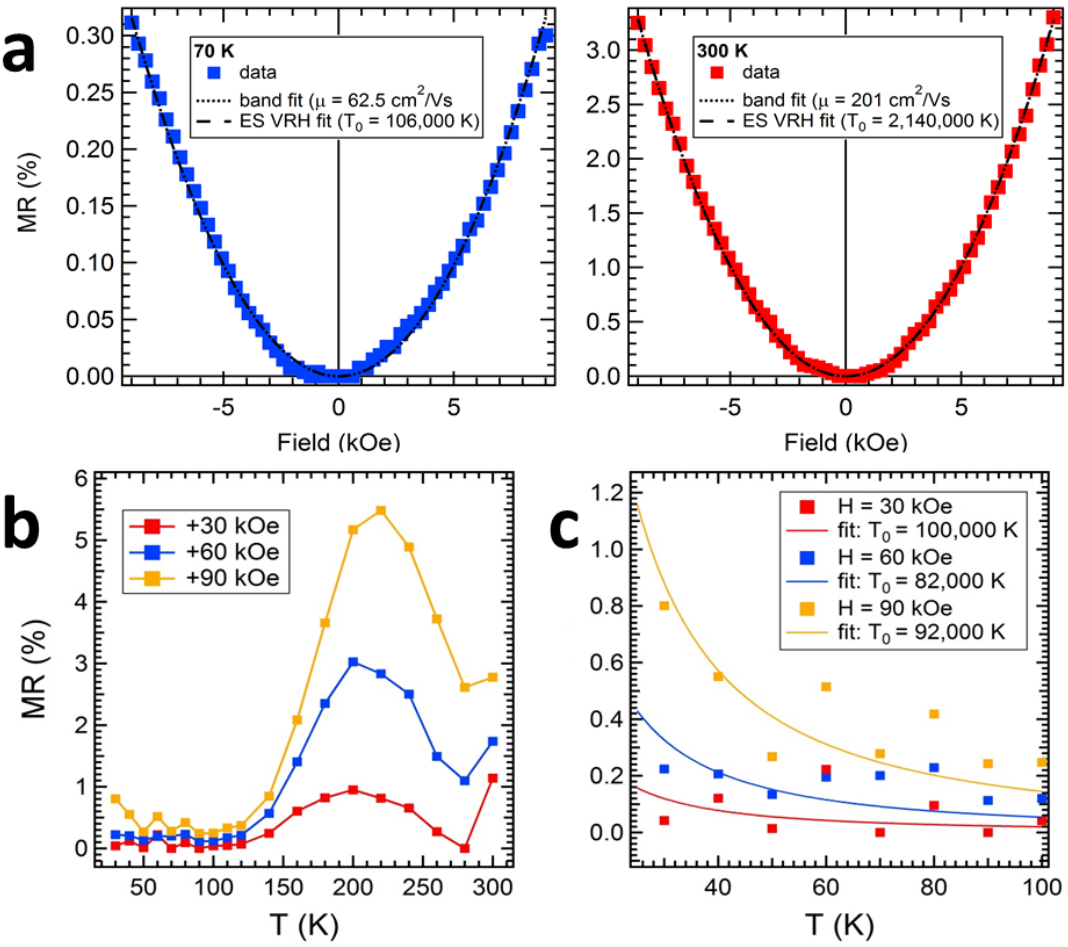

Figure 4.15: Transverse magnetoresistance [MR = 100(ρ(H) - ρ(0))/ρ(0)] of a pyrite single crystal. (a) MR as a function of magnetic field at 70 K (left) and 300 K (right), along with band transport and ES VRH fits. Qualitatively, the fits are equally good at both temperatures. However, the fits at 70 K result in unphysically large values of μ and T_0, suggesting that the MR is neither simple band nor ES VRH transport. At 300 K, the value of μ is quite reasonable, but that of T_0 is again unphysically large. The ES VRH fits shown here assume a = 6.6 $\AA$. (b) MR as a function of temperature. Data for a representative sample from 30-300 K at three different values of the magnetic field. (c) Detail view of the low-temperature region, including fits to eq. (4.2). While the data at 30 and 60 kOe are too scattered to determine the temperature dependence of the MR, the MR at 90 kOe clearly increases with decreasing temperature in qualitative agreement with eq. (4.2). However, an unphysically large value of T_0 is required to fit the data. Figure adapted from [70].

fields, at the strongest field the MR increases with decreasing temperature in qualitative agreement with eq. (4.2). However, fits to the data yield unreasonably large values for T_0 on the order of 10^5 K. Based on this lack of quantitative agreement, we conclude that the temperature dependence of MR does not support hopping transport.

Overall, the ρ(T) and ρ(H) data are inconsistent with each other and unable to provide a firm conclusion about the existence of hopping transport in these pyrite crystals. The ρ(T) analysis supports ES VRH transport, but MR(H) cannot be explained by simple hopping or band conduction and MR(T) is inconsistent with hopping. A more definitive conclusion could be obtained by determining whether the low-temperature resistivity shows an exponential dependence on the concentration of impurity states, but so far it has not proved possible to control the dopant concentration in pyrite to the degree needed for such a study. Regardless of whether hopping occurs, the results we present below establish beyond doubt the existence of a conductive inversion layer at the surface of pyrite. The open question is then whether carriers in this surface layer move by hopping, conventional band transport, or perhaps even by impurity band transport at low temperature.

We can quantitatively account for the Hall behavior of our pyrite crystals (e.g., fig. 4.11) by supposing that conduction is by a p-type surface layer in parallel with the n-type bulk of the crystal. The surface layer is an inversion layer caused by large upward band bending at the surface of the crystal. The origin of this band bending is discussed below. To model the Hall data, the crystal can be thought to consist of three layers: the bulk and a surface layer on each side of the crystal. Our model follows the approach of Petritz[89] and assumes a single donor level in the bulk and a single acceptor level in the surface layer (see section 2.7.2). Nonzero compensation in the bulk was also considered in some modeling fits. We calculate E_F(T) self-consistently from the semiconductor charge neutrality condition and then determine n(T) and p(T) in all layers, while the mobilities are inputs to the model parameterized from the Hall data in the unipolar regions. The dotted traces in fig. 4.11 show a simultaneous fit

Parameter (unit)	Parabolic DOS	DFT DOS
N_D (cm^{-3})	6.3 x 10^{18}	5.6 x 10^{19}
E_C - E_D (meV)	390	380
N_A (cm^{-3})	2.2 x 10^{20}	4.5 x 10^{19}
E_A - E_V (meV)	50	50
$E_{gap,300K}$ (meV)	700	700
μ_h (cm^2 V^{-1} s^{-1})	2.5	2.5
d_s (nm)	4.4	4.4

Table 4.2: Fit parameters used in fig. 4.11 and fig. B.3.

of the high-temperature σ and R_H data by considering only the bulk (zero compensation), without the surface layers. This fit is good at temperatures above the $|R_H|$ maximum, but of course cannot capture the unusual low temperature behavior. Including the surface layers in the model results in a good global fit over the entire temperature range (dashed traces). Parameters used in the fits in fig. 4.11 and fig. B.3, including estimates of the density and ionization energy of both the donor and acceptor, are listed in table 4.2 and are physically reasonable. Using parabolic DOS(E) functions in the model results in the following typical values for the parameters: $N_{D,bulk}$ = 6.3 x 10^{18} cm^{-3}; E_C - E_D = 390 meV; E_A - E_V = 50 meV; d_s = 4.4 nm; μ_h = 2.5 cm^2 V^{-1} s^{-1}. The surface acceptor density $N_{A,surface}$ depends on surface preparation and varies in the range of 10^{19} – 10^{21} cm^{-3}. See fig. 4.17 for typical model outputs specific to the bulk and surface layers.

This model provides a simple explanation for the existence of the maximum and sign reversal in $|R_H|$: bulk conduction of electrons dominates at temperatures higher than the maximum (giving $R_H < 0$), while surface conduction of holes dominates at temperatures lower than the maximum (and gives $R_H > 0$). The activation energy of σ at T < 90 K (i.e., in region III) may correspond to the ionization of holes from a shallow surface acceptor into the valence band. At temperatures close to the $|R_H|$ maximum, bulk and surface conduction are of similar importance, giving rise to a regime of mixed transport between bulk electrons and surface holes. Spatial separation of these charge carriers is maintained by the surface electric

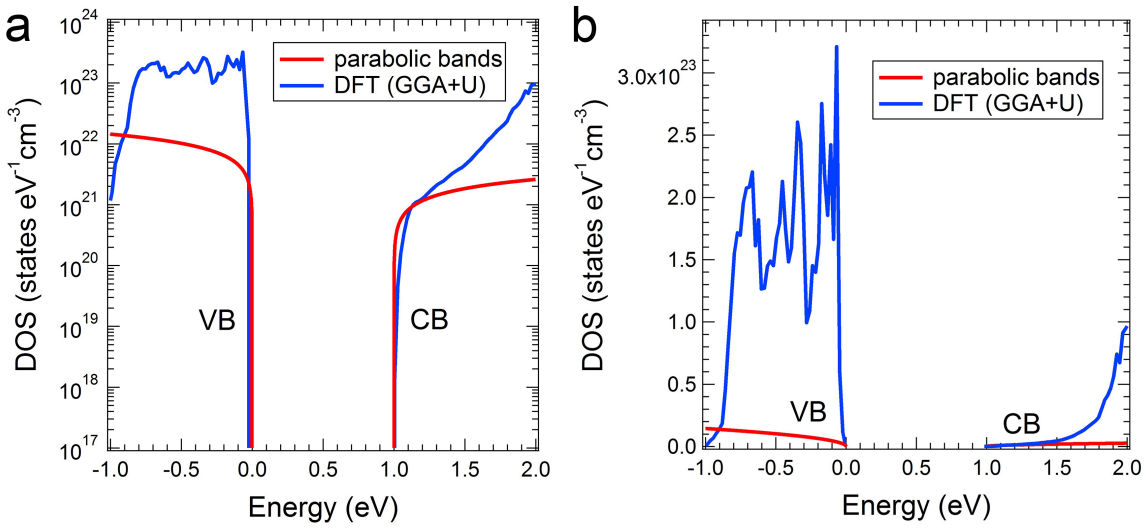

Figure 4.16: Comparison of DOS(E) functions calculated using the normal parabolic band approximation (red) versus density functional theory (GGA+U, blue), on both (a) logarithmic and (b) linear scales. These DOS(E) functions were used to model the Hall data and electronic band gap of pyrite. DFT results are taken from [52]. Figure reproduced from [70].

field that defines the inversion layer. In other words, the inversion layer is to some extent electrically isolated from the n-type bulk by a depletion region (see fig. 4.21). As we discuss below, the inversion layer revealed by our Hall measurements is likely the main reason that pyrite has a photo-voltage much smaller than its band gap permits.

Critical additional evidence for surface conduction in an inversion layer comes from the dependence of the Hall data on sample thickness. In principle, decreasing the slab thickness should decrease the ratio of the bulk to surface layer thicknesses and change σ and R_H according to eq. (2.12) and eq. (2.13). Only when surface conductivity is quite different from bulk conductivity do we expect to affect the Hall data by changing the surface-to-volume ratio. We acquired Hall data on several pyrite slabs as a function of thickness by using mechanical polishing to progressively thin the slabs between measurements. Care was taken to prepare the surfaces in the same way for each measurement in order to avoid uncontrolled differences in surface morphology or chemistry that might influence the results.

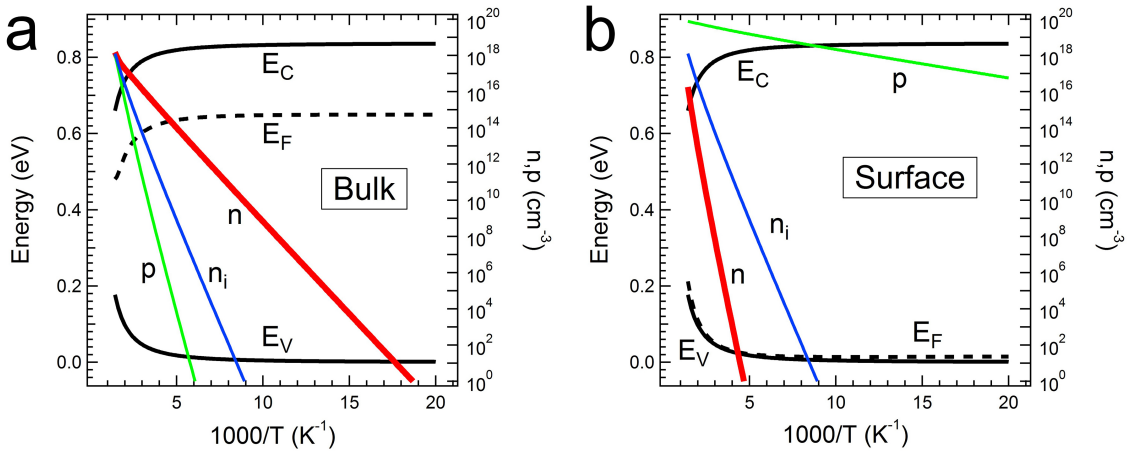

Figure 4.17: Typical examples of calculated Fermi energy E_F and carrier concentrations as a function of inverse temperature for the (a) bulk and (b) surface layers. Zero compensation is assumed. Figure reproduced from [70].

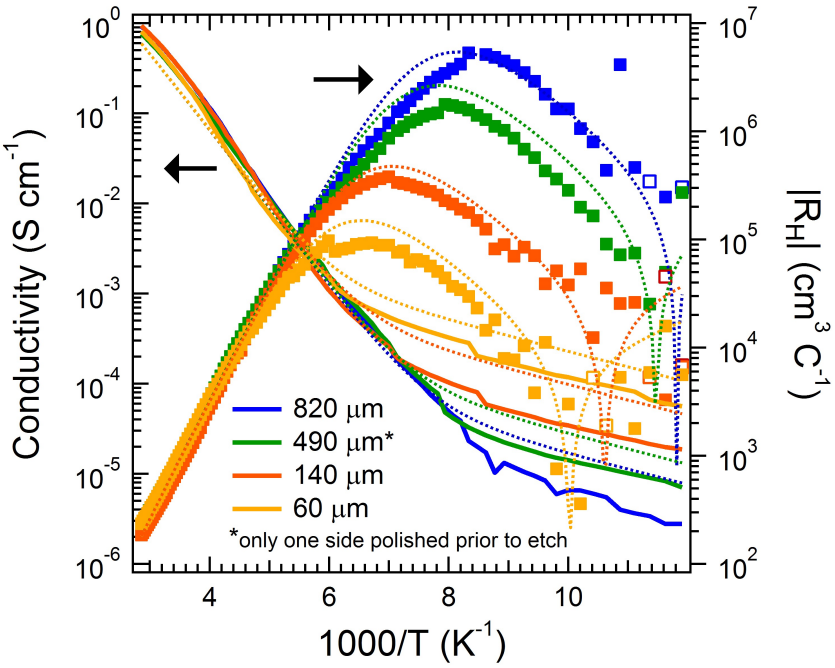

Figure 4.18: Dependence of Hall data on sample thickness. The crystal was thinned down, polished on both sides and etched in piranha solution for 2 minutes prior to each measurement (except for the 490 mm data, for which only one side was freshly polished prior to piranha treatment). After an initial fit of the 820 μm data (dotted blue curve) was performed, all other dotted curves are predictions (*not fits!*) from the multi-layer model, using the same parameters used for the original 820 μm data, only changing the sample thickness. This predictability of temperature-dependent Hall effect and conductivity data was confirmed on three more crystals that were thinned down the same way. Figure reproduced from [70].

Figure 4.18 presents Hall data (80 – 350 K) for a representative crystal at thicknesses of 820, 490, 140, and 60 μm, along with predictions from the model (dashed traces). We observe systematic changes in the low-temperature data that are in qualitative agreement with predictions from the multi-layer model. With decreasing sample thickness, the $|R_H|$ maximum shifts to higher temperatures (from 118 to 152 K in fig. 4.18) and the low-temperature σ increases by a factor of $\sim$20 with no change in activation energy. The R_H sign reversal also occurs at progressively higher temperatures (from 85 to 100 K). These effects are geometric: since surface layer conductance is a larger fraction of the total conductance in thinner samples, surface conduction starts to dominate R_H at higher temperatures as the crystal is thinned. Because the surface conductivity is much larger than bulk conductivity at low temperatures (for example, $\sigma_{bulk} = 6$ x 10^{-7} S/cm and $\sigma_{surf} = 0.53$ S/cm at 100 K), the total sample conductivity increases for thinner samples. We note that the systematic thickness dependence of $|R_H|$ and σ shown in fig. 4.18 is in itself sufficient evidence to prove that pyrite has a conductive surface layer. As expected, control experiments on silicon single crystals showed no change in $|R_H|$ or σ as a function of slab thickness because silicon lacks a conductive surface layer (see appendix, fig. B.5). These control experiments provide additional confirmation that our model and interpretation of the pyrite data are correct.

The low-temperature Hall data is also sensitive to mechanical and chemical modification of the crystal surface, as expected if surface conduction dominates transport. Figure 4.19 shows how $|R_H|$ and σ change as a typical pyrite slab is cut, polished, damaged by grinding with SiC paper, and then etched in piranha solution to remove the surface damage. Polishing the as-grown slab causes a small increase in conductivity and slight shift of the $|R_H|$ maximum to higher temperature. Damaging the surface by mechanical grinding results in a much larger change of the same kind, consistent with a thicker and/or more conductive surface layer. Rocking curves show that significant lattice disorder is induced by the grinding step. A brief piranha or nitric acid etch removes this surface damage, dramatically lowers the conductivity, and shifts the $|R_H|$ maximum to lower temperature (from 140 to 114 K),

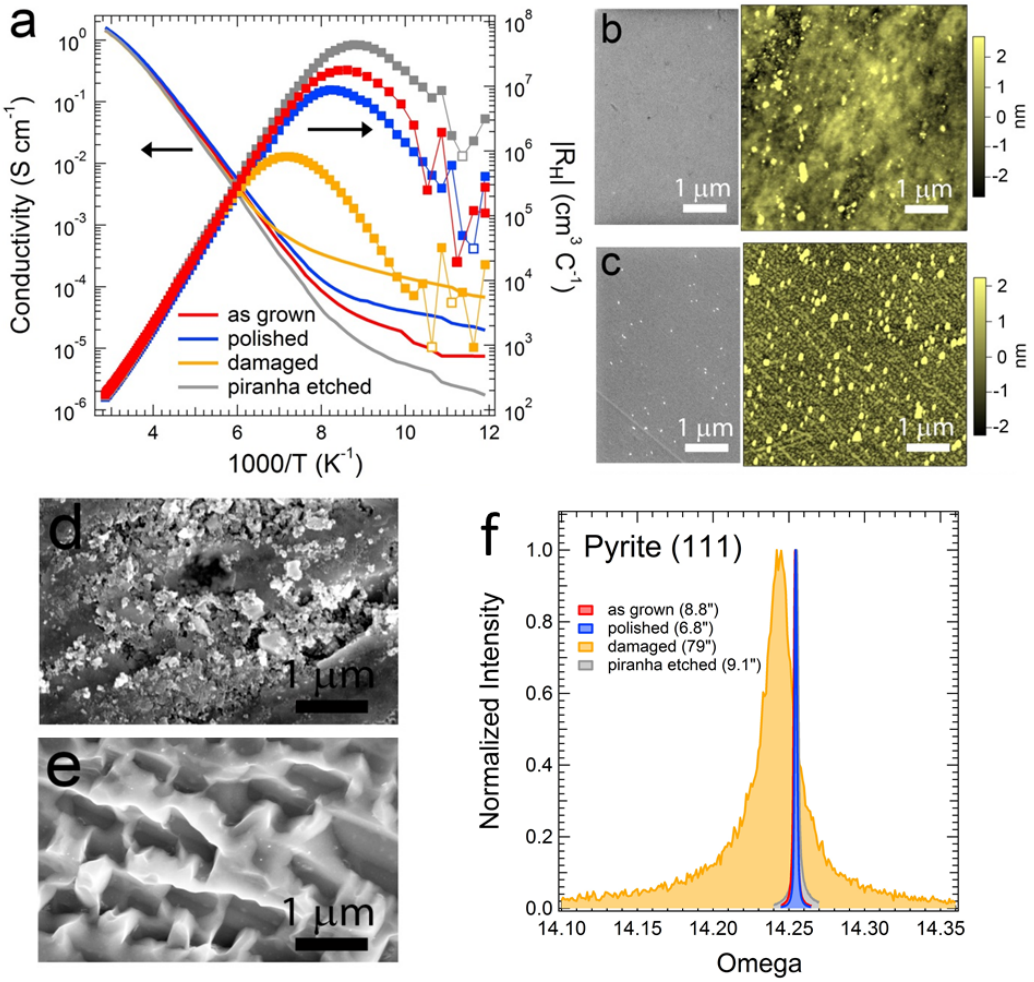

Figure 4.19: Dependence of the Hall data on gross surface modifications. (a) Data for one pyrite sample after the following sequence of surface treatments: as grown = no treatment of top surface, bottom surface rough cut with a diamond saw; polished = after polishing both sides to ∼2 nm RMS roughness (see section 2.3.1); damaged = after aggressive grinding of both sides with SiC paper; piranha etched = after a 5 min etch in piranha solution. Sample thickness: 400 – 500 μm. (b) SEM and AFM images of the as-grown crystal. RMS roughness = 1.3 nm. (c) SEM and AFM images of the polished crystal. Roughness = 1.6 nm RMS. The particles present in (b) and (c) were determined to be pyrite by energy dispersive spectroscopy (EDS). (d) SEM image of the crystal after damaging the surface with SiC grinding paper. (e) SEM image of the crystal after etching in piranha. Note that while a 5 min piranha etch of a damaged crystal results in pitting, the same etch of a polished crystal leaves an unpitted, planar surface. See fig. B.6 for SEM and AFM images of a polished, then piranha-etched sample. (f) (111) rocking curves for a pyrite slab as a function of surface modification. FWHM values are given in the legend in units of arcseconds. Figure adapted from [70].

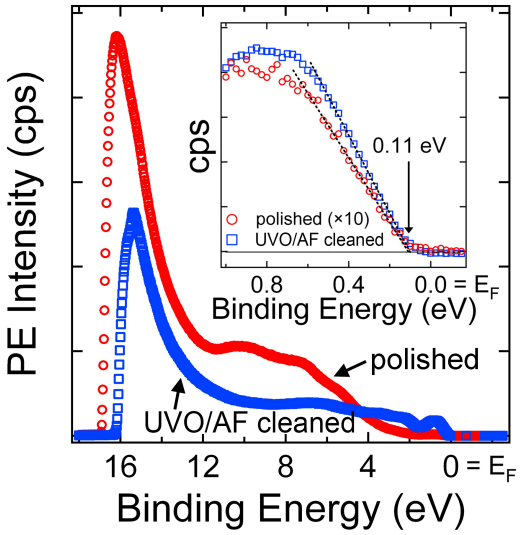

Figure 4.20: Upper valence band spectra of a polished pyrite (111) slab before and after surface cleaning by UV/ozone and aqueous NH_4F etching. Inset is a magnified view of the edge of the valence band. In both cases, E_F - $E_V \approx 0.11$ eV and the surface of the n-type crystal is p-type. Figure reproduced from [70].

indicating a decrease in the thickness and/or conductivity of the surface layer to below that of the polished crystals. Modeling shows that the effective surface acceptor density decreases by a factor of up to 20 after piranha or nitric acid etching of polished crystals. These surface modifications have a large impact on the low-temperature data (where the surface layer dominates transport), but very little impact on either σ or R_H at temperatures above ~160 K. A chemical understanding of these changes is the goal of ongoing studies. It is possible that piranha and nitric acid treatments reduce the conductivity/thickness of the surface layer by oxidizing the surface and passivating some fraction of the surface states. The partial suppression of surface conduction by oxidizing etches raises the hope that suitable chemical treatments can be devised to control and eliminate the inversion layer at the pyrite surface. See section 4.6 for further discussion of surface passivation.

We used ultraviolet photoelectron spectroscopy (UPS) to independently confirm the existence of the inversion layer (see section 2.4.5). Figure 4.20 shows room-temperature He I UP spectra of a polished pyrite (111) slab acquired before and after cleaning the surface with

a sequence of UV/ozone (UVO) and ammonium fluoride treatments to remove adventitious organic and oxide contamination. Both spectra show that the Fermi level lies 0.11 ± 0.05 eV above the valence band maximum (inset fig. 4.20), i.e., the surface is p-type in both cases assuming that the surface band gap is greater than ∼0.2 eV. In light of the Hall results presented above, it follows that the surface must feature an inversion layer with a band diagram similar to fig. 4.21.

The likely existence of an inversion layer at the surface of pyrite was established twenty years ago by Bronold and coworkers using UPS measurements of vacuum-cleaved (100) single crystals.[11,14,13] Our UPS results reproduce this early work and, together with our Hall analysis, show that it is correct for pyrite (111), (210), and (100) surfaces. Following Bronold, we attribute the pinned Fermi level and resulting inversion layer to intrinsic surface states with energies near the valence band edge. The inversion layer probably originates from a symmetry reduction at the pyrite surface and not from contamination (e.g., oxide or adsorbed organic species). Experimental evidence for the inversion layer has been overlooked in recent efforts to explain the low voltage of pyrite photocells,[124,102] yet surface conduction in accumulation or inversion layers is quite common for semiconductors, with important examples including Mg_2Sn,[43] Ge,[61] HgCdTe,[71] pyrite NiS_2,[105] and InN.[57,59] It has taken until now to demonstrate the importance of surface conduction in pyrite for two reasons: first, many pyrite samples are too impure to clearly see surface conduction in Hall data and, second, the few examples of unusual Hall data reported in the literature went unnoticed or were interpreted as hopping.[108]

The inversion layer can account for the low photovoltage of pyrite photocells.[6] As originally argued by Bronold, the low voltage may be caused by thermionic field emission through a thin triangular potential barrier at the surface of the crystal (fig. 4.21a).[13] At the pyrite surface, the iron coordination number is reduced from six to five. This symmetry reduction (distorted octahedral to square pyramidal coordination) creates iron-based surface states at energies close to the valence band edge. Fermi level equilibration of the n-type bulk with

these surface states generates strong upward band bending and an inversion layer. During equilibration, donors near the surface rise above the Fermi level and are ionized, which augments the surface field and creates a thin triangular potential barrier through which majority carriers can tunnel directly or with the assistance of empty donors (fig. 4.21a). Because this leaky potential barrier is poor at separating charge, the dark current is large and the maximum V_{OC} limited to ∼0.2 V (i.e., the portion of the barrier not shorted by tunneling). In this picture, increasing the V_{OC} will require reducing the concentration of surface states (responsible for the inversion layer) as well as near-surface donors (responsible for the triangular tunnel barrier and, ultimately, the low V_{OC}). We estimate that reducing N_D below $\sim 10^{17}$ cm^{-3} would render field emission insignificant and boost the maximum V_{OC} above 450 mV. However, our efforts to lower N_D below $\sim 10^{19}$ cm^{-3} have been unsuccessful so far and it remains to be seen whether these donors – which we believe are sulfur vacancies and associated defect clusters – are inevitable in pyrite.

The inversion layer can also explain why most polycrystalline pyrite thin films show the same electrical properties – a high hole concentration, low mobility ($\leq$1 cm^2 V^{-1} s^{-1}), and activated transport with a small activation energy of ∼30 meV – regardless of preparation method.[6,97,116,4] Thin films are often dominated by surface effects due to their large surface-to-volume ratios. In the case of pyrite films, transport may be governed by surface conduction via the hole-rich accumulation/inversion layer around each crystallite. These surface layers would form continuous networks for long-range transport through the films. Unlike pyrite single crystals, which are dominated by surface conduction only at temperatures low enough to freeze out a sufficient fraction of the bulk electrons, pyrite thin films have a large surface volume fraction and are therefore dominated by surface conduction at all temperatures. The fact that pyrite films have the same activation energy (∼25 meV) and low hole mobility ($\leq$1 cm^2 V^{-1} s^{-1}) as single crystals in the low-temperature, surface conduction regime is strong evidence that the commonly-observed p-type electrical behavior of pyrite films is caused by conduction within a hole-rich surface layer.

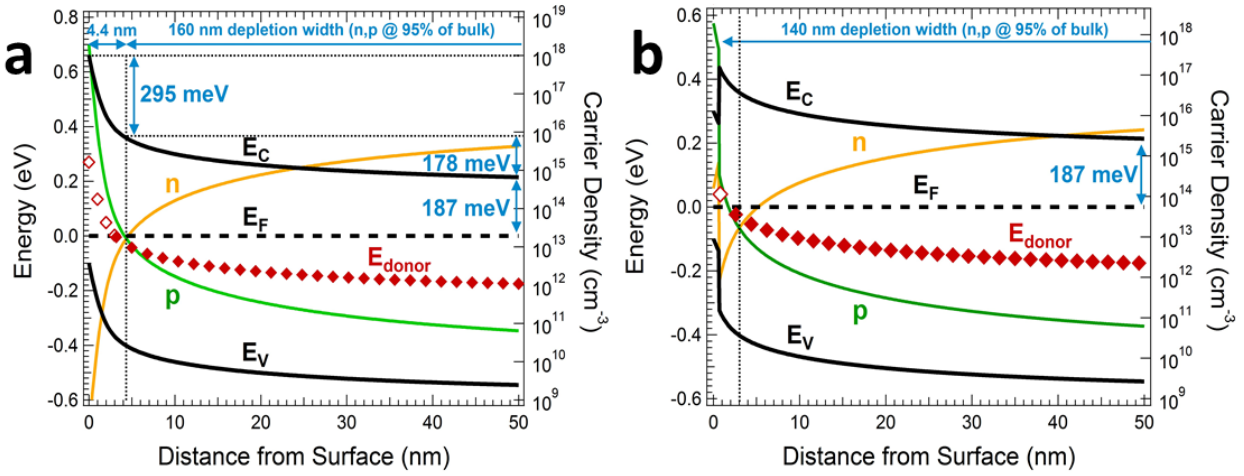

Figure 4.21: Calculated equilibrium band diagram of the pyrite surface at 300 K (see section 2.7.3). In the bulk, E_F is located ∼190 meV below the conduction band edge (consistent with N_D = 6 x 10^{18} cm^{-3} and E_C - E_D = 390 meV from Hall data). Zero compensation is assumed; including bulk compensation in the calculation did not change the qualitative features of the diagram. At the surface, E_F is pinned ∼100 meV from the valence band edge (consistent with UPS data).
(a) The surface band gap is assumed to be equal to the bulk band gap E_g = 0.76 eV (see section 4.4.3). Equilibration of bulk with surface results in steep upward surface band bending of ∼480 meV and the generation of an inversion layer (p > n) approximately 4.4 nm thick (denoted by the vertical dotted line). The inversion layer is separated from bulk by a depletion layer approximately 160 nm thick (defined here as n = 0.95 n_{bulk}). Most donors in the inversion layer are ionized (open red diamonds), which augments the surface electric field and results in a narrow triangular potential barrier across which carriers can readily tunnel. Tunneling is a loss mechanism that degrades the ability of the barrier to separate charge and produce voltage. As drawn, the top ∼295 mV of the barrier is lost to tunneling, leaving a maximum photovoltage of only ∼178 mV for any pyrite junction. The maximum V_{OC} becomes ∼340 mV if E_g is assumed to be 0.94 eV rather than 0.76 eV. (b) Assuming a reduced surface band gap of 0.40 eV, equilibration of bulk with surface results in relatively weak band bending of ∼250 meV, which represents the upper limit for the pyrite V_{OC}. Thus, tunneling is unnecessary to explain the low V_{OC} if a narrow-gap surface layer is present. An inversion layer (p > n) approximately 3.0 nm thick is also created (denoted by the vertical dotted line). It is separated from the bulk by a depletion layer approximately 140 nm thick. Figure adapted from [70].

Our Hall data can also be understood in terms of an inverted surface layer with a band gap that is smaller than the bulk band gap of pyrite. Several DFT studies have concluded that the low photovoltage of pyrite devices may be caused by narrowing of the "band gap" of the first three atomic layers of the pyrite surface (∼0.7 nm) to less than 0.6 eV by intrinsic surface states or surface nonstoichiometry.[124,127] Recently, Herbert et al. presented scanning tunneling spectroscopy (STS) evidence that the clean pyrite (100) surface has a band gap of 0.4 ± 0.1 eV.[48] We find that a thin surface layer with a reduced band gap (E_g = 0.3 – 0.6 eV) has very similar electrical consequences to an inversion layer with the same band gap as bulk pyrite, namely: (i) both layers are p-type (since E_F - $E_V \approx$ 0.1 eV at the surface) and responsible for the surface hole conduction we observe at low temperatures; (ii) both layers can restrict the V_{OC} to ≤200 mV, albeit by different mechanisms (compare the band diagrams in fig. 4.21: an inherently small built-in potential would cause the low V_{OC} in the former case, while thermionic field emission is responsible in the latter case); (iii) the two layers have the same origin (intrinsic surface states) and so the same remedy (passivation of surface states and near-surface defects). Changing the band gap of the surface layer has a negligible effect on our Hall modeling, meaning that we cannot tell whether the band gap of the surface differs from that of the bulk on the basis of the Hall data alone. Likewise, UPS probes <1 nm into the crystal surface and the data in fig. 4.20 are consistent with any value of the surface gap greater than 0.2 – 0.3 eV. A combined UPS and inverse photoemission study could complement STS to definitively establish the band gap of the pyrite inversion layer.

4.4.3 Assessment of the Bulk Band Gap of Pyrite

Above we presented evidence for an inversion layer at the surface of n-type pyrite single crystals and argued that thermionic field emission across this inversion layer is likely responsible for the low photovoltage of pyrite photocells, in line with earlier work by Bronold

et al.[13] Our data are also consistent with the presence of a narrow-gap surface layer that generates only a small potential barrier and thus a small maximum V_{OC}. Now, we evaluate an important alternative explanation for the low V_{OC} of pyrite, namely that the bulk band gap of pyrite has been overestimated in literature and is actually substantially smaller than ∼0.95 eV at room temperature. If the bulk electronic band gap was in fact 0.5 – 0.6 eV, then the maximum V_{OC} might be 0.2 – 0.3 eV, in good agreement with experiment. Indeed, a small band gap is a more parsimonious explanation for the low V_{OC} than a leaky inversion layer. It is therefore important to reassess the size of the pyrite band gap as rigorously as possible.

The main reason to suspect that pyrite may have a smaller band gap than commonly believed is a series of density functional theory (DFT) studies[124, 102, 52] showing that the conduction band of pyrite features a long tail of states extending to the edge of the gap (see fig. 4.16). Because of its low density of states (DOS) and small optical matrix elements,[22] this tail could easily be invisible to the typical spectroscopic measurements used to estimate semiconductor band gaps, leading to systematic overestimation of the pyrite gap when measured optically. To the best of our knowledge, there is no convincing experimental evidence for this tail of states. Maps of the conduction band DOS by inverse photoemission spectroscopy[42, 85] and electron energy loss spectroscopy[45] lack a clear tail, but this may simply reflect the inherent difficulty of detecting a weak DOS tail and the fact that searching for a tail was not a focus of these earlier studies. Experiments designed to detect and characterize this proposed tail of states are necessary.

For materials with soft band edges, electrical measurements can provide more accurate band gap estimates than optical measurements. The electronic band gap is commonly extracted from the temperature-dependent conductivity in the intrinsic region using $\sigma(T) = A \exp(\frac{-E_g}{2k_B T})$, with both A and E_g treated as independent of temperature.[103] However, this expression is based on several simplifications, including the parabolic band approximation, the free electron approximation, and the Boltzmann approximation, each of which may be

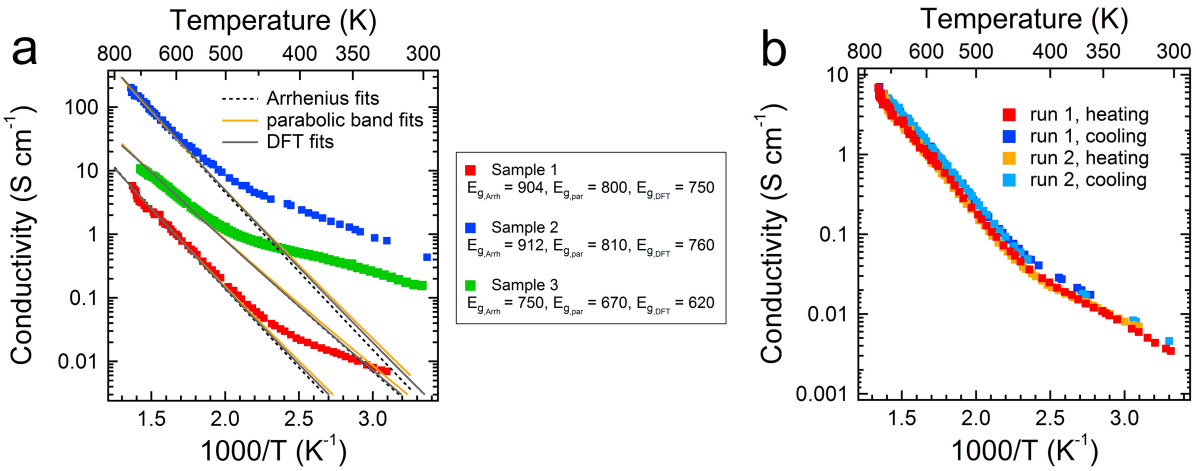

Figure 4.22: Conductivity of pyrite crystals in the intrinsic region. (a) High-temperature conductivity data for three crystals. The intrinsic region of each sample is fit with the simple Arrhenius expression (dotted lines) as well as models employing DFT or parabolic DOS(E) values (gray and yellow lines, respectively). All fits assume $\mu(\mathrm{T}) \propto \mathrm{T}^{-2.5}$. Listed to the right of the graph are room-temperature E_g values (in meV) determined by the three different approaches. (b) Two sets of heating and cooling curves (300 K to 750 K) for Sample 1. The activation energy is unchanged by heating, suggesting that surface sulfur loss and possible phase transitions from FeS_2 to sulfur-deficient Fe_xS_y and FeS do not appreciably alter the electrical properties of the samples. Heating and cooling rates = 7 – 14 K/min. Sample thickness = 700 – 1040 μm. Figure reproduced from [70].

inappropriate for pyrite. DFT results show that the valence and conduction bands of pyrite are not parabolic and the DOS(E) functions are neither free carrier like nor symmetric (the valence band has a much larger DOS than the conduction band). Violation of the parabolic band approximation by pyrite has been previously pointed out by Ferrer et al.[38,25] If the DOS from DFT is correct, then the Fermi level must lie close to the conduction band edge at high temperatures (see fig. B.4), and the slope of an Arrhenius conductivity plot will not correspond to half of the band gap. This complicates any estimate of the pyrite band gap from the intrinsic conductivity.

A further complication is that both A and E_g depend on temperature. In deriving the normal expression for σ(T), the DOS is approximated with the free electron gas and Boltzmann statistics are used to give $n_i(T) = \sqrt{N_V(T)N_C(T)}\ exp(\frac{-E_g}{2k_BT}) \propto T^{3/2}exp(\frac{-E_g}{2k_BT})$. Combining this expression with the temperature-dependent mobility due to phonon scattering (μ(T) $\propto$ $T^{-3/2}$) yields the usual σ(T) equation with constant A. This equation is probably not correct for pyrite for the reasons mentioned above, and A may change significantly with temperature depending on the explicit forms of DOS(E) and μ(T). Furthermore, E_g typically varies with temperature according to the empirical relation $E_g = E_{g_0} - \frac{aT^2}{T+b}$, resulting in a substantial change in E_g (often several hundred meV) from room temperature to within the intrinsic region. A numerical model using explicit forms of DOS(E) and E_g(T) and good estimates for μ(T) is therefore required to determine the pyrite band gap from σ(T) data. This is the approach we adopt in the following analysis.

Arrhenius conductivity plots of three pyrite crystals (300 – 750 K) are shown in fig. 4.22. Since the pyrite samples were measured at high temperature, we first checked whether sulfur loss and the formation of sulfur-deficient phases at the crystal surface may affect the conductivity data. Fig. 4.22 shows that the σ(T) curves of sample 1 are unchanged over several cycles of heating and cooling, suggesting that loss of surface sulfur has negligible impact on the data. In situ XRD scans of crystals subjected to these heat treatments confirmed that the formation of sulfur-deficient phases (FeS and Fe_7S_8) becomes appreciable only above 775

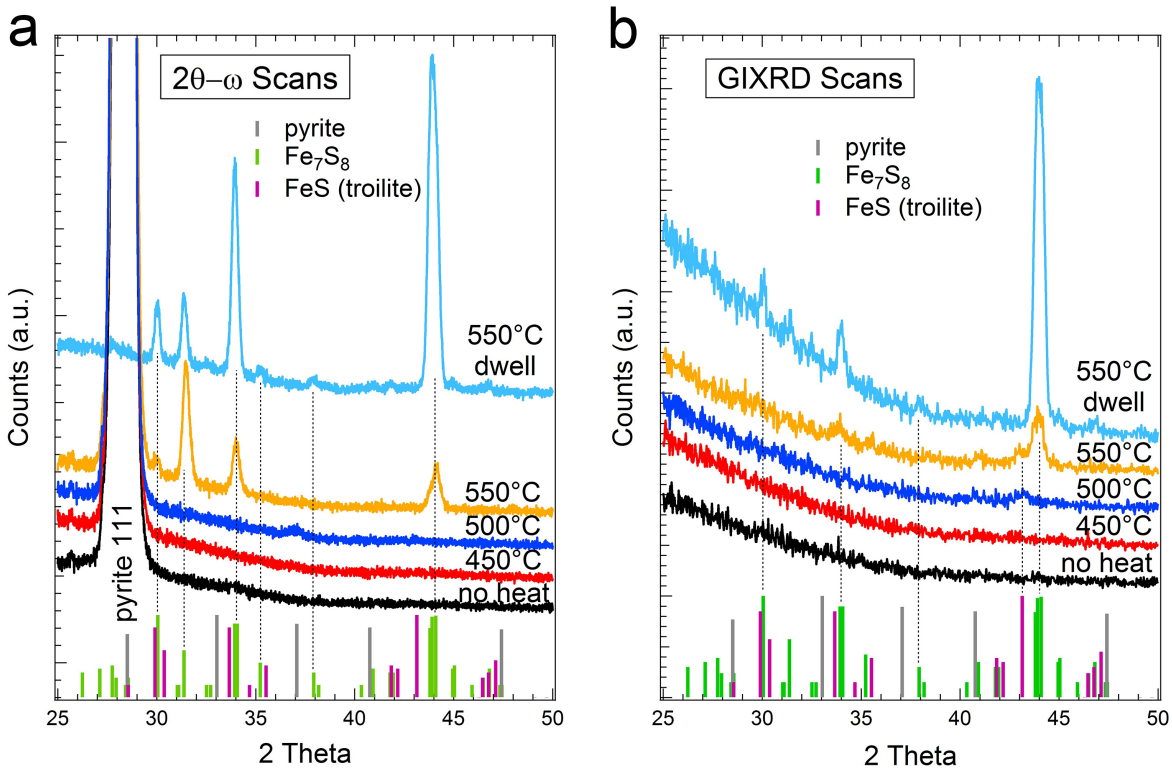

Figure 4.23: XRD patterns of a pyrite (111) single crystal before and after heating to progressively higher temperatures in ultrapure (5N nitrogen). (a) 2θ-ω scans. (b) Omega scans with a grazing incidence angle of 1.0 degree. The sample was heated within 60 minutes to the temperature indicated, held at that temperature for 1 minute, and then cooled to room temperature within 60 minutes prior to data acquisition. The data labeled "550 °C dwell" were acquired after holding the sample at 550 °C for 1 hour. Figure reproduced from [70].

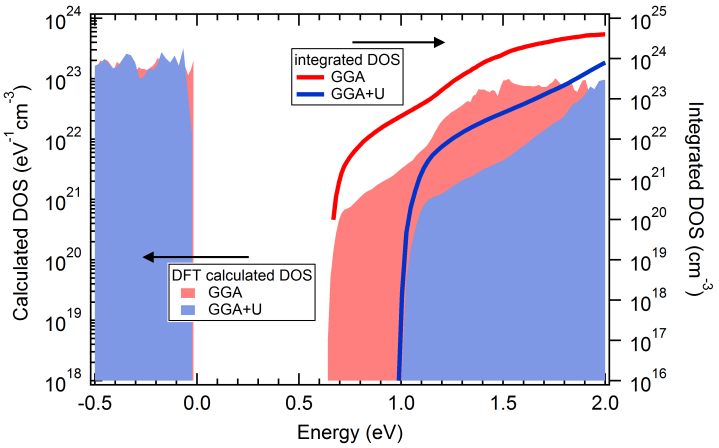

Figure 4.24: Shaded areas (left axis): the valence and conduction band density of states calculated by DFT using the GGA (red) and GGA+U (blue) levels of theory. Solid lines (right axis): the integrated density of states for the conduction band at the two levels of theory. The integrated DOS(E) at the conduction band edge is much higher than intrinsic carrier densities at all temperatures considered in the text ($\leq$ 750 K), so a significant ($>$ 25 meV) Burstein-Moss shift can be ruled out. DFT results are taken from [52]. Figure adapted from [70].

K (fig. 4.23) or after prolonged heat soaking at somewhat lower temperatures ($>$ 675 K). Furthermore, our multi-layer model shows that the buildup of a metallic surface layer of any significant thickness would produce an obvious upward shift in the conductivity curves, which is not observed. We therefore believe that the σ(T) data in fig. 4.22 reflect the behavior of pyrite itself in the intrinsic region.

Prior to analyzing the σ(T) data, we also estimated whether thermal excitation of electrons at intrinsic temperatures could fill enough of the conduction band tail of states to result in a Burstein–Moss type increase of the apparent electronic band gap. However, the intrinsic electron density at even the highest temperatures explored here ($\sim$750 K) is still several orders of magnitude smaller than the integrated DFT DOS at the edge of the conduction band (fig. 4.24). Therefore, the DOS in the tail is much too large to cause a significant Burstein–Moss shift in the intrinsic region, and we estimate that any increase in apparent band gap due to state filling is less than 25 meV. This further confirms that the σ(T) data in fig. 4.22 can be related to the room-temperature electronic band gap of pyrite

We calculated room-temperature band gaps from the σ(T) data using three different approaches. The first approach assumes the naive relation $\sigma(\mathrm{T}) = \mathrm{A}\exp(\frac{-E_g}{2k_BT})$ with a temperature-independent E_g. Simple Arrhenius fits to the intrinsic region yield band gaps of 904, 912, and 750 meV for the three samples in fig. 4.22, in good agreement with previous results using this approach.[8] In the other two approaches we employed our numerical model to iteratively fit the intrinsic σ(T) data to determine E_g at high temperature and then extrapolated this value to room temperature using a measured E_g(T) curve for pyrite (see below). Modeling the data with the DFT DOS gives room-temperature band gaps of 750, 760, and 620 meV, while using the parabolic DOS instead of the DFT DOS results in gaps of 800, 810, and 670 meV. The band gap values are $\sim$50 meV smaller for the DFT DOS because the larger asymmetry between the valence and conduction band DOS shifts the Fermi level upwards and requires a smaller calculated band gap to yield a given slope in the σ(T) data (see fig. B.4). The same effect also results in a higher calculated carrier density, which requires an unrealistically low electron mobility to fit the data with the DFT DOS. Since the parabolic DOS provides a significantly better description of the pyrite Hall data than the DFT DOS, we conclude that the larger band gaps are more accurate. However, the accessible temperature range of the intrinsic region is fairly small (constrained at the low end by doping and the high end by sulfur loss). This causes some insensitivity to the fit parameters and an error of $\pm$50 meV in the band gap estimates. We also note a striking sample-to-sample variation in E_g of $\sim$200 meV across the seven samples we measured (see fig. 4.26). This variation may result from larger band tails in lower quality samples. Using the three highest E_g values in our data set and the E_g(T) relationship described in the next paragraph, we conclude that the room-temperature electronic band gap of high-quality pyrite crystals is 0.80 $\pm$ 0.05 eV. The average E_g of the three samples in fig. 4.22 – which includes one crystal with a particularly small estimated band gap – is 0.76 eV, within the specified range.

The temperature dependence of E_g was determined by measuring the optical gap of thin polished pyrite crystals from 80 to 440 K using transmission spectroscopy. Fig. 4.25 shows

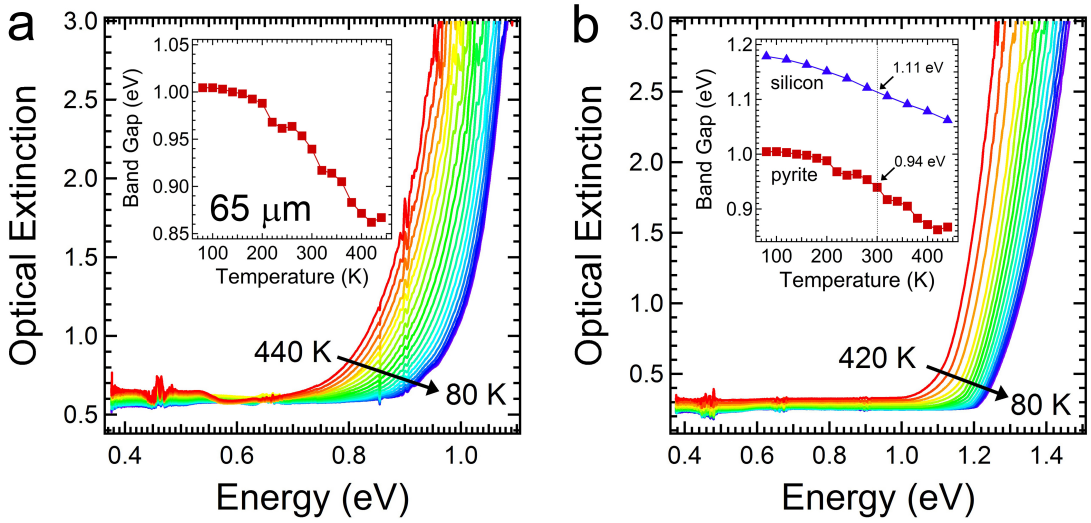

Figure 4.25: Optical extinction spectra of (a) a 65 μm thin pyrite crystal and (b) a 250 μm thick silicon crystal as a function of temperature. The crystals are polished on both sides. Data were acquired in 20 K increments. The insets show plots of band gap vs. temperature, as determined by linear extrapolation of the absorption coefficient data, after correcting for sample thickness and the dispersion of the refractive index. The inset in (b) compares the temperature dependence of the band gap for both materials. The room-temperature band gap of pyrite and silicon is 0.94 eV and 1.11 eV, respectively. Figure reproduced from [70].

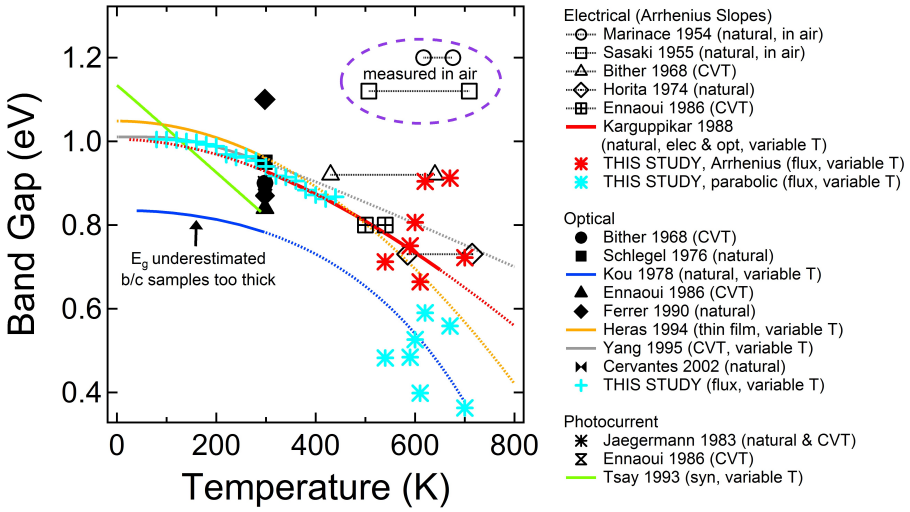

Figure 4.26: Compilation of literature values for the pyrite band gap. Dashed curves are extrapolations/interpolations from the variable-temperature experimental data (solid curves or points). The light blue crosses (optical data), light blue stars (electrical data modeled with the parabolic DOS(E)), and red stars (electrical data fit with simple Arrhenius lines) are the results of the present study. Figure reproduced from [70].

the raw extinction spectra as well as the optical gap extracted by linear extrapolation of the absorption coefficient curve to its intersection with the x-axis. Tauc plots – which presume parabolic bands – give the same E_g(T) values to within 50 meV. We find that the optical gap decreases from 1.00 eV at 80 K to 0.94 eV at 300 K and 0.86 eV at 440 K (the highest temperature possible with our equipment). Our E_g(T) curve is in good agreement with several previous reports,[62,121] particularly the work of Karguppikar and Vedeshwar[58] (see fig. 4.26 for a compilation of literature data on the pyrite gap). Although the magnitude of E_g may be overestimated by this optical method (as discussed above), the temperature dependence of E_g should be reliable, and we use the E_g(T) curve of ref. 58 to extrapolate the modeled high-temperature electronic gaps to 300 K. Based on this analysis, we find that the most probable electronic band gap of pyrite is 0.80 ± 0.05 eV at room temperature, as mentioned above. Although this value is somewhat smaller than the optical gap (0.94 eV), it is still large enough to support a photovoltage of 450 – 500 mV in pyrite photocells. We conclude that the pyrite photovoltage is not limited to ∼200 mV by a small bulk band gap.

4.5 Carrier Lifetimes

The lifetime of charge carriers τ is a crucial parameter for a potential solar photovoltaic absorber material. Together with the carrier mobility μ it determines the diffusion length $L = \sqrt{\mu\tau k_B T/e}$. The diffusion length is the average distance a carrier can diffuse before decaying by recombination, and must be equal or greater than the thickness of the absorber for efficient collection of charge carriers at their respective electrodes. In the case of pyrite, the bulk electron mobility μ_e is 300 cm^2/Vs in single crystals, but bulk hole mobility μ_h is not known experimentally and likely lower by a factor of ∼2 (based on effective masses predicted by DFT calculation). More importantly, the effective mobility in polycrystalline thin films for both carrier types is likely much lower. Using a conservative estimate of μ_e

$= \mu_h = 1$ cm^2/Vs and an absorber thickness of 300 nm, the carrier lifetimes should eb at least 35 ns. In previous work[9] carrier lifetimes in pyrite were measured using time-resolved microwave reflectivity (TRMC) and reported to reach values as high as 900 ns. Here we report carrier lifetime results on ultra-high purity pyrite single crystals grown by the flux method, using the same TRMC method.

In a first set of experiments, conducted by Dr. Steve Johnson at NREL, we compared the TRMC signal of a flux grown crystal to that of a natural crystal, both excited at a wavelength of 530 nm (fig. 4.27a). None of the two decay curves are simple exponentials, suggesting that several lifetimes resulting from different decay mechanisms are superimposed. This makes a quantitative analysis difficult, but it is obvious that carriers photo-generated in the flux grown crystal live much longer. After 80 ns about 10% of carriers, and after 300 ns about 4% of carrier are still excited. The instrument response time was estimated to $\sim$10 ns for this setup using a highly doped InP wafer.

In a second set of experiments, conducted by Andreas Fritze at University of Wuerzburg, the TRMC signal of a flux grown crystal was recorded as a function of excitation wavelength (fig. 4.27b). The instrument response time for this setup was $\sim$1 ns. Again, the quantitative analysis of the raw data is not straight-forward as decay does not follow simple exponential behavior. But looking at the raw data alone, there is an obvious trend for longer lifetimes at higher excitation wavelengths. Higher wavelengths correspond to deeper absorption in the crystal: see Fig. 4.27c for a plot of absorption length 1α vs. excitation wavelength, calculated form the spectral ellipsometry data presented in section 4.1. Assuming that mono-molecular recombination is the dominant decay process, the TRMC raw data was fitted to extract carrier lifetimes for every excitation wavelength. Combining this with the calculated absorption depth allows us to plot carrier lifetime vs. absorption depth, as shown in fig. 4.27d. For carrier that are photo-generated within the first 500 nm from the surface, carrier lifetime is limited to $\sim 20 - 50$ ns, which might already be sufficient for efficient carrier extraction in thin film pyrite absorbers (see discussion above). However, for carrier

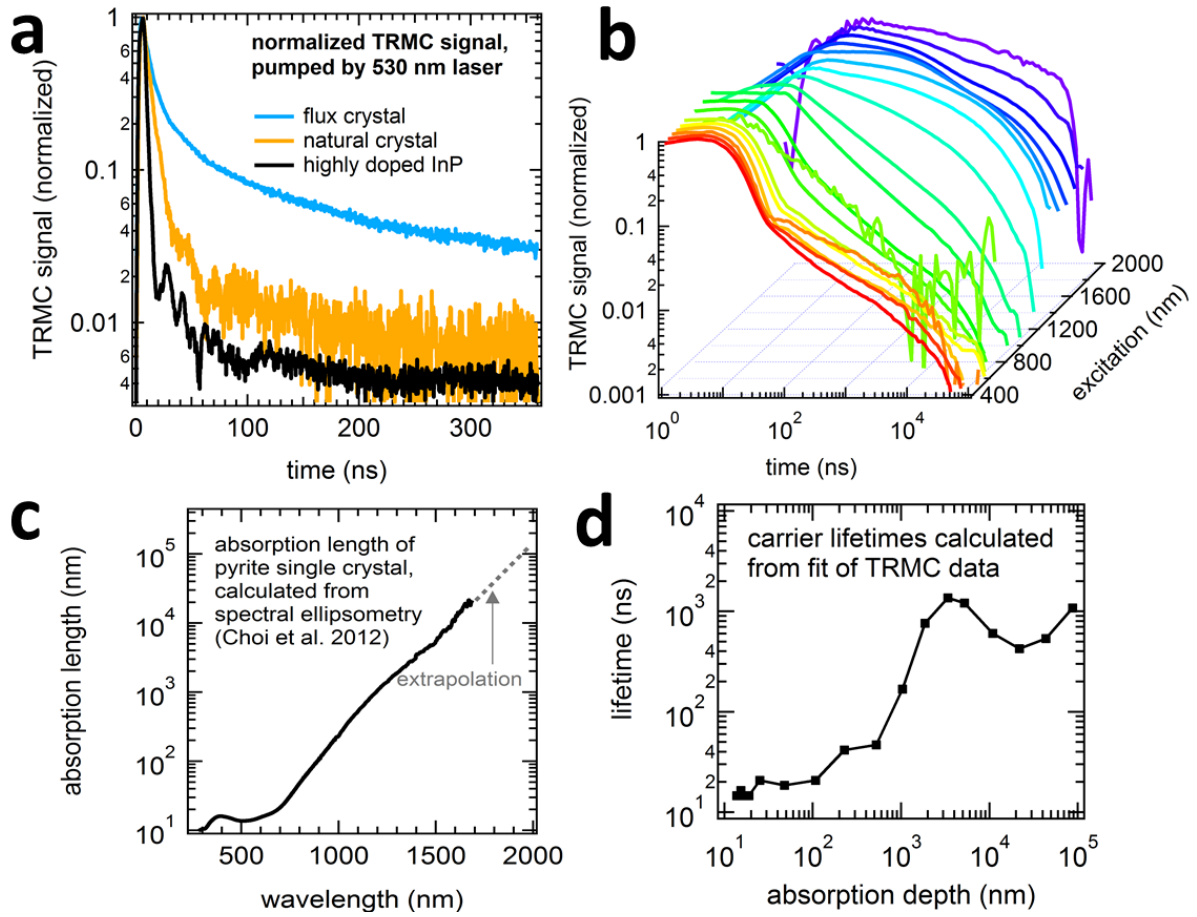

Figure 4.27: Carrier lifetimes in pyrite single crystals, probed by time-resolved microwave conductivity (TRMC). (a) TRMC measurements performed by Dr. Steve Johnson at NREL. A flux-grown (blue) and a natural (yellow) pyrite single crystal were excited with a 530 nm laser. Also shown is the response of a highly doped InP wafer, which allows an estimate of the instrument response time of ∼10 ns. (b) TRMC measurements performed by Andreas Fritze at University of Wuerzburg. A flux crystal was excited with wavelengths ranging from 435 to 1900 nm. (c) Absorption length $1/\alpha$ in pyrite as a function of wavelength, calculated from the spectral ellipsometry data presented in section 4.1. (d) Carrier lifetimes as a function of absorption depth, calculated from the TRMC data shown in (b) and the absorption length shown in (c).

photo-generated deeper in the crystal, carrier lifetime increases drastically, reaching > 1000 ns at a depth of 3000 nm. This result, though preliminary and pending more careful data analysis and fitting, is very promising as it suggests that carrier lifetimes on the order of μs are possible in pyrite. Moreover, the dependence on absorption depth is in line with the reported accumulation of defects at the surface and in the near-surface region. Future work should include variable temperature measurements, variable light intensity, and aim to distinguish the lifetime of electrons and holes.

4.6 Surface Passivation

This section restates the need for surface passivation of pyrite, and presents a methodology to systematically and quantitatively evaluate all non-destructive treatments using pyrite single crystals as a platform. Additionally it discusses some preliminary results and suggests future work to find the best surface passivation treatment for pyrite single crystals and ultimately thin films.

As motivated above, the passivation of surface states, together with a lowering of bulk donor states, is a necessity to enable photo-voltages of ∼500 mV for pyrite. Figure 4.28 illustrates the need for this passivation. While already limiting the obtainable photo-voltage for single crystals as shown above (section 4.4.2), the effect is much stronger in polycrystalline thin films. Using single crystals as a well-understood model system, the ultimate goal is to find passivation treatments that are transferable to thin film. To this end, many different treatments were tested and evaluated using temperature-dependent Hall effect measurements, according to the model described in section 4.4.2. These treatments included chemical etching, plasma etching, thermal annealing in different inert and reactive atmospheres and overcoating with sulfides and oxides.

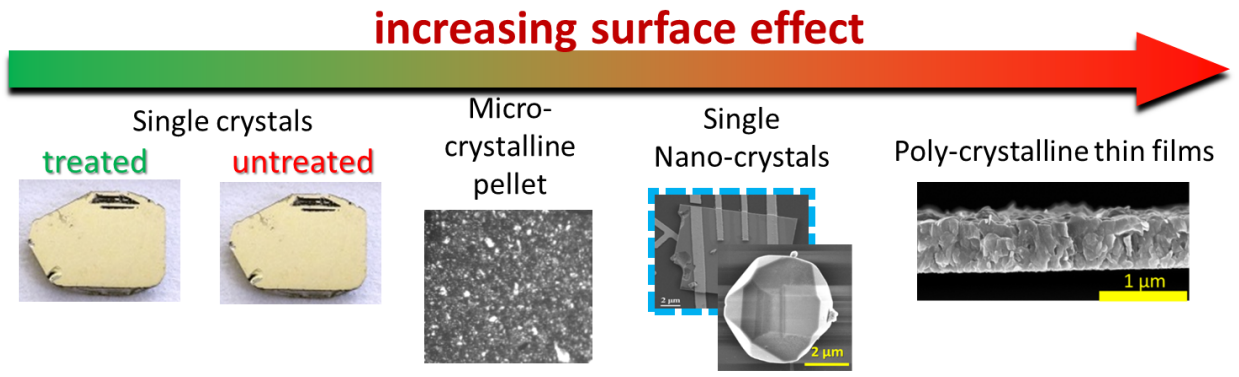

Figure 4.28: Schematic showing qualitatively the magnitude of surface effects for various pyrite materials. Surface effect increase from left to to right: Macroscopic single crystal (passivated and unpassivated), micro-crystalline pellet pressed from powdered single crystal, single nano-crystal, poly-crystalline thin film.

The purity of the flux grown crystals makes them a perfect platform to evaluate surface passivation treatments. As shown in section 4.4.2, at low temperatures (below ∼150 K) all bulk carriers are frozen out to a degree that surface conduction dominates, and both conductivity and Hall coefficient R_H become sensitive to changes in the physical and chemical state of the surface. A given crystal can thus be used to subsequently evaluate many different (non-destructive) treatments. A procedure was established to 'reset' the crystal after each treatment to a well-known and fully reproducible state. To this end the crystal was polished on both sides using 1 μm particle slurries. This reset was verified many times and reduced crystal thickness by only ∼10 μm, such that a typical sectioned crystal (thickness 200 - 1000 μm) can be used test many treatments. The resulting condition is from here on just denoted 'polished'. Figure 4.29 illustrates how the effectiveness of a given surface passivation technique can be evaluated using temperature-dependent Hall effect data, starting from the polished condition. Surface treatments only affect the low temperature region of the data, with better surface passivation showing as lower conductivity and higher $|R_H|$. Analyzing the data shown in fig. 4.29a with the model presented in section 4.4.2 reveals that the piranha treatment reduces surface acceptor states by a factor of up to ∼20. The same methodology is used to evaluate all other surface treatments.

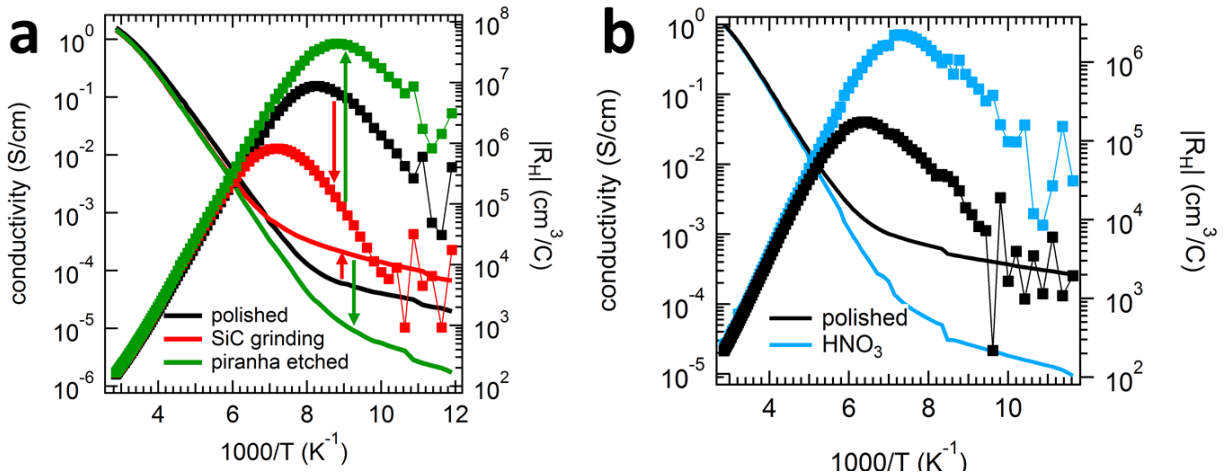

Figure 4.29: Hall Effect (squares, right axis) and conductivity data (solid lines, left axis) of two pyrite single crystals, evaluating effectiveness of surface passivation treatments. All crystals could be 'reset' to a known state after each test using a standardized polishing treatment (see text). (a) This graph illustrates how the effectiveness of a given surface passivation technique can be evaluated using temperature-dependent Hall effect data. As discussed in the text, surface treatments only affect the low temperature region (below ∼200 K), with better surface passivation showing as lower conductivity and higher $|R_H|$ (see discussion in section 4.4.2). Here, damaging a polished crystal by rough grinding with SiC paper results (at low temperatures) in lowered $|R_H|$ and increased conductivity. Etching in piranha solution then results in a larger increase in $|R_H|$ and decrease in conductivity. (b) Effect of etching in nitric acid (HNO_3). After 2 min etching in concentrated nitric acid (blue), the crystal shows lowered conductivity and increased $|R_H|$ at low temperatures, compared to the polished crystal (black).

Etching with piranha solution is commonly used to strip semiconductor wafers and other substrates of organic residues. It is a strong oxidizing agents and leaves most surfaces hydroxylated (OH group terminated). For SEM images showing what piranha does to the surface of pyrite single crystals, see fig. 4.19 and fig. B.6. It was found that piranha etching works well to reduce the impact of surface acceptor states on pyrite single crystals, i.e. surface conduction can be lowered by up to 20 times. The exact mechanism responsible for this remains unclear, but is likely a combination of (1) physical removal of damaged material and crystal imperfections and (2) complete surface oxidation. The first mechanism is evident from SEM images showing clean facets with occasional etch pits after the treatment. This results in a lowered effective surface area. The second mechanism is strongly supported by several observation. Other oxidizing etches like nitric acid, as well as annealing in air and oxygen plasma treatment have a similar, but not quite as strong effect. Also, the effect of piranha etching is air-stable, i.e. the improvement seen in the Hall effect data remains after leaving the crystal 72 h in air. An oxidation of the surface could result in stable, protective layer of amorphous Fe(II)- and Fe(III)-oxides, that prevents the crystal below from further reactions with O_2 and H_2O (see fig. 1.9).

Diluted solutions of piranha and nitric acid were also tested on pyrite thin films (see fig. 5.9). As expected, it was found that dilution by at least a factor of 2 and reduced etch times were necessary to avoid destruction of the films. No significant improvement of in-plane resistivity of the etched films was observed.

In future work, careful XPS studies of the surface should reveal what Fe species are formed upon piranha etch. Preliminary results (fig. 4.30c) taken by Dr. Yu Liu of before an air exposed (labeled "As-made") and piranha etched ("After cleaning") only show clearly that C species are effectively removed. Further, the concentration of sulfate (SO_4^{2-}, 168.5 eV) is reduced. In the Fe 2p region the relative distribution of pyrite Fe(II) and Fe(III)-O remains unchanged.

Due to the violent nature of this etch, a transfer to thin films is difficult. However, under-

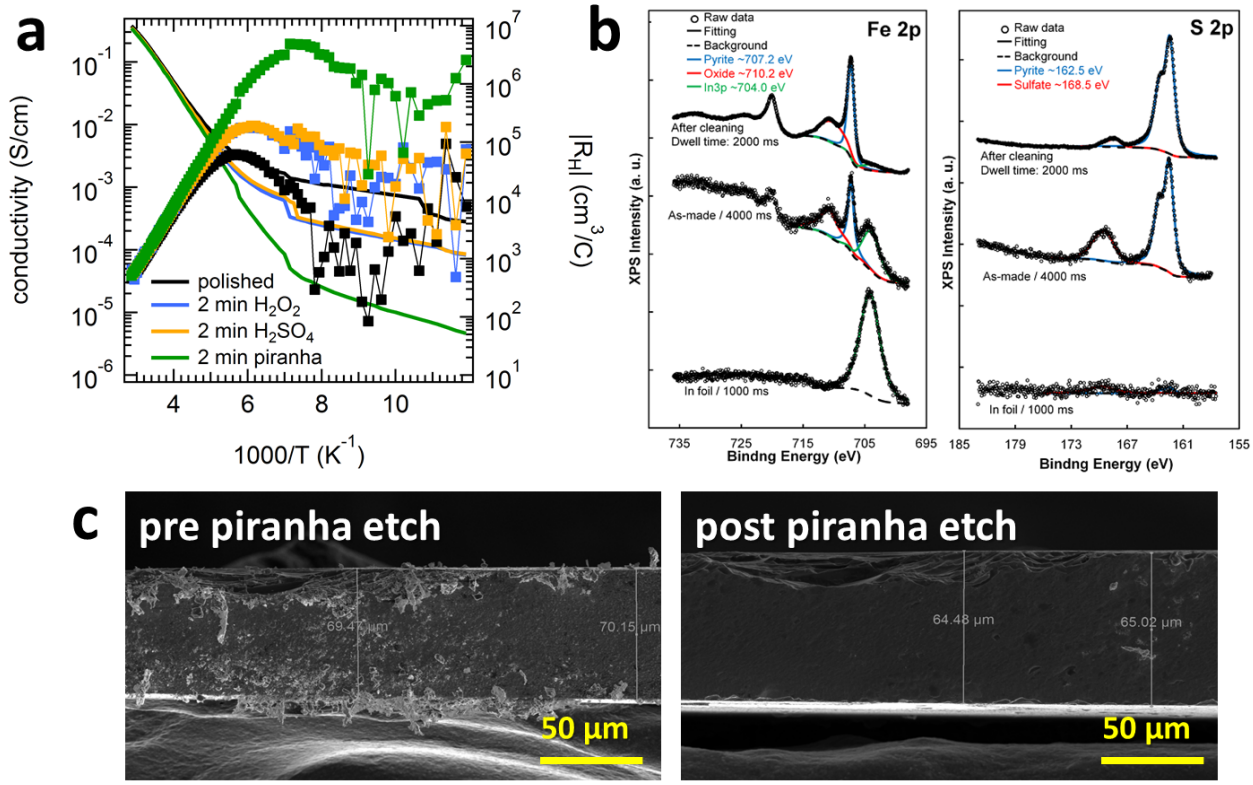

Figure 4.30: Evaluation of etching in piranha solution for surface passivation. Piranha solutions were freshly prepared from one part hydrogen peroxide (H_2O_2, 40%) and three parts sulfuric acid (H_2SO_4, conc.).(a) Deconvolution of the effects of piranha constituents. Etching for 2 min in sulfuric acid (yellow) and hydrogen peroxide (blue) results in slight surface passivation. Etching for the same time in piranha solution (green) results in much better surface passivation, showing that the special chemistry of piranha on the FeS_2 surface is more effective than its components. (b) XPS spectra, taken by Dr. Yu Liu, before ("As-made") and after ("After cleaning") piranha etching. Also shown is the background signal obtained form the In foil mount. As expected, the carbon 1s peak is greatly reduced by after etching, and both Fe and S peaks are much increased due the removal of the carbon over-layer (data not shown). The Fe 2p region shows no qualitative changes, suggesting that the Fe(II)/Fe(III) ratio does not change. The S 2p region shows a relative decrease in the peak at 168.5 eV, which is attributed to sulfate, where sulfur is in the +6 oxidation state. (c) Cross-sectional SEM images of a pyrite crystal before and after a 30 min piranha etch. The etch rate is approximately 1.4 nm/s, assuming a constant activity of the piranha solution over 30 min.

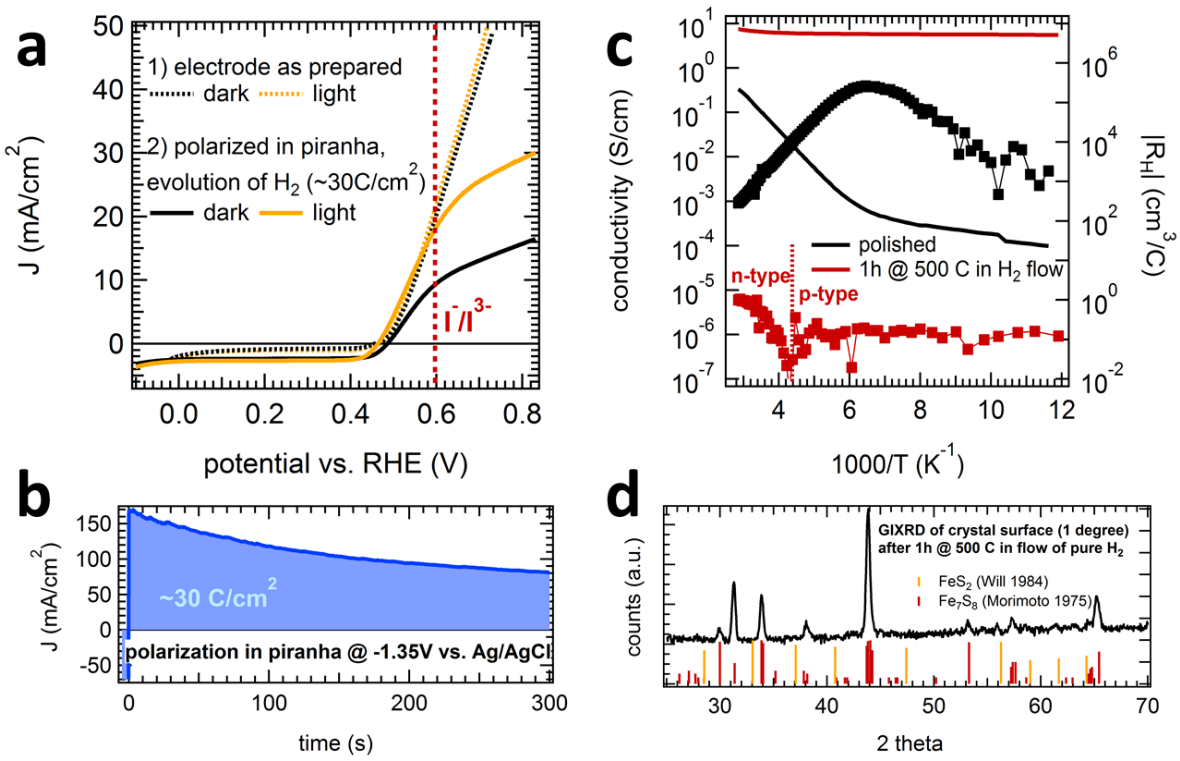

Figure 4.31: Evaluation of hydrogen treatments for surface passivation. (a) Shown here are JV curves of a pyrite single crystal wet junction (see section 5.2) before and after polarization in piranha. Application of a negative bias to the pyrite electrode causes the evolution of atomic hydrogen at the surface, and after passing a charge of about 30 C/cm^2 (b), the dark current in forward direction is reduced, while the photoresponse is greatly enhanced, reaching over 13 mA/cm^2. (c) Hall Effect (squares, right axis) and conductivity data (solid lines, left axis) of a pyrite crystal as polished (black) and after annealing for 1 h at 500 °C in a flow of pure (5N) hydrogen gas. The crystal shows much increased conductivity and lowered $|R_H|$, th sign of the latter indicating p-type transport up to ∼240 K. (d) The XRD patter of the crystal before and after annealing reveals that sulfur loss resulted in formation of a Fe_7S_8 surface layer.

standing the exact mechanism of piranha passivation will be an important step towards a rational development of an even better surface passivation for pyrite.

Another surface passivation treatment that was reported for pyrite before is cathodic etching, also known as proton reduction.[33] By applying a negative bias to a pyrite electrode in a highly acidic solution (for example piranha), highyl reactive atomic hydrogen is generated at the pyrite surface where it can passivate defect states. This treatment was used in [33] to 'activate' pyrite crystals to deliver the highest photocurrents and power conversion efficiencies

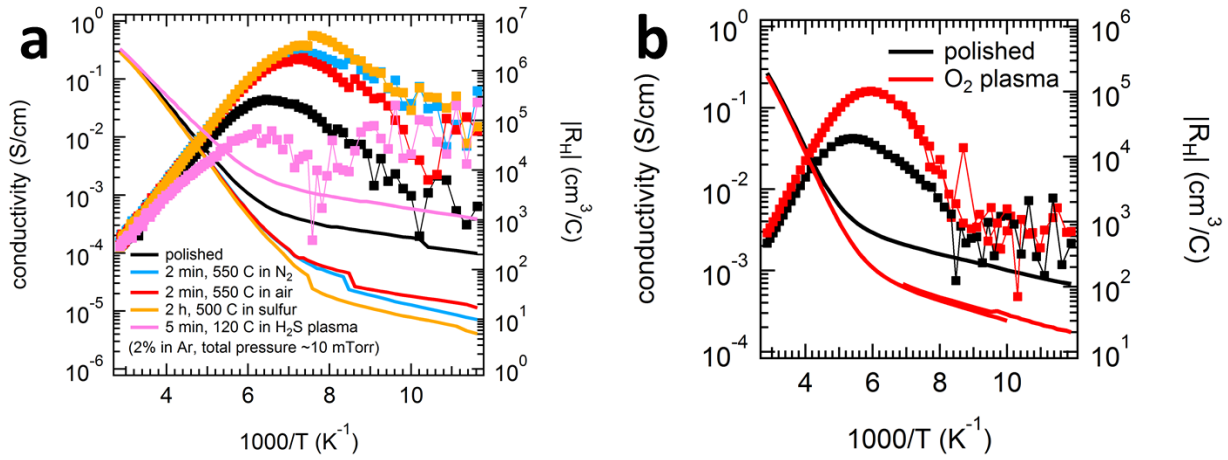

Figure 4.32: Evaluation of annealing and plasma treatments for surface passivation. Hall Effect (squares, right axis) and conductivity data (solid lines, left axis) are shown for two crystals. (a) Crystal 1: Thermal annealing in nitrogen, ambient air and sulfur atmosphere shows moderate surface passivation, with sulfurization being the most effective, comparable to piranha solution. Placing the crystal in diluted H_2S plasma (2% H_2S, 98% Ar) *increases* surface conduction. (b) Crystal 2: Oxidation in an oxygen plasma effectively passivates the surface, though the magnitude of the effect is still less than for piranha etching.

reported for pyrite photocells to date.

Using this procedure 30 C/cm^2 were passed through a pyrite electrode (see section 5.2 for setup), resulting in a high photo-current J_{SC} = 13.7 mA/cm^2 under AM1.5G illumination (fig. 4.31). Unfortunately, due the permanent way the crystal was mounted as an electrode using epoxy, no subsequent Hall effect data was recorded to quantify the effect of this surface passivation treatment. Instead, another crystal was annealed in a flow of pure hydrogen for 1 h at 500 °C. The result was the formation of a metallic Fe_7S_8 surface layer, rendering the whole crystal metallic (fig. 4.31). Future studies should evaluate hydrogen in more detail and also look at the effect of other reducing agents, such as hydrazine or ascorbic acid.

Informed by the results of piranha etch, other means of surface oxidation, without invoking wet chemistry were evaluated. As shown in fig. 4.32, annealing in ambient air (2 min at 550 °C)does indeed have a positive effect in terms of surface passivation, though rather small. Strikingly, a control run using the same annealing conditions in inert nitrogen resulted in a very similar, even slightly better passivation. The experiment was performed in a glovebox

filled with 5N nitrogen, with a sensor reading 0.0 ppm O_2. In an attempt to utilize thermal energy while preventing sulfur loss, ideally terminating all surface Fe sites with S_2, the same crystal was also annealed in sulfur atmosphere (with 50 mg elemental sulfur in an evacuated quartz ampoule) for 2 h at 500 °C. This resulted again in a similar and slightly better surface passivation.

Plasma treatments were also evaluated. Since annealing in H_2 depleted the surface of sulfur, low-temperature annealing was performed in an H_2S plasma. The motivation for this experiment was to supply a source of reactive hydrogen and sulfur simultaneously. However, after 5 min at 120 °C in a 50 W plasma, the crystal showed increased surface conduction, translating to an increased number of surface states compared to the polished baseline case. We note that the plasma composition was (limited by the setup) only 2% H_2S in Ar, and the total pressure was 10 mTorr. Future work should expand parameter space and look at higher partial pressures of H_2S in the plasma. Lastly, oxidation of a crystal in an oxygen (5 min in a 50 W plasma of 20 mTorr pure oxygen) plasma resulted in significant surface passivation, though less than etching in piranha.

The final strategy evaluated in this work was motivated by early success in using ZnS as a junction partner on pyrite thin films (see section 5.3.2). The idea is to overcoat pyrite with an insulator or semiconductor, passivating the surface in-situ the instant that the interface is formed. ZnS is a great candidate for this because the lattice constant of its cubic form is within $< 0.5\%$ of pyrite's ($\sim$5.42 $\mathring{A}$ for FeS_2 and $\sim$5.41 $\mathring{A}$ for ZnS), and they both have S in their lattice. ZnS has also been reported to substitute Fe in the pyrite lattice.[17] The study of JV characteristics across ZnS/FeS_2 junctions for both single crystals and thin films in discussed in chapter 5. Here, the effect on transport parallel to the junction, i.e. (suppression of) pyrite surface conductivity is discussed.

Figure 4.33 shows results of ZnS coating of pyrite single crystals and thin films using atomic layer deposition (ALD). The potential advantage of this deposition method is effective infilling of the polycrystalline films, as every surface accessible to gas is potentially coated.

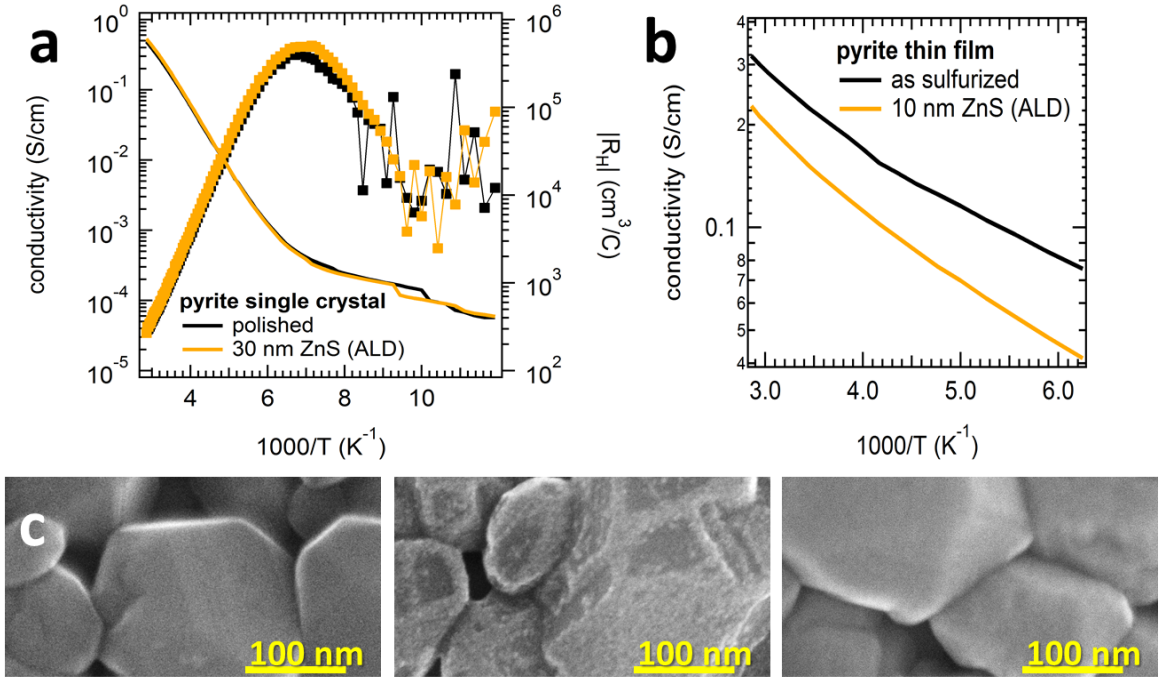

Figure 4.33: Evaluation of ZnS coverage for surface passivation. (a) Hall Effect (squares, right axis) and conductivity data (solid lines, left axis) of a crystal before (black) and after (yellow) deposition of 30 nm ZnS by atomic layer deposition (ALD) on all surfaces. The data are basically identical, no effective surface passivation could be observed. (b) The same experiments with 10 nm ZnS deposited by ALD on a pyrite thin film. The resulting decrease in conductivity is small, further studies are needed. (c) SEM images at 500,000X magnification of thin film grains as sulfurized (left) and after ZnS deposition by ALD (center) and sputtering (right).

However, as shown in fig. 4.33c, this is not necessarily the case, and might be complicated by a facet-specific nucleation efficiency. The coverage of ZnS by ALD might be incomplete, some facets appear to be not covered. An XPS experiment could verify or disprove this. Sputter coating was shown to evenly coat pyrite surfaces accessible by line-of-sight deposition, but did not yield better results than ALD.

In all cases evaluated (single crystals, thin films, ALD, sputtering), no surface passivation was observed in the Hall effect and conductivity data. To reconcile this with the observed rectification if FeS_2/ZnS pn-junctions, we note that ZnS deposition proved to be difficult to control (see section 2.2.1, section 5.3.2). Further, even rectifying FeS_2/ZnS pn-junctions were not necessarily based on passivated pyrite surfaces, as a truly passivated pyrite film would supposedly be n-type. ZnO and Al_2O_3 layers were also deposited by ALD and evaluated in the same way, without any effect (not shown). Future work should start with more careful studies of thin ZnS films, deposited by ALD on pyrite, and guided by XPS experiments.

In conclusion, it was demonstrated that pyrite single crystals of ultrahigh purity can be used as a convenient platform to evaluate surface passivation treatments. Temperature-dependent Hall effect and conductivity measurements, in conjunction with the multilayer transport model discussed above, are suitable to quantitatively analyze the effectiveness of a given treatment in removing surface acceptor states. Chemical etching, plasma etching, thermal annealing in different inert and reactive atmospheres and overcoating with sulfides and oxides were tested. It was found that thermal annealing is beneficial, as long as loss of sulfur is prevented by either limiting annealing time or annealing in sulfur atmosphere. Oxidation of the surface in oxygen plasma and by oxidizing etches also passivates the surface. Quantitatively, the best result (reduction of surface acceptor by up to 20 times) was observed for etching in piranha solution, followed by nitric acid and annealing in sulfur atmosphere.

In the future, the mechanism of piranha etching should be investigated in detail by carefully conducted XPS studies. Also, reducing agents such as hydrazine should be tested, and treatment H_2S (either as plasma treatment or thermal annealing) should be revisited. Further,

studies of molecular adsorbents that can coordinate surface Fe should be conducted. Initial molecules might include thiophene, pyridine and thiocyanate.[83] Lastly, it should be tested if field effect gating can tune and eventually shut off the surface inversion layer. Electrolyte gating of pyrite nanocrystals has recently been reported by Liang et al.[68] and a similar experiment could be adapted to macroscopic single crystals.

4.7 Summary

It was hypothesized in section 3.1 that pyrite thin films are electrically dominated by a conductive surface layer. By comparison with CVT grown and natural single crystals, pellets made from the latter and single nanocrystals, this hypothesis was confirmed. By increasing the surface to bulk ratio of a given pyrite material, surface conduction becomes more dominant.

Transport in pyrite thin films is dominated by p-type surface conduction at all temperatures, and can be described by the Werner model. Pellets and single nanocrystals are interesting intermediate (or 'mesoscopic') systems in between thin films and macroscopic single crystals. Pellets have lower overall conduction than single nanocrystals and thin films, possibly due to poor electronic coupling of grains, and both show a region of higher activation energy above room temperature, suggesting a transition to an n-type regime. This n-type regime is observed for all CVT grown single crystals at room temperature and down to about 110 - 140 K, where the activation energy decreases to the $\sim$ 30 meV value of thin films and pellets, and transport becomes hole-dominated.

To further understand and quantify this phenomenon, more crystals of larger size and even higher quality were needed. They were supplied from a flux growth synthesis. High-quality, ultra-pure iron pyrite single crystals have been grown in a sodium polysulfide flux. Hall effect measurements of these crystals show an unusual minimum and sign change of the Hall

coefficient at ∼120 K and ∼80 K, respectively. Numerical fitting of the Hall data using a multi-layer transport model that includes a self-consistent Fermi level reveals the existence of a hole-rich inversion layer at the surface of the n-type crystals. This inversion layer is a channel for the surface conduction of holes in pyrite. Electrons in the crystal bulk are frozen out at low temperatures to the extent that the holes in the inversion layer dominate conduction. The presence of the hole inversion layer is corroborated by UPS measurements showing E_F - $E_V \approx 0.1$ eV, as well as Hall effect experiments as a function of crystal thickness and physiochemical modification of the crystal surface. The inversion layer can explain both the low photo-voltage of pyrite photocells (caused by tunneling across part of the inversion layer) and the common high p-type conductivity of polycrystalline pyrite thin films (caused by the dominance of surface conduction in these high surface-to-volume ratio samples). Our data can also be understood in terms of a surface layer with a reduced band gap, with the V_{OC} in this case limited by weak band bending rather than tunneling. Hopping is ruled out as a relevant transport mechanism in pyrite single crystals to due inconsistency of the temperature-dependent magnetoresistance MR(T) data with theory. Two findings of this section were published in [70], a high concentration of deep donors and a surface-state induced inversion layer. Together they can explain the low V_{OC} in pyrite solar cells, and both were independently confirmed recently.[68,19]

We also used our single crystals to assess whether the bulk band gap of pyrite is significantly smaller than the widely accepted value of ∼0.95 eV at room temperature. Our optical measurements yield a band gap of 0.94 eV, in agreement with literature (as expected), while modeling of the intrinsic electrical conductivity using two different DOS functions results in a somewhat lower best-fit value of 0.80 ± 0.05 eV. Given the assumptions involved in calculating the pyrite band gap from conductivity data, we conclude only that the electronic gap of high-quality pyrite is probably ∼0.80 eV, which is large enough to support a photovoltage of ∼500 mV from pyrite photocells under normal sunlight. In our view, all of the experimental evidence available supports the hypothesis that the low V_{OC} of pyrite is caused

by a surface layer, not a small bulk band gap.

This study confirms that pyrite suffers from a strong inversion layer that likely limits the useful built-in voltage of pyrite junctions to ∼200 mV, but the next question is whether this conductive surface layer can be fixed. Fixing pyrite will depend on passivating the surface states that cause the surface layer and lowering the concentration of near-surface donors (probably sulfur vacancies) that promote tunneling across it. Etching polished crystals in piranha reduces the effective surface acceptor density by a factor of up to 20, but this kind of aggressive etch is not transferable to thin films. Using single crystals together with our new transport model as a test platform to controllably and quantitatively evaluate surface passivation treatments, a number of annealing, etching, plasma and coating techniques were evaluated. While none surpassed piranha in terms of reduction of surface conductivity, annealing in sulfur atmosphere and surface oxidation came close. A tool-set for further passivation research, along with suggested treatments to evaluate, is given as a clear path forward to make pyrite into an efficient solar absorber material.

Chapter 5

Pyrite Solar Cells

5.1 Design Considerations

The highest performance pyrite solar cells reported in the past were either pyrite/liquid[35,2,19] or pyrite/metal[16] junctions. Liquid junctions have unique properties such as an electrical double layer and have to be understood and modeled different than solid-state junctions. However, both pyrite/metal and pyrite/liquid junctions can qualitatively be thought of as Schottky junctions, with either a metal or a liquid electrolyte with very high density of mobile charge carriers forming a junction to pyrite. Schottky junctions in turn can be thought of as an extreme case of pn-heterojunctions, where one side (the metal/liquid) is so heavily doped that the space-charge region forms exclusively in the other junction material, in this case pyrite.[103] On the other hand, pn-heterojunctions of pyrite have not been studied before. The challenge here is to find a junction partner with high transparency and suitable doping that creates a space-charge region in the pyrite absorber.

Though not a focus of this work, solar cells from pyrite single crystals were briefly studied in liquid junctions, Schottky junctions and pn-heterojunctions. However, due to pyrite's

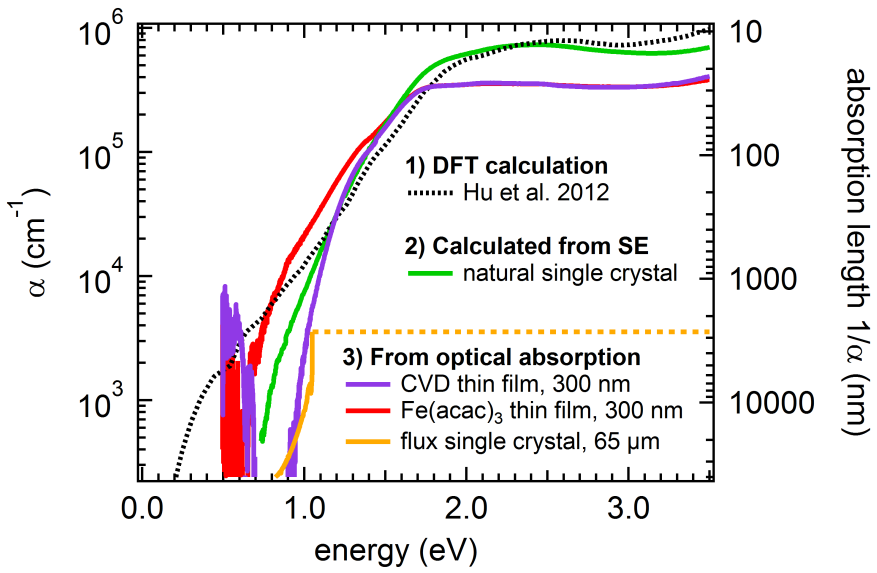

Figure 5.1: Optical absorptivity α(E) of various pyrite materials. DFT calculated values are taken from [53]. The values for the natural crystal are calculated from spectral ellipsometry data (see section 4.1 and [22]). The optical absorption data was collected using an integrating sphere from pyrite thin films (300 nm thin) and a flux grown crystal thinned down to 65 μm. The data for the flux grown crystal is limited by its thickness and the detector sensitivity to $\alpha \leq 3500$ cm^{-1}.

exceptionally strong absorption coefficient that allows for absorber layers as thin as 100 nm (fig. 5.1), the focus was set on solar cells from pyrite thin films, especially solid-state pn-heterojunctions (section 5.3.2).

5.2 Wet Junction Solar Cells

The record efficiency for any pyrite solar cell to date (2.8% PCE under non-standard spectrum[35]) was reported for a wet junction of a single crystal with an electrolyte containing the I^-/I_3^- redox couple. This cell showed very high quantum efficiency and photocurrent densities over 40 mA/cm^2, which has recently been reproduced by a different group.[19]
Here we used polished, flux-grown pyrite single crystals that were etched in piranha, then mounted on a conductive wire and covered in epoxy, with only one facet left free. Electrodes from pyrite thin films were prepared in the same manner, except they were not piranha

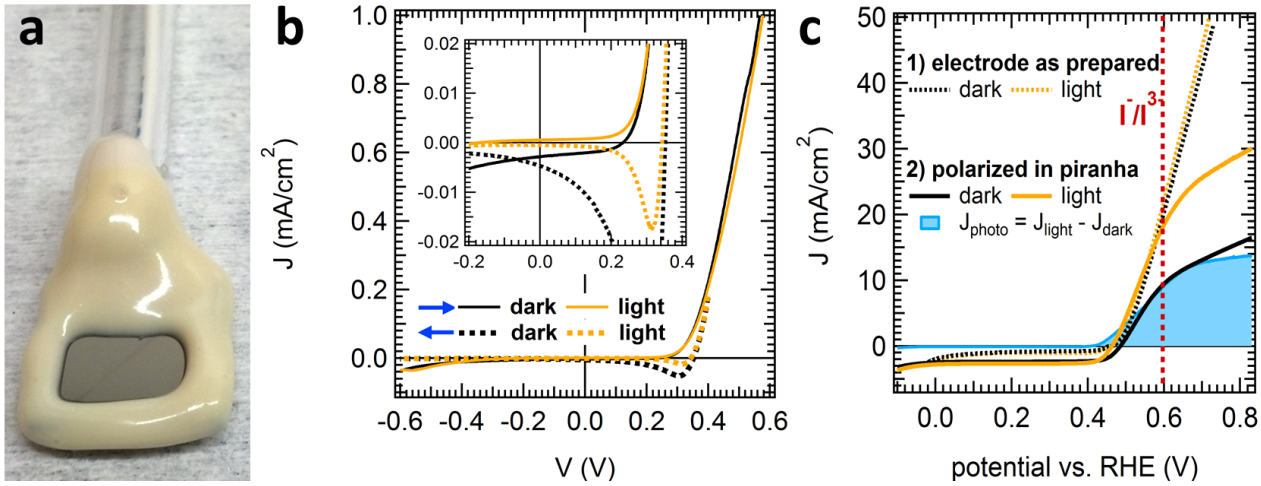

Figure 5.2: Liquid junction solar cells with pyrite absorbers. (a) Picture of a thin film electrode made by protecting the Mo back contact with epoxy, exposing only the pyrite film to the electrolyte solution. (b) JV curves for the thin film electrode, recorded in the dark (black) and under AM1.5G illumination (yellow). (c) Recorded JV curves for a pyrite single crystal electrode, shown (1) before and (2) after polarization in piranha solution. The calculated photo-current density J_{photo} (blue) after polarization is also shown.

etched (see fig. 5.2). The such prepared working electrode was then placed in a three-neck electrochemical cell along with a platinum counter electrode and a Ag/AgCl reference electrode in a typical three-cell configuration.[33] The electrochemical cell was connected to a Potentiometer and measured in the dark and under illumination with AM1.5G light from a solar simulator through a quartz window. Figure 5.2 shows the recorded JV curves in the dark and under AM1.5G (1 sun) illumination for (b) a pyrite thin film and (c) a single crystal.

For the single crystal, a freshly prepared aqueous electrolyte with 0.7 M HI, 0.15 M CaI_2, 0.03 M I_2 (pH = 0.35) was used. The as-prepared electrode shows a large dark current and little photo-response. Then the electrolyte was replaced with piranha solution, and the pyrite electrode was biased at -1.13 V for 5 min. A charge of approximately 30 C/cm^2 was passed this way through the surface of the pyrite crystal, and evolution of hydrogen bubbles was observed. After this etching procedure, the piranha solution was replaced with the electrolyte again and JV curves were recorded. The dark current was now reduced significantly, and a

photo-current density of > 13 mA/cm^2 was measured.

For the pyrite thin film, the ferracene/ferracenium redox couple with TBAP/PF_6 was used in acetonitrile as the electrolyte. Figure 5.2a shows a picture of the electrode covered in epoxy. Only a small photo-current of about 5 μA/cm^2 could be observed. Interestingly, the JV curves show diode behavior of the same polarity as the single crystal junction, indicating that (in this electrolyte) the pyrite film acts as an n-type semiconductor. No further studies were performed on this system, instead work focused on solid-state solar states made from pyrite thin films (see below).

5.3 Solid-State Junctions

5.3.1 Single Crystals

Pyrite single crystals grown by the flux method were used to fabricate solid-state Schottky-junctions and pn-junctions, see fig. 5.3. Schottky junctions with both Au and W metals resulted in linear IV curves (no rectification), however the junction with a W needle showed some photo-response, with up to $\sim$100 meV photo-voltage at 120 K. Sputtered p-type NiO (see section 3.3) did also not result in a rectifying diode. ZnS is an n-type wide-gap semiconductor, and was tested because of its success in pyrite thin film solar cells (see below). As shown in fig. 5.3c, the first test, using ZnS sputtered with 2% H_2S in the plasma resulted in linear IV response. Note the drastic increase in current for crystal #4 when depositing the ZnS/ZnO junction on a polished and etched surface (dotted red line), as compared to the polished surface (solid red line). In a second test (crystal #5), ZnS was sputtered with 0.3% H_2S in the plasma on the polished (not etched) crystal. This junction showed rectification, but still no photo-response. No further studies were performed on this system, instead the rest of this section focuses on solid-state solar states made from pyrite thin films.

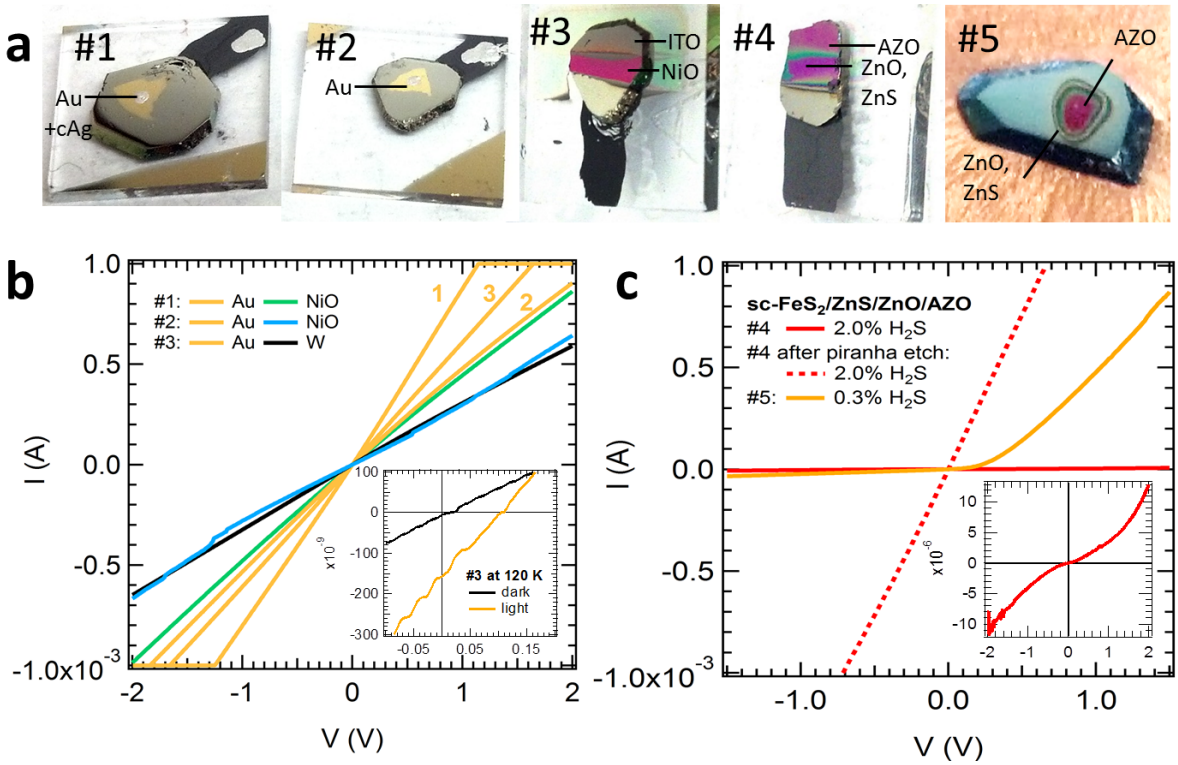

Figure 5.3: Solid-state junctions with pyrite single crystals. (a) Images of the five crystals used for this study. All five crystals were grown by the flux method and their surface prepared by polishing. #1: Au contact evaporated through shadow mask plus small dot of colloidal Ag. #2: Like #1, but without the Ag contact. #3: Successive deposition by sputtering through shadow mask of p-type NiO followed by ITO. #4 and #5: Successive deposition by sputtering through shadow mask of ZnS and ZnO, followed by Al:ZnO (AZO). (b) Current-voltage (IV) curves at 300 K in the dark for crystals 1-3, including Schottky junctions (FeS_2/Au, FeS_2/W) and pn-junctions (FeS_2/NiO). The inset shows the photo-response of crystal #3 contacted with a W needle at 120 K. Note that the active area of the contact made by the needle is tiny ($< 10^{-4}$ cm^2), thus the small value of I_{SC}. (c) IV curves at 300 K in the dark for crystals 4 & 5. The FeS_2/ZnS junction depends strongly on both FeS_2 surface preparation (#4) and ZnS deposition conditions (#4 vs. #5).

5.3.2 Thin Film Heterojunction Solar Cells

This section describes the work to develop all solid-state solar cells with pyrite thin films absorbers, as originally proposed by Prof. Matt Law (see fig. 5.4a). The study relied heavily on pyrite thin films grown by chemical vapor deposition (CVD, see section 2.1.3) by Nima Farhi and by the ink method (section 2.1.4) by Dr. Amanda Weber.

As discussed in section 3.1, pyrite thin films universally, and independent of deposition method, show high levels of p-type doping. Thus, the initial strategy was to deposit an n-type semiconductor (for example ZnS) on pyrite to form a pn-heterojunction. ZnS was the natural candidate for this n-type material, as it is (like pyrite) earth-abundant and non-toxic, and had already been used successfully in $Cu(In,Ga)(S,Se)_2$ solar cells.[80] Moreover, FeS_2 and ZnS have the same lattice constant within $< 0.5\%$ ($\sim$5.42 $\mathring{A}$ for FeS_2 and $\sim$5.41 $\mathring{A}$ for cubic ZnS) and they both have S in their lattice. ZnS has also been reported to substitute Fe in the pyrite lattice.[17]

However, according to the analysis presented in chapter 4, the universal p-type behavior of pyrite thin films is likely due to a surface inversion layer induced by a high concentration of surface acceptor states. While the bulk of elementally pure pyrite single crystals is clearly n-type, the electrical nature of the grain interior in these thin films remains unknown for now. But elemental purity here, too, is high enough to assume n-type material at a sufficient distance from the surface. Therefore surface passivated pyrite thin films, which are likely needed to lower carrier concentration to levels that can support a depletion region necessary for efficient charge separation, might also be n-type. In light of this, several junction partners for pyrite were tested, including a p-type, transparent NiO. However, only ZnS resulted in rectifying diodes, which is why the bulk of this section is focused on FeS_2/ZnS junctions in a full device stack of glass/Mo/MoS_2/FeS_2/ZnS/ZnO/AZO. A band calculation for this stack, including different scenarios for surface inversion and majority carrier type in the pyrite grain interior is shown in fig. 5.4b.

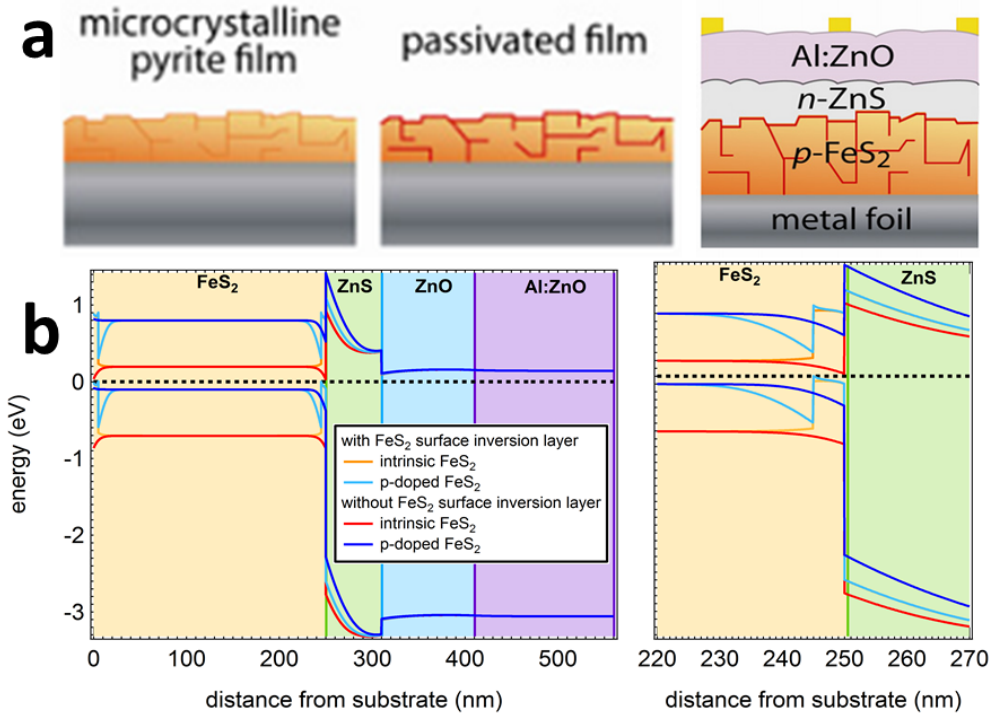

Figure 5.4: Design considerations for pyrite heterojunction solar cells. (a) Taken from original research proposal of Prof. Matt Law, this diagram shows (left) a polycrystalline, p-type pyrite thin film (p-FeS_2) on metal substrate. After surface passivation (center), window layer (n-ZnS) and top contact (Al:ZnO) are deposited on the pyrite film to complete the solar cell. (b) Calculated band structure of heterojunction solar cell, using 1DPoisson. Informed by the results of the single crystal study presented in chapter 4, these calculations taken into account the possibility that pyrite thin films are either intrinsically n-type or p-type doped. The right panel shows the same calculations, zoomed in at the FeS_2/ZnS interface.

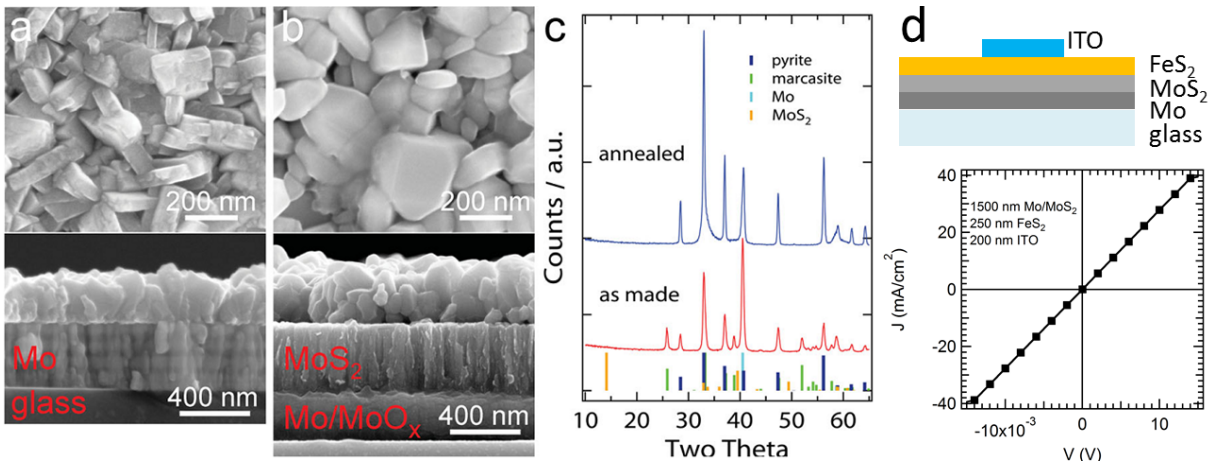

Figure 5.5: FeS_2 thin films on Mo-coated glass substrates. Plane view and crosss-ectional SEM images of a) before and b) after sulfurization. c) XRD pattern of the films, along with pyrite, marcasite, molybdenum, and MoS_2 reference patterns. Figures reproduced from [6]. (d) Diagram showing layer configuration for test device to confirm ohmic back contact and IV curve showing that the MoS_2/Mo back contact is indeed ohmic to pyrite and highly conductive (as is ITO).

Figure 5.5 shows the starting point for a typical device described in this section. A mixed-phase (pyrite/marcasite) thin film on Mo back contact is sulfurized (typically 4 h at 500 °C in a quartz ampule containing 50 mg elemental sulfur, see section 2.1.3), resulting in a pure-phase pyrite film on top of a bilayer of MoS_2/Mo (see section 3.2 for details on the bilayer formation). This MoS_2/Mo back contact is ohmic to pyrite, highly conductive and passes the 'scotch-tape test' (i.e., has sufficient adhesion to the glass substrate).

The such prepared pyrite films on MoS_2/Mo back contacts were then transferred into a vacuum chamber for sputter deposition of the window layers. This could be done without exposing the films to ambient air, by breaking the quartz ampule used for sulfurization inside a nitrogen-filled glovebox, and then transferring the films to a sputter deposition tool attached to the glovebox. See section 2.2.1 for a description of the sputter tool and typical deposition parameters used. Figure 5.6 shows SEM cross-sectional views of a completed device stack (glass/Mo/MoS_2/FeS_2/ZnS/ZnO/AZO) along with top-down views after sub-sequential deposition of the ZnS and ZnO window layers and the AZO top contact.

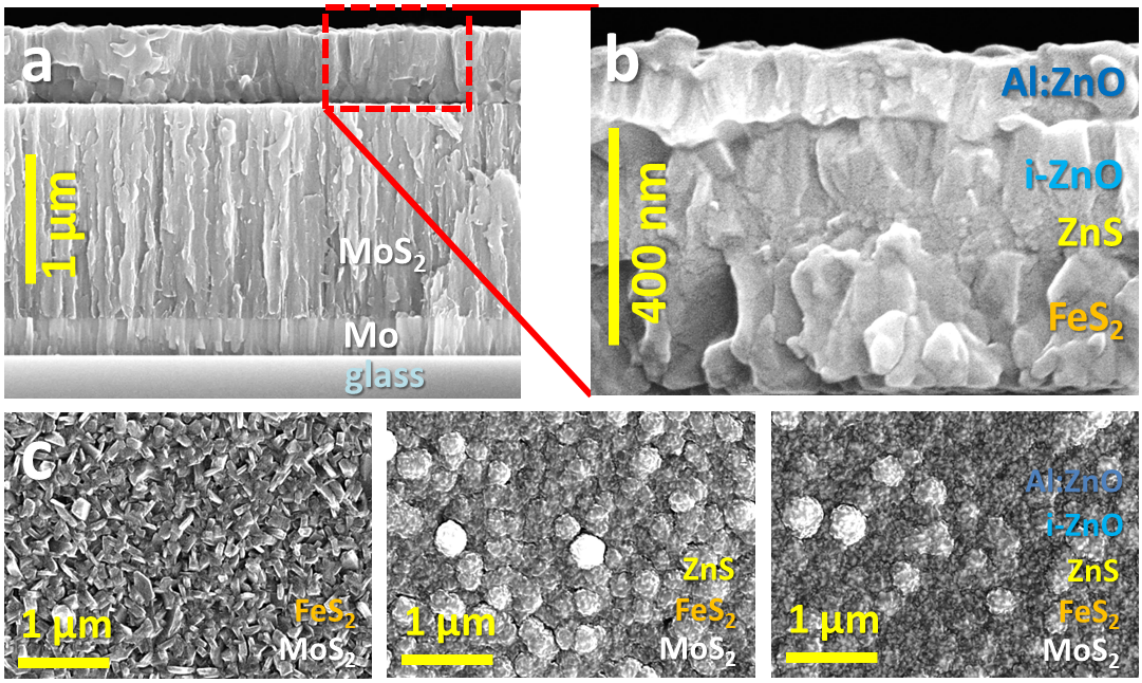

Figure 5.6: SEM images of pn-heterojunction device stack. (a) Cross-sectional view of entire device stack: AZO/ZnO/ZnS/FeS_2/MoS_2/Mo/glass. (b) Zoomed-in view showing active FeS_2/Zns pn-junction and window layer consisting of intrinsic ZnO and Al-doped ZnO (AZO). (c) Top down view of FeS_2 on MoS_2/Mo/glass as sulfurized (left), after ZnS deposition (center) and finished stack (right)

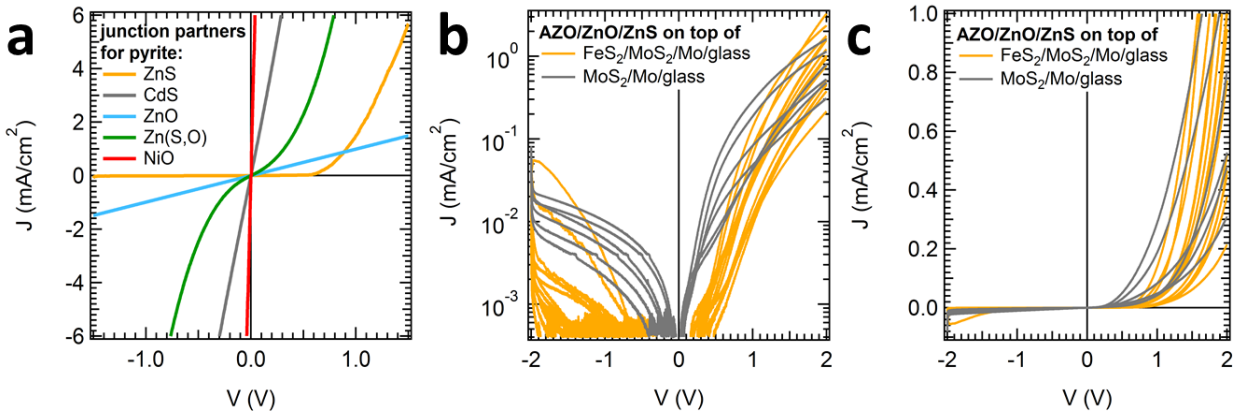

Figure 5.7: Evaluation of different combination of top and bottom device stack. (a) Dark JV curves for a number of n-type (ZnS, ZnO, Zn(O,S), CdS) and p-type (NiO) materials deposited on the bottom stack of $FeS_2/MoS_2/Mo/glass$. Only ZnS results in a rectifying pn-junction, while Zn(O,S) results in a bidirectional barrier, ZnO in a resistive ohmic contacts, and CdS and NiO in a conductive ohmic contact. (b) Dark JV curves comparing the top stack (AZO/ZnO/ZnS) deposited on either $FeS_2/MoS_2/Mo/glass$ (yellow) or $MoS_2/Mo/glass$ (grey) for a number of devices made in the same sputtering batch. (c) Same data shown on a log scale.

As shown in fig. 5.7a, among the junction partners for pyrite thin films investigated in this work (ZnS, ZnO, Zn(O,S), CdS, NiO), the only material that yielded rectifying diodes was ZnS. As control junctions of AZO/ZnO/ZnS/ZnO/AZO were either too resistive to measure any current or ohmic (see fig. 5.8), the rectifying junction was identified as FeS_2/ZnS. To rule out that possible pinholes or other shunts in the pyrite films facilitate bypassing of the pyrite film, enabling an effective MoS_2/ZnS junction, stacks of $Mo/MoS_2/FeS_2/ZnS/ZnO/AZO$ were compared to stacks of $Mo/MoS_2/ZnS/ZnO/AZO$. As shown in fig. 5.7b,c, the stacks without FeS_2 were also rectifying to a lesser extent, opened up at smaller forward bias ($\sim$0.1 V compared to 0.5 - 0.7 V) and showed no photo-response, compared to small to moderate photo-response for the stacks with pyrite absorbers (see below).

Despite initial success with ZnS layers and 'champion' devices with record performance for solid-state, thin film pyrite solar cells (see below), reactive sputtering of ZnS layers and control of the film stoichiometry turned out to be challenging. ZnS films were deposited onto pyrite thin films by RF magnetron sputtering from a ZnS target, with a H_2S content of

0 - 5% in Ar gas. It was found that 1) nominally identical, new ZnS targets (same vendor) give different results and that 2) a single target gives different results over its lifetime, likely due to changes in the surface composition (see fig. 5.8e).

Figure 5.8a shows the partial pressure of gas species (mass/charge ratios 31 - 40) in a plasma containing 0, 2 and 4% H_2S in Ar at a total pressure of 10 mTorr, as measured by a residual gas analyzer (RGA). A clear increase in H_2S-relates species (HS^+, H_2S^+) is seen upon introduction of H_2S gas. We note that the RGA detector was connected to the plasma containing chamber by a short steel pipe, thus due to mass-dependent capture of species on the steel walls the absolute and relative partial pressure values might be inaccurate. XRD patterns of ZnS films (fig. 5.8b) show little dependence on H_2S concentration, though the film deposited without any H_2S appears the most crystalline. A clear identification of ZnS phase (cubic vs. wurtzite) was not possible due to similarity of ZnS reference patterns.

As mentioned, variation in solar cell results suggested a strong dependence of ZnS film properties on H_2S concentration and ZnS target surface stoichiometry. This was confirmed by test stacks of Mo/AZO/ZnO/ZnS/ZnO/AZO/Mo containing ZnS layers deposited back-to-back using different H_2S concentrations. As shown in fig. 5.8c the through-plane resistivity of the ZnS film is orders of magnitude higher when even small amounts of H_2S are present in the plasma, in this case the measured current is in the noise floor of the setup used. No change of appearance or morphology in SEM images (fig. 5.8d) for different H_2S content was observed. See section 2.2.1 for a detailed description of the method used to sputter ZnS, and a discussion of the challenges associated with it.

While these challenges made methodical and comparative studies of FeS_2 hard, it is clear that ZnS is a very promising junction partner for pyrite and has the potential for efficient heterojunction solar cells. In future work, feedback-control for the H_2S gas (see section 2.2.1) should be implemented to achieve better control of the ZnS target and reproducibility of the ZnS film stoichiometry. Alternatively, chemical bath deposition (CBD) or atomic layer deposition (ALD) of ZnS films should be explored.

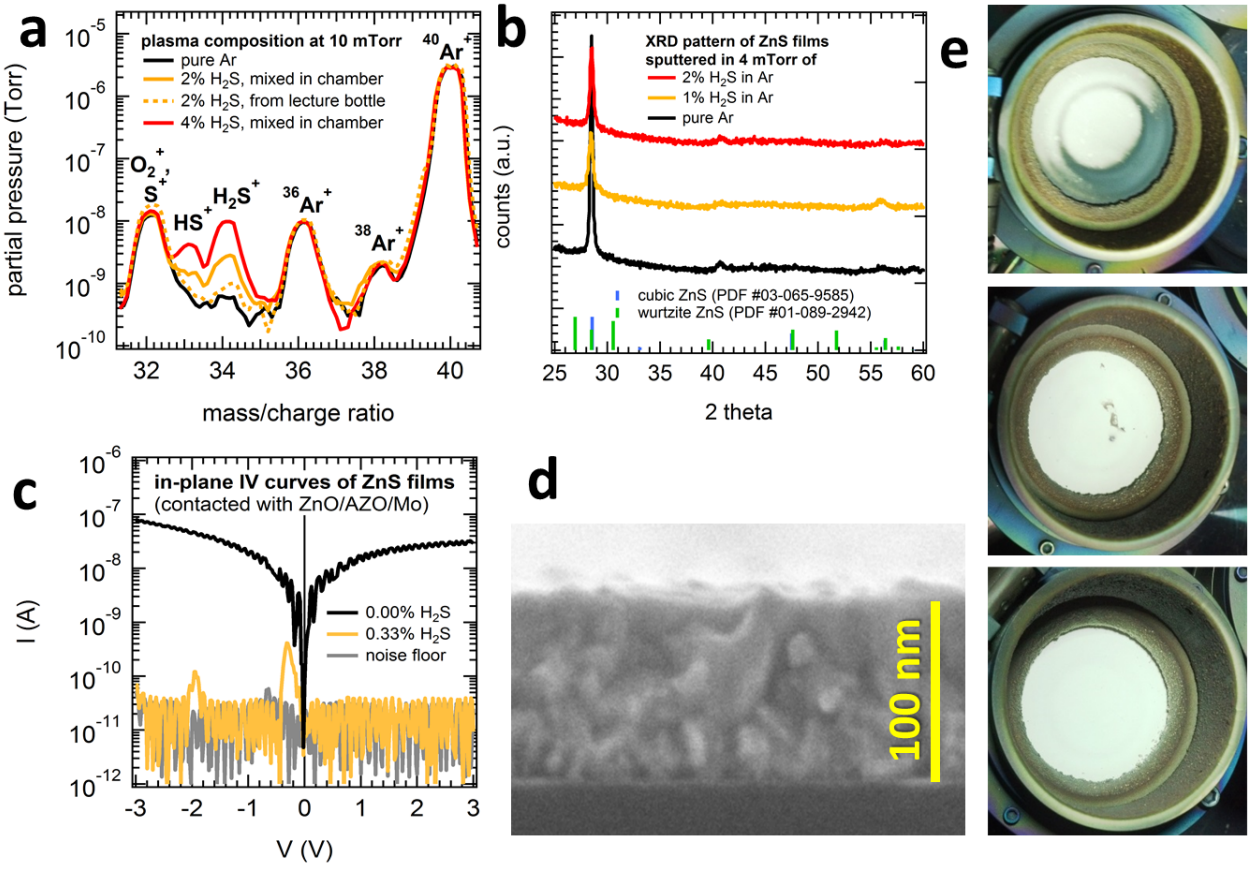

Figure 5.8: Control of H_2S content in the sputter plasma and its effect on ZnS target and films. (a) Plasma composition during typical ZnS sputtering conditions, at a total pressure of 10 mTorr, measured with residual gas analyzer (RGA). (b) XRD patterns of the resulting ZnS films on Si substrates, as a function of H_2 content in the plasma. (c) In-plane IV curves of ZnS films deposited with 0.00% and 0.33% H_2S in the plasma, deposited back to back. (d) SEM cross-sectional view of a representative ZnS film deposited on Si substrate (using 1% H_2S content in Ar plasma). A change of appearance or morphology in SEM images for different H_2 content was not observed. (e) Photographs showing the changes in surface composition of a ZnS target. In the top image the target surface is depleted of sulfur after sputtering in pure Ar gas, showing spots of metallic Zn. After sputtering in plasma containing 2% H_2S the target surface is partially recovered (center) and eventually fully recovered (bottom).

Many attempts were made to improve the diode characteristics of pyrite pn-heterojunctions. Looking at dark current voltage (JV) curves, a low reverse current is a requisite for high photo-voltage V_{OC}, while a high forward current is necessary to support high photo-current densities J_{SC}.[103] Two examples of these attempts are shown in fig. 5.9.

Sodium plays an important role in the grain growth of pyrite thin films, but also in the conversion process from marcasite to pyrite.[6,116] It should be noted that Na is *not* incorporated in the pyrite lattice, but acts at the grain boundaries, and washes off easily with water.[6,70] Without presence of Na (or another suitable alkali metal[116]) the conversion to rigorously phase-pure pyrite film requires very harsh sulfurization conditions (T > 500 ° and/or t > 4 h) that cause problems with the Mo/MoS_2 back contact. It is therefore beneficial to have small concentrations of Na present during the sulfurization step. As Na can easily diffuse through the Mo/MoS_2 back contact,[122,6,123] using soda-lime glass as the substrate is a sufficient source of Na. However, this source has the disadvantage that the amount of Na leaching out of the glass (and made available in the pyrite film) depends on the exact type of soda-lime glass used, cleaning procedure for the glass and sulfurization temperature, and is overall hard to control quantitatively. In fact we found that soda-lime glass supplies *too much* Na, resulting in excessive grain growth and increased surface roughness (fig. 5.9b). Several better methods to controllably and quantitatively introduce Na were developed in our lab, including addition of a Na containing MeOH solution to the sulfurization ampule and direct incorporation of Na into the pyrite ink.[116] Both methods yield phase-pure pyrite using Na-free borosilicate glass substrates, with better properties than using soda-lime glass. Surface roughness is lower (fig. 5.9c), dark current is lower and diode characteristics are improved (fig. 5.9a).

Another strategy to improve the pn-heterojunctions was to etch pyrite thin films prior to ZnS deposition, motivated by the observed partial passivation of surface defect states in single crystals (chapter 4). Both piranha solution (1 part H_2O_2, 3 parts H_2SO_4) and nitric acid (HNO_3) were tested. Compared to the concentrated etches used for single crystals,

both etches had to be diluted by a factor of 2 - 4 (piranha) or 5 - 10 (nitric acid) to prevent destruction of the thin films. Treatment with nitric acid showed no effect for low concentrations, and increased overall device conductivity, likely caused by thinned and partially shunted pyrite films, for higher concentrations. Treatment with piranha showed improvement of rectification in some batches, with the best results observed for a brief 1 s dip into 50% piranha solution, followed by rinse in water and blow-drying, immediately prior to ZnS deposition. However, the improvement was small and not well-reproducible. Figure 5.9a shows JV curves in the dark of cells from the same batch, with and without piranha etching, where the piranha etching yielded increased forward dark current while maintaining low reverse current. The photo-response of these diodes was however not improved significantly (not shown). The in-plane conductivity of films changed little upon etching, other than the expected reduction in absolute conductivity due to decrease in film thickness (see fig. 5.9e, constant thickness was assumed to calculate these conductivity values). Figure 5.9f shows a SEM cross-sectional view of a pyrite film after etching in piranha. The film thickness is reduced to ∼140 nm and pyrite grain facets appear very sharp and clear. See fig. 4.30 for an estimation of the etch rate for pyrite single crystals in concentrated piranha.

As mentioned above, strong diode rectification (i.e., low reverse current and high forward current) is a requisite for high performance solar cells (high photo-voltage V_{OC}, high photocurrent densities J_{SC}).[103] Using the recipe described in section 2.8.2, highly rectifying heterojunction cells based on CVD pyrite absorbers were achieved, along with small to moderate photo-response. These rectifying diodes were reproducibly fabricated over several weeks to months at a time, until the same procedure ceased to yield rectification and photo-response. This phenomenon was later attributed to likely changes in the ZnS stoichiometry. Rectifying behavior and photo-response was later re-established for some weeks to months, until the same problem occurred again. This reproducibility issue, superimposed by issues with punch-through effects and a change in device layout (see below), made methodical and comparative studies difficult. Nonetheless, well-behaved and rectifying diodes with small to

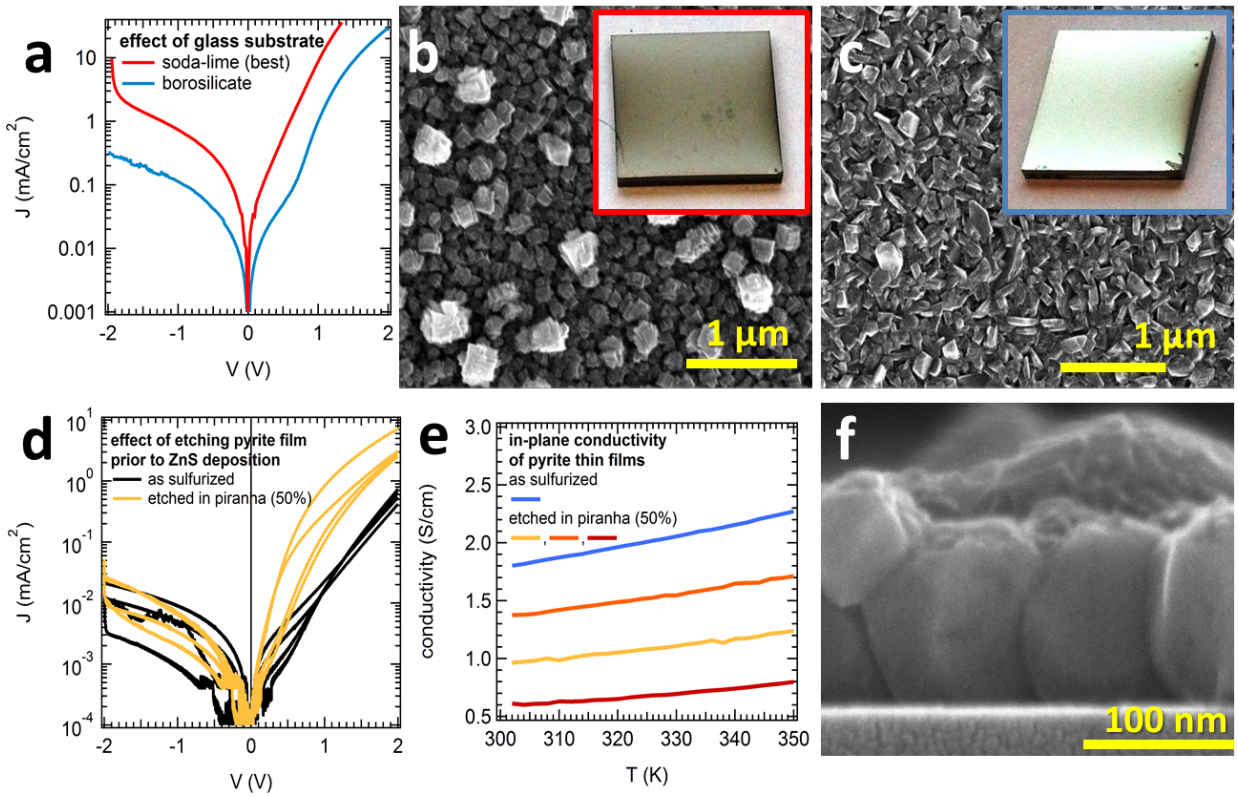

Figure 5.9: Attempts to improve rectification characteristics of pyrite thin film diodes by improving surface roughness (top row) and surface passivation (bottom row). (a) JV curves (log scale) of AZO/ZnO/ZnS/FeS_2/MoS_2/Mo devices fabricated on sodalime glass (red) vs. borosilicate glass (blue). SEM top-down images of pyrite films fabricated on (b) sodalime and (c) borosilicate glass. Insets show photographs of these films. (d) JV curves (log scale) of AZO/ZnO/ZnS/FeS_2/MoS_2/Mo devices made from as sulfurized (black) and etched pyrite films (yellow). The etch is a 1 sec dip in 50% piranha solution followed by rinse in MeOH immediately prior to loading the substrate into the vacuum chamber for ZnS deposition. (e) In-plane conductivity of pyrite thin film as sulfurized (black) compared to three identical films that were etched 30 sec in 50% piranha (yellow, orange, red). (f) SEM cross-sectional view of pyrite film after 30 sec etch in 50% piranha solution.

moderate photo-response were obtained reproducibly at times, as summarized in fig. 5.10. Figure 5.10a shows dark JV curves (log scale) of typical diodes based on CVD pyrite (black) and ink pyrite films (blue). Rectification was consistently higher for devices based on CVD pyrite films, with forward/reverse ratios of several thousand at ±1.5 V. Cell performance in the dark and under solar illumination was generally maintained for a few days in air, though overall device resistivity slowly increased, eventually resulting in diminishing photo-current (fig. 5.10b). Storage in a nitrogen-filled glovebox for several weeks had only a small, but similar effect (reduced current levels).

The temperature-dependence of solar cell performance was tested in a croystat down to 12 K. Figure 5.10c shows JV curves in the dark from 12 to 300 K, exhibiting loss of rectification quickly below room temperature, limited by overall stack resistivity. Note that this cell was contacted in the cryostat by a contact needle on the AZO top contact and likely was partially shunted in the process, explaining the increased reverse current levels and small V_{OC}. The photo-response of the same cell is shown in fig. 5.10d, with a plot of V_{OC} and J_{SC} under illumination with a halogen lamp (> 100 mW/cm^2). As expected, V_{OC} increases with decreasing temperature to ∼130 mV at 12 K. J_{SC} shows a maximum of ∼20 μA/cm^2 at 250 K.

The best solar cells made using both CVD and ink pyrite absorbers ('champion cells') were tested under a AM1.5G solar simulator. Light was coupled through a quartz window into a nitrogen-filled glovebox and reflected onto the cells with mirrors, resulting in a power density of ∼50 mW/cm^2 (0.5 suns) on the cell. Results for the two champion cells are shown in fig. 5.11a and b. While CVD pyrite based cells were limited to 200 - 240 mV V_{OC}, as expected from tunneling losses across a narrow surface potential barrier (chapter 4), ink pyrite based films reached $>$ 400 mV V_{OC}, which is puzzling. Aging the cells in air even increased V_{OC} to over 600 mV (not shown), though this went along with a drastic reduction in photo-current. J_{SC} was limited to ∼3 μA/cm^2 in CVD pyrite based cells and ∼6 μA/cm^2 in ink pyrite based cells under 0.5 suns. Higher J_{SC} of > 30 μA/cm^2 was observed under intense

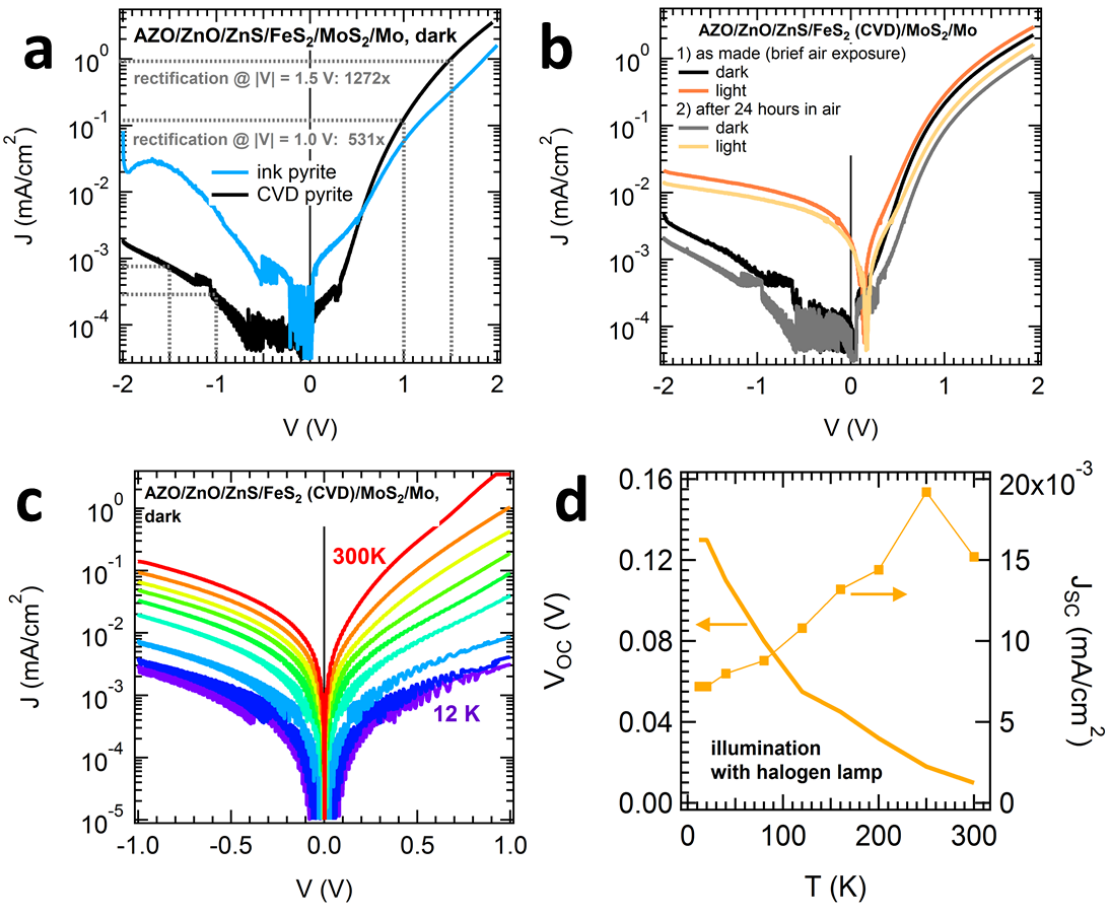

Figure 5.10: Rectification, air stability and temperature-dependence of pyrite thin film solar cells. (a) Dark JV curves (log scale) of heterojunction cells based on CVD (black) and ink (blue) deposited pyrite. Rectification ratios at ±1 V and ±1.5 V are indicated for the CVD based device. (b) JV curves (log scale) of a CVD pyrite device before (black/orange) and after (gray/yellow) exposure to air for 24 h (dark/illuminated). (c) Dark JV curves (log scale) of a CVD pyrite device recorded at temperatures from 12 to 300 K. (d) Open-circuit voltage V_{OC} (left axis) and short-circuit current density J_{SC} for the same device shown in (c), under illumination with a halogen lamp (> 100 mW/cm^2).

(> 100 mW/cm^2) illumination with a halogen lamp (fig. 5.11c). Fill-factors were generally poor ($< 40\%$), and overall power conversion efficiencies (PCE) calculate to 0.0002% and 0.0014% for the devices shown in fig. 5.11a and fig. 5.11b, respectively.

The surprising combination of high V_{OC} (for pyrite) and low J_{SC} brings up questions about whether the photo-response is truly from absorption in the pyrite layer, or maybe from absorption in the ZnS/ZnO window layer. To probe this, we used a halogen lamp with and without various longpass filters that limit the lamp's light to wavelengths that are not absorbed in ZnS/ZnO (fig. 5.11d). The combined absorption of ZnS/ZnO films on glass was determined with transmission and reflection measurements using an integrating sphere. As shown in fig. 5.11c it was found that the photo-response must indeed come from the pyrite absorber, but is mostly limited to the blue part of the spectrum. For example, using a $\lambda >$ 495 nm longpass filter, to which ZnS/ZnO is transparent, the photo-current was reduced to $\sim$1/4, even though only a small part of the photon flux from the halogen lamp is cut out. The cells tested in this work were too small to focus monochromatic light from our EQE (external quantum efficiency) setup on, but future work needs to include EQE measurements. One possible explanation for the observed small J_{SC} would be a misalignment of the ZnS and FeS_2 conduction bands at the junction, where a barrier prevents electron extraction from the pyrite absorber. See fig. 5.4 for an illustration of a few of many possible scenarios. Future work to clarify this needs to include XPS/UPS studies of the (valence) band alignment (see [63] for suggested procedure), coupled with numerical calculations (e.g. 1DPoisson). Another explanation would be a very high surface recombination velocity at the interface that kills photo-generated charge carriers before they can be extracted. Further, the fact that red light contributes less than blue light suggests that bulk recombination is also high. In that case, charge carriers photo-generated even 100 nm away from the pyrite surface might be unlikely to reach the interface. Future work to probe this needs to include wavelength-dependent TRMC studies, as layed out in section 4.5.

In summary, though photo-current is very low, the solar cells reported here are the first solid-

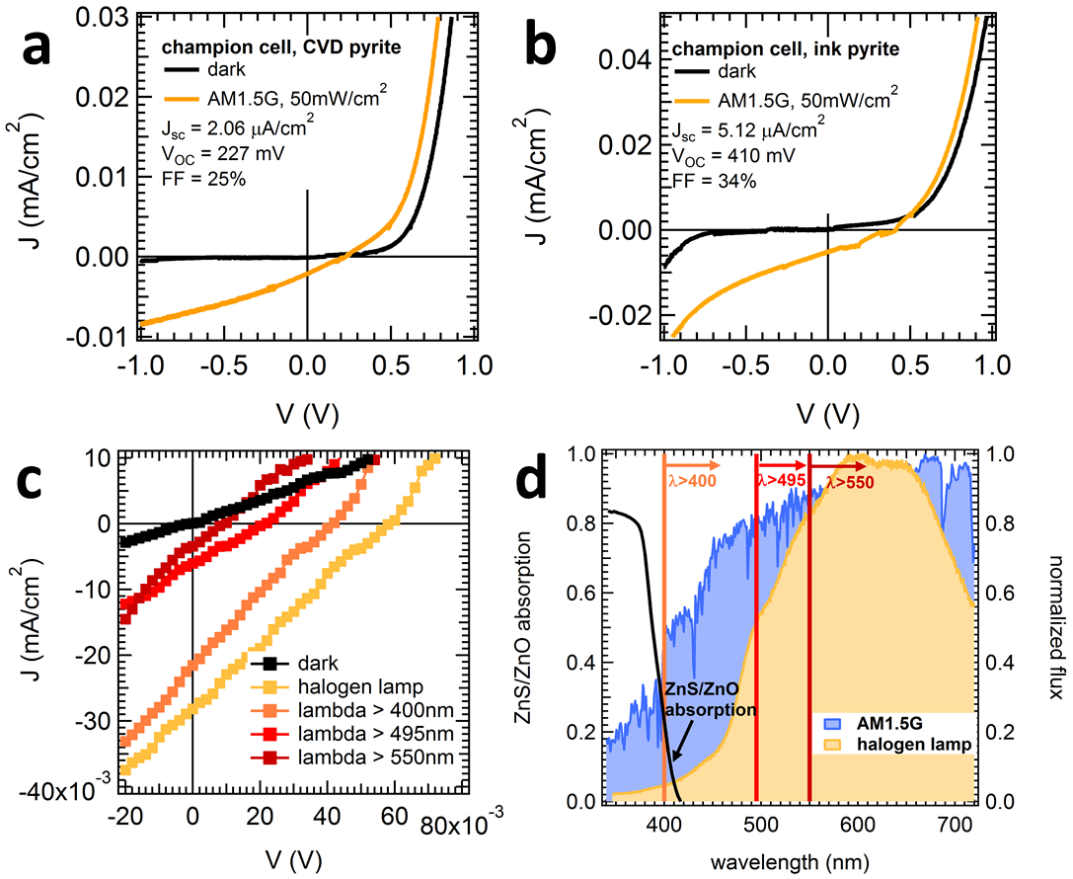

Figure 5.11: JV curves of thin film solar cell 'champion' devices based on CVD pyrite (a) and ink pyrite (b) in the dark and under illumination (AM1.5G spectrum, $\sim$ 50 mW/cm^2). (c) JV curves for CVD based device under halogen lamp illumination (yellow, $>$ 100 mW/cm^2), along with curves under illumination by the same lamp through longpass filters (orange, red). (d) Normalized spectra for AM1.5G (blue) and halogen lamp (yellow) illumination (right axis), along with measured absorption of combined ZnS/ZnO film (black line). The three vertical lines denote the cut-off wavelength of the longpass filters used to record the data shown in (c).

state heterojunctions with pyrite thin films, and the V_{OC} values of the ink pyrite devices are the highest ever reported for any solid-state pyrite junction.

In addition to the reproducibility issues with ZnS layers mentioned above, comparative studies were made difficult by two more complications.

First, pyrite thin films supplied in-house by both CVD and ink method were subject to variability. Film thickness, roughness, uniformity, particle count and organic residue were not constant over the course of this study. Cell-to-cell variation was generally low, apart

from occasional 'punch-through' complications (see below), demonstrating good uniformity of both individual pyrite films and sputtered window layers. Within one pyrite batch (CVD method: deposited in one run; ink method: spun-cast from same ink), device-to-device variation was generally also low (see 'device 1' and 'device 2' in fig. 5.12a), but occasionally showed inexplicable discrepancies. Batch-to-batch variation for devices made from pyrite films of different batches (but with window layers made in the same run) was typically too large to allow comparative studies, often even for pyrite batches made on consecutive days. See for example 'device 1' (or 2) vs. 'device 3' in fig. 5.12a. Shown here are three devices with 4 individual cells each, where the four cells of a substrate are represented by identically colored lines.

Second, the mesa structure originally used for device architecture (see fig. 5.14) required contacting of the AZO top contact by needle probe, which often caused (partial) shunting of the device to the underlying MoS_2/Mo back contact, due to the mechanical softness of the MoS_2 layer. Figure 5.12b shows the extreme case of complete 'punch-through': a device is first contacted very carefully by placing a tungsten needle probe on the AZO top electrode, showing the typical diode-like JV curve (solid line). After applying even a small amount of force on the needle probe the same device is irreversibly shunted (dashed line). Figure 5.12c shows SEM top-down views afterwards, illustrating the damage done to the cell. While the AZO/ZnO/ZnS top layers are very hard, the underlying FeS_2 and especially the thick MoS_2 layer are soft, causing the AZO/ZnO/ZnS stack to crack under pressure and the cell to shunt. Even preventing extreme shunting cases as shown here, some degree of partial shunting and thus cell-to-cell variation was the result of this issue, which eventually led to a change in cell architecture (see below).

Since MoS_2/Mo back contacts are soft, they are prone to punch-throughs and other mechanical problems. To prevent these issues, Fe back contacts were investigated as an alternative back contact. As Fe sulfurizes to metallic troilite (FeS) and pyrrhotite (Fe_7S_8), and eventually FeS_2, this back contact should in theory be ohmic to pyrite after sulfurization, too, and

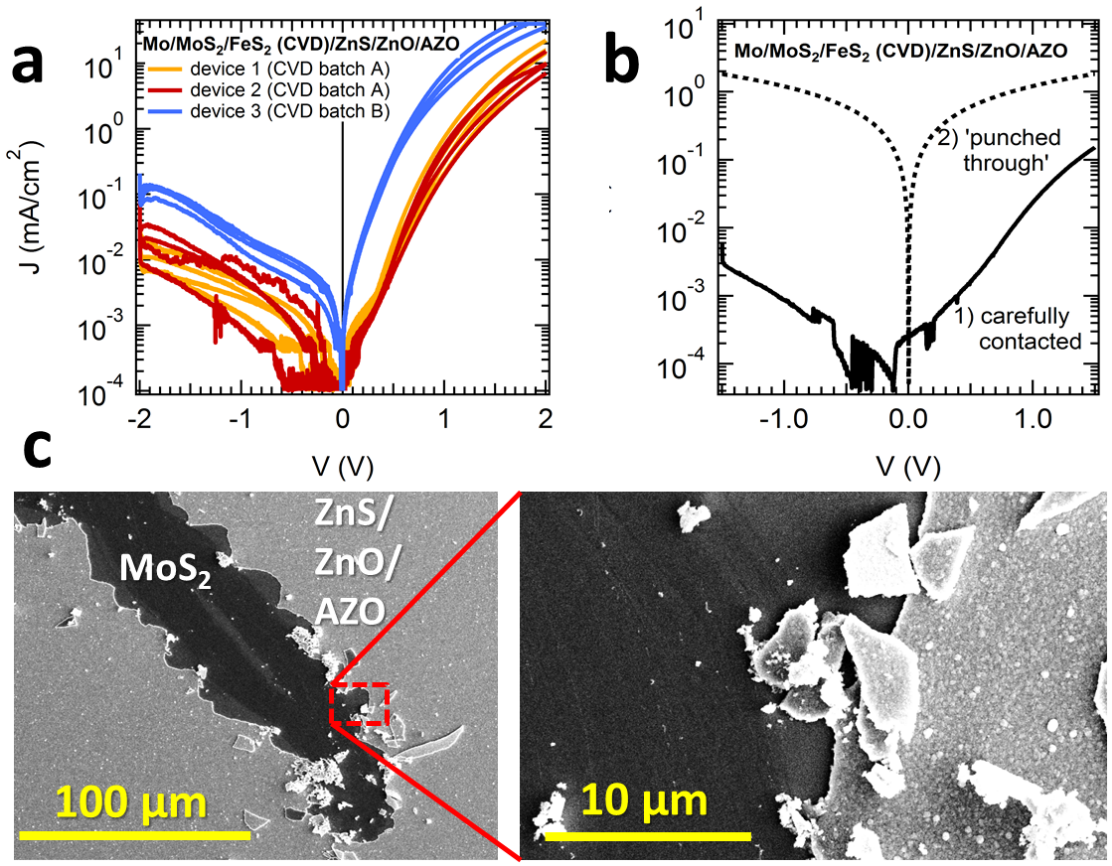

Figure 5.12: Reproducibility and 'punch-through' issues of thin films solar cells. (a) JV curves (log scale) showing three CVD-based devices with 4 cells each. The ZnS/ZnO/AZO top layers were deposited simultaneously for all three devices. (b) JV curve (log scale) for a CVD-based cell before (solid line) and after (dotted line) the 'punch-through' that occurs when the contacting needles pushes through the soft MoS_2 layer, shorting the cell. (c) SEM top-down images showing the damage inflicted from the tungsten probe needle 'punching through'.

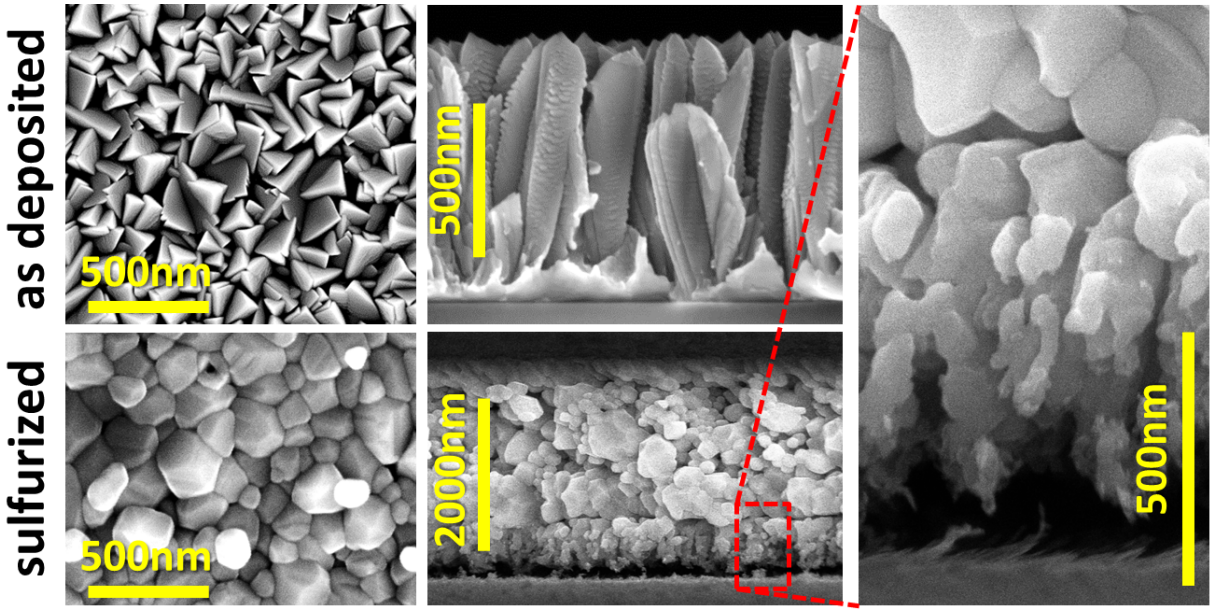

Figure 5.13: SEM top down (left column) and cross-sectional (center column) views of Fe back contact on glass as deposited by sputtering (top row) and after sulfurization (bottom row). The zoomed-in view on the right illustrates the poor adhesion of the sulfurized layer to the glass substrate.

potentially have better mechanical properties.

Fe thin films were deposited on glass by DC magnetron sputtering from a 99.9% (3N) pure Fe target (see section 2.2.1). The resulting films (fig. 5.13) were dense, uniform, highly crystalline, mechanically robust and had sheet resistance as low as 1 Ω/cm (at 800 nm thickness). However, after sulfurization the films showed weak adhesion or even flaked off the substrate completely. Control annealing in inert nitrogen atmosphere (6 h at 550 °C) did not result in weak adhesion, suggesting that the problem is not a result of different thermal expansion coefficients between glass and Fe films, but a consequence of mechanically weak Fe_xS_y phases forming at the glass interface, as illustrated in fig. 5.13.

Due to these adhesion problems, as well as preventively high maintenance on the Fe sputter gun (see section 2.2.1), Fe back contact were not further pursued. Future work on alternative back contacts compatible with sulfurization might also look at S-diffusion blocking layers like TiN.

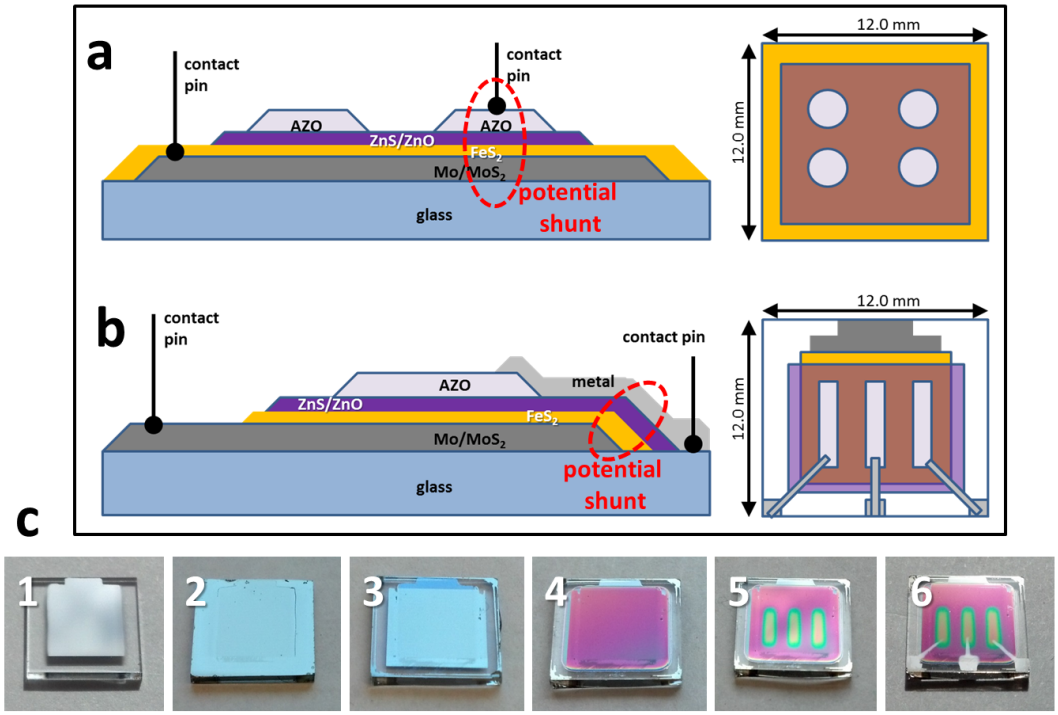

Figure 5.14: Illustration of solar cell architecture and fabrication steps. (a) First device architecture, called 'mesa structure', used for pyrite thin film solar cells. Fabrication is easy, as the pyrite layer does not have to be structured, but prone to the top contact 'punching through' to the back contact, due to the soft MoS_2 layer (see fig. 5.12). (b) Second device architecture, making punch-throughs impossible, but requiring lithography (see section 2.2.4) and introducing potential shunting paths at the Mo/MoS_2 'cliff' (see fig. 5.15). (c) Fabrication steps for second architecture. (1) Mo films are sputter-deposited on glass through a shadow mask, and the bottom edge is defined via photo-lithography. The pyrite layer is then deposited on top (2) and also defined via photo-lithography (3). The ZnS/ZnO window layer (4) and AZO top contact (5) are then deposited through their respective shadow masks. Finally the metal top contacts are sputter-deposited through a shadow mask (6).

In order to avoid 'punch-through' problems, independently of choice of back contact metal, solar cell device architecture was switched from a mesa structure to a geometry where the top contact can be made physically separated from the back contact layer (see fig. 5.14), making punch-throughs impossible. All fabrication steps are described in detail in section 2.8.2 and illustrated in fig. 5.14c. While punch-throughs were successfully avoided using this device layout, a new problem arose, as discussed below.

Definition of thin films deposited by sputtering through a shadow mask resulted in rather broad edges. Looking at the profile of such a film, the decrease from full thickness to zero corresponds to a width of up to over 500 μm. In a shadow mask like the one shown in fig. 2.4, the steel mask sits < 0.5 mm away from the substrate surface, yet the profile is as broad as shown in fig. 5.15a. While sputter deposition is not necessarily a line-of-sight method (like thermal evaporation), the magnitude of broadening is unexpected and the mechanism responsible unclear. Having the mask in direct contact with the substrate was avoided, in order to prevent substrate scratching and particle contamination. This kind of broadening, while unexpected, is not a problem in itself, but becomes a problem when a Mo layer with such a profile is sulfurized. As discussed in detail in section 3.2, the conversion from Mo to MoS_2 progresses in a sharp line from the top of the film downwards during sulfur annealing. When this 'conversion front' reaches the glass substrate, it results in a 'fracture' between the tail end of the original Mo profile that is now fully converted to MoS_2, and the bulk of the film that is now a MoS_2/Mo bilayer. The phenomenon is illustrated in fig. 5.15b-f. Despite many trials with varied sulfurization conditions as well as original Mo layer thickness and deposition conditions, this fracture could not be avoided. Depositing subsequent layers over this fractured regions creates an opportunity for shunts, especially running metal lines (fig. 5.14c-6) over it. A way to avoid the tailing Mo/MoS_2 layer and its fracture is to sharply 'cut off' the Mo layer after deposition (and before sulfurization) by photo lithography. This was achieved using a 2:3:3 mixture of nitric acid, phosphoric acid and water, but introduces a new problem. Figure 5.15f shows the resulting steep cliff of Mo/MoS_2 after sulfurization. The bilayer is so thick (typically $\sim$1500 nm) that the comparatively thin pyrite layer on top disconnects where it grows over the cliff. This introduces another potential shunt, when the top layers (especially metal lines) are deposited over the cliff.

In summary, the sulfurization process necessary to obtain phase-pure pyrite thin films causes a gradual conversion of the Mo back contact to MoS_2. The latter is mechanically too soft to make a mesa device structure (fig. 5.14a) workable, and the conversion process causes a

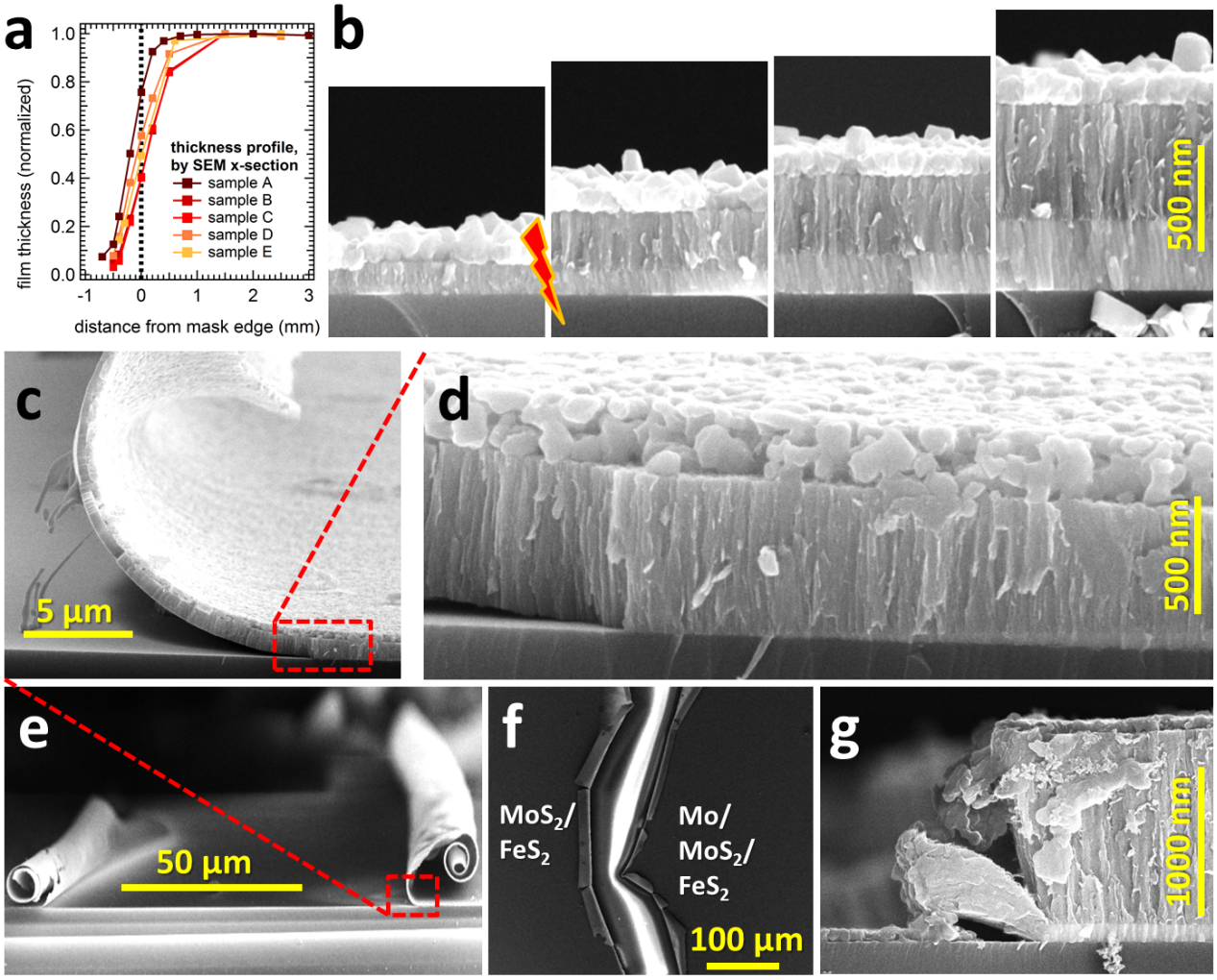

Figure 5.15: De-lamination issues with Mo/MoS_2 back contacts defined through shadow masks. (a) Thickness profile of Mo films sputter-deposited through shadow mask, relative to the mask edge, as measured by SEM. (b) SEM cross-sectional view of $Mo/MoS_2/FeS_2$ stack around the fracture (see text). At the point where all Mo is converted to MoS_2, the fissure forms, indicated by the lightning bolt symbol. (c - e) Cross-sectional view at different magnifications and (f) top-down view of the fracture. (g) Cross-sectional view of resulting $Mo/MoS_2/FeS_2$ stack after defining a sharp edge in the Mo film by photo-lithography.

fissure that makes an offset device structure (fig. 5.14b) in combination with shadow masks also impractical. A sharp Mo edge defined by lithography (fig. 5.15g) also enables local shunts. Thus, either a different back contact metal should be established, or a method to make phase-pure pyrite films without sulfurization.[116]

5.4 Summary

In summary, many different solar cells with pyrite absorbers were tested in this work, including wet junctions and solid-state junctions.

The wet junction cells reproduced results previously published and confirmed that polarization in piranha (cathodic etching) drastically improves the photo-response of pyrite single crystals. Thin film wet junctions produced only a small photo-response, interestingly showing the same qualitative JV characteristics as single crystals, indicating that the films act as n-type semiconductors in this test cell.

Solid-state junctions with single crystals gave mixed results and were not further investigated. Instead, this work focused on solid-state pn-heterojunctions from pyrite thin films. Ohmic Mo/MoS_2 back contacts were used for these devices, but due to mechanical issues might have to be replaced with a different metal (for example Fe), or, a procedure to obtain phase-pure pyrite films without sulfurization[116] will need to be established. ZnS turned out the most promising junction partner for pyrite, and is the only window-layer material tested that produced rectifying pn-junctions. Thus, the majority of this work focused on glass/Mo/MoS_2/FeS_2/ZnS/ZnO/AZO stacks. It was found that deposition of ZnS by reactive sputtering is hard to control in terms of film stoichiometry and resistivity, resulting in problems reproducing successful stack recipes. This is evident in changes of the ZnS target surface, known as target 'poisoning' as a function of deposition history. Especially H_2S content in the plasma has a huge impact on target conditions and film properties. In future

work a feedback loop between working pressure and H_2S flow should be implemented, as described in [100].

Despite these challenges, cells with high rectification (several 1000x) were reproduced over periods of several weeks, before ZnS properties changed again, making these results elusive, only to become reproducibly good again several months later. This problem, together with the Mo/MoS_2 issues discussed, largely frustrated methodical optimization of solar cell performance. Nonetheless, champion devices with 410 meV open-circuit voltage (610 meV after aging in air) and 5 $\mu A/cm^2$ short-circuit current under 50 mW/cm^2 AM1.5G spectrum (30 $\mu A/cm^2$ under intense halogen light) were recorded, representing record values for solid-state thin film solar cells with pyrite absorbers. The small photo-current is predominantly produced from high-energy photons, and might be limited by high surface recombination velocities or a conduction band offset to ZnS. Further studies of these cells need to include EQE, XPS and TRMC measurements.

Chapter 6

Summary and Conclusions

Iron pyrite FeS_2 absorbers, both polycrystalline films and macroscopic single crystals, synthesized from various gas-phase and liquid-phase methods, were studied regarding their potential as solar photovoltaic absorbers. The previously noted limitation to low photo-voltages of $\sim$200 meV is explained in a quantitative model, and overcome experimentally in thin film pn-heterojunctions.

Earlier findings that all pyrite thin films, regardless of synthesis and elemental doping, are universally heavily p-type doped, suggested that the surface dominates electrical transport in thin film. Thus, a systematic study of electrical transport in pyrite materials as a function of surface/bulk ratio was conducted, including macroscopic single crystals, microcrystalline pellets, nanoscopic single crystals and nanocrystalline thin films (in order of increasing ratio). It was found that with increasing surface/bulk ratio the elemental composition of the pyrite material becomes less and less important, and p-type conduction, only seen at low temperatures in single crystals, becomes dominant at higher and higher temperatures. For example, for two macroscopic single crystals, one artificial and of very high purity, the other natural and of low purity, show very different transport properties. But, microcrystalline pellets fabricated from each crystal show nearly identical transport properties.

To improve upon this understanding of surface dominance, quantitatively describe it, and develop methods to passivate it, more crystals of larger size and even higher quality were needed. They were supplied from a new flux synthesis developed in our lab, and allowed development of a quantitative transport model. Temperature-dependent Hall effect data of crystals of this purity revealed two uncommon features of the Hall coefficient R_H: a maximum in $|R_H|$ at ∼120 K, along with a sign change of R_H at ∼80 K. These features were reported before for pyrite, but either not discussed, or falsely attributed to a transition from hopping to band transport. Numerical fitting of the Hall data using a multi-layer transport model that includes a self-consistent Fermi level reveals the existence of a hole-rich inversion layer at the surface of the n-type crystals. This inversion layer is a channel for the surface conduction of holes in pyrite. Electrons in the crystal bulk are frozen out at low temperatures to the extent that the holes in the inversion layer dominate conduction. The presence of the hole inversion layer is corroborated by UPS measurements showing E_F - $E_V \approx 0.1$ eV, as well as Hall effect experiments as a function of crystal thickness and physiochemical modification of the crystal surface. The inversion layer can explain both the low photo-voltage of pyrite photocells (caused by tunneling across part of the inversion layer) and the universal high p-type conductivity of polycrystalline pyrite thin films.

This newly developed model for the multilayer transport, coupled with temperature-dependent Hall effect measurements on high-purity pyrite single crystals, represents an excellent test platform to rationally and quantitatively evaluate a wide range of surface passivation strategies. While many strategies have only been only touched upon and need to be investigated further, piranha etching and annealing in sulfur atmosphere were found to be most efficient for single crystals, reducing the concentrations by up to a factor of 20 in the case of piranha etching. For thin films, passivating the surface with ZnS showed the most promise and should be studied further.

Single crystals were also used to assess whether the bulk band gap of pyrite is significantly smaller than the widely accepted value of ∼0.95 eV at room temperature. Our optical

measurements yield a band gap of 0.94 eV, in agreement with literature, while modeling of the intrinsic electrical conductivity using two different DOS functions results in a somewhat lower best-fit value of 0.80 ± 0.05 eV. In conclusion the electronic gap of high-quality pyrite is probably ∼0.80 eV, which is large enough to support a photo-voltage of ∼500 mV from pyrite solar cells.

Wet-junction solar cells with pyrite absorbers were tested, also solid-state junctions with pyrite single crystals. However, the focus of this work was set on thin film pn-heterojunctions in glass/Mo/MoS_2/FeS_2/ZnS/ZnO/AZO stacks. Formation of the Mo/MoS_2 bilayer, including electrical and optical properties of the polycrystalline MoS_2 layer, were studied in some detail. Despite challenges with the Mo/MoS_2 back contact and control over the sputter-deposited ZnS film properties, cells with high rectification (several 1000x) were achieved. Champion devices with 410 meV open-circuit voltage (610 meV after aging in air) and 5 μA/cm^2 short-circuit current under 50 mW/cm^2 AM1.5G spectrum (30 μA/cm^2 under intense halogen light) were recorded. These represent the first ever demonstrated all-solid-state pyrite thin films solar cells, as well as the highest photo-voltage ever for any solid-state pyrite solar cell. The small photo-current is predominantly produced from high-energy photons, and might be limited by high surface recombination velocities or a conduction band offset to ZnS. In light of future passivated pyrite thin films that might be n-type, sputtered NiO was studied as a p-type window layer, resulting in optically transparent films with tunable resistivity.

To maximize the impact of the findings in this work, future research should follow up with combined XPS/UPS, Hall effect and DFT studies on the mechanism of the passivation results described here (most notable piranha etching and ZnS overcoating), then use the test platform developed here to find even better surface passivation methods. To this end, field-effect gating should be tested, along with surface passivation using reduction agents and molecular adsorbates such as thiophene. Carrier-lifetime measurements (e.g. TRMC) should be expanded to include temperature-dependent and wavelength-dependent measure-

ments on both single crystals and thin films. The pn-heterojunction devices presented here can be improved by first eliminating the mechanical problems induced by the Mo/MoS_2 back contact. Then, better control of the ZnS buffer needs to be established, for example by implementing a feedback loop between working pressure and H_2S gas flow. Alternatively, ZnS buffers could be applied via chemical bath deposition. To rationalize and overcome the small photo-current, EQE measurements to probe its wavelength-dependence will be necessary, along with XPS/UPS measurements to understand junction band alignment, and carrier life-time measurements to evaluate surface recombination.

Overall, this work represents an important step towards fully understanding the shortcomings of pyrite absorbers, and developing the methods necessary to enable pyrite to live up to its potential of becoming a low-cost, non-toxic, earth-abundant absorber material for deployment of solar photovoltaics on the terawatt scale.

Bibliography

[1] V. Antonov, L. Germash, A. Shpak, and A. Yaresko. Electronic structure, optical and x-ray emission spectra in FeS_2. *physica status solidi (b)*, 246(2):411–416, 2009.

[2] V. Antonucci, A. Arico', N. Giordano, P. Antonucci, U. Russo, D. Cocke, and F. Crea. Photoactive screen-printed pyrite anodes for electrochemical photovoltaic cells. *Solar Cells*, 31(2):119–141, Mar. 1991.

[3] J. Ares, I. Ferrer, F. Cuevas, and C. Sanchez. Growth of pyrite thin-films investigated by thermoelectric measurements. *Thin Solid Films*, 387(1):97–99, 2001.

[4] J. Ares, A. Pascual, I. Ferrer, and C. Sanchez. Lattice intrinsic defects and electrical resistivity in pyrite thin films. *Thin Solid Films*, 451:233–236, 2004.

[5] M. Awais, M. Rahman, J. D. MacElroy, N. Coburn, D. Dini, J. G. Vos, and D. P. Dowling. Deposition and characterization of NiO_x coatings by magnetron sputtering for application in dye-sensitized solar cells. *Surface and Coatings Technology*, 204(16):2729–2736, 2010.

[6] N. Berry, M. Cheng, C. L. Perkins, M. Limpinsel, J. C. Hemminger, and M. Law. Atmospheric-pressure chemical vapor deposition of iron pyrite thin films. *Advanced Energy Materials*, 2(9):1124–1135, 2012.

[7] M. Birkholz, D. Lichtenberger, C. Höpfner, and S. Fiechter. Sputtering of thin pyrite films. *Solar energy materials and solar cells*, 27(3):243–251, 1992.

[8] T. A. Bither, R. Bouchard, W. Cloud, P. Donohue, and W. Siemons. Transition metal pyrite dichalcogenides. high-pressure synthesis and correlation of properties. *Inorganic Chemistry*, 7(11):2208–2220, 1968.

[9] O. Blenk. *Herstellung und Characterisierung von FeS_2 (Pyrit) fuer die Photovoltaik*. PhD thesis, University of Konstanz, 1995.

[10] C. Breyer, A. Gerlach, D. Schafer, and J. Schmid. Fuel-parity: New very large and sustainable market segments for PV systems. In *Energy Conference and Exhibition (EnergyCon), 2010 IEEE International*, pages 406 –411, 2010.

[11] M. Bronold, K. Büker, S. Kubala, C. Pettenkofer, and H. Tributsch. Surface preparation of FeS_2 via electrochemical etching and interface formation with metals. *physica status solidi (a)*, 135(1):231–243, 1993.

[12] M. Bronold, S. Kubala, C. Pettenkofer, and W. Jaegermann. Thin pyrite (FeS_2) films by molecular beam deposition. *Thin Solid Films*, 304(1):178–182, 1997.

[13] M. Bronold, C. Pettenkofer, and W. Jaegermann. Surface photovoltage measurements on pyrite (100) cleavage planes: Evidence for electronic bulk defects. *J. Appl. Phys.*, 76(10):5800–5808, Nov. 1994.

[14] M. Bronold, Y. Tomm, and W. Jaegermann. Surface states on cubic d-band semiconductor pyrite (FeS_2). *Surface Science*, 314(3):L931–L936, Aug. 1994.

[15] K. Büker, N. Alonso-Vante, R. Scheer, and H. Tributsch. Influence of electrochemical activation and surface orientation on the photoresponse of single crystalline pyrite/electrolyte and pyrite/metal junctions. *Berichte der Bunsengesellschaft für physikalische Chemie*, 98(5):674–682, 1994.

[16] K. Büker, N. Alonso-Vante, and H. Tributsch. Photovoltaic output limitation of n-FeS_2 (pyrite) schottky barriers: A temperature-dependent characterization. *Journal of applied physics*, 72(12):5721–5728, 1992.

[17] K. Büker, S. Fiechter, V. Eyert, and H. Tributsch. Photoelectrochemistry of highly zn-doped pyrite as compared with isostructural FeS_2. *Journal of the Electrochemical Society*, 146(1):261–265, 1999.

[18] G. Busch and H. Schade. *Lectures on Solid State Physics: International Series in Natural Philosophy*, volume 79. Elsevier, 1976.

[19] M. Cabán-Acevedo, N. S. Kaiser, C. R. English, D. Liang, B. J. Thompson, H.-E. Chen, K. J. Czech, J. C. Wright, R. J. Hamers, and S. Jin. Ionization of high-density deep donor defect states explains the low photovoltage of iron pyrite single crystals. *Journal of the American Chemical Society*, 136(49):17163–17179, 2014.

[20] M. Caban-Acevedo, D. Liang, K. S. Chew, J. P. DeGrave, N. S. Kaiser, and S. Jin. Synthesis, characterization, and variable range hopping transport of pyrite (FeS_2) nanorods, nanobelts, and nanoplates. *ACS nano*, 7(2):1731–1739, 2013.

[21] H.-L. Chen and Y.-S. Yang. Effect of crystallographic orientations on electrical properties of sputter-deposited nickel oxide thin films. *Thin Solid Films*, 516(16):5590–5596, 2008.

[22] S. Choi, J. Hu, L. Abdallah, M. Limpinsel, Y. Zhang, S. Zollner, R. Wu, and M. Law. Pseudodielectric function and critical-point energies of iron pyrite. *Physical Review B*, 86(11):115207, 2012.

[23] M. L. Cohen and J. R. Chelikowsky. *Electronic structure and optical properties of semiconductors*. Springer, 2nd edition, 1989.

[24] C. De las Heras, J. de Vidales, I. Ferrer, and C. Sánchez. Structural and microstructural features of pyrite FeS_{2-x} thin films obtained by thermal sulfuration of iron. *Journal of materials research*, 11(01):211–220, 1996.

[25] C. De las Heras, I. Ferrer, and C. Sanchez. Temperature dependence of the optical absorption edge of pyrite FeS_2 thin films. *Journal of Physics: Condensed Matter*, 6(46):10177, 1994.

[26] C. De las Heras and C. Sanchez. Characterization of iron pyrite thin films obtained by flash evaporation. *Thin Solid Films*, 199(2):259–267, 1991.

[27] P. Denholm, R. M. Margolis, S. Ong, and B. Roberts. Breakeven cost for residential photovoltaics in the united states: Key drivers and sensitivities. Technical report, NREL, 2009.

[28] C. M. Eggleston, J.-J. Ehrhardt, and W. Stumm. Surface structural controls on pyrite oxidation kinetics: An XPS-UPS, STM and modeling study. *American Mineralogist*, 81(9):1036–1056, 1996.

[29] A. Einstein. Über einem die erzeugung und verwandlung des lichtes betreffenden heuristischen gesichtspunkt. *Annalen der Physik*, 4, 1905.

[30] K. Ellmer. Magnetron sputtering of transparent conductive zinc oxide: relation between the sputtering parameters and the electronic properties. *Journal of Physics D: Applied Physics*, 33(4):R17, 2000.

[31] K. Ellmer and C. Höpfner. On the stoichiometry of the semiconductor pyrite (FeS_2). *Philosophical Magazine A*, 75(4):1129–1151, 1997.

[32] K. Ellmer, D. Lichtenberger, A. Ennaoui, C. Höpfner, S. Fiechter, and H. Tributsch. Comparison of structural, optical and electrical properties of pyrite (FeS_2 layers prepared by mocvd (normal and low pressure) and reactive magnetron sputtering. In *Photovoltaic Specialists Conference, 1993., Conference Record of the Twenty Third IEEE*, pages 535–538. IEEE, 1993.

[33] A. Ennaoui, S. Fiechter, W. Jaegermann, and H. Tributsch. Photoelectrochemistry of highly quantum efficient single crystalline FeS_2 (pyrite). *Journal of The Electrochemical Society*, 133(1):97–106, Jan. 1986.

[34] A. Ennaoui, S. Fiechter, C. Pettenkofer, N. Alonso-Vante, K. Bueker, M. Bronold, C. Hoepfner, and H. Tributsch. Iron disulfide for solar energy conversion. *Solar Energy Materials and Solar Cells*, 29(4):289–370, May 1993.

[35] A. Ennaoui, S. Fiechter, G. Smestad, and H. Tributsch. Preparation of iron di-sulphide and its use for solar energy conversion. In *Proceedings of 1st World Renewable Energy Congress*, pages 458–64, 1990.

[36] A. Ennaoui and H. Tributsch. Iron sulphide solar cells. *Solar Cells*, 13(2):197–200, Dec. 1984.

[37] L. Essaleh, J. Galibert, S. Wasim, E. Hernandez, and J. Leotin. Positive magnetoresistance in the variable-range-hopping regime in copper indium diselenide on either side of the critical field b c. *Physical Review B*, 52(11):7798, 1995.

[38] I. Ferrer, D. Nevskaia, C. De las Heras, and C. Sanchez. About the band gap nature of FeS_2 as determined from optical and photoelectrochemical measurements. *Solid State Communications*, 74(9):913–916, 1990.

[39] I. Ferrer and C. Sanchez. Characterization of FeS_2 thin films prepared by thermal sulfidation of flash evaporated iron. *Journal of applied physics*, 70(5):2641–2647, 1991.

[40] S. Fiechter, J. Mai, A. Ennaoui, and W. Szacki. Chemical vapour transport of pyrite (FeS_2) with halogen (Cl, Br, I). *Journal of Crystal Growth*, 78(3):438–444, Dec. 1986.

[41] J. Fleming. Growth of FeS_2 (pyrite) from Te melts. *Journal of Crystal Growth*, 92(1–2):287–293, Oct. 1988.

[42] W. Folkerts, G. Sawatzky, C. Haas, R. De Groot, and F. Hillebrecht. Electronic structure of some 3d transition-metal pyrites. *Journal of Physics C: Solid State Physics*, 20(26):4135, 1987.

[43] H. Frederikse, W. Hosler, and D. Roberts. Electrical conduction in magnesium stannide at low temperatures. *Physical Review*, 103(1):67, 1956.

[44] H. Fritzsche. Resistivity and hall coefficient of antimony-doped germanium at low temperatures. *Journal of Physics and Chemistry of Solids*, 6(1):69–80, 1958.

[45] L. A. Garvie and P. R. Buseck. Unoccupied states of pyrite probed by electron energy-loss spectroscopy (EELS). *American Mineralogist*, 89(4):485–491, 2004.

[46] N. Hamdadou, A. Khelil, and J. Bernede. Pyrite FeS_2 films obtained by sulphuration of iron pre-deposited films. *Materials chemistry and physics*, 78(3):591–601, 2003.

[47] T. Harada. Transport properties of iron dichalcogenides FeX_2 (X = S, Se and Te). *Journal of the Physical Society of Japan*, 67(4):1352–1358, 1998.

[48] F. Herbert, A. Krishnamoorthy, K. Van Vliet, and B. Yildiz. Quantification of electronic band gap and surface states on FeS_2 (100). *Surface Science*, 618:53–61, 2013.

[49] C. Ho, Y. Huang, and K. Tiong. Characterization of near band-edge properties of synthetic p-FeS_2 iron pyrite from electrical and photoconductivity measurements. *Journal of alloys and compounds*, 422(1):321–327, 2006.

[50] C.-H. Ho, M.-H. Hsieh, and Y.-S. Huang. Compensation and carrier conduction in synthetic $Fe_{1-x}Ni_xS_2$ (0¡x¡0.1) single crystals. *Journal of The Electrochemical Society*, 155(4):H254–H258, 2008.

[51] C. Höpfner, K. Ellmer, A. Ennaoui, C. Pettenkofer, S. Fiechter, and H. Tributsch. Stoichiometry-, phase-and orientation-controlled growth of polycrystalline pyrite (FeS_2 thin films by MOCVD. *Journal of crystal growth*, 151(3):325–334, 1995.

[52] J. Hu, Y. Zhang, M. Law, and R. Wu. First-principles studies of the electronic properties of native and substitutional anionic defects in bulk iron pyrite. *Phys. Rev. B*, 85(8):085203–, Feb. 2012.

[53] J. Hu, Y. Zhang, M. Law, and R. Wu. Increasing the band gap of iron pyrite by alloying with oxygen. *J. Am. Chem. Soc.*, pages –, July 2012.

[54] C. Jacoboni, C. Canali, G. Ottaviani, and A. A. Quaranta. A review of some charge transport properties of silicon. *Solid-State Electronics*, 20(2):77–89, 1977.

[55] D. L. Jacobson and A. E. Campbell. Molybdenum work function determined by electron emission microscopy. *Metallurgical and Materials Transactions B*, 2(11):3063–3066, 1971.

[56] M. Jagadeesh and M. S. Seehra. Electrical resistivity and band gap of marcasite (FeS_2). *Physics Letters A*, 80(1):59–61, 1980.

[57] R. Jones, K. Yu, S. Li, W. Walukiewicz, J. Ager, E. Haller, H. Lu, and W. Schaff. Evidence for p-type doping of InN. *Physical review letters*, 96(12):125505, 2006.

[58] A. Karguppikar and A. Vedeshwar. Electrical and optical properties of natural iron pyrite (FeS_2). *physica status solidi (a)*, 109(2):549–558, 1988.

[59] P. King, T. D. Veal, and C. F. McConville. Unintentional conductivity of indium nitride: transport modelling and microscopic origins. *Journal of Physics: Condensed Matter*, 21(17):174201, 2009.

[60] C. Kloc, G. Willeke, and E. Bucher. Flux growth and electrical transport measurements of pyrite (FeS_2). *Journal of crystal growth*, 131(3):448–452, 1993.

[61] A. Kobayashi, Z. Oda, S. Kawaji, H. Arata, and K. Sugiyama. Impurity conduction of cleaned germanium surfaces at low temperatures. *Journal of Physics and Chemistry of Solids*, 14:37–42, 1960.

[62] W. W. Kou and M. S. Seehra. Optical absorption in iron pyrite (FeS_2). *Physical Review B*, 18(12):7062, 1978.

[63] E. Kraut, R. Grant, J. Waldrop, and S. Kowalczyk. Precise determination of the valence-band edge in x-ray photoemission spectra: Application to measurement of semiconductor interface potentials. *Physical Review Letters*, 44(24):1620, 1980.

[64] S. Lauer, A. Trautwein, and F. Harris. Electronic-structure calculations, photoelectron spectra, optical spectra, and Mössbauer parameters for the pyrites MS_2 (M = Fe, Co, Ni, Cu, Zn). *Physical Review B*, 29(12):6774, 1984.

[65] S. Lehner, N. Newman, M. Van Schilfgaarde, S. Bandyopadhyay, K. Savage, and P. Buseck. Defect energy levels and electronic behavior of Ni-, Co-, and As-doped synthetic pyrite (FeS_2). *Journal of Applied Physics*, 111(8):083717, 2012.

[66] S. Lehner, K. Savage, and J. Ayers. Vapor growth and characterization of pyrite (FeS_2) doped with Co, Ni, and As: variations in semiconducting properties. *Journal of crystal growth*, 286(2):306–317, 2006.

[67] E. L. Li, S. Seki, L. Feng-Bo, and J.-B. Zheng. Electrodeposition of pyrite thin films for solar cell. *Semicond. Photon. Technol.*, 7(2), 2001.

[68] D. Liang, M. Cabán-Acevedo, N. S. Kaiser, and S. Jin. Gated hall effect of nanoplate devices reveals surface-state-induced surface inversion in iron pyrite semiconductor. *Nano letters*, 14(12):6754–6760, 2014.

[69] D. Lichtenberger, K. Ellmer, R. Schieck, S. Fiechter, and H. Tributsch. Structural, optical and electrical properties of polycrystalline iron pyrite layers deposited by reactive dc magnetron sputtering. *Thin Solid Films*, 246(1):6–12, 1994.

[70] M. Limpinsel, N. Farhi, N. Berry, J. Lindemuth, C. L. Perkins, Q. Lin, and M. Law. An inversion layer at the surface of n-type iron pyrite. *Energy & Environmental Science*, 7(6):1974–1989, 2014.

[71] L. Lou and W. Frye. Hall effect and resistivity in liquid-phase-epitaxial layers of HgCdTe. *Journal of applied physics*, 56(8):2253–2267, 1984.

[72] Y.-M. Lu, W.-S. Hwang, J. Yang, and H. Chuang. Properties of nickel oxide thin films deposited by RF reactive magnetron sputtering. *Thin Solid Films*, 420:54–61, 2002.

[73] J. Luck, A. Hartmann, and S. Fiechter. Stoichiometry and impurity concentration in synthetically grown iron pyrite crystals and their constituents. *Fresenius' Zeitschrift für analytische Chemie*, 334(5):441–446, 1989.

[74] M. E. Makkaoui. Solution-based syntheses of iron pyrite thin films for photovoltaic and protein foot-printing applications. Master's thesis, University of California, Irvine, 2015.

[75] B. Meester, L. Reijnen, A. Goossens, and J. Schoonman. Synthesis of pyrite (FeS_2) thin films by low-pressure MOCVD. *Chemical Vapor Deposition*, 6(3):121–128, 2000.

[76] L. Meng and M. Liu. Thin pyrite (FeS_2) films prepared by thermal-sulfurating iron films at various temperatures. *Materials Science and Engineering: B*, 60(3):168–172, 1999.

[77] L. Meng, Y. Liu, and L. Tian. Structural, optical and electrical properties of polycrystalline pyrite (FeS_2) films obtained by thermal sulfuration of iron films. *Journal of crystal growth*, 253(1):530–538, 2003.

[78] S. Mrowec and K. Przybylski. *Transport properties of sulfide scales and sulfidation of metals and alloys*, volume 23. Springer Netherlands, 1985.

[79] R. Murphy and D. R. Strongin. Surface reactivity of pyrite and related sulfides. *Surface Science Reports*, 64(1):1–45, 2009.

[80] T. Nakada and M. Mizutani. 18% efficiency Cd-free Cu(In,Ga)Se_2 thin-film solar cells fabricated using chemical bath deposition (CBD)-ZnS buffer layers. *Japanese Journal of Applied Physics*, 41(2B):L165, 2002.

[81] S. Nakamura and A. Yamamoto. Electrodeposition of pyrite (FeS_2) thin films for photovoltaic cells. *Solar Energy Materials and Solar Cells*, 65(1):79–85, 2001.

[82] H. Nesbitt and I. Muir. X-ray photoelectron spectroscopic study of a pristine pyrite surface reacted with water vapour and air. *Geochimica et Cosmochimica Acta*, 58(21):4667–4679, 1994.

[83] N. K. Noel, A. Abate, S. D. Stranks, E. S. Parrott, V. M. Burlakov, A. Goriely, and H. J. Snaith. Enhanced photoluminescence and solar cell performance via Lewis base passivation of organic–inorganic lead halide perovskites. *ACS nano*, 8(10):9815–9821, 2014.

[84] J. Oertel, K. Ellmer, W. Bohne, J. Röhrich, and H. Tributsch. Growth of n-type polycrystalline pyrite (FeS_2) films by metalorganic chemical vapour deposition and their electrical characterization. *Journal of crystal growth*, 198:1205–1210, 1999.

[85] T. Ollonqvist, R. Perälä, and J. Väyrynen. Unoccupied electronic states of the FeS_2 (100) surface studied by inverse photoemission. *Surface science*, 377:201–205, 1997.

[86] S.-Y. Park, H.-R. Kim, Y.-J. Kang, D.-H. Kim, and J.-W. Kang. Organic solar cells employing magnetron sputtered p-type nickel oxide thin film as the anode buffer layer. *Solar Energy Materials and Solar Cells*, 94(12):2332–2336, 2010.

[87] A. Pascual, P. Diaz-Chao, I. Ferrer, C. Sánchez, and J. Ares. On the growth and doping of Fe/Ti chalcogenide thin films. *Solar energy materials and solar cells*, 87(1):575–582, 2005.

[88] C. L. Perkins and F. S. Hasoon. Surfactant-assisted growth of CdS thin films for photovoltaic applications. *Journal of Vacuum Science & Technology A*, 24(3):497–504, 2006.

[89] R. L. Petritz. Theory of an experiment for measuring the mobility and density of carriers in the space-charge region of a semiconductor surface. *Physical Review*, 110(6):1254, 1958.

[90] J. Puthussery, S. Seefeld, N. Berry, M. Gibbs, and M. Law. Colloidal iron pyrite (FeS_2) nanocrystal inks for thin-film photovoltaics. *J. Am. Chem. Soc.*, 133(4):716–719, Dec. 2010.

[91] J. Sangster and A. Pelton. The Na-S (sodium-sulfur) system. *Journal of phase equilibria*, 18(1):89–96, 1997.

[92] H. Sato, T. Minami, S. Takata, and T. Yamada. Transparent conducting p-type NiO thin films prepared by magnetron sputtering. *Thin solid films*, 236(1):27–31, 1993.

[93] A. G. Schaufuß, H. W. Nesbitt, I. Kartio, K. Laajalehto, G. M. Bancroft, and R. Szargan. Incipient oxidation of fractured pyrite surfaces in air. *Journal of Electron Spectroscopy and Related Phenomena*, 96(1):69–82, 1998.

[94] H. Scheel. Crystallization of sulfides from alkali polysulfide fluxes. *Journal of Crystal Growth*, 24:669–673, 1974.

[95] R. Schieck, A. Hartmann, S. Fiechter, R. Könenkamp, and H. Wetzel. Electrical properties of natural and synthetic pyrite (FeS_2) crystals. *Journal of Materials Research*, 5(07):1567–1572, 1990.

[96] A. Schlegel and P. Wachter. Optical properties, phonons and electronic structure of iron pyrite (FeS_2). *Journal of Physics C: Solid State Physics*, 9(17):3363, 1976.

[97] S. Seefeld, M. Limpinsel, Y. Liu, N. Farhi, A. Weber, Y. Zhang, N. Berry, Y. J. Kwon, C. L. Perkins, J. C. Hemminger, et al. Iron pyrite thin films synthesized from an $Fe(acac)_3$ ink. *Journal of the American Chemical Society*, 135(11):4412–4424, 2013.

[98] J. Y. Seto. The electrical properties of polycrystalline silicon films. *Journal of Applied Physics*, 46(12):5247–5254, 1975.

[99] B. Shklovskii and A. Efros. *Electronic Properties of Doped Semiconductors*. Springer, Berlin, 1984.

[100] W. Sproul. Practice of reactive sputter deposition. AVS Short Course Program, October 2012.

[101] S. Suga, K. Inoue, M. Taniguchi, S. Shin, M. Seki, K. Sato, and T. Teranishi. Vacuum ultraviolet reflectance spectra and band structures of pyrites (FeS_2, CoS_2 and NiS_2) Nio measured with synchrotron radiation. *Journal of the Physical Society of Japan*, 52(5):1848–1856, 1983.

[102] R. Sun, M. Chan, and G. Ceder. First-principles electronic structure and relative stability of pyrite and marcasite: Implications for photovoltaic performance. *Physical Review B*, 83(23):235311, 2011.

[103] S. M. Sze and K. K. Ng. *Physics of Semiconductor Devices*. Wiley, 3rd edition, 2007.

[104] N. Takahashi, T. Sawada, T. Nakamura, and T. Nakamura. Preparation of pyrite thin films by atmosphericpressure chemical vapor deposition using $FeCl_3$ and CH_3CSNH_2. *J. Mater. Chem.*, 10(10):2346–2348, 2000.

[105] T. Thio and J. Bennett. Hall effect and conductivity in pyrite NiS_2. *Physical Review B*, 50(15):10574, 1994.

[106] B. Thomas, T. Cibik, C. Höpfner, K. Diesner, G. Ehlers, S. Fiechter, and K. Ellmer. Formation of secondary iron-sulphur phases during the growth of polycrystalline iron pyrite (FeS_2) thin films by MOCVD. *Journal of Materials Science: Materials in Electronics*, 9(1):61–64, 1998.

[107] B. Thomas, K. Diesner, T. Cibik, and K. Ellmer. Phase transitions during the deposition of polycrystalline iron pyrite (FeS_2)-layers by low-pressure metalorganic chemical vapor deposition. *Solid State Phenomena*, 51:301–308, 1996.

[108] Y. Tomm, R. Schieck, K. Ellmer, and S. Fiechter. Growth mechanism and electronic properties of doped pyrite (FeS_2) crystals. *Journal of crystal growth*, 146(1):271–276, 1995.

[109] L. Vadkhiya and B. Ahuja. Electronic and optical properties of iron pyrite. *Journal of Alloys and Compounds*, 509(6):3042–3047, 2011.

[110] L. J. Van der Pauw. A method of measuring specific resistivity and hall effect of discs of arbitrary shape. Technical report, Philips, 1958.

[111] G. Von Oertzen, R. Jones, and A. R. Gerson. Electronic and optical properties of Fe, Zn and Pb sulfides. *Physics and chemistry of minerals*, 32(4):255–268, 2005.

[112] G. Von Oertzen, W. M. Skinner, and H. Nesbitt. Ab initio and xps studies of pyrite (100) surface states. *Radiation Physics and Chemistry*, 75(11):1855–1860, 2006.

[113] C. Wadia, A. P. Alivisatos, and D. M. Kammen. Materials availability expands the opportunity for large-scale photovoltaics deployment. *Environ. Sci. Technol.*, 43(6):2072–2077, Feb. 2009.

[114] P. Walder and A. Pelton. Thermodynamic modeling of the fe-s system. *Journal of phase equilibria and diffusion*, 26(1):23–38, 2005.

[115] D. Wan, Y. Wang, B. Wang, C. Ma, H. Sun, and L. Wei. Effects of the crystal structure on electrical and optical properties of pyrite FeS_2 films prepared by thermally sulfurizing iron films. *Journal of crystal growth*, 253(1):230–238, 2003.

[116] A. Weber, M. Limpinsel, N. Farhi, and M. Law. A low-toxic ink using elemental precursors for fabricating pyrite thin films. manuscript in preparation, 2015.

[117] J. Werner. Origin of curved Arrhenius plots for the conductivity of polycrystalline semiconductors. *Solid State Phenomena*, 37-38:213–218, 1994.

[118] N. E. Widjonarko, E. L. Ratcliff, C. L. Perkins, A. K. Sigdel, A. Zakutayev, P. F. Ndione, D. T. Gillaspie, D. S. Ginley, D. C. Olson, and J. J. Berry. Sputtered nickel oxide thin film for efficient hole transport layer in polymer–fullerene bulk-heterojunction organic solar cell. *Thin solid films*, 520(10):3813–3818, 2012.

[119] G. Willeke, O. Blenk, C. Kloc, and E. Bucher. Preparation and electrical transport properties of pyrite (FeS_2) single crystals. *Journal of alloys and compounds*, 178(1):181–191, 1992.

[120] A. Yamamoto, M. Nakamura, A. Seki, E. Li, A. Hashimoto, and S. Nakamura. Pyrite (FeS_2) thin films prepared by spray method using $FeSO_4$ and $(NH_4)_2S_x$. *Solar energy materials and solar cells*, 75(3):451–456, 2003.

[121] T.-R. Yang, J.-T. Yu, J.-K. Huang, S.-H. Chen, M.-Y. Tsay, and Y.-S. Huang. Optical-absorption study of synthetic pyrite FeS_2 single crystals. *Journal of applied physics*, 77(4):1710–1714, 1995.

[122] J.-H. Yoon, S. Cho, W. M. Kim, J.-K. Park, Y.-J. Baik, T. S. Lee, T.-Y. Seong, and J.-h. Jeong. Optical analysis of the microstructure of a Mo back contact for $Cu(In,Ga)Se_2$ solar cells and its effects on Mo film properties and Na diffusivity. *Solar Energy Materials and Solar Cells*, 95(11):2959–2964, 2011.

[123] J.-H. Yoon, T.-Y. Seong, and J.-h. Jeong. Effect of a Mo back contact on Na diffusion in CIGS thin film solar cells. *Progress in Photovoltaics: Research and Applications*, 21(1):58–63, 2013.

[124] L. Yu, S. Lany, R. Kykyneshi, V. Jieratum, R. Ravichandran, B. Pelatt, E. Altschul, H. A. S. Platt, J. F. Wager, D. A. Keszler, and A. Zunger. Iron chalcogenide photovoltaic absorbers. *Adv. Energy Mater.*, 1(5):748–753, 2011.

[125] A. Zabrodskii and K. Zinoveva. Low-temperature conductivity and metal–insulator transition in compensate n-Ge. *Zh. Eksp. Teor. Fiz*, 86:742, 1984.

[126] X. Zhang, M. Manno, A. Baruth, M. Johnson, E. S. Aydil, and C. Leighton. Crossover from nanoscopic intergranular hopping to conventional charge transport in pyrite thin films. *ACS nano*, 7(3):2781–2789, 2013.

[127] Y. N. Zhang, J. Hu, M. Law, and R. Q. Wu. Effect of surface stoichiometry on the band gap of the pyrite FeS_2(100) surface. *Phys. Rev. B*, 85(8):085314–, Feb. 2012.

Appendix A

Elemental Purity of Materials Used

MOMENTIVE™

Typical Trace Element Composition (ppm by weight) Analysis via Direct Reading Spectrometer

Type	Al	Ca	Cu	Fe	Li	Mg	Mn	K	Na	Ti	Zr	*OH-
214	15	0.4	<0.05	0.2	0.6	0.1	<0.05	0.6	0.8	1.0	0.9	<5
219	15	0.4	<0.05	0.2	0.6	0.1	<0.05	1.0	0.8	na	0.9	<5
254	15	0.6	<0.05	0.2	0.6	0.1	<0.05	2.2	1.2	na	1.6	<5
214A	15	0.4	<0.05	0.2	0.6	0.1	<0.05	0.6	0.8	1.0	0.9	<1
214 Rod	15	0.4	<0.05	0.2	0.6	0.1	<0.05	0.6	0.8	1.0	0.9	10
214 LD/SC	15	0.4	<0.05	0.2	0.6	0.1	<0.05	0.6	0.8	1.0	0.9	10
224/224 Rod	8	0.6	<0.009	0.2	0.2	<0.1	<0.05	<0.2	<0.2	1.4	0.3	10
224 LD	15	0.4	<0.009	0.2	0.001	0.1	<0.05	0.4	<0.05	1.0	0.9	10
244	8	0.6	<0.05	0.2	0.2	<0.1	<0.05	<0.2	<0.2	1.4	0.3	10
244 Rod	8	0.6	<0.009	0.2	0.2	<0.1	<0.05	<0.2	<0.2	1.4	0.3	10
244 LD	8	0.6	<0.009	0.2	0.001	0.1	<0.05	0.2	<0.05	1.4	0.3	10
124	15	0.4	<0.05	0.2	0.6	0.1	<0.05	0.6	0.8	1.0	0.9	<5
144	8	0.6	<0.009	0.2	0.2	<0.1	<0.05	<0.2	<0.4	1.4	0.6	<5
098	0.2	<0.05	<0.03	0.08	<0.05	<0.05	<0.02	<0.05	<0.05	<0.02	na	10
095	11	<0.05	<0.03	0.08	<0.05	<0.05	<0.02	<0.05	<0.05	<0.02	na	< 10
510,520,530	15	0.4	<0.05	0.2	0.5	0.1	<0.05	0.6	0.8	1.0	0.9	50
512, 532	8	0.6	<0.05	0.2	0.3	<0.1	<0.05	0.5	0.7	1.4	0.2	50
567, 587	15	0.4	<0.05	0.2	<0.005	0.1	<0.05	<0.02	<0.01	1.0	0.9	70
568, 588	8	0.6	<0.05	0.2	<0.005	<0.1	<0.05	<0.02	<0.01	1.4	0.2	70

This table shows the typical levels of the trace elements that are routinely monitored by Momentive Performance Materials, as well as the hydroxyl level. Please note they are typical levels, but not the maximum allowed levels specified by Momentive. Typical levels are not, and should not be used as, specifications.
*Types 214 LD and 224 LD may contain a higher amount of surface hydroxyl (OH) ions, but the values represent a bulk average for the total wall thickness

Figure A.1: Typical trace element composition of the type 214 quartz ampoules used in this study. Figure reproduced from [70].

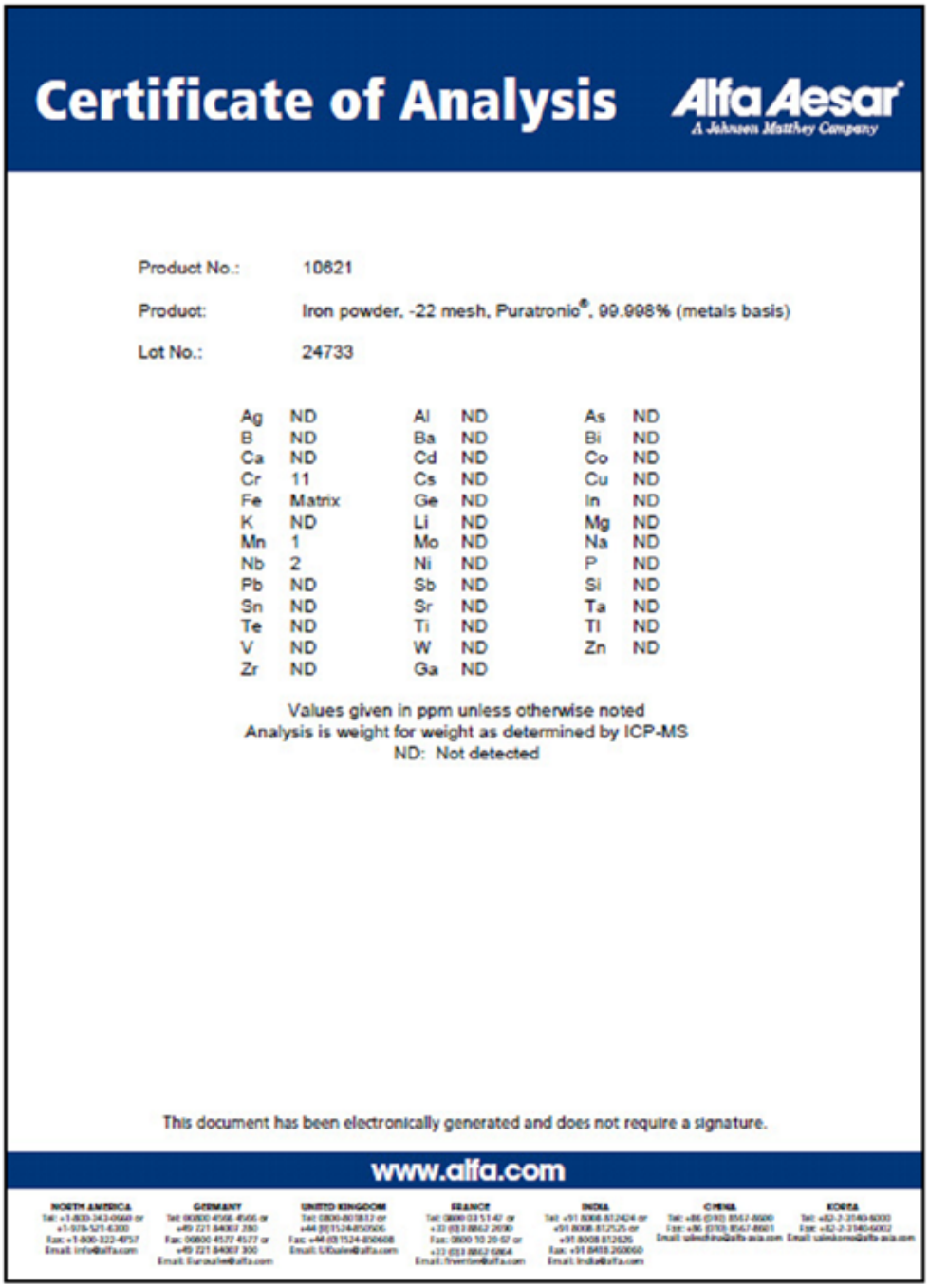

Certificate of Analysis

Alfa Aesar
A Johnson Matthey Company

Product No.: 10621

Product: Iron powder, -22 mesh, Puratronic®, 99.998% (metals basis)

Lot No.: 24733

Ag	ND	Al	ND	As	ND
B	ND	Ba	ND	Bi	ND
Ca	ND	Cd	ND	Co	ND
Cr	11	Cs	ND	Cu	ND
Fe	Matrix	Ge	ND	In	ND
K	ND	Li	ND	Mg	ND
Mn	1	Mo	ND	Na	ND
Nb	2	Ni	ND	P	ND
Pb	ND	Sb	ND	Si	ND
Sn	ND	Sr	ND	Ta	ND
Te	ND	Ti	ND	Tl	ND
V	ND	W	ND	Zn	ND
Zr	ND	Ga	ND		

Values given in ppm unless otherwise noted
Analysis is weight for weight as determined by ICP-MS
ND: Not detected

This document has been electronically generated and does not require a signature.

www.alfa.com

NORTH AMERICA GERMANY UNITED KINGDOM FRANCE INDIA CHINA KOREA

Figure A.2: Certificate of analysis for a batch of the iron powder used for pyrite flux synthesis. Figure reproduced from [70].

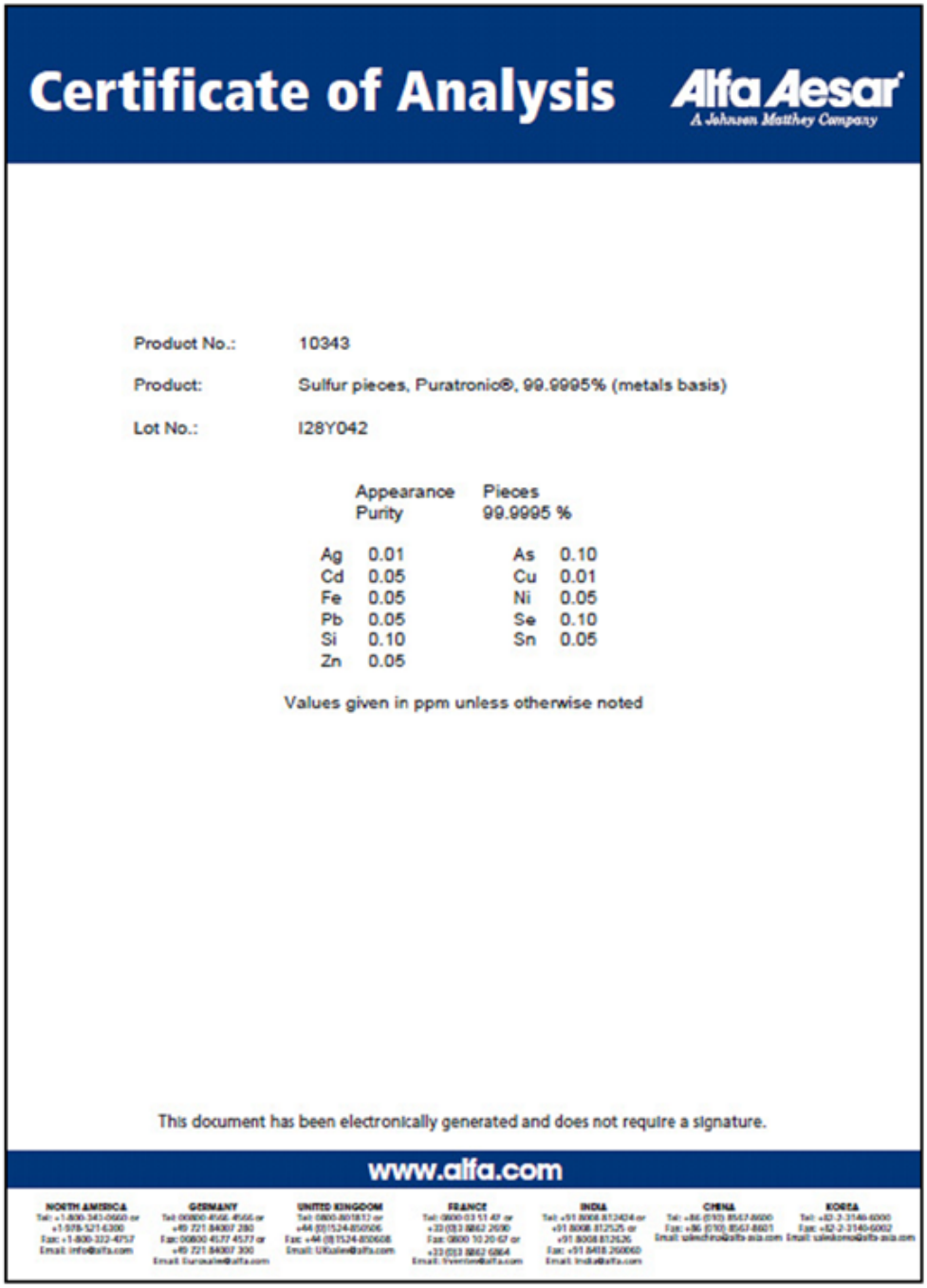

Certificate of Analysis

Alfa Aesar
A Johnson Matthey Company

Product No.: 10343

Product: Sulfur pieces, Puratronic®, 99.9995% (metals basis)

Lot No.: I28Y042

Appearance	Pieces
Purity	99.9995 %

Ag	0.01	As	0.10
Cd	0.05	Cu	0.01
Fe	0.05	Ni	0.05
Pb	0.05	Se	0.10
Si	0.10	Sn	0.05
Zn	0.05		

Values given in ppm unless otherwise noted

This document has been electronically generated and does not require a signature.

www.alfa.com

NORTH AMERICA GERMANY UNITED KINGDOM FRANCE INDIA CHINA KOREA

Figure A.3: Certificate of analysis for a batch of the sulfur powder used for pyrite flux synthesis. Figure reproduced from [70].

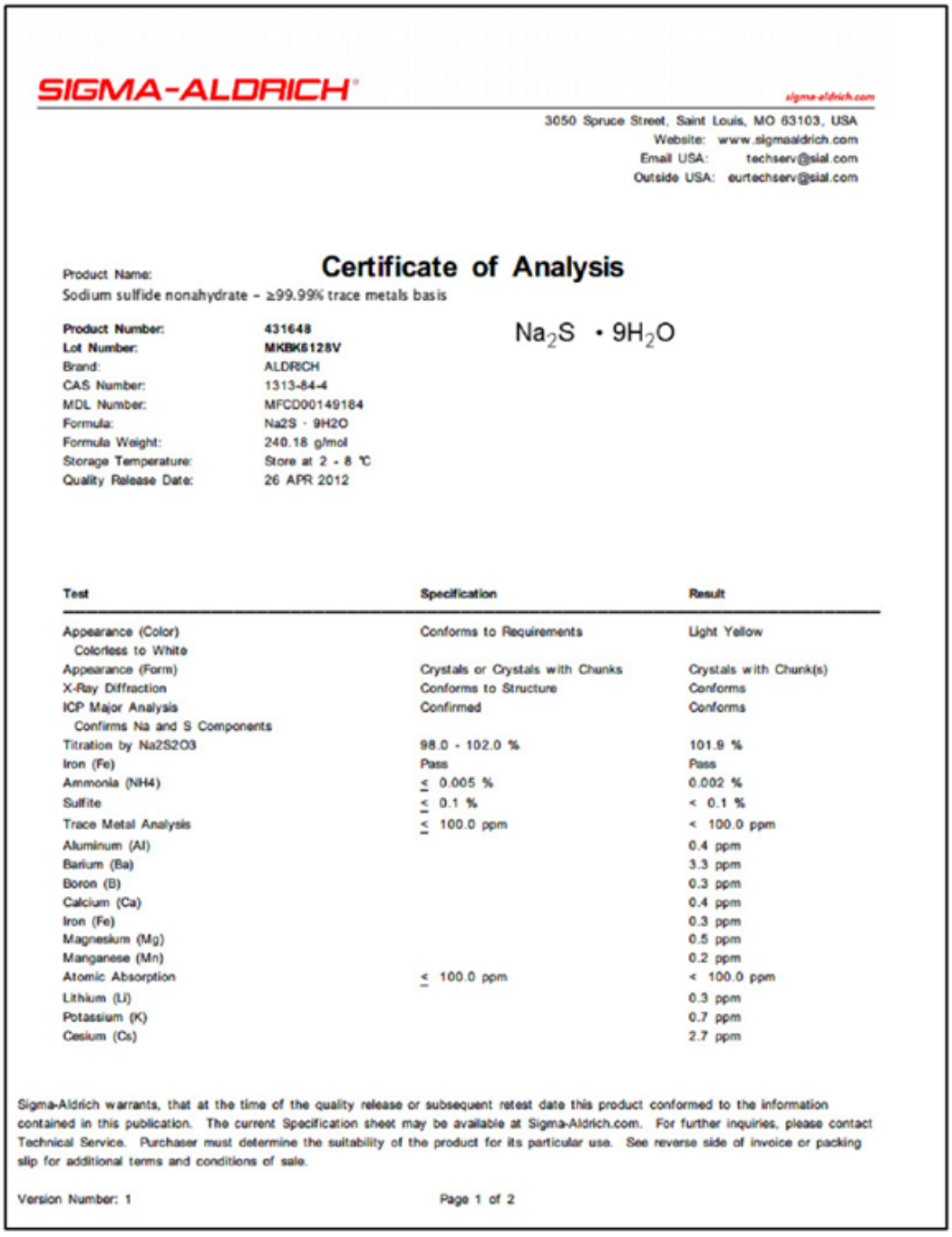

SIGMA-ALDRICH®

sigma-aldrich.com

3050 Spruce Street, Saint Louis, MO 63103, USA
Website: www.sigmaaldrich.com
Email USA: techserv@sial.com
Outside USA: eurtechserv@sial.com

Certificate of Analysis

Product Name:
Sodium sulfide nonahydrate – ≥99.99% trace metals basis

$Na_2S \cdot 9H_2O$

Product Number:	**431648**
Lot Number:	**MKBK6128V**
Brand:	ALDRICH
CAS Number:	1313-84-4
MDL Number:	MFCD00149184
Formula:	Na2S · 9H2O
Formula Weight:	240.18 g/mol
Storage Temperature:	Store at 2 - 8 °C
Quality Release Date:	26 APR 2012

Test	Specification	Result
Appearance (Color) Colorless to White	Conforms to Requirements	Light Yellow
Appearance (Form)	Crystals or Crystals with Chunks	Crystals with Chunk(s)
X-Ray Diffraction	Conforms to Structure	Conforms
ICP Major Analysis Confirms Na and S Components	Confirmed	Conforms
Titration by Na2S2O3	98.0 - 102.0 %	101.9 %
Iron (Fe)	Pass	Pass
Ammonia (NH4)	≤ 0.005 %	0.002 %
Sulfite	≤ 0.1 %	< 0.1 %
Trace Metal Analysis	≤ 100.0 ppm	< 100.0 ppm
Aluminum (Al)		0.4 ppm
Barium (Ba)		3.3 ppm
Boron (B)		0.3 ppm
Calcium (Ca)		0.4 ppm
Iron (Fe)		0.3 ppm
Magnesium (Mg)		0.5 ppm
Manganese (Mn)		0.2 ppm
Atomic Absorption	≤ 100.0 ppm	< 100.0 ppm
Lithium (Li)		0.3 ppm
Potassium (K)		0.7 ppm
Cesium (Cs)		2.7 ppm

Sigma-Aldrich warrants, that at the time of the quality release or subsequent retest date this product conformed to the information contained in this publication. The current Specification sheet may be available at Sigma-Aldrich.com. For further inquiries, please contact Technical Service. Purchaser must determine the suitability of the product for its particular use. See reverse side of invoice or packing slip for additional terms and conditions of sale.

Figure A.4: Certificate of analysis for a batch of the Na2S powder used for pyrite flux synthesis. Figure reproduced from [70].

Appendix B

Additional Data and Calculations

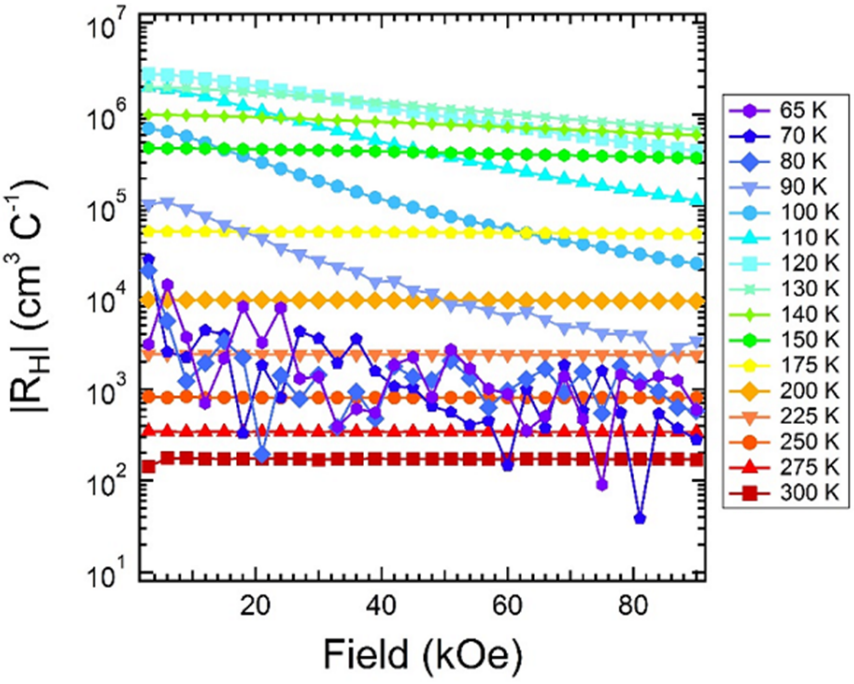

Figure B.1: Representative plots of Hall coefficient versus magnetic field for a pyrite crystal as a function of temperature (65 - 300 K). In the unipolar region (T ¿ 150 K), R_H is constant with field (in other words, the Hall voltage is linear with magnetic field). In the mixed-carrier region (intermediate temperatures), R_H decreases with increasing field. Finally, for T ¡ 90 K, R_H becomes noisy but appears to flatten out with increasing field at higher values of applied field. Figure reproduced from [70].

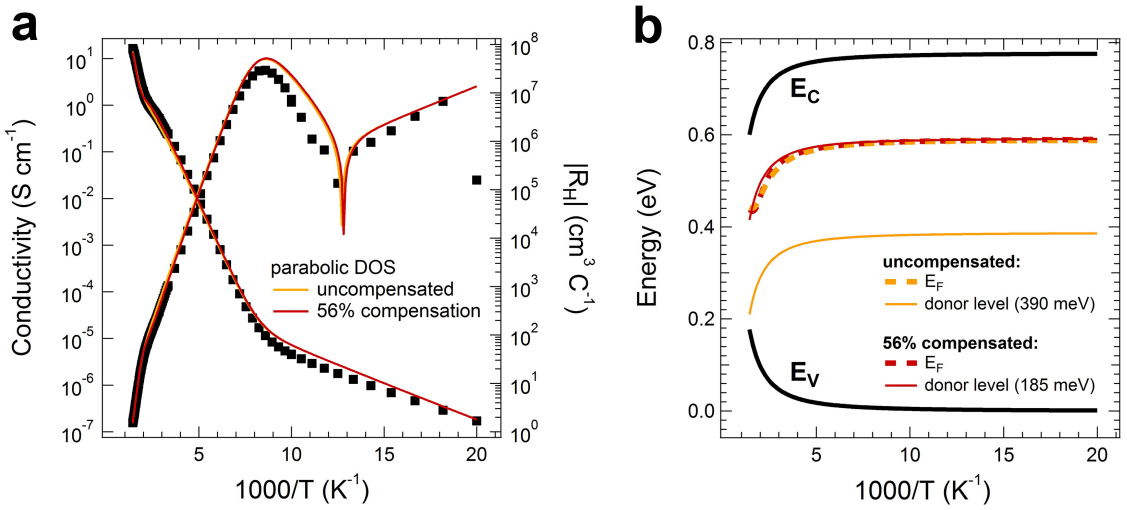

Figure B.2: (a) Comparison of fits to the Hall data of fig. 4.11 assuming zero compensation (yellow traces) and finite compensation (red traces). For the latter, the compensation ratio N_A/N_D was allowed to float freely to achieve a best fit. We found a best fit at 56% compensation with the following bulk parameters: $N_D = 1.0 \times 100^{18}$ cm^{-3}, $E_C - E_D = 185$ meV, $N_{A,bulk} = 5.6 \times 100^{17}$ cm^{-3}, E_A - $E_V = 50$ meV. (b) Comparison of E_D and the Fermi level E_F as a function of inverse temperature for the uncompensated case (yellow) and 56% compensated case (red). Figure reproduced from [70].

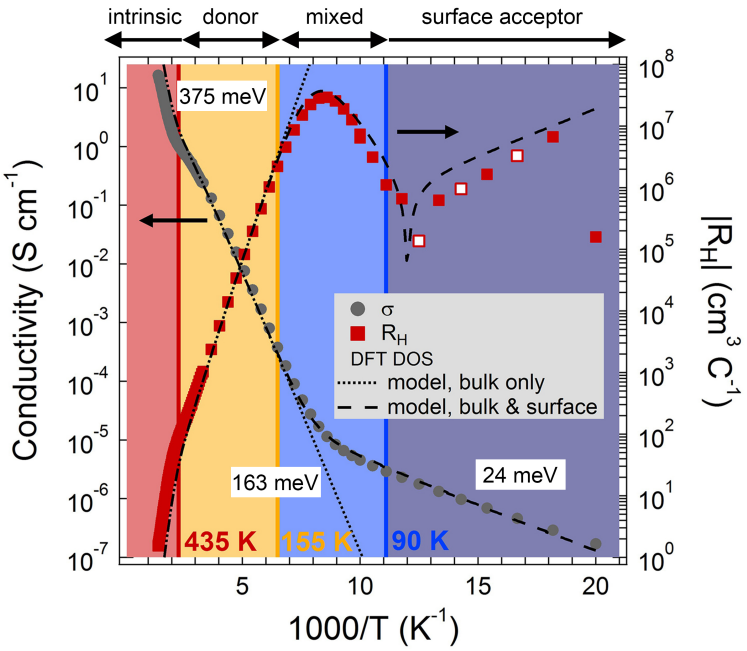

Figure B.3: Hall data modeled using the DFT DOS(E) values and the Fermi-Dirac distribution function. Zero compensation is assumed. Parameters used are $N_{D,bulk} = 5.6 \times 10^{19}$ cm^{-3}; E_C - E_D = 380 meV; $N_{A,surface} = 4.5 \times 10^{19}$ cm^{-3}; E_A - E_V = 50 meV; d_s = 4.4 nm; μ_h = 2.5 cm^2/Vs. Figure reproduced from [70].

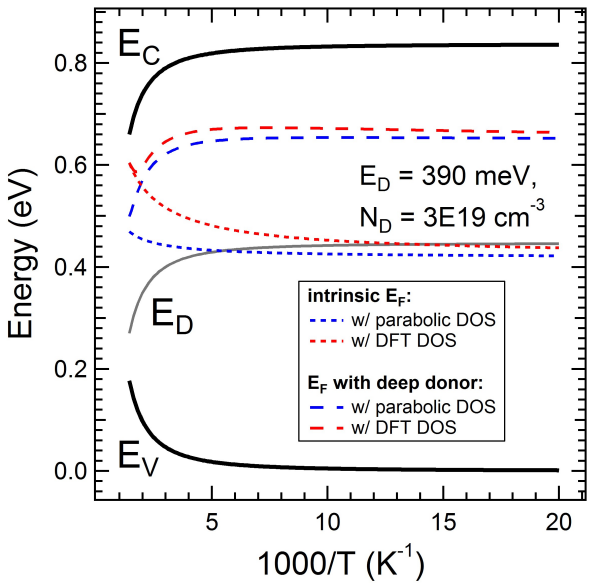

Figure B.4: Comparison of the calculated Fermi level as a function of inverse temperature using the parabolic DOS(E) versus DFT DOS(E) functions. Results are shown for both intrinsic pyrite and pyrite with a deep donor (gray line). Zero compensation is assumed. Figure reproduced from [70].

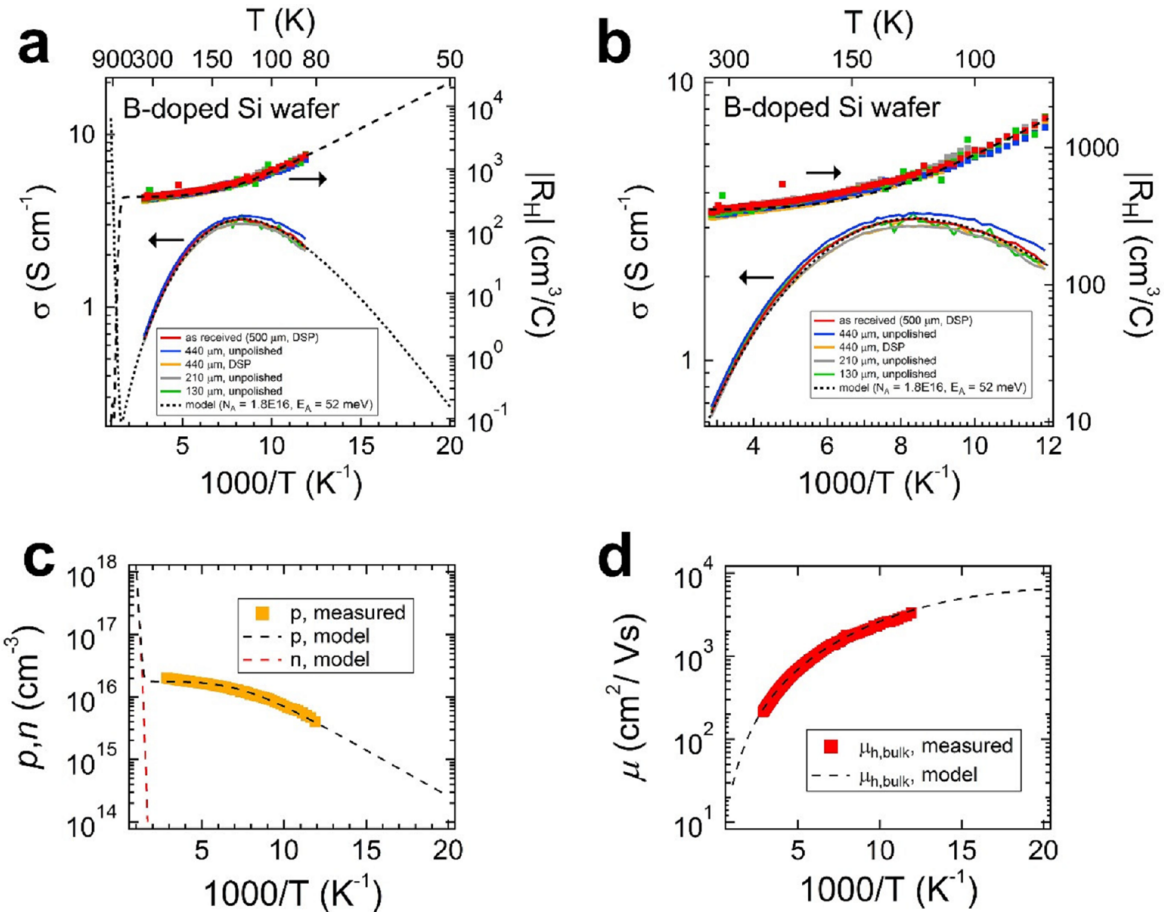

Figure B.5: (a) Temperature dependence of the Hall coefficient and conductivity of a boron-doped silicon single crystal as a function of crystal thickness. The data (80 - 350 K) are independent of thickness and surface polishing, showing that silicon lacks the type of conductive surface layer found on pyrite. The dotted/dashed curves are fits from the model (giving an acceptor concentration of 1.8×10^{16} cm^{-3} and an ionization energy of 52 meV, close to the accepted value of 45 meV for boron in silicon). DSP = double side polished. (b) Magnified view of the temperature range from 80 - 350 K. (c) Carrier concentration and (d) mobility for the as-received 500 μm thick wafer. These control experiments provide additional confirmation that our model and interpretation of the pyrite data are correct. Figure reproduced from [70].

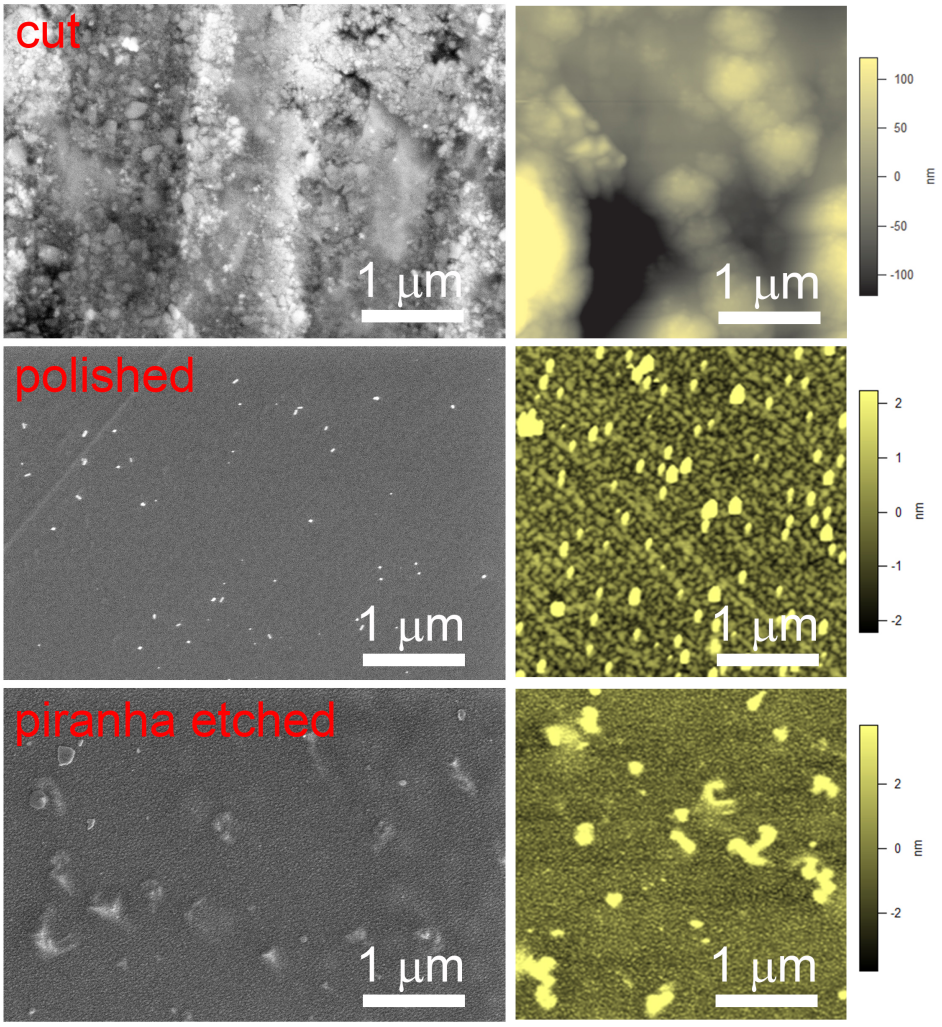

Figure B.6: SEM and AFM images of the surface of a pyrite crystal (top) as cut with a diamond saw, (middle) after fine polishing, and (bottom) after etching the surface with piranha solution. Figure reproduced from [70].

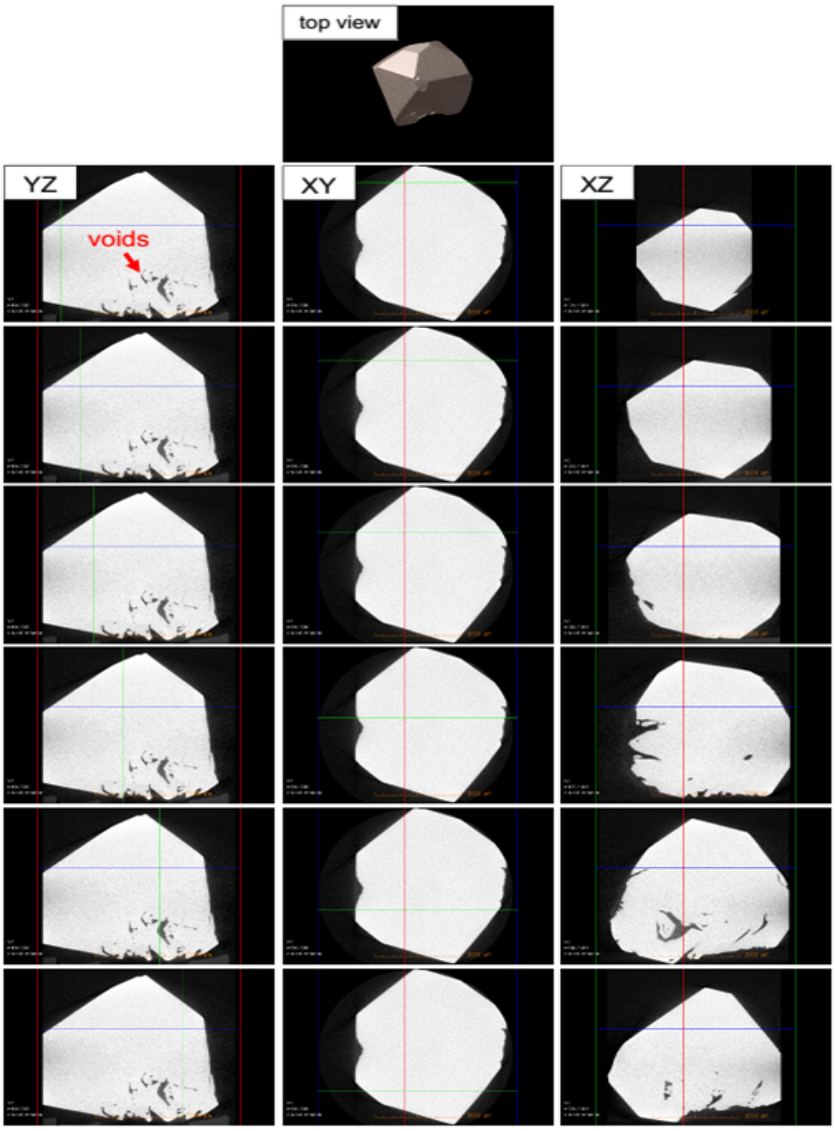

Figure B.7: X-ray tomography images of a flux-grown pyrite crystal. (*top*) Top view of a 3D reconstruction of the crystal. (*left column*) Images of a yz cut through the crystal. The horizontal blue line denotes the position of the xy cut shown in the middle column. The vertical green lines denote the positions of the xz cuts shown in the right column. Voids are present in the bottom half of this crystal. (*middle column*) Images of an xy cut through the crystal. The vertical red line denotes the position of the yz cuts shown in the left column. The horizontal green lines denote the positions of the xz cuts shown in the right column. (*right column*) Images of a series of xz cuts through the crystal, showing voids only in the lower half of the specimen. The scale bar is 2 mm. Figure reproduced from [70].

Appendix C

Igor Pro Fitting Procedure

```
// MODELING OF TEMPERATURE-DEPENDENT HALL EFFECT AND CONDUCTIVITY DATA
// tested in Igor Pro 6.37
//
//
// This data fitting routine was developed for better insight into iron pyrite (FeS2) single crystals,
// but is also particularly suited for all other pyrite materials, all other semiconductors with inversion
// layer, and all other semiconductors in general.
//
// This script is by no means perfect, and many improvements should be made. But it works.
// Moreover, documentation is poor, and might or might not be improved in the future
//
// Credit goes to Dr. Carsten Deibel for teaching me how to use Igor Pro in 2008,
// and Dr. Matt Beard solving some issues with this routine in 2012.
//
// A copy of this procedure file, along with limited technical support from the author is available at:
// moritz@limpinsel.com
//
//
//
// Five easy steps to fit data:
// 1) Input (best guess) material parameters
// 2) Select DOS (option a: run MakeDOS to calculate, option b: import explicit DOS waves)
// 3) Plot conductivity and |RH| vs. 1000/T
// 4) Run local fit for conductivity data, use range restrictions to find decent fit parameters
// 5) Run global fit with these parameters, fitting conductivity and |RH| simultaneously
// 5) Plot output: carrier densities, mobilities, Fermi level etc.... vs. T

#pragma rtGlobals=1        // Use modern global access method.

Menu "Macros"
    SubMenu "Model Hall Effect Data"
        "Input parameters, step 1", HallParametersFE1()
        "Input parameters, step 2", HallParametersFE2()
        "Choose DOS", MakeDOSFE()
    End
End

Macro HallParametersFE1(samplename,Ndb,Nab,Nds,Nas,Edb,Eab,Eds,Eas)
    string samplename
    variable Ndb,Nab,Nds,Nas,Edb,Eab,Eds,Eas
    prompt samplename, "sample ID"
    prompt Ndb, "log of bulk donor concentration"
    prompt Nab, "log of bulk acceptor concentration"
    prompt Nds, "log of surface donor concentration"
    prompt Nas, "log of surface acceptor concentration"
    prompt Edb, "ionization energy of bulk donor"
    prompt Eab, "ionization energy of bulk acceptor"
    prompt Eds, "ionization energy of surface donor"
    prompt Eas, "ionization energy of surface acceptor"
    HallParameters1(samplename,Ndb,Nab,Nds,Nas,Edb,Eab,Eds,Eas)
End

Macro HallParametersFE2(samplename,ds,me,mh,mue,muh,Egap0)
    string samplename
    variable ds,me,mh,mue,muh,Egap0
    prompt samplename, "sample ID"
```

```
	prompt ds, "log of thickness ratio surface/bulk"
	prompt me, "effective electron mass"
	prompt mh, "effective hole mass"
	prompt mue, "electron mobility at RT"
	prompt muh, "hole mobility at RT"
	prompt Egap0, "band gap at 0K"
	HallParameters2(samplename,ds,me,mh,mue,muh,Egap0)
End

Macro MakeDOSFE(samplename,flag2)
	string samplename
	variable flag2=2
	prompt samplename, "Input sample ID. For explicit DOS: provide 'DOS_CB_ID', 'energy_CB_ID', etc..."
	prompt flag2, "For parabolic DOS: set value to 1."
	MakeDOS(samplename,flag2)
End

function HallParameters1(samplename,Ndb,Nab,Nds,Nas,Edb,Eab,Eds,Eas)
	string samplename
	variable Ndb,Nab,Nds,Nas,Edb,Eab,Eds,Eas
	string wcoef="wcoef_"+samplename
	Make/O/N=17 $wcoef
	wave w=$wcoef
	w[0]=Ndb
	w[1]=Nab
	w[2]=Nds
	w[3]=Nas
	w[4]=Edb
	w[5]=Eab
	w[6]=Eds
	w[7]=Eas
end

function HallParameters2(samplename,ds,me,mh,mue,muh,Egap0)
	string samplename
	variable ds,me,mh,mue,muh,Egap0
	string wcoef="wcoef_"+samplename
	Make/O/N=17 $wcoef
	wave w=$wcoef
	w[8]=ds
	w[9]=me
	w[10]=mh
	w[11]=mue
	w[12]=muh
	w[13]=Egap0
end

Function MakeDOS(samplename,flag2)
	string samplename
	variable flag2
	string wcoef="wcoef_"+samplename
	wave w=$wcoef
	variable Eg=w[13], me=w[9], mh=w[10]
	w[15]=flag2
	Make/O/N=200 DOS_CB, DOS_VB, energy_CB, energy_VB
	if (flag2==1) //parabolic DOS
```

```
        variable EC=Eg, EV=0
        variable q=1.602e-19, h=6.626e-34
        me=me*9.11e-31
        mh=mh*9.11e-31
        energy_CB=EC+x*0.01
        energy_VB=EV-x*0.01
        DOS_CB=8*pi*Sqrt(2)*me^1.5/h^3*q^1.5*Sqrt(energy_CB-EC)/1e6
        DOS_VB=8*pi*Sqrt(2)*mh^1.5/h^3*q^1.5*Sqrt(EV-energy_VB)/1e6
    else //explicit DOS
        string DOSCB="DOS_CB_"+samplename, DOSVB="DOS_VB_"+samplename, enCB="energy_CB_"
        wave w1=$DOSCB, w2=$DOSVB, w3=$enCB, w4=$enVB
        DOS_CB=w1
        DOS_VB=w2
        energy_CB=w3
        energy_VB=w4
    endif
end

function fitHall(w,y,Twave): fitfunc
    wave w,y,Twave
    variable ds=10^w[8], mue=w[11], muh=w[12], Egap0=w[13], flag1=w[14]
    Wavestats/Q Twave
    variable i=0, imax=V_npnts
    variable EFb,EFs,nb,pb,ns,ps, mueb, muhb, mues, muhs, cb,cs,c, RHb, RHs,RH
    variable k=8.62e-5, q=1.602e-19, h=6.626e-34, hbar=1.055e-34
    variable g=1, me=w[9]*9.11e-31, mh=w[10]*9.11e-31
    variable db=1

    variable timer1=StartMSTimer
   i=0
   do
    variable T=1000/Twave[i] // => take T from Twave
    variable fullTshrink = (1.89e-3*T^2) / (T+1915) //from Karguppikar1988
    variable Egap=Egap0 - fullTshrink  //results in Eg(0K) - Eg(300K) = 0.077 eV
    variable EV= 0 + fullTshrink/2
    variable EC= Egap0 - fullTshrink/2
    w[16] = T // pass on parameter wave with T to bulk function
    FindRoots/Q/L=0/H=(Egap) bulk, w
    EFb=V_Root
    FindRoots/Q/L=0/H=(Egap) surf, w
    EFs=V_Root

    //calculation of n, p:
        wave DOS_CB, energy_CB, DOS_VB, energy_VB
        Make/O/N=200 zwickelCBbulk, zwickelVBbulk ,zwickelCBsurf, zwickelVBsurf
        //include offset to set band edge to DOS edge at every T:
        Duplicate/O energy_CB, energy_CB_T
        Duplicate/O energy_VB, energy_VB_T
        energy_CB_T=energy_CB - (energy_CB[0] - EC)
        energy_VB_T=energy_VB - (energy_VB[0] - EV)
        //calculate carrier concentration from integration over DOS(E)*f(E):
        zwickelCBbulk=DOS_CB / (exp((energy_CB_T - EFb)/(k*T)) + 1)
        zwickelVBbulk=DOS_VB / (exp((-energy_VB_T + EFb)/(k*T)) + 1)
        zwickelCBsurf=DOS_CB / (exp((energy_CB_T - EFs)/(k*T)) + 1)
        zwickelVBsurf=DOS_VB / (exp((-energy_VB_T + EFs)/(k*T)) + 1)
        nb = areaXY(energy_CB_T,zwickelCBbulk,EC,2)
```

```
        pb = areaXY(energy_VB_T,zwickelVBbulk,-1,EV)
        ns = areaXY(energy_CB_T,zwickelCBsurf,EC,2)
        ps = areaXY(energy_VB_T,zwickelVBsurf,-1,EV)

    // carrier mobilities
    mueb=11*(0.07 / ( 1/(1.2e5*mue*T^-2.0) + 1/ (150e-4*mue*T^1.5)))      //adjust numbers based on experiment
    muhb=mueb*me/mh                 //assumption
    mues=muh                        //assumption
    muhs=muh                        //assumption

    cb=q*(nb*mueb + pb*muhb)
    cs=q*(ns*mues + ps*muhs)
    c=cb*db+cs*ds
    RHb=q*(pb*muhb^2-nb*mueb^2)/cb^2
    RHs=q*(ps*muhs^2-ns*mues^2)/cs^2
    RH=abs( RHb*(cb/c)^2*db/1 +  RHs*(cs/c)^2*ds/1 ) //eqn (2) in petritz1958
    if(flag1==1)
        y[i]=c // =>write y-wave
    endif
    if(flag1==2)
        y[i]=abs(RH) // =>write y-wave
    endif
    i=i+1
    while(i<imax)
    layersolver(Twave, w,"fit") //make waves (n,p,EF, etc...) for plotting
    variable t1=StopMSTimer(timer1)*1e-6
    print "all in all, this took ",t1, " seconds"
end

Function bulk(w,EF) //solves charge neutrality eqn for EF, given parameters  and T in wave w
    wave w // parameter wave (wcoef)
    variable EF
    variable Edb=w[4], Ndb=10^w[0], Eab=w[5], Nab=10^w[1], Egap0=w[13], T=w[16]
    variable k=8.62e-5, q=1.602e-19, h=6.626e-34
    variable g=1, me=w[9]*9.11e-31, mh=w[10]*9.11e-31
    variable fullTshrink = (1.89e-3*T^2) / (T+1915)
    variable Egap=Egap0 - fullTshrink
    variable EV= 0 + fullTshrink/2
    variable EC= Egap0 - fullTshrink/2
    variable Ndbi = Ndb / (1 + g * Exp( (EF-EC+Edb)/(k*T) ) )
    variable Nabi = Nab / (1 + g * Exp((Eab+EV-EF)/(k*T) ) )

    //calculation of n, p:
        wave DOS_CB, energy_CB, DOS_VB, energy_VB
        Make/O/N=200 zwickelCBbulk, zwickelVBbulk
        //include offset to set band edge to DOS edge at every T:
        Duplicate/O energy_CB, energy_CB_T
        Duplicate/O energy_VB, energy_VB_T
        energy_CB_T=energy_CB - (energy_CB[0] - EC)
        energy_VB_T=energy_VB - (energy_VB[0] - EV)
        //calculate carrier concentration from integration over DOS(E)*f(E):
        zwickelCBbulk=DOS_CB / (exp((energy_CB_T - EF)/(k*T)) + 1)
        zwickelVBbulk=DOS_VB / (exp((-energy_VB_T + EF)/(k*T)) + 1)
        variable n = areaXY(energy_CB_T,zwickelCBbulk,EC,2)
        variable p = areaXY(energy_VB_T,zwickelVBbulk,-1,EV)
```

```
    return Ndbi + p - n - Nabi
end

Function surf(w,EF) //solves charge neutrality eqn for EF, given parameters  and T in wave w
    wave w // parameter wave = {Ed1, Nd1, Eab, Nab, Eas, Nas, ds, b=mue/muh, T}
    variable EF
    variable Eds=w[6], Nds=10^w[2], Eas=w[7], Nas=10^w[3], Egap0=w[13],T=w[16]

    variable k=8.62e-5, q=1.602e-19, h=6.626e-34
    variable g=1, me=w[9]*9.11e-31, mh=w[10]*9.11e-31
    variable fullTshrink = (1.89e-3*T^2) / (T+1915)
    variable Egap=Egap0 - fullTshrink
    variable EV= 0 + fullTshrink/2
    variable EC= Egap0 - fullTshrink/2
    variable Ndsi = Nds / (1 + g * Exp( (EF-EC+Eds)/(k*T) ) )
    variable Nasi = Nas / (1 + g * Exp((Eas+EV-EF)/(k*T) ) )

    //calculation of n, p:
        wave DOS_CB, energy_CB, DOS_VB, energy_VB
        Make/O/N=200 zwickelCBsurf, zwickelVBsurf
        //include offset to set band edge to DOS edge at every T:
        Duplicate/O energy_CB, energy_CB_T
        Duplicate/O energy_VB, energy_VB_T
        energy_CB_T=energy_CB - (energy_CB[0] - EC)
        energy_VB_T=energy_VB - (energy_VB[0] - EV)
        //calculate carrier concentration from integration over DOS(E)*f(E):
        zwickelCBsurf=DOS_CB / (exp((energy_CB_T - EF)/(k*T)) + 1)
        zwickelVBsurf=DOS_VB / (exp((-energy_VB_T + EF)/(k*T)) + 1)
        variable n = areaXY(energy_CB_T,zwickelCBsurf,EC,2)
        variable p = areaXY(energy_VB_T,zwickelVBsurf,-1,EV)

    return p - n - Nasi + Ndsi
end

Macro BatchSolver(Twave,w,out,i,Vmin,Vmax,dV)
    wave Twave,w
    string out
    variable,i,Vmin,Vmax,dV,V
    variable n=(Vmax-Vmin)/dV+1

    variable j=0
    do V=Vmin+dV*j
    w[i]=V
    string outn=out+num2str(V)
    LayerSolver(Twave,w,outn)
    j=j+1
    while j<n+1
end

Function LayerSolver(Twave,w,out) //creates waves for EC,EV,EF,n,p, ... for a parameter set given by w
    //calls functions bulk and surf for each T-point given in Twave
    wave Twave,w
    string out
    variable ds=10^w[8], mue=w[11], muh=w[12], Egap0=w[13]
    Wavestats/Q Twave
    string iTout="invT_"+out //make invT wave for fit outputs
```

```
Duplicate/O Twave, $iTout

variable i=0, imax=V_npnts
Make/N=(imax)/O EC
Make/N=(imax)/O EV
Make/N=(imax)/O EFbulk
Make/N=(imax)/O EFsurf
Make/N=(imax)/O nbulk
Make/N=(imax)/O pbulk
Make/N=(imax)/O ni
Make/N=(imax)/O nsurf
Make/N=(imax)/O psurf
Make/N=(imax)/O debye
Make/N=(imax)/O mueb
Make/N=(imax)/O muhb
Make/N=(imax)/O mues
Make/N=(imax)/O muhs
Make/N=(imax)/O cbulk
Make/N=(imax)/O csurf
Make/N=(imax)/O RHbulk
Make/N=(imax)/O RHsurf
Make/N=(imax)/O cond
Make/N=(imax)/O RH
wave EC,EV,EFbulk, EFsurf, nbulk, pbulk, ni, nsurf, psurf, l_debye, mueb, muhb, mues, muhs, cbulk, csurf,
variable k=8.62e-5, q=1.602e-19, h=6.626e-34, hbar=1.055e-34
variable g=1, me=w[9]*9.11e-31, mh=w[10]*9.11e-31, eps=21,eps0=8.854e-12
variable db=1

do
variable T=1000/Twave[i]
w[16]=T
variable Egap=Egap0 - (1.89e-3*T^2) / (T+1915) //results in Eg(0K) - Eg(300K) = 0.077 eV
variable EVB= 0+ (1.89e-3*T^2) / (T+1915) /2
variable ECB= Egap0 - (1.89e-3*T^2) / (T+1915) /2
EC[i]=ECB
EV[i]=EVB
FindRoots/Q/L=0/H=(Egap) bulk, w
variable EFb=V_Root
FindRoots/Q/L=0/H=(Egap) surf, w
variable EFs=V_Root
EFbulk[i]=EFb
EFsurf[i]=EFs

//calculation of DOS, n, p:
    Make/O/N=200 zwickelCBbulk, zwickelVBbulk,zwickelCBsurf, zwickelVBsurf
    wave DOS_CB, energy_CB, DOS_VB, energy_VB
    //include offset to set band edge to DOS edge at every T:
    Duplicate/O energy_CB, energy_CB_T
    Duplicate/O energy_VB, energy_VB_T
    energy_CB_T=energy_CB - (energy_CB[0] - ECB)
    energy_VB_T=energy_VB - (energy_VB[0] - EVB)
    //calculate carrier concentration from integration over DOS(E)*f(E):
    zwickelCBbulk=DOS_CB / (exp((energy_CB_T - EFb)/(k*T)) + 1)
    zwickelVBbulk=DOS_VB / (exp((-energy_VB_T + EFb)/(k*T)) + 1)
    zwickelCBsurf=DOS_CB / (exp((energy_CB_T - EFs)/(k*T)) + 1)
    zwickelVBsurf=DOS_VB / (exp((-energy_VB_T + EFs)/(k*T)) + 1)
```

```
        nbulk[i] = areaXY(energy_CB_T,zwickelCBbulk,ECB,2)
        pbulk[i] = areaXY(energy_VB_T,zwickelVBbulk,-1,EVB)
        nsurf[i] = areaXY(energy_CB_T,zwickelCBsurf,ECB,2)
        psurf[i] = areaXY(energy_VB_T,zwickelVBsurf,-1,EVB)
        ni[i] = Sqrt(nbulk[i]*pbulk[i])

debye[i] = (2*eps*eps0*k*T/q/(nbulk[i]*1e6))^0.5
//// carrier mobilities
mueb[i]=11*(0.07 / ( 1/(1.2e5*mue*T^-2.0) + 1/ (150e-4*mue*T^1.5)))          //adjust numbers based on exp
muhb[i]=mueb[i]*me/mh
mues[i]=muh
muhs[i]=muh

cbulk[i]=q*(nbulk[i]*mueb[i] + pbulk[i]*muhb[i])
csurf[i]=q*(nsurf[i]*mues[i] + psurf[i]*muhs[i])
RHbulk[i]=q*(pbulk[i]*muhb[i]^2-nbulk[i]*mueb[i]^2)/cbulk[i]^2
RHsurf[i]=q*(psurf[i]*muhs[i]^2-nsurf[i]*mues[i]^2)/csurf[i]^2
cond[i]=cbulk[i]*db+csurf[i]*ds //eqn(3) in petritz1958
RH[i]=abs( RHbulk[i]*(cbulk[i]/cond[i])^2*db/1 +  RHsurf[i]*(csurf[i]/cond[i])^2*ds/1 )
i=i+1
while(i<imax)

string ECout="EC_"+out
string EVout="EV_"+out
string EFbout="EFb_"+out
string EFsout="EFs_"+out
string nbout="nb_"+out
string pbout="pb_"+out
string niout="ni_"+out
string nsout="ns_"+out
string psout="ps_"+out
string debyeout="l_debye_"+out
string muebout="mueb_"+out
string muhbout="muhb_"+out
string muesout="mues_"+out
string muhsout="muhs_"+out
string cbout="cb_"+out
string csout="cs_"+out
string RHbout="RHb_"+out
string RHsout="RHs_"+out
string cout="c_"+out
string RHout="RH_"+out
Duplicate/O EC, $ECout
Duplicate/O EV, $EVout
Duplicate/O EFbulk, $EFbout
Duplicate/O EFsurf, $EFsout
Duplicate/O nbulk, $nbout
Duplicate/O pbulk, $pbout
Duplicate/O ni, $niout
Duplicate/O nsurf, $nsout
Duplicate/O psurf, $psout
Duplicate/O debye, $debyeout
Duplicate/O mueb, $muebout
Duplicate/O muhb, $muhbout
Duplicate/O mues, $muesout
Duplicate/O muhs, $muhsout
```

```
	Duplicate/O cbulk, $cbout
	Duplicate/O csurf, $csout
	Duplicate/O RHbulk, $RHbout
	Duplicate/O RHsurf, $RHsout
	Duplicate/O cond, $cout
	Duplicate/O RH, $RHout
	waveclear EC,EV,EFbulk, EFsurf, nbulk, pbulk, ni, nsurf, psurf, debye, mueb, muhb, mues,muhs, cbulk, csurf,
end

function FormatSign(name) //duplicates a wave, taking abs of the original and deleting all positive entries of the co
	string name
	string RH="RH"+name
	string RHpos="RH"+name+"pos"
	string RHneg="RH"+name+"neg"
	wave R=$RH
	wavestats/Q R
	Make/O/N=(V_npnts) $RHpos=R
	Make/O/N=(V_npnts) $RHneg=R
	wave Rp=$RHpos, Rn=$RHneg

	variable i=0
	do
		if(Rn[i]>0)
			Rn[i]=nan
		endif
		if(Rp[i]<0)
			Rp[i]=nan
		endif
		i=i+1
	while( i<(V_npnts+V_numNans))//use sum of entries and NaN's
	Rp=abs(Rp)
	Rn=abs(Rn)
	waveclear R,Rn,Rp
End

Function Poisson1D(w) //calculate V(z) starting from z=0 for surface into bulk. all energies w.r.t. constant EF
	//coefficient wave is wcoef
	wave w
	variable Ea=w[0],Na=10^w[1],Ed=w[2],Nd=10^w[3],ds=100 //ds is surface thickness in nm

	variable i=0
	variable k=8.62e-5, q=1.602e-19, h=6.626e-34, hbar=1.055e-34
	variable g=2, me=0.49*9.11e-31, mh=1.5*9.11e-31

	variable T=300, Eg=0.95
	w[10]=T//use only one T, pass it to bulk() and surf() functions
	variable EV=0, EC=Eg

	FindRoots/Q/L=0/H=(Eg) bulk, w
	variable EFb=V_Root
	FindRoots/Q/L=0/H=(Eg) surf, w
	variable EFs=V_Root
	variable Vbi=EFb-EFs //definition of built-in potential

	//calculate nb and ps for boundary conditions:
		Make/O/N=200 zwickelCBbulk, zwickelVBbulk,zwickelCBsurf, zwickelVBsurf
```

```
        wave DOS_CB, energy_CB, DOS_VB, energy_VB
        //include offset to set band edge to DOS edge at every T:
        Duplicate/O energy_CB, energy_CB_T
        Duplicate/O energy_VB, energy_VB_T
        energy_CB_T=energy_CB - (energy_CB[0] - EC)
        energy_VB_T=energy_VB - (energy_VB[199] - EV)
        //calculate carrier concentration from integration over DOS(E)*f(E):
        zwickelCBbulk=DOS_CB / (exp((energy_CB_T - EFb)/(k*T)) + 1)
        zwickelVBbulk=DOS_VB / (exp((-energy_VB_T + EFb)/(k*T)) + 1)
        zwickelCBsurf=DOS_CB / (exp((energy_CB_T - EFs)/(k*T)) + 1)
        zwickelVBsurf=DOS_VB / (exp((-energy_VB_T + EFs)/(k*T)) + 1)
        variable nbulk = areaXY(energy_CB_T,zwickelCBbulk,EC,2.5)
        variable pbulk = areaXY(energy_VB_T,zwickelVBbulk,-1,EV)
        variable nsurf = areaXY(energy_CB_T,zwickelCBsurf,EC,2.5)
        variable psurf = areaXY(energy_VB_T,zwickelVBsurf,-1,EV)

    //use EC(z) as V(z), all energies w.r.t. EF
    //boundary conditions: EC(0)=0.95-EFs, EC(inf)=0.95-EFb
    //use IntegrateODE() for 2 coupled eqns of order 1:
    // V'[x]=E[x] and E'[x]=q/eps*(Ni[V[z]]+p[V[z]]-n[V[z]])
    //IntegrateODE derivFunc,  cwaveName,  ywaveSpec
end
```